University of Bergamo
Department of Engineering and Applied Sciences

Additively manufactured aluminium alloys for light mobility: from material qualification to prototype manufacturing

Academic Supervisors:
Prof. Sergio Lorenzi
Prof. Marina Cabrini

Doctoral Dissertation of:
Davide Asperti
ID: 1046313

Ph.D. Cycle: XXXVIII
Academic Year: 2025 / 2026

Preface

The aim of this thesis is to perform a comprehensive analysis of the potential applications of LPBF-processed aluminium alloys in light electric mobility. The research employs a material-process-design approach, starting from the alloy selection and characterisation and progressing to the development, manufacturing and testing of full-scale prototypes

Chapter 1 introduces the context of light electric vehicles, with a specific focus on e-bikes. The materials-selection strategy described in this chapter is based on the stiffness- and strength-to-weight ratios of competing materials, using Ashby selection charts and taking into account the sustainability in terms of recyclability, embodied energy and durability.

Chapter 2 focuses on the corrosion behaviour of high-strength aluminium alloys, considered one of the fundamental aspects for extending component durability. Following a comprehensive review of the corrosion behaviour of traditional high-strength aluminium alloys, the focus moves to the LPBF-intrinsic features that govern the corrosion behaviour of LPBF high strength aluminium alloys. On this basis, the corrosion behaviour of a newly developed LPBF AlSi9Cu3 alloy is investigated under a range of different heat treatments. The influence of alloying elements on mechanical and corrosion performance is then assessed by comparing three LPBF alloys: an Al-Si-Mg alloy, an Al-Si-Cu alloy and Al-Cu-Mg-Ag alloy.

Chapter 3 provides an in-depth analysis of the mechanical behaviour exhibited by LPBF lattice structures in AlSi10Mg. The effects of relative density, unit-cell size and specimen geometry on stiffness, strength and deformation mode are analysed, with particular attention to the transition between bending- and stretch-dominated behaviours. The subsequent use of topological aspect ratio and Gibson-Ashby model makes it possible to identify the most suitable lattice structure configuration for integration into a bike-frame component.

Chapter 4 explores hybrid welding between LPBF AlSi10Mg and wrought 6xxx series alloys, using both fusion and solid-state joining techniques to evaluate their suitability in lightweight structures. A detailed analysis of gas tungsten arc welded joints between LPBF AlSi10Mg and AW6061-T6 is carried out to investigate metallurgical, mechanical and corrosion challenges. The second part of the chapter is dedicated to friction stir welding of hybrid joints between LPBF AlSi10Mg and AW6082-T6 under different welding parameters, in order to assess their mechanical and corrosion behaviour.

Finally, in Chapter 5, the material- and structural-level findings are synthesised to guide the development of two innovative e-bike prototype frames for light mobility. The first study concerns the conceptualisation, design, and manufacturing of a lattice-integrated component for the rear triangle of an aluminium e-bike frame, aiming to increase rear-triangle compliance without compromising safety factors. The second part presents the conceptualisation, design and manufacturing of a 3D-printed functional joints for a modular aluminium e-bike frame, addressing both functional and regulatory requirements. Subsequent full-frame mechanical tests demonstrate the reliability of the developed solution, in terms of estimated 10-year frame failure rate, with respect to traditional frames.

Table of contents

1 Materials selection and sustainability in light electric vehicles design

The present research activities are focused on the investigation of the mechanical and corrosion resistance properties of innovative high-strength alloys. These alloys have been designed for use in lightweight and hybrid modular electric vehicles, thereby supporting the advancement of active and sustainable mobility. In the initial phase of the project, the objective is to study and characterise new high-strength aluminium alloys and new technological solutions for the light mobility field, with the aim of improve the mechanical properties and reduce the weight of a bicycle frame, through the achievement of a Technology Readiness Level (TRL) of 4 - 5. Following the qualification stages, the project involves the conceptualisation and fabrication of a prototype lightweight modular vehicle with the aim of reaching, at the end of the research period, a TRL of 7. In this second phase, the activities focused on design and realised innovative bicycle frames, using different materials, in order to evaluate and compare the sustainability, the performances and the ergonomics. The use of Additive Manufacturing (AM) technologies enables the implementation of modular and detachable solutions, which are integral to the design of these frames. This ensure the rapid assembly of systems that are compatible with portable cycling tools.

1.1 Materials selection

The decarbonization of our society is one of the biggest challenges faced by scientists in this century. Based on the International Energy Agency (IEA), the main contributors to carbon emissions are electricity generation (42%), transportation (23%) and industrial emissions (19%) [1,2]. The European Commission state that, within the road transport, the urban mobility is responsible for the 40% of all CO_2 emissions [3,4]. In this framework, creating a smart, efficient and sustainable mobility system is a key factor. Two of the most important strategies to reduce the total emissions generated by vehicles focuses on weight reduction and use of electrified powertrain [5]. Lightweight design led to a reduction in fuel demand and a mitigation in CO_2 emissions. Over the past years, the use of bicycles for everyday urban trips has increased markedly in many cities worldwide, driven by growing environmental and health awareness as well as investments in cycling infrastructure and shared-mobility services. In parallel, the rapid uptake of electric bicycles has further expanded the role of two-wheeled light vehicles in urban mobility, lowering physical effort and enabling longer trips for a wider range of users [6]. Electric bicycles are distinguished from traditional ones by the integration of three additional components such as an electric motor, a storage battery and a battery controller. Weight reduction is mandatory for this vehicle in order to improve the battery efficiency and range. The lightweight design is not only the main driver in light mobility, as sustainability, performance modularity and, above all, safety remain fundamental. Despite this aspect, in the materials selection strategies, the topic of sustainability is strictly connected with the reduction of weight and the reduction of environmental costs. The most common and useful instruments that can

be used in the materials selection strategies are the Ashby charts, a scatter plots which displays two or more properties of many materials or classes of materials [7]. These charts are provided with guidelines used for selecting appropriate material as per requirements. As reported in Figure 1, the guidelines with a linear relation - i.e. E/ρ and σ_f/ρ – led to a materials selection based on the high stiffness to mass ratio and high strength to mass ratio for different structural configurations. For example, the E/ρ represent the loci of points for a structural configuration with axial load, while $E^{1/2}/\rho$ stand for structure with torsional loading [8]. It is evident that moving towards the upper-left corner of the graph results in an increase in the corresponding performance index. This is due to the fact that it serves to highlight materials that provide higher stiffness at a lower weight for the given design constraint [8].

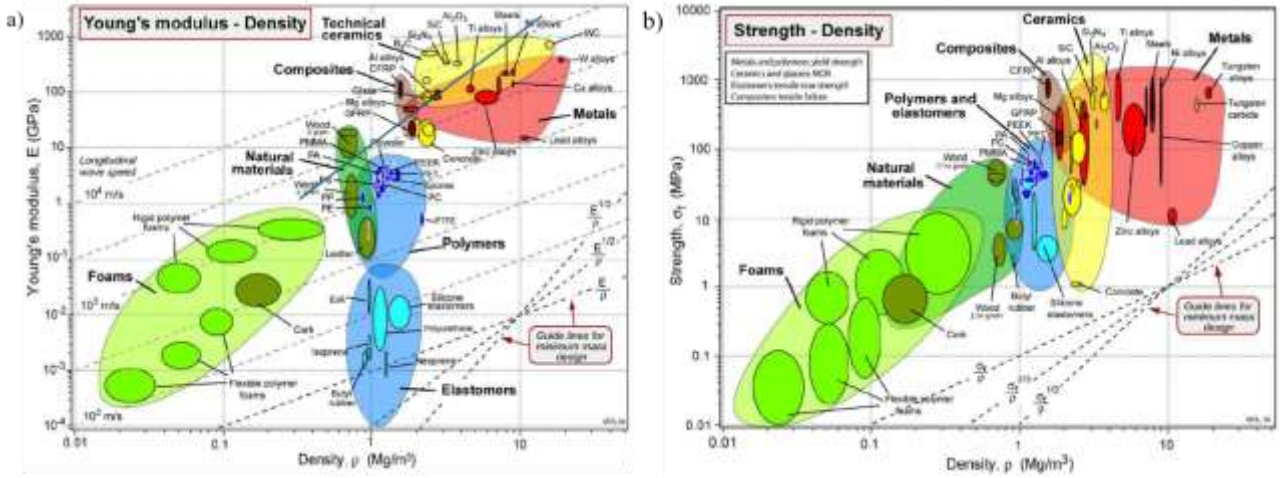

Figure 1 - Ashby chart of (a) Young's modulus versus density and (b) strength versus density [7].

Several studies reported that, in a bicycle frame, the tubular structures behave like beams subjected mainly to axial compression loads [9–11]. With regard to this scenario and to the aforementioned structural configurations, the appropriate guideline is E/ρ and σ_f/ρ. As demonstrated in Figure 2, the frame can be produced using a wide range of materials, including steel, aluminium alloys, Ti alloys, Mg alloys and composites. Within the composite materials, the best solution for a bicycle frame, could be the Carbon Fiber Reinforced Polymer (CFRP), leading to the highest stiffness to mass ratio and strength to mass ratio.

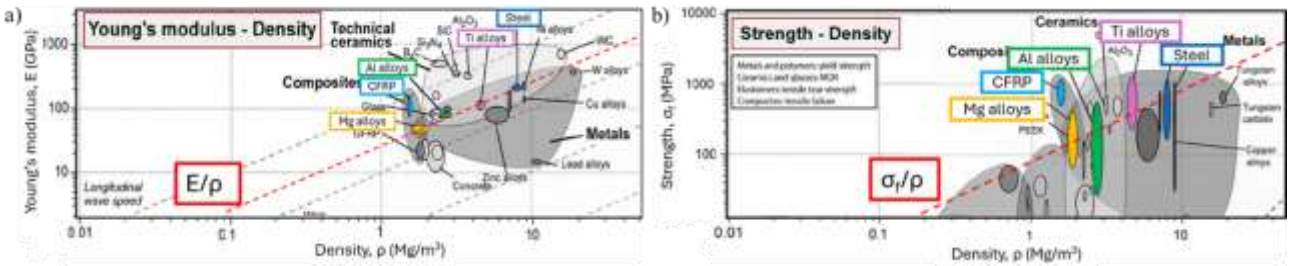

Figure 2 - Ashby charts of (a) E versus ρ and (b) σ_f versus ρ related to metals and composite materials.

Despite all of these materials can fulfill the strength requirements of a bicycle frame, there are dissimilar intrinsic properties that lead to different performance. A CFRP bicycle frame, due to the

different values of density, stiffness and resistance to deflection, exhibit significant distinct characteristics respect to the same frame made of other metals or composite material [12].

As previously stated, along with parameters such as stiffness and weight, the sustainability of materials has emerged as a pivotal constraint rather than a secondary criterion . This approach opens up to a conscious decision regarding the selection of materials, where the lightest option is not necessarily the optimal one. As illustrated in Figure 3, the energy per unit volume and per unit mass consumed in extracting and refining the materials is taken into account, including CO_2, NO_x and SO_x emissions [13]. It is evident from the data that aluminium and steel emerge as the most suitable solutions for the frame production, notwithstanding their increased weight respect to the composite-based solutions.

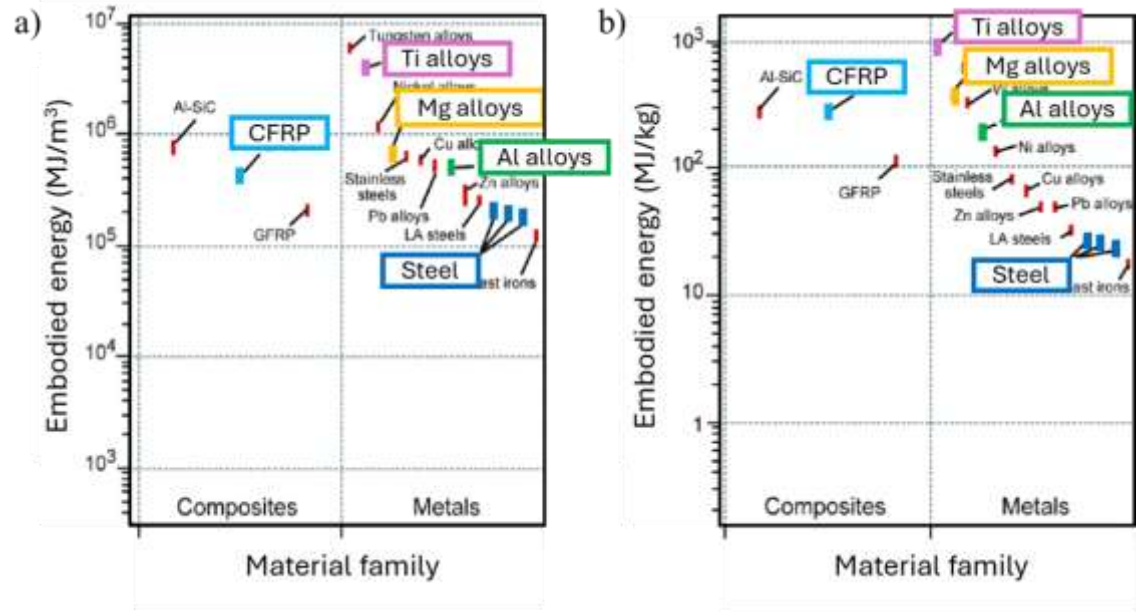

Figure 3 - (a) Energy per unit volume and (b) per unit mass related with material production.

Within the domain of light mobility, mostly when vehicle electrification is taken into account, the performance discrepancy between metallic frames and CFRP frames becomes less noteworthy, as the mass difference can be largely balanced by electric assistance. Furthermore, the employment of steel or aluminium has been proven to improve the overall sustainability balance, since metals are virtually infinitely recyclable without significant loss of properties [14,15].

Therefore, when designing a vehicle within the electric light-mobility context, and considering all the previously mentioned criteria, aluminium and its alloys arise as the most suitable choice for the development of an e-bike frame. The concept of a “sustainable vehicle” thus becomes a key design principle, integrating both environmental and performance requirements into the material-selection process.

1.2 New technology solutions: Additive Manufacturing

The introduction of the concept of “sustainable vehicle” exerts influence on the material selection process, as previously described. In a context where weight reduction, the use of recyclable materials

and, more generally, design aimed at making light mobility more sustainable are increasingly becoming the main paradigms, the choice and use of production technologies also becomes a fundamental aspect. In this context, additive manufacturing (AM) is an enabling technology capable of satisfying and further amplifying these benefits. It has been demonstrated by numerous studies that the “near-net-shape” nature of additive manufacturing leads to a substantial reduction in material waste when compared with traditional technologies. Furthermore, these processes have been shown to enhance the efficiency of the production process [16,17]. Comparative studies have demonstrated that the mass of the final component can be reduced by between 30 and 80 %, based on the geometry and design constraints, when the design is specifically adapted for AM [18]. In the context of light electric mobility, these aspects assume greater relevance. In the context of light electric mobility, these aspects assume greater relevance. In the specific case of a bicycle frame, and particularly for an e-bike, the integration of specific weight reduction and optimised geometries through AM allows for a reduction in weight while maintaining or improving mechanical performance, resulting in a direct benefit to energy consumption [19]. In this perspective, AM does not seek to replace existing production processes, but rather to serve as a design tool to integrate lightness, performance and sustainability.

One of the most distinctive aspects of AM is the design freedom afforded to the user. In the structural field, this suggests the feasibility of integrating variable thicknesses, localised reinforcements, internal cavities and geometric shapes derived from topological optimisation or generative design methods [20,21]. The implementation of these strategies ensures a targeted distribution of material, thereby guaranteeing the necessary levels of stiffness, strength, and durability. From a lightweight design perspective, lattice structures emerge as one of the most promising possible solutions. The use of these variable and programmable density structures in the light mobility industry enables precise modulation of stiffness and energy absorption capacity, resulting in components with a mechanical behaviour that is tailored to a specific application. AM also facilitates the integration of functional elements into a single component, overcoming the need for assembly of multiple parts in traditional frames. Such components may include internal passages for wiring, dedicated battery compartments, or modular fastening systems. The combination of geometric freedom and functional integration is set to provide AM with a strategic role in the development of innovative frames, moving beyond the conventional concept of a series of tubes to achieve a structure that is holistically optimised for performance, ergonomics and sustainability. The integration of AM into the design of light electric mobility vehicles further reinforces the choice of aluminium as the most suitable solution for sustainable design. The employment of aluminium alloys, produced by AM, has the potential to become a pivotal element in the design of lightweight structural elements for bicycle frames. In recent years, new high-strength aluminium alloys have been developed for additive processes, combining high mechanical strength, good toughness and adequate corrosion resistance [22].

Among the various additive manufacturing technologies, Laser Powder Bed Fusion (LPBF) is the most mature and widespread solution for the production of aluminium alloy components [23]. The elevated cooling rates and thermal gradients that are characteristic of this technology result in the formation of specific microstructures, which, while conferring enhanced mechanical performance, also give rise to critical issues [24]. LPBF technology has been shown to be capable of producing components with mechanical properties that are comparable to, and in some cases superior to, those of the corresponding cast or wrought alloys [22]. This technology is well-suited in the production of

small to medium-sized components, particularly those of a complex nature. In the field of light mobility, these components can be integrated into larger parts, where conventional technologies remain the optimal solution. However, LPBF of aluminium alloys is subject to certain limitations and critical issues, including high laser reflectivity, a strong tendency to oxidise, and, for some high-strength alloys, susceptibility to hot cracking [25,26]. This requires the optimisation of process parameters to limit these problems and, concurrently, avoid the formation of porosity, lack of fusion, or excessive residual stresses associated with the strong thermal gradients typical of this technology [24,27]. In order to address these issues, different strategies can be adopted, including the design of alloys with specific compositions to enhance the fluidity of the molten bath and reduce the susceptibility to hot cracking. Additionally, the application of post-process heat treatments, such as stress relieving, solubilisation or ageing treatment, can be implemented to reduce residual stresses and modulate the microstructure in order to optimise mechanical performance and corrosion resistance [28].

As discussed in this chapter, additive manufacturing, and more specifically, LPBF technology for aluminium alloys, is emerging as a pivotal solution for integrating lightweight design, mechanical performance and sustainability. In recent years, there has been rapid development in the field of aluminium alloy powders, with a wide range of commercial powders now available. These powders find use in the manufacture of components for a variety of industrial applications [29–32]. However, the employment of high-strength aluminium alloys, obtained by LPBF, requires a comprehensive understanding of the correlations between composition, processability and microstructure, and their impact on mechanical and corrosion behaviour. The following chapters will discuss the study of new high-strength LPBF aluminium alloys, with a particular focus on their corrosion behaviour. The study will explore innovative structural solutions promoted by AM, including lattice structures, and the challenges associated with integrating LPBF components into traditional structures using hybrid joints. The analysis will then conclude with the design and manufacturing of innovative bicycle frame prototypes, which will demonstrate the material-process-design approach, enabled by novel production technologies and advanced materials.

2 Corrosion behaviour of AM high-strength aluminium alloys

The applications of pure aluminium are somewhat limited due to its inherent properties. For this reason, it is commonly combined with other elements such as silicon, magnesium, copper or zinc [33]. The specific elements and their concentrations contribute to achieve specific physical and chemical properties. When weight reduction and mechanical performance are the primary drivers, such as in automotive or aerospace applications, the most used aluminium alloys are those belonging to the family of high-strength aluminium alloys [34]. Conventionally, the high mechanical properties of this type of aluminium alloy are achieved through precipitation hardening mechanism, typically involving alloying systems such as Al-Cu (2xxx series), Al-Mg-Si (6xxx series) and Al-Zn-Mg (7xxx series). However, the advent of additive manufacturing technologies has profoundly altered the criteria governing alloy selection and design, introducing new constraints related to solidification behaviour, microstructural features and defect susceptibility. Furthermore, conventional high-strength aluminium alloys demonstrate limited processability through AM technologies. In order to overcome this problem, during the last decades, new alloy systems have been developed specifically for AM [35].

This chapter provides an overview of high-strength aluminium alloys from the perspective of materials availability and processing methods. Particular emphasis was placed on the limitations of traditional alloys in AM processes, the rationale behind the development of new alloys for AM and the role of processing conditions and post-processing treatments on the resulting microstructure features, mechanical performance and corrosion behaviour.

2.1 Traditional high-strength aluminium alloys

Conventional high-strength aluminium alloys have been extensively developed and optimised for wrought and cast processing methods, where mechanical strength is primarily achieved through precipitation hardening mechanisms. The 2xxx (Al-Cu) and 7xxx (Al-Zn-Mg) series are the most widely used alloy families in high-performance applications [36]. The performance of these alloys can be improved and tuned for specific requirements by tailoring their microstructure, such as controlling the type, size and distribution of strengthening precipitates. In the case of high-strength aluminium alloys, this is mainly achieved through precise selection of heating rates, solution-treatment temperatures and ageing times.

In the 2xxx series, copper is the principal strengthening element. The presence of this alloying element promotes the formation of finely dispersed metastable precipitates during the ageing process, resulting in a substantial enhancement in yield and tensile strength [37]. The addition of magnesium is often a strategy employed to enhance the precipitation kinetics and thereby optimise the strengthening response of the material [33]. However, from an electrochemical perspective, Cu-rich intermetallic phases and precipitates exhibit a higher degree of nobility in comparison to the

aluminium matrix [37]. This difference promotes micro-galvanic coupling, leading to an increased susceptibility of the surrounding matrix to preferential dissolution in corrosive environments.

In the 7xxx series of alloys, the strengthening mechanism is reliant upon the combined addition of zinc and magnesium, which presence promotes the formation of strengthening precipitates during the ageing process [32]. Nevertheless, the presence of these alloying elements also increases chemical heterogeneity, particularly at grain boundaries, where solute segregation and precipitate formation are promoted.

Historically, the development of high-strength aluminium alloys has been focused on conventional manufacturing processes. In this scenario, the solidification conditions, deformation paths, heat treatment stages and alloy chemistry are meticulously controlled and extensively optimised to achieve the desired compromise between mechanical performance and corrosion resistance. However, the adoption of additive manufacturing technologies introduces significantly different processing environments. As already discussed, AM is mainly characterised by extremely high cooling rates and repeated thermal cycles markedly different from those of conventional processes. Consequently, these alloy systems designed for wrought or cast production technologies can exhibit several limitations during AM processes. Due to their wide solidification range and segregation tendencies, 2xxx and 7xxx series can exhibit a high susceptibility to solidification cracking if applied in additive manufacturing processes [31]. Moreover, the intrinsic need of AM parts for post-processing treatments, such as stress relief, may induce over-aging in these high-strength aluminium alloys, reducing their mechanical and corrosion performance [38]. As results, the application of traditional high-strength aluminium alloys in AM remains challenging, requiring optimised conditions and tailored chemical compositions modifications. These limitations drive the development of new aluminium alloys specifically developed for additive manufacturing processes.

2.1.1 Corrosion behaviour in traditional high-strength aluminium alloys

A considerable amount of research has been dedicated to the corrosion behaviour of traditional high-strength aluminium alloys, given their extensive utilisation in safety-critical structural applications [32]. In these alloys, corrosion is rarely uniform and is instead dominated by localised corrosion mechanisms [39]. These mechanisms arise from the intrinsic chemical and microstructural heterogeneity introduced by alloying and thermomechanical processing. In environments containing chloride, the trigger of corrosion attacks is typically associated with the localised breakdown of the passive oxide film, resulting in the occurrence of pitting corrosion [39]. Pit nucleation is frequently promoted by intermetallic particles or precipitates, whose electrochemical potential differs from that of the aluminium matrix. For instance, in Cu- and Zn-containing alloys, Cu-rich intermetallics typically function as cathodic sites, thereby accelerating the local dissolution of the surrounding aluminium matrix [40]. In wrought high-strength alloys, particularly those belonging to the 2xxx and 7xxx series, corrosion frequently propagates along grain boundaries, resulting in intergranular corrosion (IGC)[41]. This behaviour is significantly influenced by the distribution of precipitates and the presence of precipitate-free zones formed during the ageing process. A further critical issue identified in high-strength aluminium alloys is stress corrosion cracking (SCC), which is the result of an interaction between an IGC susceptible microstructure, tensile stress and a corrosive environment [42]. The susceptibility of SCC is known to be associated with the alloy composition, the thermal treatment history, and the residual stress state. SCC frequently represents a limiting factor in the selection of alloys and heat treatments for structural applications. The overall corrosion response of

traditional high-strength aluminium alloys is governed by the interplay between alloying elements, microstructural features introduced by processing and heat treatment, and local electrochemical heterogeneities. Whilst these mechanisms are well-established for conventionally processed materials, significant differences in their appearance may be observed in additively manufactured alloys, where microstructure, defects density and chemical distributions deviate from those of traditional products.

2.2 High-strength aluminium alloys for additive manufacturing

The majority of aluminium alloys that were initially implemented in the AM process were casting alloys. These alloys are distinguished by their near-eutectic compositions, which afford them excellent fluidity and low susceptibility to hot tearing. This combination of properties serves to minimise the risk of cracking during processing. Al-Si, Al-Mg or Al-Cu-Mg represent some of the initial materials employed in AM technologies [35]. However, due to the continuous development in AM, these alloys have become inadequate for applications requiring high mechanical properties. To overcome this issue, AM-tailored aluminium alloys with specific chemical composition have been developed in order to ensure good printability, avoid hot cracking and provide excellent mechanical properties.

Al-Si alloys, and particularly AlSi10Mg alloy, represent the most established and industrially mature type of aluminium alloy for additive manufacturing and, particularly, for laser powder bed fusion. The widespread uptake of this alloy can be attributed to its optimal solidification behaviour during the printing process. The high silicon content reduces the solidification range, improves fluidity and reduce the susceptibility to hot cracking [43]. The microstructure of LPBF-processed Al-Si alloys is characterised by the formation of a fine cellular structure, where a Si-rich eutectic network is established along the cell boundaries as a consequence of rapid solidification [44]. As reported by Revilla et al. [45], this finer as-built microstructure is highly heterogenous at the microscale. Finer cells in the melt pool centre (MPC), coarser cells in the melt pool boundary (MPB) and partially broken silicon network along the heat affected zone (HAZ). This fine microstructure contributes to relatively high strength in the as-built condition compared to conventionally cast counterparts. The presence of Mg enables the precipitation of hardening phases such as Mg_2Si, allowing further enhancement of mechanical properties [46]. Nevertheless, Al-Si-Mg alloys demonstrate intrinsic constraints with regard to achievable levels of strength. The strengthening effect of Mg-containing precipitates is comparatively negligible in relation to that of Cu-based systems [33], and peak mechanical properties frequently remain below the levels required for high-load structural applications. Notwithstanding this, Al-Si-Mg alloys are widely recognised as benchmark or reference materials for LPBF processes, offering high reliability and reproducibility.

In order to surmount the inherent limitations of Al-Si-Mg systems, considerable research efforts have been directed towards the development of Al-Cu alloys. It is evident that copper is a highly effective strengthening element in aluminium alloys. This is due to its strong precipitation hardening response, which has the potential to enable mechanical properties comparable to those of conventional high-strength wrought alloys [47]. A rapid solidification and repeated thermal cycling promote the formation of a supersaturated solid solution and a fine cellular microstructure. This process is accompanied by pronounced Cu segregation at cell and melt pool boundaries. Consequently, the as-built microstructure of LPBF Al-Cu alloys is characterised by the prevalence of

non-equilibrium Cu-rich phases [48]. While this microstructural feature provides a suitable basis for subsequent precipitation strengthening, it also makes Al-Cu alloys particularly sensitive to post-processing conditions. Consequently, post-processing heat treatments are imperative to activate the strengthening potential. For instance, Al-Cu-Mg-Ag alloys achieve its maximum strength through the presence of plate-like Al_2Cu precipitates, whose precipitation is attributable to homogeneous nucleation from nanometric Mg- and Ag-rich co-clusters during the early stages of the ageing treatment [49]. However, it is important to note that extensive solution and ageing treatments may substantially modify, or even partially disrupt, the fine microstructural features generated during LPBF. This underscores a fundamental trade-off between optimising strength and preserving the AM-induced microstructural refinement.

As discussed in the previous chapter, the steep thermal gradients and repeated thermal cycles intrinsic to LPBF processing give rise to elevated residual stresses and a microstructure that is both supersaturated and chemically heterogeneous. A stress-relief treatment is therefore usually required to reduce these stresses and to ensure the dimensional stability and structural integrity of AM components. In the case of precipitation-hardenable aluminium alloys, stress relieving constitutes a critical step due to the fact that the temperatures required for effective residual stress reduction may coincide with those determining microstructural evolution and precipitation phenomena [50]. Conventional stress-relief treatments (approximately 250-350 °C [24]) have been observed to induce partial over-ageing or microstructural coarsening, resulting in a reduction in strength and, in certain instances, the loss of the fine microstructural features generated during LPBF. Conversely, solution treatment and ageing are often necessary to activate precipitation hardening but may further result in the homogenisation of the microstructure and the inhibition of the benefits associated with rapid solidification [50]. Post-processing strategies for AM aluminium alloys must address the balance between mitigating residual stress, achieving microstructural homogenisation, and promoting precipitation strengthening. Several approaches have been advanced to address this challenge. For instance, T5-type treatments may be employed to preserve the as-built microstructure [51], and meanwhile the optimisation of process parameters, such as elevated build platform temperatures, may be used to reduce residual stresses during fabrication [52].

2.2.1 Corrosion mechanisms in AM high-strength aluminium alloys

As previously discussed for conventional high-strength alloys, the combination of elements such as Cu, Zn and Mg generates chemically heterogeneous microstructures, in which precipitates, depleted zones and intermetallic phases give rise to galvanic micro-pairs. These have been shown to be responsible for pitting, IGC and SCC. In the context of alloys engineered for AM, particularly those designated for LPBF, this inherent heterogeneity is further exacerbated by macro- and microstructural characteristics arising from the process itself. These include the occurrence of overlapping melt pools, anisotropic eutectic networks, and local composition gradients.

It has been demonstrated by a considerable number of studies that, in Al-Si/Al-Si-Mg LPBF alloys (for example, AlSi10Mg), corrosion behaviour is subject to strict control by the non-equilibrium microstructure that is developed during the printing process. Following immersion in chloride-containing solutions, marked selective corrosion of the α-Al cells is observed in the MPB and HAZ areas, driven by the galvanic coupling between the matrix and the silicon phase [53–58]. Rubben et al. [59], attributed this behaviour to the local discontinuity of the Si network, which in these regions loses the continuous shielding character that is observable elsewhere.

In LPBF alloys with higher copper content, such as the 2xxx series Al-Cu alloys adapted to AM, the Cu-rich precipitates present along the MPBs and in the interdendritic zones introduce an even more pronounced galvanic component [60]. These particles, functioning as noble cathodes within the matrix, enhance the selective dissolution of aluminium and promote the initiation of deeper and more extensive attack, while preserving a predominantly inter-melt-pool attack morphology. In certain instances, this selective damage has been observed to be concomitant with the emergence of microcracks in thermally altered regions, in the presence of high residual stresses [61].

Another critical factor for the corrosion behaviour of LPBF alloys is the presence of defects and residual stresses. The presence of surface defects, such as partially melted particles, surface porosity, or topographical irregularities, has been demonstrated to compromise the formation and stability of the oxide film [62,63]. This, in turn, has been shown to promote the initiation of localised attacks. Concurrently, volumetric defects and residual stress fields have been observed to increase susceptibility to stress corrosion cracking, acting as preferential sites for stress concentration and co-localisation of corrosion and deformation [45].

2.2.2 Effect of heat treatment on corrosion behaviour

The corrosion behaviour of LPBF aluminium alloys is also strongly influenced by post-process heat treatments, which have the capacity to modify both the microstructure and residual stresses.

In Al-Si-Mg systems, stress relieving treatments performed at low temperatures do not alter the melt pool macrostructure. However, they do cause coarsening and greater discontinuity of the Si network at the melt edge. This leads to a much more aggressive selective attack than in the as-built case. It is evident that high-temperature treatments profoundly modify the microstructure, thereby reducing susceptibility to selective attack. However, this process also results in the formation of a more porous and less protective surface oxide film compared to that observed in the as-built case [59,64–67]. In the context of Al-Cu alloys, the high-temperature heat treatment has been observed to result in a modest enhancement in corrosion resistance, accompanied by a selective attack morphology, albeit with a reduced penetration depth. Notwithstanding this enhancement, the elevated nobility of the Cu-rich particles sustains a pronounced local cathodic component and elevated anodic currents in comparison to Al-Si-Mg systems, thereby preserving a considerable sensitivity to localised corrosion [38,48,60].

As discussed in previous sections, conventional high-strength Al-Cu and Al-Zn-Mg alloys offer excellent mechanical performance. However, their processability by LPBF and their corrosion behaviour remain critical issues due to hot-cracking susceptibility, residual stresses and poor corrosion performance. In contrast, Al-Si-Mg alloys, such as AlSi10Mg, demonstrate excellent processability but their intermediate mechanical properties can be a constraints for application requiring high structural integrity. Consequently, recent research has concentrated on Al-Si-Cu alloys, which combine good printability with enhanced strength. The present study aims to investigate the LPBF AlSi9Cu3 system in detail, with a focus on its corrosion response under different heat treatments.

2.3 Corrosion behaviour of new LPBF high-strength aluminium alloy

As previously discussed, through proper heat treatment Al-Si-Mg alloy can exhibit satisfactory mechanical performance. In order to further enhance strength, hardness and, at the same time, ensuring the best mechanical properties for both as-built and heat-treated conditions, the addition of Cu in Al-Si-Mg alloys could represent a suitable approach [37,68]. Another commonly added alloying element to improve the temperature performance of Al-based alloys is Fe. Nonetheless, Fe must be kept at a low percentage as it might cause a decrease in ductility and promote brittle phases that could negatively affect the material performance [69]. Thanks to this combination of alloying elements, Al-Si-Cu alloys with small quantities of Fe and Mg have been widely employed for automotive applications, where high mechanical performance combined with light weight for reducing fuel consumption are required [70]. Among them, the AlSi9Cu3 is one of the most widely used alloys in the automotive industry [71]. Its extensive use in high-pressure die casting is primarily driven by its optimal balance of castability, strength, and machinability, coupled with a well-established response to heat treatment [72]. The good processability of AlSi9Cu3 via LPBF is guaranteed thanks to the high Si content [73], while the presence of 3 wt.% of copper makes it an age-hardening alloy [74]. In addition, the high cooling rates inherent to LPBF promote a strong supersaturation of the solid solution, which further enhances the achievable strength levels [71,75]. As demonstrated by numerous studies, the LPBF processing method yields a fine cellular microstructure, distinguished by a supersaturated α-Al matrix encircled by a Si-rich network and meticulously dispersed Cu-rich phases. This microstructure is significantly distinct from the coarse dendritic structure that is characteristic of cast AlSi9Cu3 alloys. However, the addition of copper provides high strength but usually compromises the corrosion resistance due to galvanic coupling between Cu-rich precipitates and Al matrix [76]. In conventionally processed AlSi9Cu3 alloys, corrosion has been reported to occur preferentially at Cu- and Fe-rich intermetallics. These act as cathodic sites, thereby promoting localised dissolution of the surrounding matrix [72].

In the current context, where sustainability and reduction of environmental footprints are of growing interest, the scientific research focus is moving towards the use of sustainable and durable solutions. This perspective highlights the importance of corrosion prevention, as it extends the service life of structures and decreases the need for raw materials to replace them. Previous studies have mainly focused on the corrosion behaviour of LPBF AlSi10Mg [53,54,77] and Al-Cu alloys [60], showing that corrosion behaviour is strongly linked to the melt pool microstructure and the second phases distribution. Specifically, it has been demonstrated that microstructural heterogeneities at melt pool boundaries and in heat-affected zones play a pivotal role in the initiation and propagation of corrosion in LPBF aluminium alloys [61]. Conversely, conventional AlSi9Cu3 alloy produced by casting have been extensively studied [78–81], but the unique solidification conditions of LPBF, leading to oversaturation of the Al matrix and redistribution of Cu- and Si-rich precipitates, suggest that corrosion mechanism could be significantly different. To the best of the authors' knowledge, no systematic investigation on the corrosion behaviour of LPBF AlSi9Cu3 alloy under different heat treatments has been reported so far, which motivated the investigation presented in this chapter.

2.3.1 AlSi9Cu3: materials and methodology

A collaboration with the Polytechnic University of Turin enabled the study of the corrosion behaviour of an innovative Al-Si-Cu-Mg alloy obtained using Laser Powder Bed Fusion technology.

A commercial gas-atomized AlSi9Cu3 powder, supplied by ECKA Granules, was used as feedstock material for the LPBF sample production. The chemical composition of the feedstock powder provided by the supplier is reported in Table 1.

Table 1 - Chemical composition (wt.%) of the feedstock powder.

Elements (wt.%)	Al	Cu	Si	Mg	Mn	Zn	Fe
AlSi9Cu3	bal.	3.0	9.3	0.29	0.21	0.81	0.91

Cylindrical specimens used for hardness and corrosion tests (15 mm diameter, 5 mm height, oriented with the axis of revolution parallel to the building platform) were produced using an EOS M270 Dual Mode 3D under a high-purity Argon atmosphere. The machine is equipped with a continuous Nd: YAG fiber laser capable of delivering up to 200 W of power, with a laser spot diameter of 100 μm. The LPBF process parameters were applied based on the optimization study previously conducted by the authors [82].

The specimens were studied in as-built (AB) condition and after different post-process heat treatments, as summarised in Table 2. A low-temperature direct aging (DA) heat treatment was carried out at 160 °C for 3 hours. This parameter was selected on the basis of thermal treatments specifically developed for PBF-ed alloys, with the aim of enhancing mechanical properties without substantially altering the microstructure [28,83]. In addition to DA, three high-temperature heat treatment were applied. The first consisted of a solution treatment followed by water quenching (S), designed to isolate the effect of a lone solubilisation step at high temperature. The second was a T4 heat treatment, involving solutioning quenching and subsequent natural ageing at room temperature. Although this treatment is typical of Al-Cu alloys [60], it was selected in this study to investigate the influence of natural ageing on an alloy similar to AlSi10Mg but containing a significantly higher Cu content. Finally, a T6 heat treatment was performed, combining solutioning, quenching and artificial ageing. While T6 is the standard condition for Al alloys [71], in this study both the solutioning and ageing steps were consciously shortened to evaluate their effect and to explore the potential for industrial applicability to LPBF AlSi9Cu3. This experimental design allowed the individual roles of solution treatment, natural ageing, and artificial ageing to be distinguished, while the DA condition provided a useful comparison with alternative precipitation strategies commonly investigated in LPBF alloys.

Table 2 - Heat treatments performed.

Heat treatment	Solubilization conditions	Cooling rate	Ageing conditions
DA	-	Air cooling	160 °C for 3 h
S	510 °C for 1.5 h	Water quenching	-
T4	485 °C for 1 h	Water quenching	25 °C for 72 h
T6	510 °C for 1.5 h	Water quenching	160 °C for 2 h

Metallographic investigation

Microstructural analysis on AB and heat-treated conditions was performed on cross sections parallel to the building direction. In order to obtain a surface finishing suitable for micrographic analysis, the specimens were mechanically ground with SiC emery papers up to 4000 grit and then polished with a 1 µm diamond suspension. The microstructures were revealed by chemical etching with Keller reagent and analysed using a Keyence VHX-7100 digital-optical microscope and a Zeiss Sigma 300 field emission scanning electron microscope (FESEM), equipped with an Oxford x-act probe for energy-dispersive X-ray spectroscopy (EDS). Vickers hardness tests were carried out applying a 1 kg load for 15 s, according to ISO 6507. A nanoindentation mapping was done in order to characterise the mechanical properties of the microstructure. This analysis was done using Park Systems NX-10 atomic force microscope with a NM-RC-SEM cantilever, a single crystal diamond tip with a resonant frequency of 750 kHz and a spring constant of 350 N/m specifically designed for nanoindentation. The analysis was performed in displacement-controlled mode with a maximum depth of 70 nm. A fine spatial resolution of 750 nm was used to cover an area of 50 µm x 50 µm. The loading and unloading speed were set to 0.02 µm/s with a sampling rate equal to 100 Hz.

Electrochemical test

Electrochemical impedance spectroscopy (EIS) and potentiodynamic (PD) polarization tests were performed with an Ivium CompactStat potentiostat, in a 1 L glass cell (according to ASTM G5) with two graphite electrodes and a saturated calomel reference electrode (SCE) placed in a Luggin probe. The electrochemical tests were conducted using a (PTFE) sample holder, with an exposed area of 0.8 cm^2. To ensure optimal surface preparation, the specimens were ground with SiC papers up to 4000 grit, followed by a polishing with a 1 µm diamond suspension. Then, the specimens were degreased using acetone and then a passivation process was performed in a dryer for 48 h at room temperature. EIS and PD tests were conducted at room temperature (23 ± 2 °C) in an aerated solution with 1 g/L sodium chloride and 41.18 g/L sodium sulphate. The selection of this solution was made with the aim of avoiding an excessively aggressive environment, as evidenced by previous research conducted on the AlS10Mg alloy [60]. Before the EIS tests, a stabilization phase was carried out for 3600 s, with a monitoring of the open circuit potential (OCP). Subsequently, the EIS spectrum was obtained with a sinusoidal polarization of 10 mV amplitude in a frequency range between 0.01 and 10'000 Hz, with 5 frequency values collected for each decade. After the EIS tests, the OCP was monitored for 300 s, until a stable value was reached. Then, the PD tests started, with a potential scanning rate of 10 mV/minute, starting from − 10 mV with respect to the OCP, up to an anodic current density of 1 mA/cm^2. In the potentiodynamic curves, the ohmic drop was corrected using the ohmic resistance value of the solution, which was obtained from the EIS spectrum in the high frequency range. A minimum of two specimens were tested for each condition.

To characterise the stability of the aluminium oxide and the effect of high-temperature heat treatment on its stability, electrochemical impedance spectroscopy tests were carried out in aerated solution with 0.5 g/L sodium chloride and 41.18 g/L sodium sulphate every 3 hours up to 130 h of immersion. At the end of the test, the specimens were washed with distilled water, rinsed with acetone in ultrasonic bath and dried. The morphologies were observed by means scanning electron microscopes.

Intergranular corrosion test

Susceptibility to selective corrosion was assessed in accordance with EN ISO 11846 standard (Method B). The specimens were mechanically ground with SiC papers up to 2400 grit. The initial diameter and height were measured with a Vernier caliper. The samples were then degreased with acetone, immersed for 3 minutes in a sodium hydroxide solution (8 % by weight at 55 ± 2 °C), rinsed in distilled water, immersed for 2 minutes in concentrated nitric acid, rinsed again in distilled water and dried. Subsequently, the specimens were immersed in the test solution, containing 30 g/L sodium chloride and 10 mL/L concentrated hydrochloric acid, at room temperature for 24 h. The temperature of the test solution was maintained within a range of 21–25 °C. Afterwards, the samples were rinsed in distilled water and dried. Corrosion products were removed with a non-metallic brush, followed by a systematic rinsing in distilled water, then immersed in an ultrasonic bath of acetone and subsequently allowed to dry. The mass loss during the test was measured through the difference between the initial mass of the specimen and the one measured after the immersion period, measured with a Sartorius analytical balance (Readability 0.01 mg). To ensure the repeatability of the results, weighing was repeated three times. A metallographic section perpendicular to the exposed surface was then evaluated in order to determine the presence, depth and morphology of the corrosion attacks

Volta potential measurements

Scanning Kelvin Probe Force Microscope (SKPFM) analyses were performed using Park Systems NX-10 atomic force microscope. To investigate the distribution of the surface potential, topographic and potential measurements were acquired simultaneously with an ElectriMulti75-G cantilever with a resonant frequency of 75 kHz, a spring constant of 3 N/m and a Pt-covered tip with a radius of less than 25 nm. Maps with variable sizes ranging from 100 x 100 μm to 10 x 10 μm were recorded with a scan frequency ranging from 0.05 to 0.02 Hz. The measured potential signal between the tip and the sample corresponds to the difference between the probe's work function and the surface, which is directly related to the Volta potential of the material. A bias was applied to the tip, and to ensure consistency with the polarity of the Volta potential, the recorded potential was inverted.

2.3.2 Results and Discussion

Analysis of the microstructure

The FESEM analyses reported in Figure 4a highlighted microstructural differences in the grain structures between the centre and the boundary of the melt pool. In particular, microstructure is constituted by a α-Al cells matrix surrounded by a network enriched in second phases, as confirmed by FESEM micrographs acquired in BSD mode (Figure 4b,c). At higher magnification, this network resulted finer within the melt pool centre (MPC), whilst at the melt pool boundaries (MPB) it becomes slightly coarser. In addition, the AB specimens exhibited a heat-affected zone (HAZ) near the MPB, where the network appeared fragmented. The presence of this region can be ascribed to the overheating of the underlying layer during the printing process of a new layer, as already postulated in a study on LPBF AlSi10Mg by Thijs et al. [84]. The differences among these regions are not only microstructural but also compositional. EDS analyses performed at low magnification (Figure 4e) clearly revealed that silicon is concentrated within the network. Consequently, the Si presence appears more finely distributed in the MPC region due to the smaller network size. In contrast, the silicon-enriched network is more visibly developed at MPB. In the HAZ region, the Si distribution becomes

finer and more uniform again as a result of the network fragmentation. Copper follows a similar trend, though its cellular distribution is not clearly visible at MPB. and it is significantly less abundant than expected, suggesting that the local thermal history may have caused Cu to partially re-dissolve into the matrix due to overheating during layer deposition. High-magnification EDS maps indicate that Cu is concentrated in small, localized spots within the Si-enriched network (Figure 4d). These precipitates could be likely attributable to the Al_2Cu phase due to the high Cu content of this alloy. This hypothesis is supported by Fousova et al. [85] who corroborated the occurrence of Al_2Cu phase within the microstructure of an Al-Si-Cu alloy with a very similar chemical composition manufactured by LPBF.

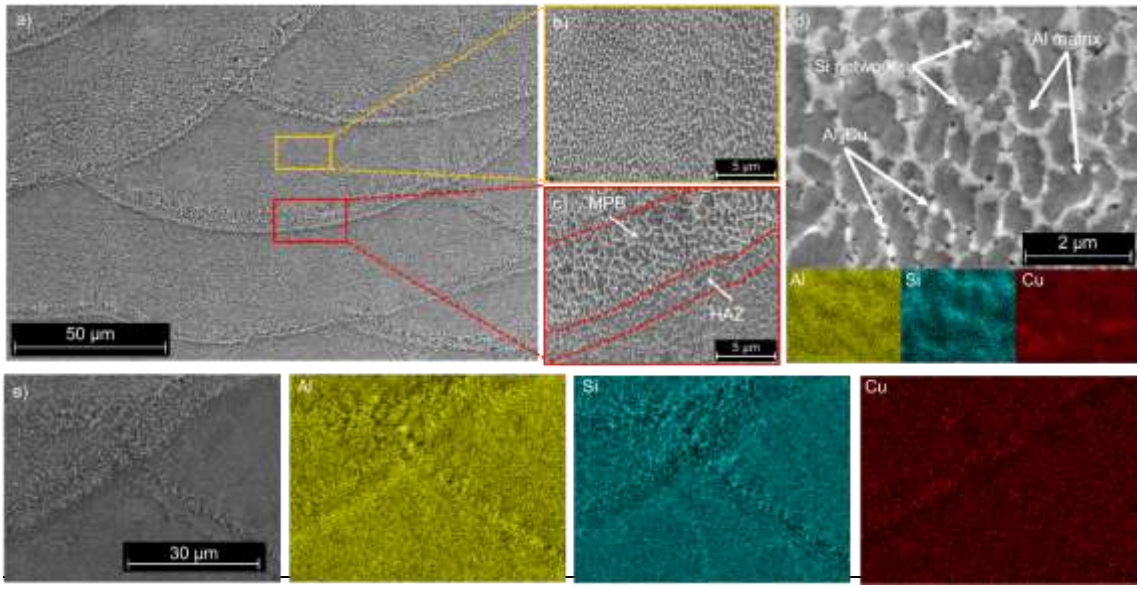

Figure 4 - Low-magnification FESEM micrograph of the AlSi9Cu3 alloy in AB condition (a) with higher magnification images highlighting (b) melt pool core and (c) boundary. (d) High-magnification FESEM micrograph with second phase morphology in the AB condition and relative main element distribution EDS maps. (e) Low magnification EDS maps highlighting Al, Si and Cu distribution inside the melt pool in the AB condition.

Figure 5 presents a correlative analysis of the AlSi9Cu3 alloy in its as-built condition, in which microstructural observation is accompanied by High-Speed Nanoindentation Mapping (HSNM). As illustrated in Figure 5a, the image provides a clear visual representation of the melt pool structure typically observed in LPBF materials. As previously outlined, MPC can be distinguished from MPB due to the varying solidification conditions, which result in local variations in microstructure and alloy element distribution. As demonstrated in Figure 5b, the nanoindentation map reveals a heterogeneous distribution of local stiffness, which reproduces the microstructural "footprint" observed in Figure 5a. Along the area associated with the MPB, regions exhibiting a divergent local elastic response in comparison to the MPC regions can be identified. A similar observation was reported by Dedry et al. [86] who found higher stiffness in LPBF AlSi10Mg in areas with a higher silicon content compared to depleted areas. As reported by Rossi et al. [87], the measured stiffness is particularly sensitive to local variations in microstructure and composition on a micrometric scale, and the combination with electron microscopy allows the construction of a true correlative mechanical microscopy.

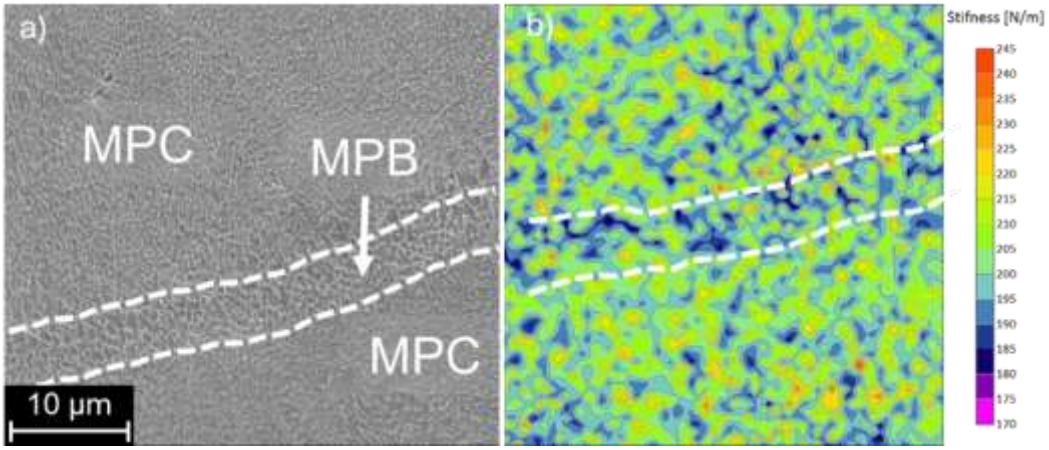

Figure 5 – (a) FESEM micrograph and (b) nanoindentation map on AB alloy AlSi9Cu3. Scan size: 50 x 50 μm^2.

For the studied alloy, T5 direct ageing (DA) heat treatments, with ageing temperatures ranging from 150 to 180 °C and ageing times between 2 and 6 hours, were typically adopted to slightly reduce residual thermal stresses while also preserving the remarkable AB microstructure, which is responsible for the alloy distinctive mechanical properties while also preserving the remarkable AB microstructure, which is responsible for the alloy distinctive mechanical properties [88]. In this work, T5 heat treatment was performed at a temperature of 160 °C for 3 h. The micrographs shown in Figure 6 were obtained via SEM on the DA-treated sample. The microstructure and melt pool configuration were very close to that of the AB condition, as expected. In addition, no significant alterations were observed in the size or distribution of Si and Cu precipitates. Similarly, EDS analysis showed a MPB with a different distribution of Cu-rich phases, with a higher concentration at the boundaries (Figure 6c). The HAZ showed a difference in Cu concentration, with a lower amount of Cu with respect to the adjacent regions. The temperature of the DA heat treatment is lower than the peak temperature for precipitation, coarsening and spheroidization of the Si precipitates, which was proved to be around 273 °C [50,88]. However, this process can still promote the formation of secondary phases that are rich in silicon [89]. Alongside, despite Cu usually exhibits a low solid-state diffusion within the Al matrix at room temperature, its diffusion capacity is known to sensibly increase at higher temperatures, resulting in the coarsening of Cu-rich precipitates [90]. Even though both time and temperature are too low for promoting Si precipitation, DA heat treatment might have led to the formation of Si- and Cu-rich precipitates, which however remained undetectable since they are at the micrometer scale. Santos et al. [91] reported the coarsening of the Al_2Cu phase in an Al-Si-Cu alloy following ageing treatments in a temperature range between 160 and 190 °C.

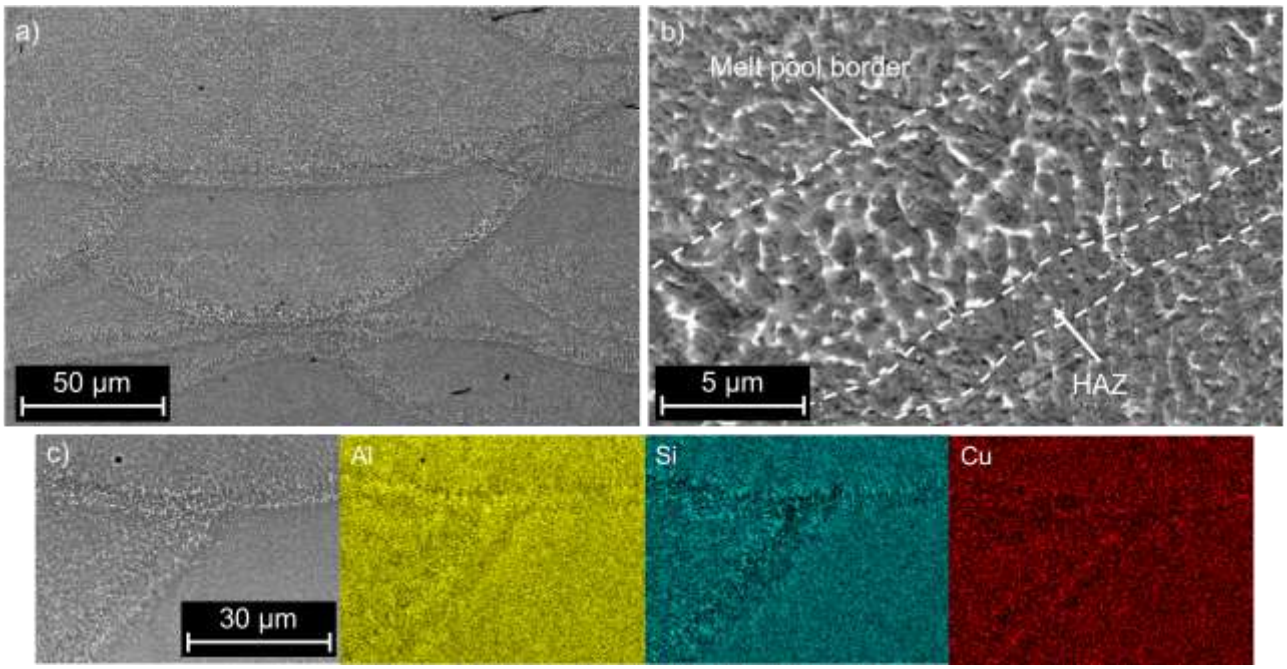

Figure 6 - (a) Low magnification FESEM micrograph of the AlSi9Cu3 alloy in DA condition with (b) higher magnification image highlighting melt pool core and boundary. (c) Low magnification EDS maps highlighting Al, Si and Cu distribution inside the melt pool in the DA condition.

Heat treatment at higher temperatures resulted in significant modifications of the microstructure (Figure 7). The heat treatment named S led to a complete breakdown of the Si- and Cu-rich network and a less defined melt pool structure (Figure 7a). In fact, according to studies already published on similar composition, solution heat treatment at higher temperatures activates the interdiffusion of Si within the α-Al matrix that leads to the breakup of the network [50] and to a redistribution of soluble phases containing Cu and Mg in the solid solution [83]. As shown in the higher magnification micrograph (Figure 7b) and confirmed by the EDS map (Figure 7c), the microstructure consists of coarse and globular Si particles while Cu remains dispersed within the Al matrix. The effects of the T4 heat treatment on AlSi9Cu3 alloys are very similar to those of the S heat treatment (Figure 7d). The absence of marked microstructural differences (Figure 7a,d) suggests that both the slight variation in solutioning temperature and the natural ageing process had a negligible effect on microstructural evolution. At higher magnification (Figure 7c,f), the microstructure was characterized by coarse Si precipitates, while Cu segregated into fine precipitates [38,92]. The FESEM micrographs of the T6 condition reported in Figure 3g showed a complete disappearance of the MPB and the presence of large Si particles. The latter are probably the result of the rupture of the Si network and the subsequent coarsening during the solution heat treatment. EDS analysis confirmed the additional presence of slightly coarser Cu-rich precipitates.

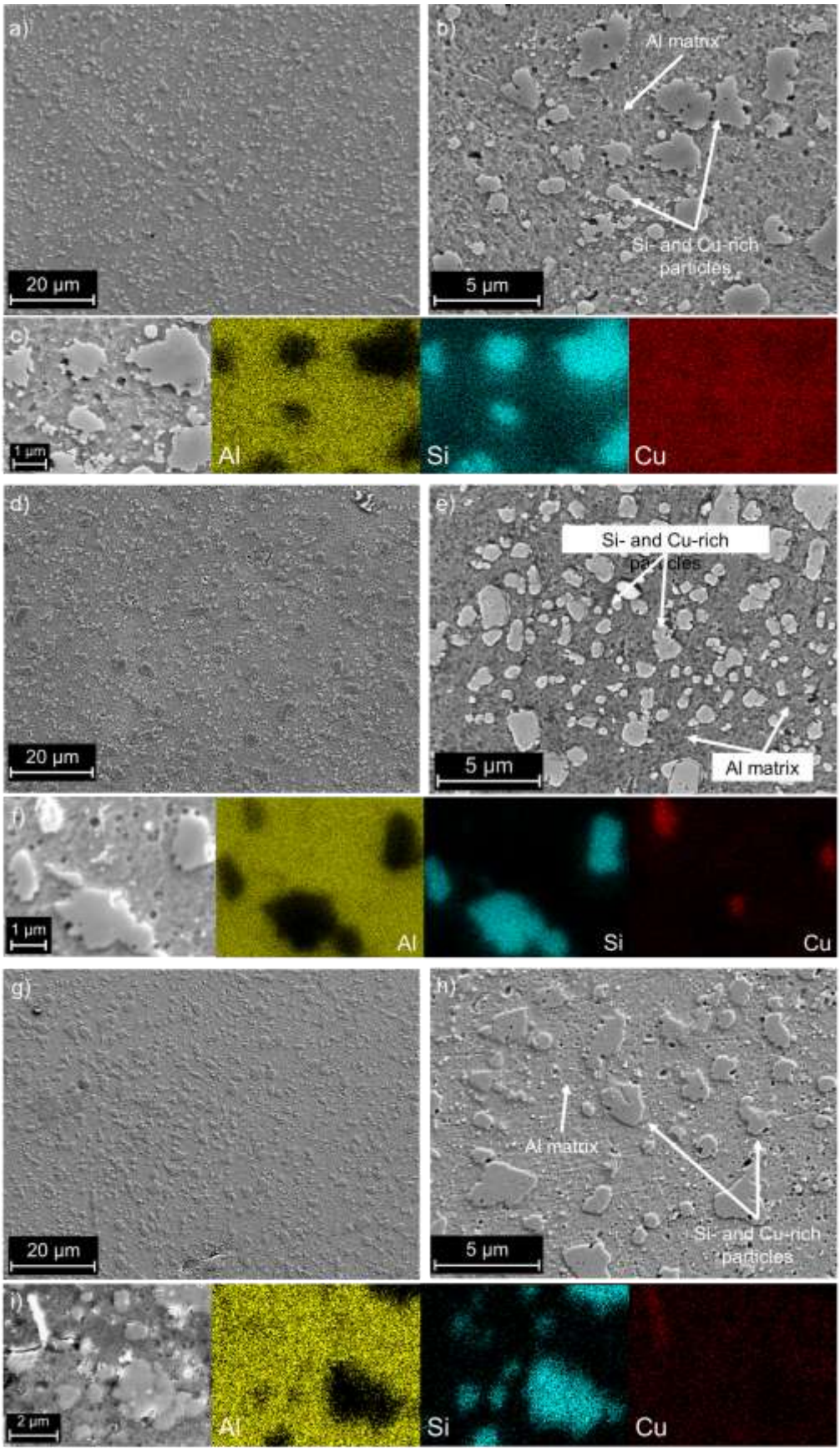

Figure 7 - Low-magnification FESEM micrograph, with second phase morphology and relative main element distribution, of the alloy AlSi9Cu3 after S (a,b,c), T4 (d,e,f) and T6 (g,h,i).

To gain a deeper understanding of the phase transformations and the evolution of second-phase particles induced by the applied heat treatments, XRD was used as a complementary technique alongside SEM and FESEM microstructural investigations and EDS compositional analyses. The XRD patterns, reported in Figure 8, were analysed to identify the crystalline phases present under each treatment condition. Peaks of Al and eutectic Si were distinctly recognizable in each condition. However, Si peaks appear more intense after T4, S and T6. Indeed, the major precipitation of Si phases out of the supersaturated solution coupled with the network dismantle and particles coarsening increase the amount of detectable Si during the analysis, increasing the Si signal and therefore the peak intensity. On the other hand, no significant difference could be reported observing the peaks after DA compared to the AB condition, suggesting that the Si network is almost unaltered by the low-temperature heat treatment, and that no significant precipitation had taken place, confirming what was already observed by image analysis. Small peaks of minor phases rich in Cu and Fe could also be observed. In particular, Al2Cu phases could be detected in all conditions. As observable in Figure 4 and Figure 5, the Cu-rich compounds are present in the network along with the eutectic Si in both AB and DA conditions, whereas they appear as bigger precipitates in the S, T4 and T6 conditions. It is worth noting that a higher amount of Cu in solution can be detected after S, as evidenced by the phase map (Figure 7c). Indeed, the higher solutioning temperature, which exceeds the Al2Cu melting one, i.e. 507 °C [93], presumably led to a solutioning of the Cu-rich phases, causing an enrichment in Cu of the solid solution. This enrichment is further increased by the absence of the ageing treatment, either natural or artificial, following the solubilization step, as happens for T4 and T6. Additionally, more minor peaks can be spotted in the XRD pattern of T4, S and T6 conditions: these minor peaks are more likely to be associated with phases like Al_7Cu_2Fe, Al_5FeSi and Al_2CuMg. However, their detection through XRD analysis is challenged by their small amount and reduced size, which hinders their identification through map analysis; indeed, their peaks tend to be small and most of them overlap with bigger peaks like Si and Al. Even though the ageing following the solubilization step in the T6 had increased the amount and size of phases, as previously described, no significant differences in the peaks between S and T6 could be evidenced, presumably due to a coarsening of the phases below the detectability of the XRD analysis.

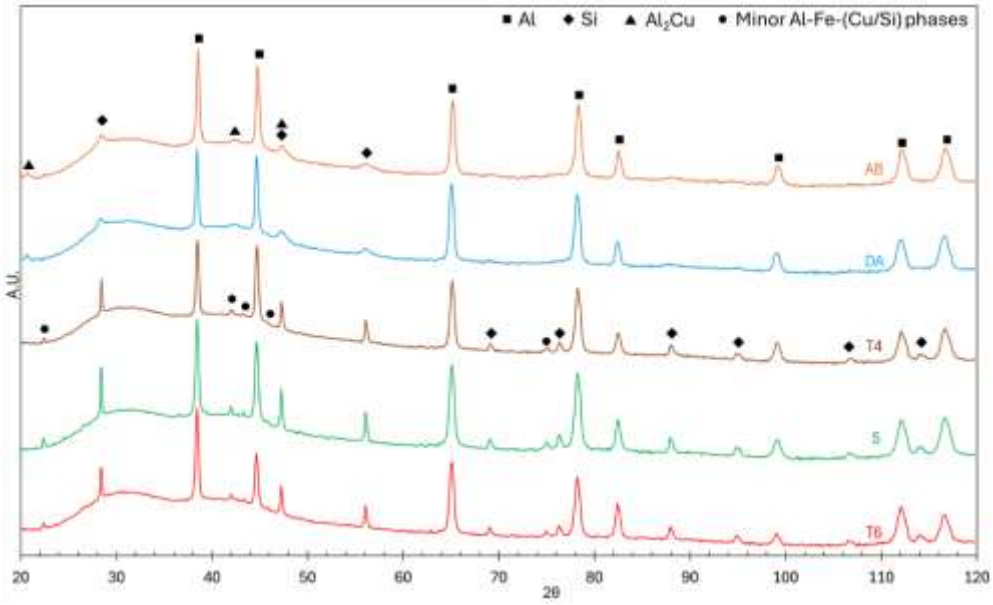

Figure 8 - XRD pattern of the alloy AlSi9Cu3 in the AB condition and after different heat treatments.

Indeed, to correlate the microstructural and phase changes induced by the different heat treatments with the mechanical response, Vickers microhardness measurements were carried out on all samples. The results of these measurements are summarized in Figure 9, which shows the hardness values for all the investigated heat treatment conditions. The alloy in the AB condition exhibited relatively high hardness, due to the rapid cooling rates characteristic of the LPBF process and the related metallurgical advantages previously described. The AB AlSi9Cu3 hardness was significantly higher than its as-cast counterpart [94]. Following DA, a slight increase in hardness was detected, with values comparable to those reported by Lagalante et al. after a similar treatment (160 °C for 8 h) [72]. The same authors demonstrated that this increase can be ascribed to a strengthening mechanism related to the formation of finely dispersed Si-rich secondary phases, which hinder dislocation motion. The relatively low Vickers hardness observed in the S condition was consistent with the XRD and metallographic analyses (Figure 8 and Figure 6), which revealed the segregation of coarse Si-rich particles that proved to be ineffective in enhancing the material mechanical strength. Furthermore, Bosio et al. [95] reported that similar Al-Si-Mg-Cu alloys subjected to solution treatments exhibited also grain coarsening, which contributes to the mechanical properties deterioration. The T4 alloy exhibited a partial response to natural ageing and a consequent increase in hardness, although the values remained lower than those of the AB and DA conditions. This thermal treatment is typically employed for Al alloys containing copper, due to the formation of Cu-rich strengthening phases. In fact, Al-Si-Cu-Mg alloys are known to develop hardening precipitates after solution treatment even without additional thermal input during ageing, due to their significant Cu content [83]. Moreover, Mg contents up to 0.7 wt.% are reported to sensibly accelerate the precipitation kinetics of such phases in these alloys [96]. Conversely, Al-Si-Mg alloys do not respond effectively to such heat treatments and require higher ageing temperatures for the precipitation of strengthening phases. In fact, the T6 parameters adopted are specifically prescribed to enhance the mechanical properties of the similar AC46000 cast alloy [78,81,97,98]. However, the AlSi9Cu3 alloy in T6 condition showed an increase in hardness with respect to the S condition, but with significantly lower hardness compared to AB, DA and T4 conditions, most likely due to an incomplete formation

of the strengthening phases. This outcome indicates a different response of the LPBF alloy with respect to the conventionally cast alloy, which is quite known for LPBF alloys.

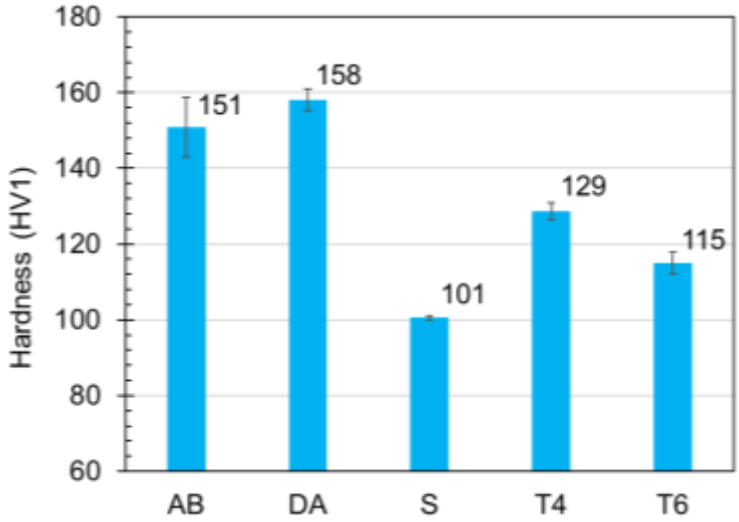

Figure 9 - Effect of different heat treatments on the hardness of AlSi9Cu3 alloy.

Corrosion behaviour assessment

Electrochemical tests on the AB condition revealed a substantially active behaviour just after the exposure to the test solution. In fact, the Bode diagram (Figure 10a) exhibits two distinct and well-defined phase constants, one at low frequencies and the other at high frequencies. A similar behaviour in the EIS spectra was also observed in previous works on both Al-Si and Al-Cu alloys, where the presence of such constants has been associated with the occurrence of localized corrosion [60,99]. The interpretation of the EIS spectra was performed by applying one of the most widely used equivalent electrical circuits for processing the Bode diagrams of aluminium alloys, as shown in the inset in Figure 10a [99]. This simplified model was chosen, as the EIS measurements were performed after 1 hour of immersion, before localized corrosion could propagate significantly. The equivalent circuit consists of three elements composed of resistances (R) and constant-phase elements (CPE). R1 represents the electrolyte resistance, R2-CPE2 are related to the oxide film and to a high-frequency response, while R3-CPE3 represent the corrosion processes, related to the low-frequency response. The R3, related to the charge transfer resistance, provides information on the corrosion resistance, as it is inversely proportional to the corrosion rate [100]. However, only minor differences were observed among different heat treatment conditions, with comparable EIS spectra. The results of the potentiodynamic polarization test (Figure 10b) further confirmed the active behaviour of the material in the AB condition. According to Scully et al [101], the oxygen reduction process occurs preferentially on the noblest intermetallic precipitates with lower overpotential for the oxygen electrochemical reaction (OER). This led to the preferential dissolution of the adjacent matrix. Furthermore, it has been well established that the cathodic phases driving the corrosion of the Al matrix of Al-Si and Al-Cu alloys are the idiomorphic silicon crystals and copper-rich precipitates, respectively. As demonstrated in Figure 4, the microstructure of the AlSi9Cu3 alloy in the AB condition is characterized by a network of both Si and Cu-rich precipitates. Among these, the Al2Cu phase is a much more efficient cathode than the idiomorphic Si crystals [53,101]. For this reason, the

presence of copper in an Al-Si-Cu alloy, as observed in this study, proved to strongly accelerate the onset of corrosion attacks, thereby decreasing corrosion resistance. This hypothesis was corroborated by the lower low-frequency impedance modulus value (Table 3), if compared to an AlSi10Mg alloy, which, under the same test conditions, exhibited an impedance modulus value of $|Z|_{0.01\ Hz}$ = 839 ± 78 kΩ·cm2 [60].

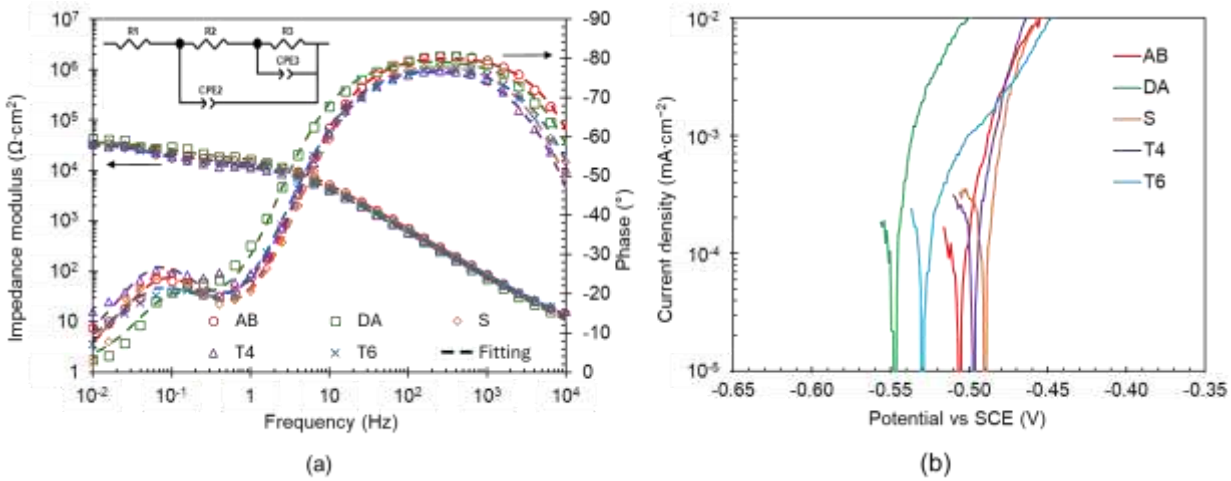

Figure 10 - (a) EIS spectra with equivalent electrical circuit and (b) Potentiodynamic polarization curves of AlSi9Cu3 alloy.

Table 3 - Fitting parameters and modulus at 0.01 Hz of AlSi9Cu3 alloy in different heat treatment conditions.

Condition	R_1 (Ω·cm²)	R_2 (kΩ·cm²)	CPE2 (μF·cm^{-2})	n_2	R_3 (kΩ·cm²)	CPE_3 (μF·cm^{-2})	n_3	X^2	$\|Z\|_{0.01\ Hz}$ (kΩ·cm²)
AB	3.8	16	5.1	0.90	26	107	0.88	$2.5\cdot10^{-2}$	35
DA	4.1	20	5.6	0.90	16	127	0.94	$8.1\cdot10^{-3}$	43
S	7.0	14	5.3	0.89	24	128	0.90	$4.1\cdot10^{-3}$	37
T4	6.5	13	4.8	0.89	24	148	0.88	$4.2\cdot10^{-3}$	36
T6	5.6	15	5.7	0.88	20	153	0.83	$4.9\cdot10^{-3}$	32

The EIS spectra of the heat-treated specimens in Figure 6a showed a similar behaviour to the AB condition. The fitting results and the impedance modulus values at low frequencies (Table 3) are close to the one obtained for AB condition. Furthermore, the potentiodynamic polarization curves did not exhibit any significant changes in the overall corrosion behaviour following the heat treatment, as shown in Figure 10b. The R3 values obtained from the fitting of the EIS spectra show a trend, depending on the heat treatment, similar to that identified by analysing the current density values obtained from the potentiodynamic polarisation tests, Table 4. From the OCPs and current density values Table 4, it is evident that all the specimens exhibited an active behaviour. The corrosion current density was extrapolated from the Tafel plots of the PD polarization curves, with Tafel lines derived from an overpotential greater than 100 mV with respect to the OCP value. The obtained data confirmed a lack of significant change, thereby concluding that the heat treatments performed did not modify the corrosion behaviour of the AlSi9Cu3 alloy during potentiodynamic tests.

Table 4 - Open circuit potentials, breakdown potentials and corrosion current densities of the tested specimens.

Condition	OCP vs SCE (E_{bd} vs SCE)[a] (mV)	I_{corr} (μA·cm^{-2})

AB	−511 ± 7	7 ± 3
DA	−547 ± 4	20 ± 3
S	−491 ± 2	7 ± 1
T4	−498 ± 1	4 ± 2
T6	−530 ± 5	13 ± 4

[a] For active specimens the OCP was considered as breakdown potential.

In order to evaluate the long-term stability of the oxide film and the effect of high-temperature heat treatments, EIS measurements were repeated every 3 hours up to 130 hours of immersion in a less aggressive environment, 0.5 g/L NaCl + 41.18 g/L Na_2SO_4, due to the fully active behaviour exhibited during the electrochemical tests reported in Figure 10. EIS curves corresponding to significant changes in impedance response over time were selected for detailed analysis. The rationale behind this approach is to focus on meaningful transitions in corrosion behaviour while avoiding redundancy associated with analyse a large number of quasi-overlapping spectra. Due to a lack in specimens' availability, these tests were performed on AB conditions and after high-temperature heat treatments. Figure 11show the modification of EIS curves over time. Shortly after immersion, both AB and T4 specimens demonstrate a high impedance value at low frequency ($|Z| \approx 10^3\ k\Omega \cdot cm^2$), related to a passive behaviour [64]. The bode-phase diagram is characterised by a wide peak in the middle range, between 10^2 and 10^{-1} Hz. In T6 condition, the EIS response exhibited a markedly different behaviour already after a few hours of immersion. The modulus of impedance at low frequency was observed to be approximately one order of magnitude lower than AB and T4 condition (Figure 12) and the bode-phase diagram exhibit a quasi-horizontal plateau in the low frequency range, as illustrated in Figure 11e,f. The lower impedance modulus and the plateau in the low frequency range can be related to an active behaviour from the first instance of immersion. Moreover, as stated by Mousavi et al. [102], the occurrence of these features in the low frequency range can be related to diffusion of corrosion phenomena, thus corroborating the occurrence of severe corrosion attacks on the exposed surface from the first instant of immersion. After 5 h of immersion, for the T6 condition, the impedance spectra were characterised by significant noise and poorly defined Bode-phase diagram, preventing reliable analyses. This behaviour can be attributed to the rapid occurrence of severe localised corrosion, leading to highly unstable electrochemical conditions. Consequently, this finding was regarded as an inherent outcome, indicative of the poor corrosion resistance of the T6 condition. The behaviour changes over time for the AB and T4 specimens are quite similar, with small differences related to the time at which they occur. For the AB specimens, after 57 h the broad peak in the bode-phase diagram shift toward higher frequencies, accompanied by a decrease of the low-frequency impedance modulus(Figure 12). This effect becomes more evident after 100 h of immersion, when a quasi-horizontal phase plateau at approximately 30° - 40° appears in the low-frequency range indicates the onset and subsequently growth of diffusion-controlled localised corrosion processes [103]. T4 specimens exhibit the same behaviour but the decrease of impedance modulus and the appearance of a quasi-horizontal plateau arise early, around 19 h of immersion (Figure 11 and Figure 12). Thus, suggesting the decreased stability of the oxide film after T4 and T6 heat treatments.

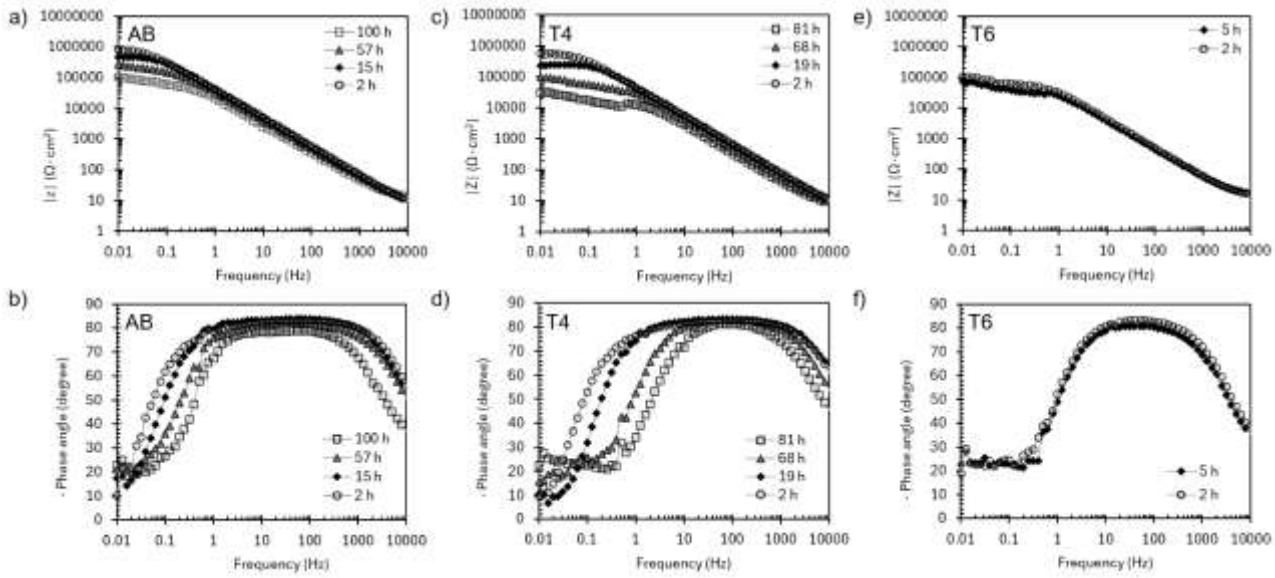

Figure 11 - Effect of exposure time on EIS bode diagram of (a,b) AB, (c,d) T4 and (e,f) T6 AlSi9Cu3 specimens.

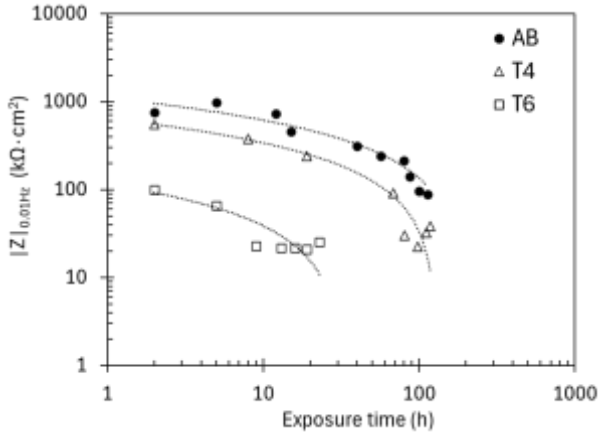

Figure 12 - Effect of exposure time on the impedance modulus at 0.01 Hz.

Figure 13 shows the corrosion morphology observed on the exposed surfaces of AB, T4 and T6 specimens. The effect of heat treatments on the oxide film stability is clearly evident. As illustrated in Figure 13a,b, the melt pool macrostructure strongly affects the corrosion phenomenon, leading to a selective attack along preferential path at the melt pool boundary and heat affected zone. These regions correspond to areas characterised by coarser cellular structures, discontinuous Si-network and enhanced chemical heterogeneity. In AB condition the attacks follow the melt pool macrostructure, indicating a microstructure-controlled corrosion mechanism rather than a purely random pitting phenomenon. For heat-treated conditions, corrosion morphologies evolve towards more extended and penetrating attacks, assuming a large pit morphology, as illustrated in Figure 13,c,e. In both conditions, the corrosion attacks seem to be driven by the selective dissolution of α-Al matrix near the Si-rich and Cu-rich precipitates, due to their different nobility [53]. The artificial ageing treatment performed subsequent to the solubilisation treatment in T6 specimens stimulate the precipitation of Cu- and Si rich second phases within the Al matrix, affecting the stability of the oxide film and thus reducing the corrosion performance, as highlighted by the long-term EIS tests. The presence of thick

corrosion products within the corroded regions provides direct explanation of the diffusion-controlled response detected in the EIS curves for T4 and mainly for T6 (Figure 13f). The accumulation of corrosion products within deep and confined attack sites hinders ionic transport, giving rise to a diffusion-limited electrochemical behaviour that becomes increasingly dominant with immersion time [102].

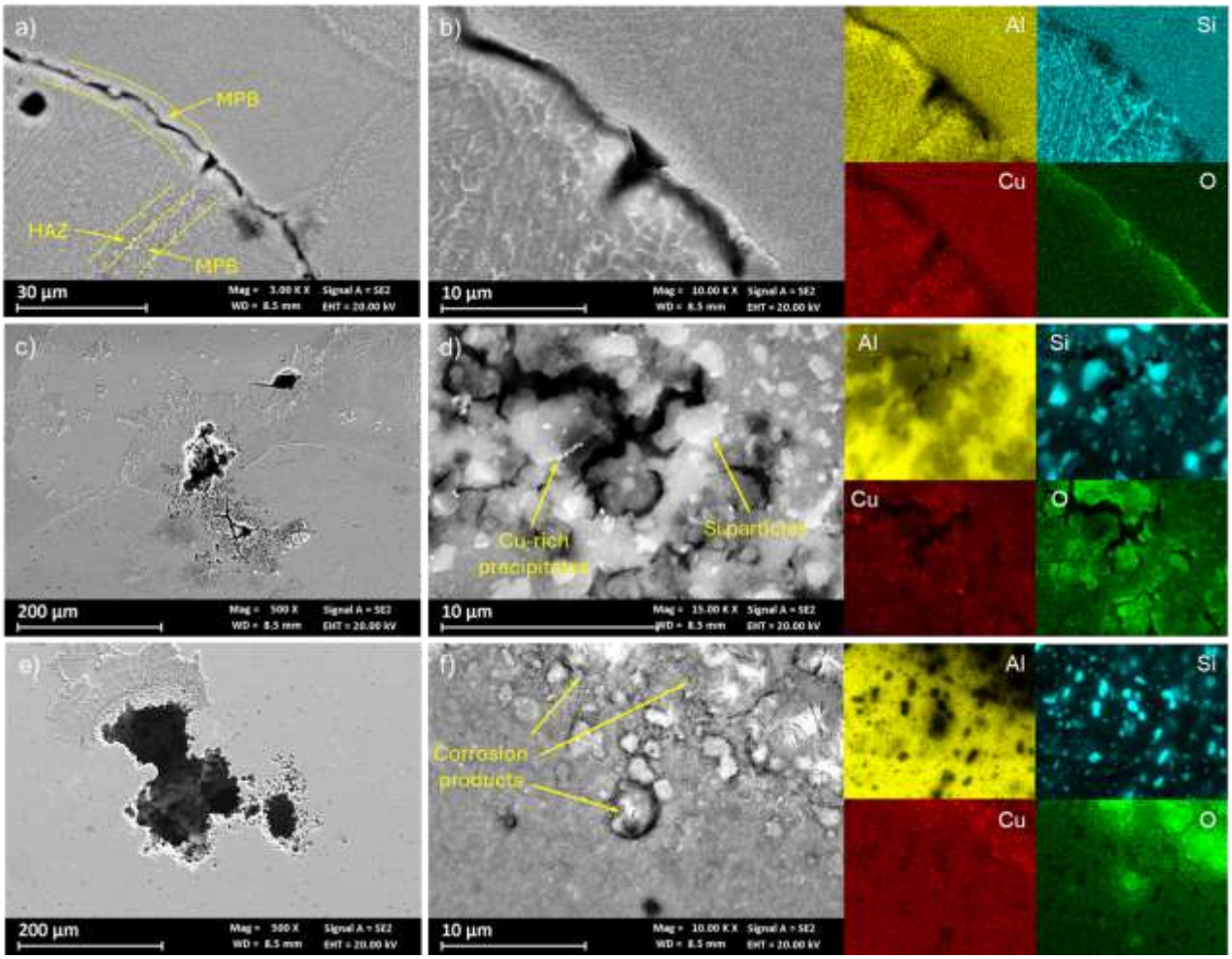

Figure 13 – Low- and high-magnification FESEM images with relative EDS maps of corrosion attacks on (a,b) AB, (c,d) T4 and T6 specimens.

Intergranular corrosion tests were conducted to assess the intergranular susceptibility of AlSi9Cu3 alloy, in AB condition as well as after different heat treatments. AB specimens showed a predisposition to selective corrosion, with well-defined preferential corrosion paths. Indeed, Figure 14a shows several corrosion attacks distributed over the entire exposed surface. The melt pool macrostructure and in particular the MPB affected significantly the selective corrosion behaviour, which assumes an inter-melt pool morphology. When dealing with LPBF specimens, such corrosion morphology is typical for AB condition. For instance, Lorenzi et al [60] highlighted that in the case of the alloy belonging to the 2xxx series, the boundary of the melt pool has a microstructure with coarser Al_2Cu precipitates that exhibits a preferential corrosion path due to galvanic coupling between Cu and α-Al matrix. Dealing with AB LPBF Al-Si alloys, Revilla et al [61] stated that the corrosion starts in the MPB, with higher Volta potential difference, and then continue through the HAZ due to the discontinuities of the Si network. For AB AlSi9Cu3, the corrosion path was more similar to the

latter one observed in Al-Si alloy, with relevant differences between MPB and HAZ and the corrosion path evidently following the HAZ area and then progressing in the MPF below (Figure 14b,c). Furthermore, the EDS map in Figure 14d highlights a noticeable amount of residual Al_2Cu along the corrosion attack, suggesting that the galvanic coupling between nobler Cu-rich phases and α-Al matrix could be the main driving force for the corrosion phenomena.

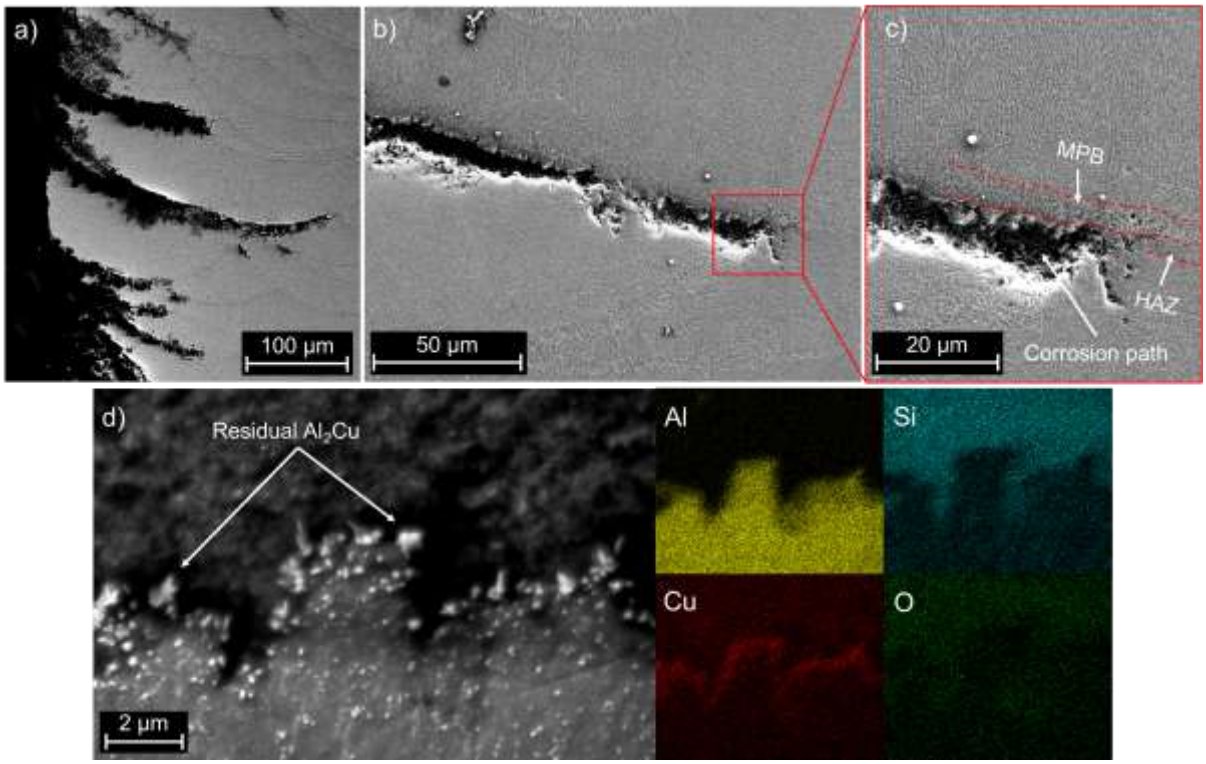

Figure 14 - (a) Morphology of the selective attack at the edge of the specimens, (b,c) relative propagation and (d) inset of the corroded area with EDS maps of the corrosion products in the AB AlSi9Cu3 alloy.

Despite the microstructural modification induced by the heat treatments did not affect the global corrosion behaviour of AlSi9Cu3 alloy, dramatically increase in the susceptibility to selective corrosion was assessed after intergranular corrosion tests (Table 5).

Table 5 - Results of the susceptibility to intergranular corrosion test on the AlSi9Cu3 alloy in AB and heat-treated conditions.

Condition	Exposed surface (cm^2)	Mass loss (mg)	Average corrosion rate ($mg \cdot dm^{-2} \cdot day^{-1}$)	Average depth (µm)	Maximum depth (µm)	Attack linear density (mm^{-1})
AB	5.59	133 ± 45	2373 ± 787	204 ± 133	1332	9.3
DA	5.56	289 ± 13	5198 ± 247	261 ± 87	765	8.2
S	5.36	3 ± 1	49 ± 4	-[1]	-[1]	-[1]
T4	5.60	10 ± 2	187 ± 26	-[1]	-[1]	-[1]
T6	5.40	297 ± 17	5498 ± 46	170 ± 115	1038	6.5

1 – Not reported due to different corrosion morphology highlighted.

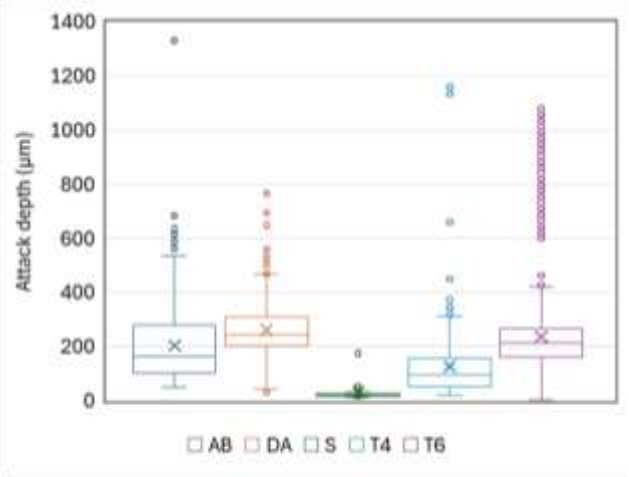

(a)

Anova	
$df_{between\ groups}$	4
$df_{within\ groups}$	2039
F	55
F_{crit}	2.4
P-value	$3.6 \cdot 10^{-44}$

(b)

Figure 15 - (a) Box plots of intergranular corrosion attack depth for AlSi9Cu3 specimens in the as-built (AB) condition and after different heat treatments (DA, S, T4 and T6). (b) One-way ANOVA statistical analysis.

The AlSi9Cu3 DA specimens were still characterized by a selective corrosion attack with an inter melt pool morphology, as observed in AB specimens. The investigation of the selective attack paths in the cross-sections of the DA specimens showed an even more severe attack with respect to the as-printed condition (Figure 16a,b). Furthermore, the attack resulted in melt pool dropping morphology - in analogy to the well-known grain dropping morphology of some wrought alloys susceptible to IGC. This mechanism led to mass loss of the specimens, leading to very high overall corrosion rates (Table 5). The EDS maps of the corrosion products showed a relevant amount of Cu, Si and O at the corroded area (Figure 16c), thus confirming the preferential dissolution of the α-Al matrix during the attack propagation. The statistical analysis reported in Figure 15 confirmed significant differences in corrosion attack depth between the AB and DA conditions, highlighting the pronounced influence of heat treatment on the corrosion behaviour of the alloy.

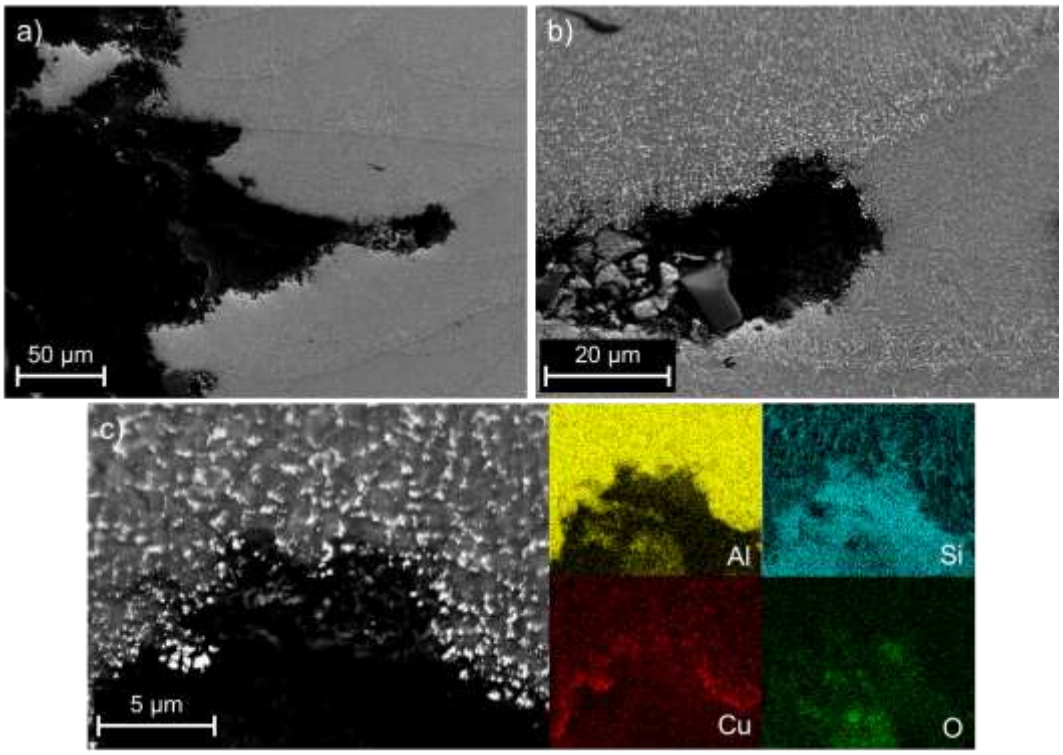

Figure 16 - (a,b) Morphology of the selective corrosion attack and (c) higher magnification of the corroded area with EDS maps of the corrosion products in the DA AlSi9Cu3 alloy.

The high-temperature heat treatments S and T4 resulted in a major variation in both selective corrosion susceptibility and attack morphology (Figure 17). After solutioning, the S AlSi9Cu3 alloy still exhibited a selective attack between Al matrix and Si/Cu precipitates, but the corrosion propagation no longer followed a preferential path (Figure 17a), being general due to the dismantling of the peculiar melt pool and network features. In the case of T4 specimens, localized attack was observed (Figure 17c). The statistical analysis reported in Figure 15 confirmed significant differences in the corrosion behaviour of the tested specimens, further highlighting the pronounced effect of heat treatment. On the other hand, the T6 heat treatment resulted in a completely different corrosion morphology (Figure 17e). The corrosion attacks in this case assume an intergranular morphology, similar to that observed in traditional aluminium alloys. It is evident that, across all examined conditions, the corrosion mechanism remains driven by the galvanic coupling between the Al matrix and Cu-rich and Si-rich particles. This assumption is further corroborated by the results of the EDS analysis performed in a corroded zone, which revealed a significant amount of Si and Cu within the corrosion products (Figure 17b,d,f). Moreover, the improvement of the corrosion resistance after S and T4 heat treatments is testified by the reduction of the corrosion rate (V_{corr}) reported in Table 5. The T6 heat treatment resulted in the formation of coarser precipitates rich in Si and Cu, as shown in Figure 7h, in comparison to S and T4 heat treatments. This microstructure led to an increase in intergranular susceptibility, as evidenced by corrosion rate and mass loss reported in Table 5.

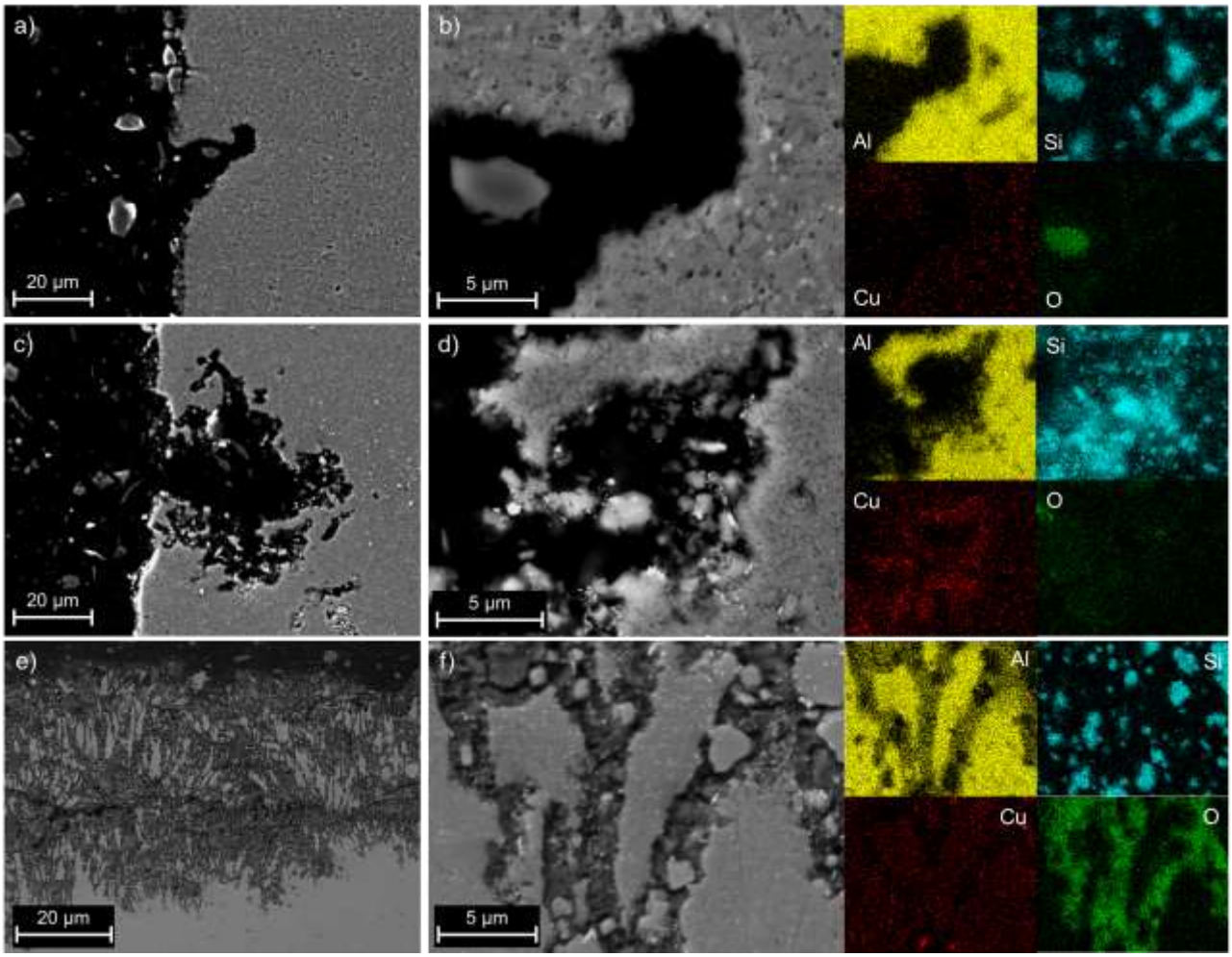

Figure 17 - Morphologies of the selective attack and related EDS maps of the (a,b) S, (c,d) T4 and (e,f) T6 AlSi9Cu3 specimens, respectively, after the intergranular corrosion tests.

In order to corroborate the impact of Cu-rich phases on the selective corrosion mechanism, a SKPFM analysis was performed on AB and heat-treated specimens. This technique led to the evaluation of Volta potential differences between the α-Al matrix and the Si and Cu-rich network. The measurement of Volta potential provides an assessment of the nobility of each particle with respect to the surrounding matrix, an essential information for understanding their role in the galvanic interactions that control the corrosion mechanism [104]. Starting from the AB condition, a comparison of the FESEM (Figure 18a) and SKPFM (Figure 18b) images reveals that the microstructural differences observed in the MPC, MPB and HAZ led to distinct Volta potential values. In the MPB, the presence of coarser Si- and Cu-rich network resulted in a more pronounced Volta potential difference between the Al matrix and the secondary phases. Conversely, the much finer network in the MPC led to a less evident Volta potential difference. The HAZ exhibited the lowest Volta potential in comparison to the adjacent areas, suggesting a lower concentration of precipitates within the HAZ, as demonstrated in Figure 18.

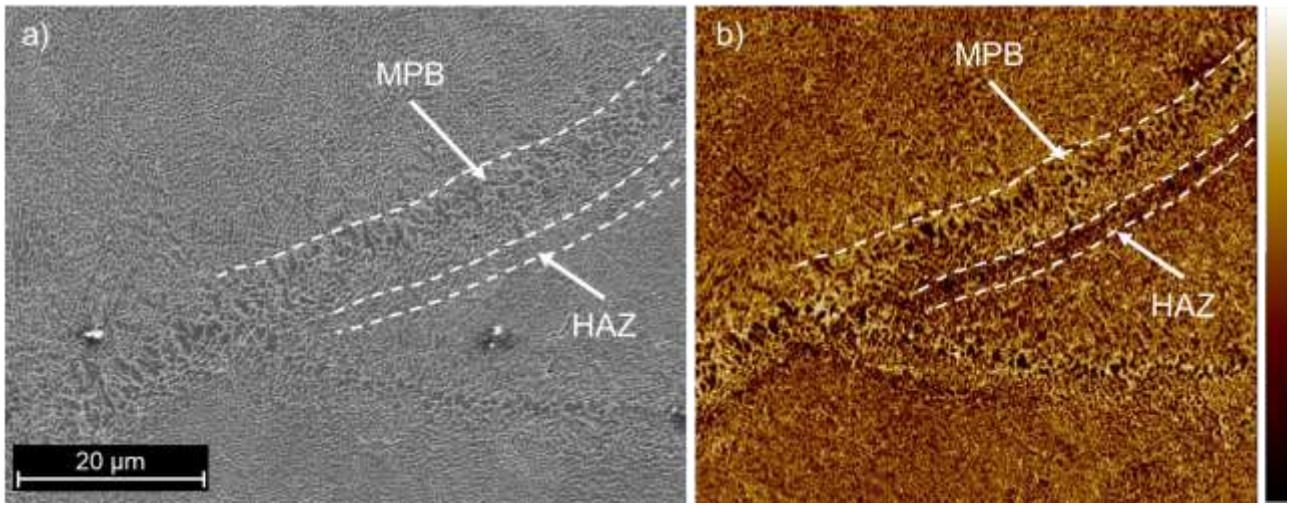

Figure 18 - (a) FESEM micrograph and (b) relative Volta potential map obtained with SKPFM technique in AB alloy AlSi9Cu3. Scan size: 80 x 60 µm^2. Colour bar: 800 mV range.

To evaluate the corrosion mechanism, a more detailed SKPFM analysis was performed across the MPB and HAZ zones (Figure 19). The Volta potential linescan in Figure 19b,d revealed a significantly higher Volta potential difference at the MPB-HAZ interface (593 mV) if compared to the values measured within the MPB (408 mV) and the MPC (316 mV). This indicates that the precipitates distributed at the MPB-HAZ interface induce a strong galvanic coupling with the adjacent Al matrix, creating a preferential path for corrosion phenomena, as assessed after IGC tests. Figure 19c,e shows further results from a SKPFM analysis carried out in the same area but with a wider averaged linescan, to better characterize the MPB, MPC and HAZ macro-zones. The average linescan confirms the results obtained with local potential linescan, furthermore showing that there is also a noticeable global difference in Volta potential between HAZ and MPB/MPC, in addition to the aforementioned local differences. This increase can be ascribed to a more efficient cathodic effect triggered by the higher concentration of Si and Cu-rich phases at the HAZ interface. Moreover, the averaged linescan showed that the MPB has two distinct zones characterized by different Volta potential values. The inner zone of the MPB has lower potential values with respect to the outermost zone. The EDS analysis reported in Figure 4, carried out across the MPB and the HAZ, revealed that MPB has a higher concentration of Cu than Si.

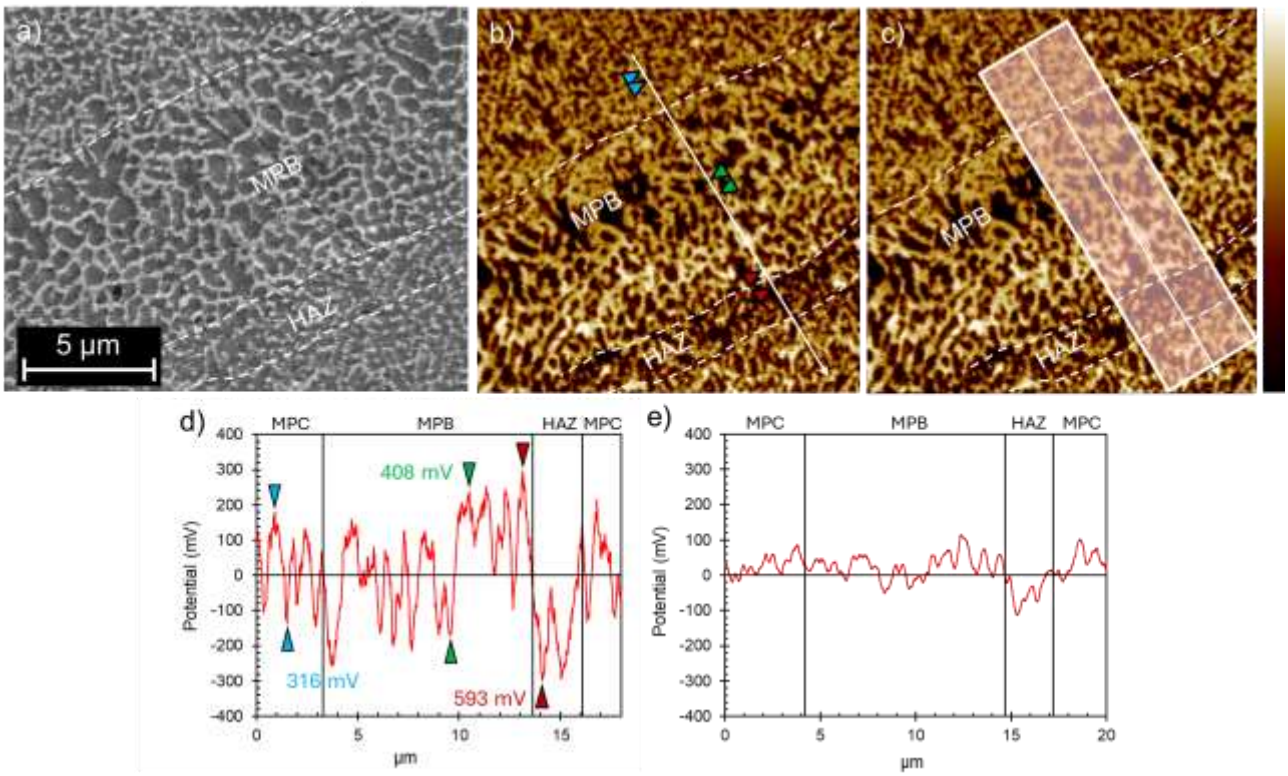

Figure 19 - (a) FESEM micrograph and (b,c) relative Volta potential map with (d) Volta potential local line scan and (e) average Volta potential line scan in AB alloy AlSi9Cu3. Scan size: 20 x 20 µm^2. Colour bar: 800 mV range.

The DA heat treatment does not affect the melt pool macrostructure in the AB specimens due to the relatively low heat treatment temperature. The SKPFM analysis (Figure 20b) revealed a less pronounced Volta potential difference between HAZ and MPC, attributable to the different second phases distribution. MPB and HAZ regions did not exhibit significantly higher Volta potential difference between the α-Al matrix and Si- and Cu-rich phases than the MPC (Figure 21b,d). However, further analysis averaged over a larger area showed that the HAZ has a lower average Volta potential value than the MPB and MPC (Figure 21c,e), similarly to the AB material.

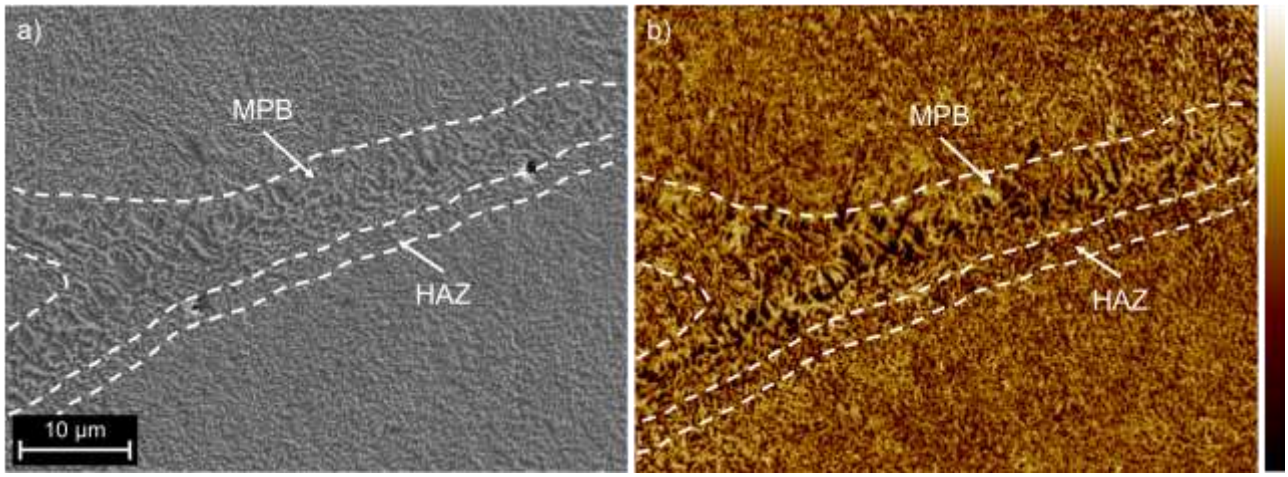

Figure 20 - (a) FESEM micrograph and (b) relative Volta potential map obtained with SKPFM technique on DA alloy AlSi9Cu3. Scan size: 80 x 60 µm^2. Colour bar: 800 mV range.

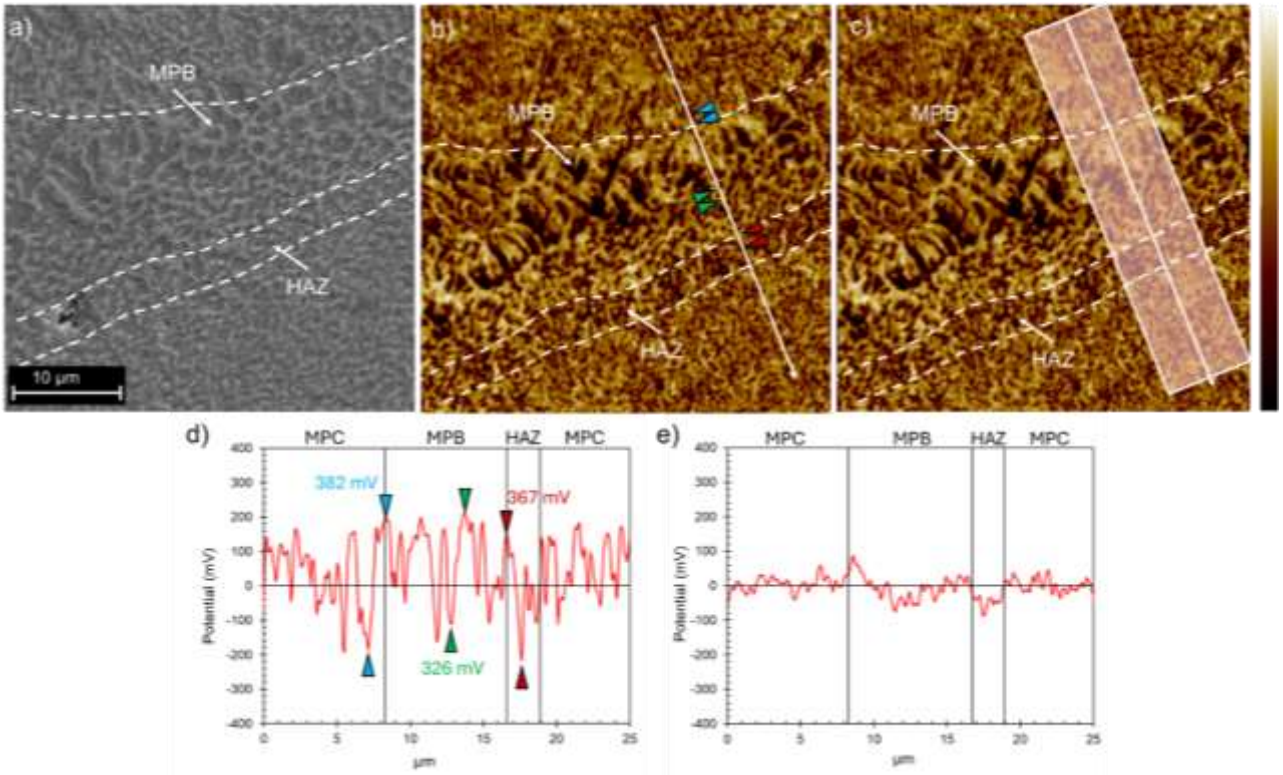

Figure 21 - (a) FESEM micrograph and (b,c) relative Volta potential map with (d) Volta potential local line scan and (e) average Volta potential line scan in DA alloy AlSi9Cu3. Scan size: 30 x 30 µm^2. Colour bar: 800 mV range.

The SKPFM analysis of the S AlSi9Cu3 alloy (Figure 22a,d) showed that the dissolution of secondary phases at elevated temperatures results in a homogeneous matrix with a strongly reduced Volta potential difference (238 mV). SKPFM analysis on T4 specimens highlighted a higher Volta potential in correspondence of Cu-rich particles with respect to the Volta potential of Si-rich particles, despite the coarser size (Figure 22a,d). The difference in terms of Volta potential between Cu-rich phases and Al matrix (490 mV) is similar to AB condition. The artificial ageing process involved in T6 heat treatment promotes the precipitation of Cu- and Si-rich particles, thereby increasing their

Volta potential difference (476 mV) respect to the Al matrix (Figure 22c,f). This heat treatment also leads to the formation of smaller and more dispersed precipitates within the matrix.

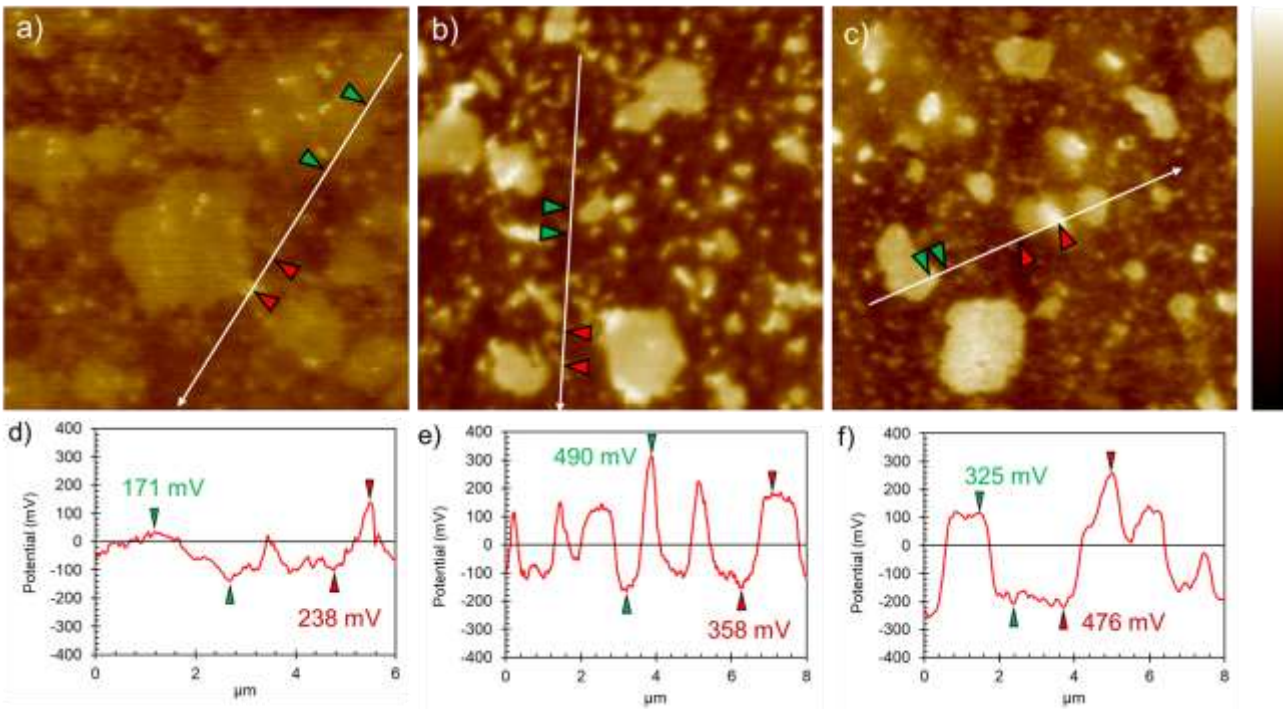

Figure 22 - Volta potential maps and linescans crossing large and small Si- and Cu- rich particles in (a,d) S, (b,e) T4 and (c,f) T6 AlSi9Cu3 alloy, respectively. Scan size: 20 x 20 µm^2. Colour bar: 800 mV range.

Corrosion mechanism

The obtained results revealed a pronounced cathodic effect of Cu-rich precipitates in the AlSi9Cu3 alloy, in comparison to Si-rich phases. This is due to the fact that Al_2Cu is a nobler intermetallic precipitate respect to idiomorphic Si crystals being a more efficient cathode for the corrosion process [53,101]. This enhances the preferential dissolution of the adjacent Al matrix, as the cathodic phases drive localized corrosion. The presence of Cu in an Al-Si alloy, as observed in this study, has been demonstrated to accelerate the onset of corrosion, consequently reducing the corrosion resistance of the material. The intensified cathodic activity near Cu-rich precipitates leads to alkalinization, resulting in the degradation of the passive film. Once the passive layer is broken, the corrosion propagates leaving behind corrosion products characterised by the presence of Si- and Cu-rich precipitates. The tests and analysis conducted in this work highlighted a strong influence of microstructure and precipitate distribution on the oxide film stability and on selective corrosion behaviour of the AlSi9Cu3 alloy produced via LPBF. At the micro level, the preferential dissolution of alpha-Al matrix was driven by micro-galvanic coupling with nobler Si- and Cu-rich intermetallics. Such mechanism resembles that of conventionally cast AlSi9Cu3 alloy [79,80]. At the macroscopic scale, the selective corrosion path was primary linked with microstructural and, mainly, compositional inhomogeneities among MPC, MPB, and HAZ (Figure 23a), consistently with corrosion mechanisms reported for other LPBF-processed Al-Si alloys [105]. These differences are evident also from the Volta potential point of view, with the MPB that exhibited an average Volta

potential significantly higher respect to the adjacent HAZ. This results, in conjunction with the outcomes in Figure 14d and Figure 18, demonstrates that the high concentration of Cu-rich phases at the interface with the HAZ and their strong galvanic coupling with the Al matrix are the driving forces for the selective corrosion phenomena, creating a preferential path along the HAZ, as illustrated in Figure 23b,c,d.

A low-temperature heat treatment, such as DA, has been shown to preserve the melt pool structure while promoting the precipitation of extremely fine Cu- and Si-rich phases. The SKPFM analysis reveals a less pronounced Volta potential difference between HAZ, MPB and MPC. However, the melt pool macrostructure contributes to the maintenance of an inter-melt corrosion morphology. As demonstrated in Figure 6, the observed difference in Cu concentration in this region and its galvanic coupling with the surrounding Al matrix act as the main driving force for the corrosion phenomena. Although the corrosion mechanism remains similar to that observed in the AB specimens, the greater amount of Cu- and Si-rich second phases distributed within the MPC promotes a more severe corrosion attack, as highlighted in Figure 16a and indicated by the weight losses and corrosion rates, Table 5. Rubben et al. [105] reported that the precipitation of secondary phases and the partial breakdown of the eutectic network following a T5 treatment, such as that applied to the AlSi9Cu3 alloy, resulted in a deterioration of the alloy's corrosion performance. The depletion of alloying elements within the Al matrix, combined with the enhanced precipitation of secondary phases acting as micro-galvanic cells [106], led to a poorer corrosion resistance compared with the AB condition, as demonstrated in the Figure 16 and Table 5.

The microstructural modifications induced by the T4 and S heat treatment are similar, with the material undergoing dissolution and redistribution of Si- and Cu-rich phases. The homogeneous distribution of these phases within the matrix leads to a more uniform and less penetrating selective attack. The absence of natural ageing after quenching, as occurs in S heat treatment, results in a higher amount of Cu remaining in solution without forming strengthening precipitates. The absence of Cu-rich precipitates, which are known to be highly active, leads to a significant improvement in corrosion resistance.

The T6 heat treatment, with an artificial ageing step, has been shown to stimulate the precipitation of smaller and more dispersed second phases that are rich in Si and Cu. This enhances the galvanic effect and increases the intergranular corrosion susceptibility.

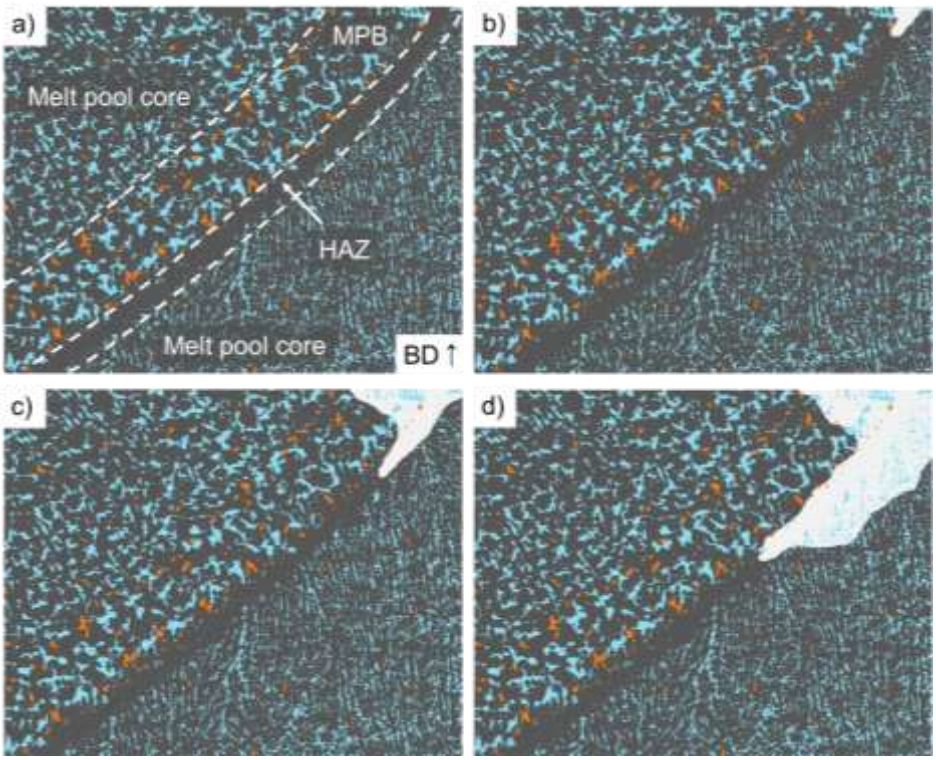

Figure 23 - Schematic representation of the selective corrosion mechanism in as-built (AB) AlSi9Cu3 alloy. The aluminium phase is represented with grey, the Si-rich precipitates with blue and the Cu-rich phases with orange. (a) the microstructure is characterised.

2.4 Effect of alloying elements on corrosion behaviour

Mechanical and corrosion properties of metallic materials are governed by the interplay between chemical composition and manufacturing route, through their combined effect on microstructure and second-phase distribution. Additive manufacturing, and in particular LPBF, represents an extreme application of this concept, given that the layer-by-layer processing, the presence of steep thermal gradient and the occurrence of very high solidification rate give rise to microstructures that are far from equilibrium and exhibit a strong dependency on alloy chemistry and process parameters [107].

In the context of LPBF aluminium alloys, it has been observed that cooling rates of up to approximately $10^6 – 10^7$ K/s can significantly extend the solubility of alloying elements within the α-Al matrix [61]. This phenomenon results in a substantial supersaturation, characterised by the presence of solute contents that can exceed the equilibrium solubility limit within the solid solution. As reported by Martucci et al. [82], LPBF processing can produces supersaturated aluminium matrix with lattice parameters deviating from near-equilibrium conditions due to excess Cu and Si trapped in solid solution, with a delay in the formation of Al_2Cu and Q-type phases. This supersaturation state, in conjunction with the non-equilibrium solidification path is demonstrated to be a key factor in the nucleation of metastable phases and the formation of unique spatial distribution of precipitates, such as Si- and Cu-rich intermetallics, on a scale comparable to that of the mel pool [107]. As well-known, the three-dimensional Si-rich network in AlSi10Mg and its heterogeneities distribution directly affect corrosion initiation and propagation [54]. In Al-Si-Cu alloys with elevated Cu content, as previously discussed, LPBF process facilitates the formation of supersaturated solid solution and finely dispersed

Al_2Cu precipitates within the eutectic network in configuration that are not achievable under conventional casting condition. This LPBF-induced microstructure enable aluminium alloys with significantly enhanced strength, due to the combined effect of solid solution strengthening and nanoscale precipitation. When coupled with the intrinsically low density of Al, this results in an excellent strength-to-weight ratio, making this material highly attractive for advanced lightweight applications. However, this raises important issues regarding the influence of non-equilibrium microstructures and solute distributions on the corrosion behaviour of these alloys.

In this study, the effect of alloying elements on corrosion behaviour was assessed by comparing three LPBF alloys with increasing Cu content and decreasing Si contribution to the eutectic network: AlSi10Mg, AlSi9Cu3 and AM2139. The chemical compositions of these three alloys are reported in Table 6 .

Table 6 - Chemical composition (wt.%) of the feedstock powder of AlSi10Mg, AlSi9Cu3 and AM2139 alloys.

Element (wt%)	Al	Cu	Mg	Ag	Mn	Fe	Si	Ti	Zn
AlSi10Mg	bal.	≤ 0.05	0.35	-	≤ 0.45	≤ 0.55	10	≤ 0.15	-
AlSi9Cu3	bal.	3.0	0.29	-	0.21	0.91	9.3	-	0.81
AM2139	bal.	5	0.5	0.5	0.5	≤ 0.15	≤ 0.10	≤ 0.15	-

AlSi10Mg was selected as a reference Al-Si-Mg alloy characterised by good mechanical properties and corrosion resistance [108]. AlSi9Cu3 represent an intermediate condition where the Al-Si cellular framework is enriched by Al_2Cu precipitates, leading to good LPBF processability and enhanced mechanical properties respect to Al-Si-Mg alloy [73]. AM2139 is an Al-Cu-Mg-Ag alloy that is strengthened by an Al2Cu precipitates [109].

2.4.1 Microstructural differences

Numerous studies [44,51,66,86,110–112] have documented that the microstructure of AlSi10Mg is characterised by an α-Al cellular matrix surrounded by a Si-rich network, which becomes progressively coarser near the MPB (Figure 24a,b). Along the heat-affected zone, the network appears more discontinuous, and idiomorphic Si crystals are observed. This is in relation to the partial recrystallisation induced by the heat input of the laser scans in the adjacent areas. As demonstrated in Figure 24c, AlSi9Cu3 exhibits a microstructure that is closely comparable to that of AlSi10Mg, but with slightly more discontinuous MPB and HAZ. The addition of copper has been shown to result in the formation of fine, dispersed Al_2Cu precipitates, with a higher concentration observed at the interface between the melt pool border and the heat-affected zone (Figure 24d) [82]. In contrast, the AM2139 alloy exhibited a distinct microstructure, characterised by the presence of α-Al cells surrounded by a discontinuous layer of Al_2Cu [60]. This layer exhibited increased coarseness along the MPB, as illustrated in Figures 24e, f, and no discernible heat-affected zone was observed in this alloy.

From a microstructural perspective, the progressive addition of Cu and the simultaneous reduction of Si result in a substantial difference in the ability to form a continuous network around the aluminium grains. The underlying causes of this phenomenon can be ascribed to the thermodynamics of solidification and the kinetics and stability of the phases present. From a thermodynamic

perspective, within an AlSi10Mg alloy, the Al-Si system, close to the eutectic composition, produces substantial quantities of liquid with a eutectic composition. This liquid subsequently solidifies at a later stage than the α-Al matrix, effectively surrounding the cells and establishing the continuous network that is characteristic of this alloy [113]. The gradual addition of copper has been shown to reduce the continuity of this network, since the Cu-rich precipitates have growth and coarsening kinetics that make the continuous lattice morphology unstable under the repeated thermal cycles of the LPBF process [38,114]. In Al-Si alloys, a similar phenomenon of network disruption occurs only at higher temperatures, making the continuous network formed during rapid cooling relatively stable in the as-built condition [88].

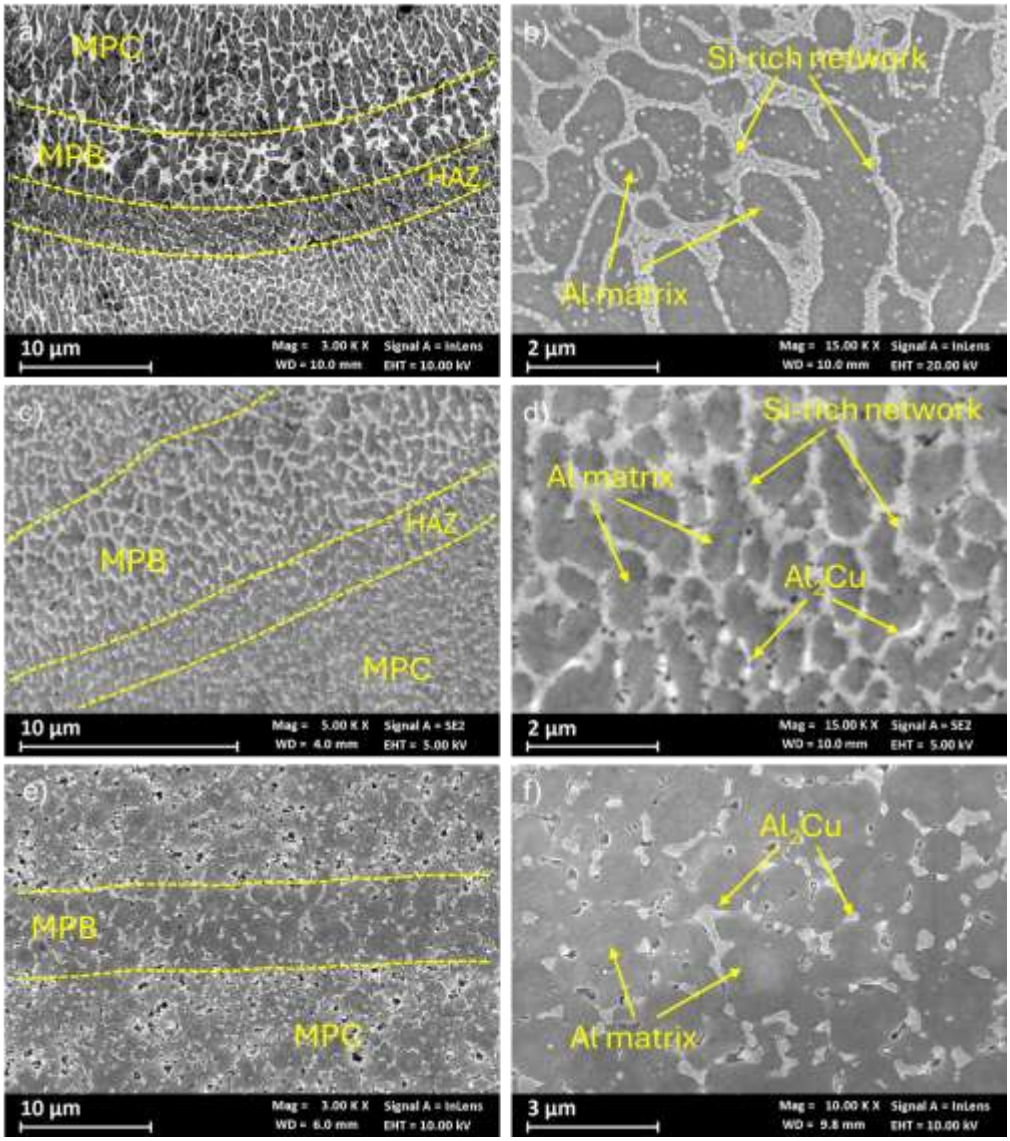

Figure 24 – High-magnification FESEM images of melt pool macrostructure and second phase morphology in the as-built condition of (a,b) AlSi10Mg [54], (c,d) AlSi9Cu3 and (e,f) AM2139 [60].

2.4.2 Mechanical performance

In as-built condition, these LPBF alloys demonstrate elevated yield and tensile strengths, resulting from rapid solidification, the presence of fine cellular structures, and strong supersaturated solid solution. However, these alloys exhibit divergent strength-ductility balances. AlSi10Mg exhibits a yield strength of approximately 240-270 MPa and an ultimate tensile strength of approximately 400-450 MPa, with elongations of approximately 4-10 % [88,115–117]. The fine grains structure and silicon network provide solution and dispersion hardening, while still allowing favourable plastic strain deformation. In the AlSi9Cu3 alloy, the presence of finely dispersed Cu- and Fe-containing intermetallics enhance the mechanical properties, achieving yield strength and ultimate tensile strength to approximately 240-270 MPa and 440-460 MPa respectively, but reduce elongation to approximately 3-6 % due to a strain localization effect by hard particles and along melt-pool edges [71,118–120]. AM2139 thanks to extremely fine α-Al cells combined with Cu-rich precipitates and a highly supersaturated matrix exhibit the higher mechanical properties between these alloys, with a yield strength of approximately 260-330 MPa, an ultimate tensile strength around 420-480 MPa and 4-8 % of elongation at break [22,121].

The progressive addition of copper and reduction of silicon content is indicative of a systematic enhancement in mechanical performance.

2.4.3 Corrosion behaviour

As demonstrated in the previous chapter, the corrosion behaviour of AlSi9Cu3 is strictly related to its microstructural features. This result has also been demonstrated by other authors for AlSi10Mg and AM2139 [60,64,105]. As illustrated in Table 7, a series of electrochemical corrosion indicators were evaluated for AB condition during an electrochemical test in a solution containing 1 g/L of NaCl and 41.18 g/L of Na_2SO_4. AlSi10Mg demonstrates optimal corrosion resistance, as evidenced by its high impedance modulus at low frequencies and reduced current density, indicating the stability of the oxide layer. In contrast, AM2139 and AlSi9Cu3 exhibit diminished corrosion resistance, exhibiting a current density that is two orders of magnitude higher than that of AlSi10Mg.

Table 7 - Open circuit potentials, breakdown potentials, corrosion current densities and low frequencies modulus of AlSi10Mg, AlSi9Cu3 and AM2139 in AB condition.

Alloy	OCP vs SCE (mV)	E_{bd} vs SCE (mV)	I_{corr} ($\mu A \cdot cm^{-2}$)	$\lvert Z \rvert_{0.01\ Hz}$ ($K\Omega \cdot cm^2$)	Reference
AlSi10Mg	- 670 ± 22	+ 225 ± 92	0.062 ± 0.008	839 ± 78	[60]
AlSi9Cu3	- 511 ± 7	- 511 ± 7	7.036 ± 2.765	35 ± 4	-
AM2139	- 591 ± 15	- 591 ± 15	6.311 ± 2.813	29 ± 9	[60]

The present analysis provides further evidence to support the hypothesis that the presence of Si- and Cu-rich second phases within the microstructure promotes strong alkalinisation in the areas adjacent to the precipitates. This, in turn, has the effect of destabilising the passive film [101]. Furthermore, an increase in the copper content results in a reduction in the stability of the oxide film, attributable to the higher nobility of Cu-rich precipitates in comparison with silicon.

In order to provide further clarification regarding the role of copper in the corrosion behaviour of these alloys, it is necessary to investigate their selective corrosion response. It is widely acknowledged that microstructural heterogeneities, which are intrinsic to LPBF-processed aluminium alloys, play a pivotal role in the control of corrosion phenomena in these materials [61].

A comparison of the intergranular corrosion test results reveals that all three alloys exhibit an inter-melt pool morphology, driven by the galvanic coupling between the α-Al matrix and the Si- and Cu-rich precipitates. In all cases considered, corrosion propagates along regions where the local microstructural conditions are most detrimental. For AlSi10Mg and AlSi9Cu3, the attack occurs in the heat-affected zone (Figure 25), where the silicon network is more discontinuous. In contrast, for AM2139, as reported by other authors [60], the attack preferentially advances along the melt pool boundary, where the Al_2Cu precipitates are coarser.

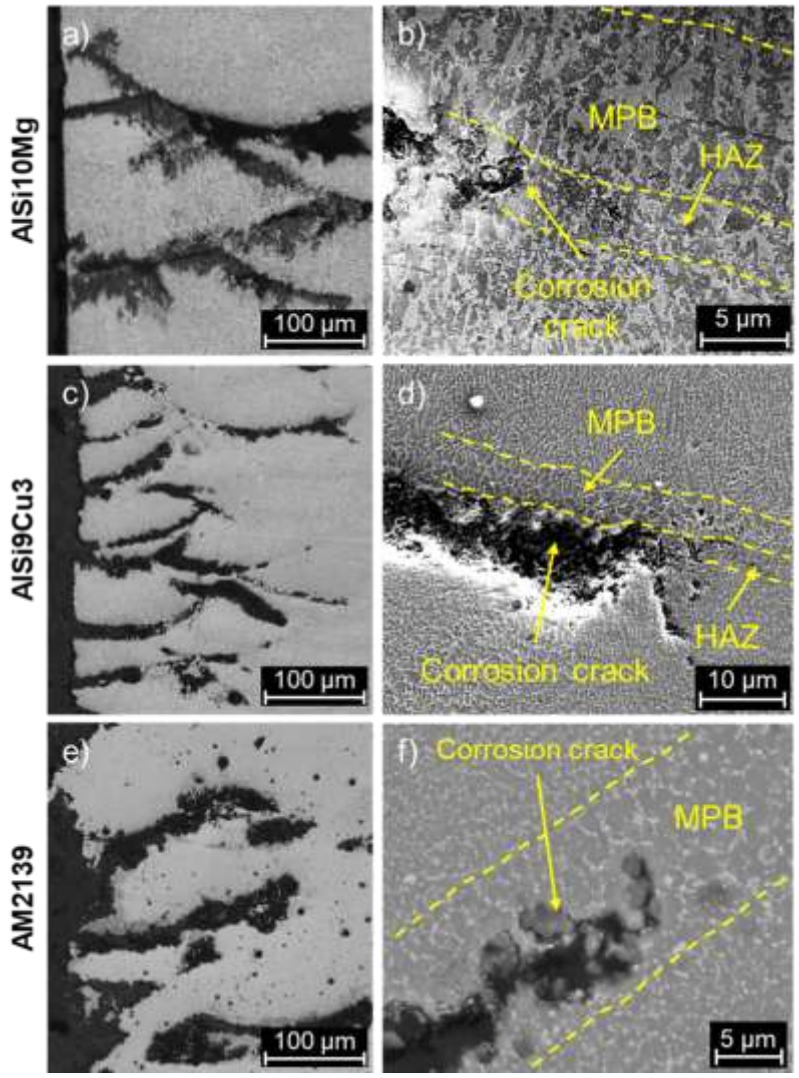

Figure 25 – (a,c,e) Morphology of the selective attack at the edge of the specimens and (b,d,f) relative propagation in the AlSi10Mg [60], AlSi9Cu3 and AM2139 [60] alloys, respectively

The IGC results reported in Table 8 demonstrate three distinct behaviours in terms of severity and selectivity of the corrosion attacks. The AlSi10Mg alloy exhibits the lowest susceptibility to selective corrosion, as evidenced by its minimal mass loss and corrosion rate. However, it undergoes profound

selective attacks. AlSi9Cu3 displays an intermediate behaviour, with a significantly higher corrosion rate and extremely penetrating selective attacks, associated with the presence of Cu-rich phases that promote preferential dissolution along the MPB. The AM2139 alloy demonstrates the highest susceptibility, but with less penetrating attacks than those observed in the other alloys.

Table 8 - Results of the susceptibility to intergranular corrosion test on the AlSi10Mg, AlSi9Cu3 and AM2139 alloys in AB conditionn

Alloy	Mass loss (mg)	V_{corr} ($mg \cdot dm^{-2} \cdot day^{-1}$)	Average depth (μm)	Maximum depth (μm)	Reference
AlSi10Mg	29 ± 14	525 ± 261	539 ± 271	899	[60]
AlSi9Cu3	133 ± 45	2373 ± 787	204 ± 133	1332	-
AM2139	240 ± 50	4220 ± 789	248 ± 88	641	[60]

A comparison of the FESEM images (Figure 26a,c,e) and SKPFM maps (Figure 26b,d,f) acquired at the MPBs confirms that, for all three alloys, the corrosion mechanism is governed by the cathodic effect of second phases dispersed in the aluminium matrix. In addition, the macro-galvanic coupling among MPB, HAZ and MPC defines a preferential path for corrosion propagation. This effect is further enhanced as the copper content in the alloy increases.

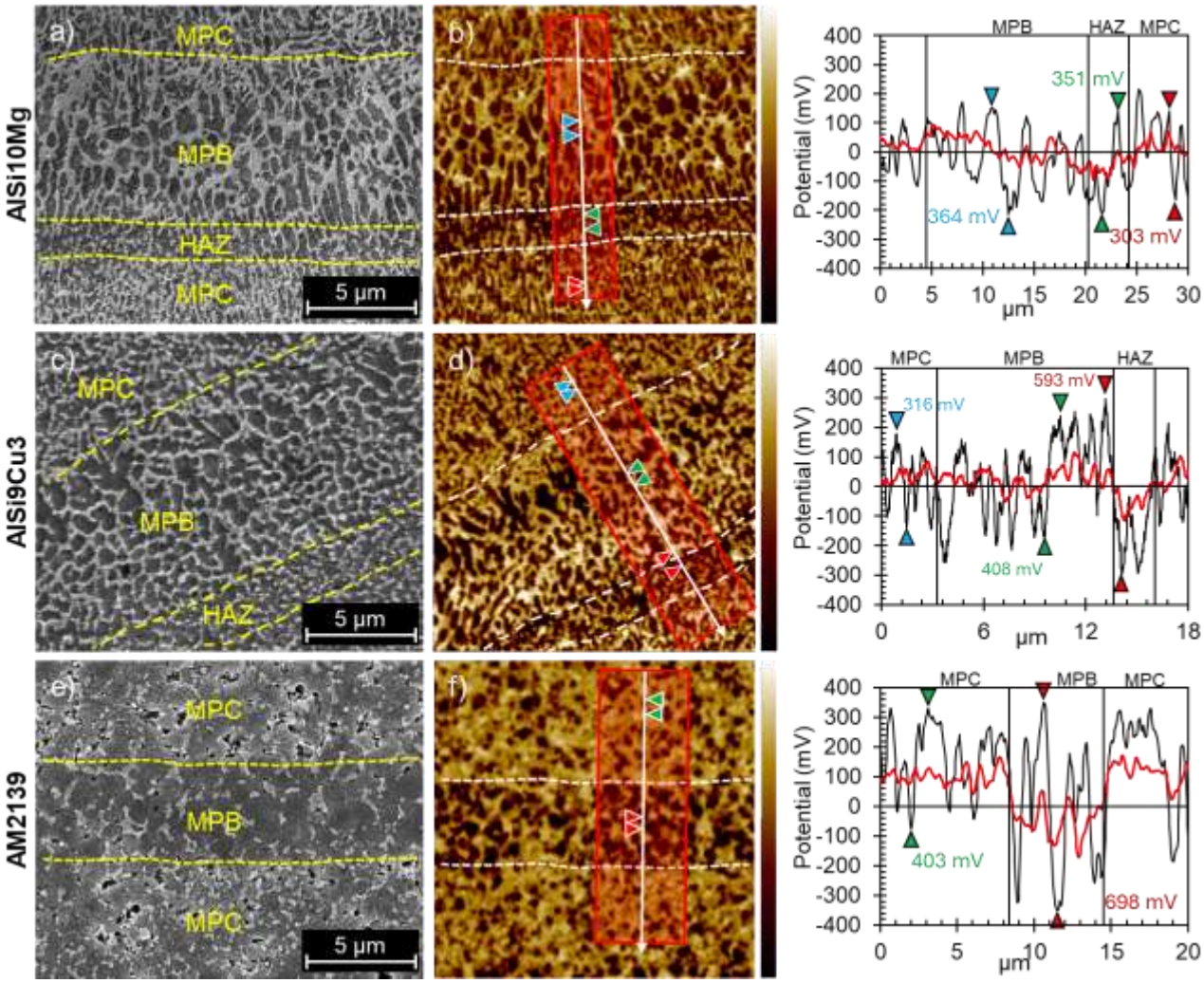

Figure 26 – (a,c,e) FESEM micrograph and (b,d,f) relative Volta potential map with Volta potential local line scan (black line) and average Volta potential line scan (red line) in AlSi10Mg, AlSi9Cu3 and AM2139, respectively. Scan size: 30 x 30 µm^2. Colour bar: 800 mV range.

In the case of the AlSi10Mg alloy, the presence of a continuous silicon network in both the melt pool centre and the melt pool boundary hinders the propagation of corrosion towards these regions, which is therefore stimulated along the HAZ where the Si network is more discontinuous. The addition of copper, as previously discussed, results in a preferential build-up of coarse Cu-rich precipitates along the MPB/HAZ interface. As illustrated in Figure 25c,d, the microstructure of the specimen, which still resembles that of AlSi10Mg, exhibits an accelerated corrosion rate along the HAZ. This phenomenon can be attributed to the augmented galvanic coupling that occurs within the microstructure, resulting in a more pronounced driving force for the corrosion phenomena. A further increase in copper content, when combined with a reduction in silicon content, produces a profound modification of the microstructure, resulting in a much more discontinuous network in both the MPC and MPB. This, in conjunction with the presence of Cu-rich precipitates that function as more efficient cathodes in comparison to Si, promotes a more aggressive yet more diffuse selective corrosion within the material, which becomes less penetrating. The present comparative analysis demonstrates that alloying elements play a dominant role in defining corrosion mechanisms in LPBF aluminium alloys, not only through their intrinsic electrochemical behaviour, but also by shaping the

AM-specific microstructural heterogeneities that govern both local and macro-galvanic coupling between the microstructural features present in these alloys.

While silicon-rich networks can locally hinder corrosion propagation, their protective role becomes ineffective when combined with copper-rich precipitates exhibiting higher cathodic efficiency. In LPBF alloys, this effect is amplified by the inherent melt-pool-driven microstructural heterogeneity, which promotes both local and macro-galvanic coupling. As a result, increasing copper content leads to more aggressive corrosion mechanisms, whose severity and morphology are dictated by the interplay between alloy chemistry and AM-specific microstructural features.

3 Lattice structures

3.1 Introduction

In recent years there has been a marked increase in demand for engineering materials that are lighter and more sustainable. This demand has been driven by significant progress in fields such as aerospace, automotive, biomedical and robotics [122,123]. In order to satisfy these needs, it has become crucial to reconsider the traditional structural components. The development of advanced additive manufacturing techniques has unveiled new pathways for the study of complex and highly optimised structures, unfeasible with traditional processes [124]. These structures, known as lattice structures (LS), are defined as objects with a porous arrangement created by organising unit cells in three dimensions [125]. The implementation of these structures in design facilitates the optimisation of mechanical properties while minimising the weight, thanks to their high strength-to-weight ratio, and emerges extremely useful when considering product life cycles. The LS allow for a reduction in material wastage and energy consumption during manufacturing [20]. The advantages of lattice structures are exploited in a variety of industries. In the biomedical sector, LS have been demonstrated to be useful for the characterisation and production of optimised scaffolds for tissue and bone replacement, with a focus on promoting osseointegration [126,127]. The aerospace industry has implemented the use of lattice components to enhance the performance and reduce the weight of parts, whilst at the same time reducing fuel consumption and environmental footprint [128,129]. The employment of lattice structures within the automotive industry has been demonstrated to have numerous advantages, including reduced noise conduction, enhanced weight reduction and easier recycling of automotive parts [130].

Typically, lattice structures can be divided into two distinct architectural types based on their topology: stochastic or periodic.

Periodic lattice structures are characterised by a periodic arrangement of a specific shape, called unit cell, composed of a group of struts interconnected with each other in points called nodes. The most common periodic lattice structures employ unit cells such as body-centered cubic (BCC), face-centered cubic (FCC) and diamond lattices [131]. The number of struts and nodes are pivotal factors in predicting the mechanical properties of this particular lattice structure, due to their marked impact on the degree of connectivity and freedom of the unit cell. The mechanical behaviour of these lattice structures could be evaluated preliminarily through the Maxwell criterion [132]:

$$M = s - 3n + 6 \tag{4.1}$$

Where M is the Maxwell number, s is the number of struts and n is the number of nodes inside the unit cell.

If $M < 0$, the lattice structure is under-stiff. The number of struts is insufficient to equilibrate the bending moment at nodes, leading to bending stresses on the struts. Therefore, the lattice structure experience a bending-dominated behaviour, characterised by low strength [133]. If $M \geq 0$, the structure has a sufficient number of struts to equilibrate the external forces and the struts experience

only axial stresses. In this case the just-stiff ($M = 0$) or the over-stiff ($M > 0$) lattice structure exhibits a stretch-dominated behaviour with high structural efficiency [134].

Based on these assumptions, stretch-dominated unit cells are suitable configurations for the design of lightweight structures, where high specific stiffness and strength are required. Conversely, bending-dominated structures are more fitting for applications that require high energy absorption, where the deformation of the structure represents the first priority.

Stochastic lattice structures use a distribution of points that are generated algorithmically with no hidden planes of high stiffness [135]. As stated by Munford et al. [136], the implementation of this approach is especially well-suited for components with irregular geometry and curved surfaces. These randomised structures, due to their nature, cannot be recreated or predicted precisely, which introduces additional complexity in the design and in the assessment of their mechanical properties [137]. Kechagias et al. [138] introduced an approach based on the nodal connectivity, defined as the number of struts connected to a node, to describe the stochastic lattice structure's mechanical behaviour and performance. This method has been found to be reliable in predicting bending- or stretch-dominated behaviour for stochastic lattice structures with porosity greater than 60%.

The Maxwell criterion is a theoretical framework that characterises the mechanical behaviours of a single unit cell at a micro-scale level. However, the overall behaviour of the lattice structures is strictly linked to the connections between multiple unit cells, requiring the evaluation of mechanical properties at a macro-scale level. The introduction of lattice structures in industrial applications has given rise to a lack of standardisation with regard to the testing of such structures. For instance, the ISO 13314:2011 standardises the compressive test for porous and cellular materials with a porosity of 50% or more. Nevertheless, the standard can be employed as a guideline for compression testing on lattice structures, with porosity lower than 50%, in order to evaluate the mechanical behaviour at the macro-scale level. As demonstrated in Figure 27, under quasi-static compression test conditions, the lattice structure exhibits three distinct phases. The initial phase is distinguished by a linear elastic region where the structure exerts resistance to the applied load, characterised by an elastic modulus that is associated with the topology and the relative density of the lattice structure. The onset of the second phase, otherwise referred to as the plateau regime, is characterised by the yielding of the struts due to bending or stretching. In this phase, the cells begin to undergo a progressive collapse as a result of the reduction in load-bearing capacity. At this stage, the presence of preferential failure bands within the lattice structure becomes discernible, as illustrated in Figure 27. The third phase is characterised by the densification phenomenon, which is related to the complete collapse of the structure. The different mechanical behaviours predicted by Maxwell criterion at the micro-scale level appear also at the macro-scale level. As demonstrated in Figure 27, the stress-strain curves of a stretch-dominated lattice exhibit higher stiffness and yield strength compared to a bending-dominated lattice with equivalent density. The most significant differences can be identified in the plateau regime. Structures dominated by stretch exhibit a plateau consisting of peaks and valleys, a consequence of progressive failure of layers. In contrast, yielding of bending-dominated structures is driven by the plasticisation of the struts at nodal locations. In this phase, the specimen demonstrates a compression at an approximately constant load [139].

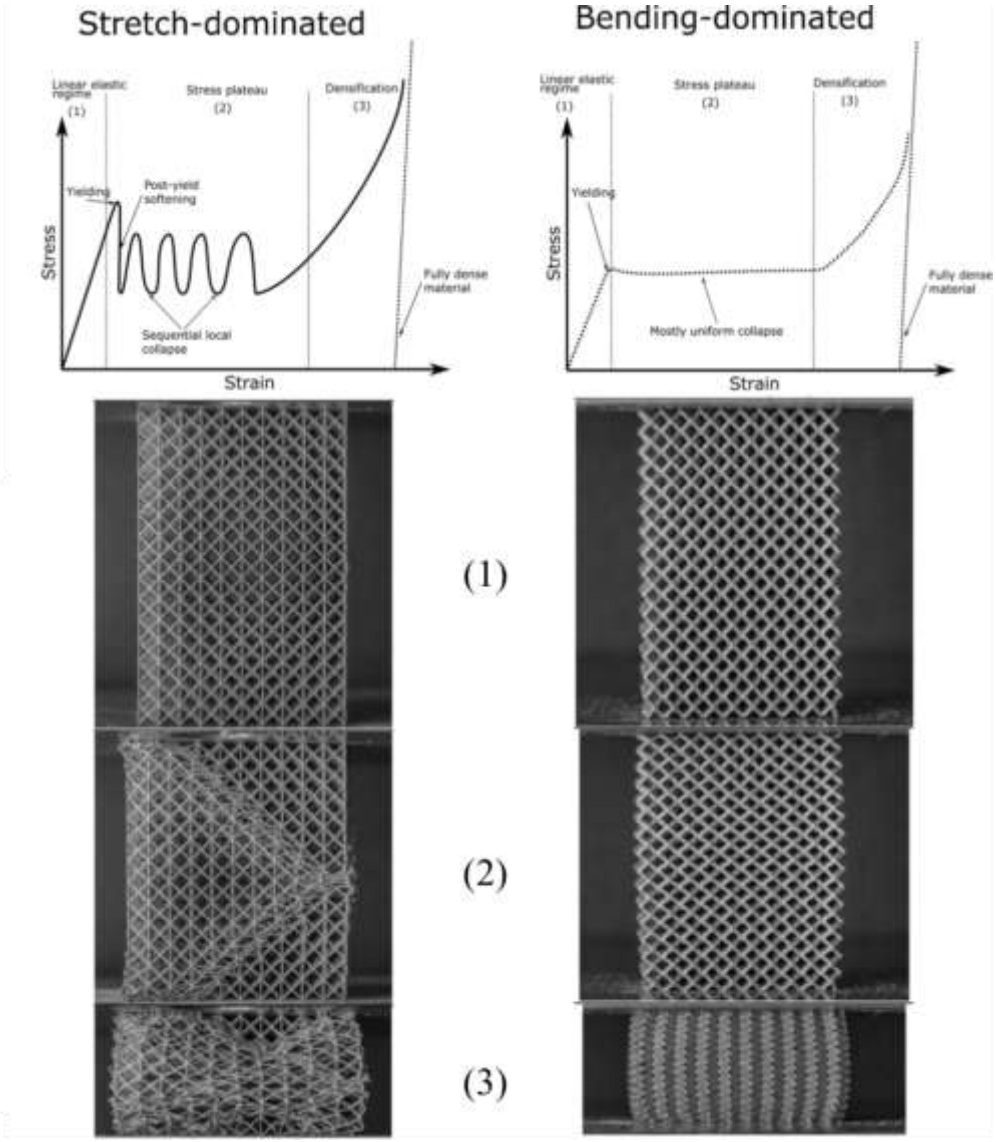

Figure 27 - Compressive stress-strain curves for bending- and stretching-dominated lattice structures with same relative density; (1) linear-elastic region, (2) plateau regime and (3) densification [140]

Despite the numerous contributions to understanding and predicting the mechanical behaviour of lattice structures present in the scientific literature, the most significant contribution comes from the work of Gibson and Ashby. The so-called Gibson-Ashby model represents the base model for analysing the mechanical behaviour of lattice structures based on their topology and porosity. This relationship is based on Euler-Bernoulli beam theory and can be applied to elastic modulus (E) and yield strength (σ_y) of the lattice structures:

$$\frac{E}{E_s} = C_1 \left(\frac{\rho}{\rho_s}\right)^n \tag{4.2}$$

$$\frac{\sigma_y}{\sigma_{ys}} = C_2 \left(\frac{\rho}{\rho_s}\right)^m \tag{4.3}$$

where E_s and σ_{ys} are the elastic modulus and yield strength of the base material, *C1* and *C2* are constants related to the specific unit cell fitted to experimental data. The value of n and m is related to the mechanical behaviour of the lattice structure, in particular, $n = m = 1$ in an ideal stretch-dominated behaviour and $n = 2; m = 3/2$ in an ideal bending-dominated behaviour [141]. Benedetti

et al. [141] analysed a collection of experimental data published in literature for several unit-cell architectures and materials. This analysis demonstrated a correlation between the trend of the data and the Gibson-Ashby model in predicting the mechanical behaviour, as demonstrated in Figure 28.

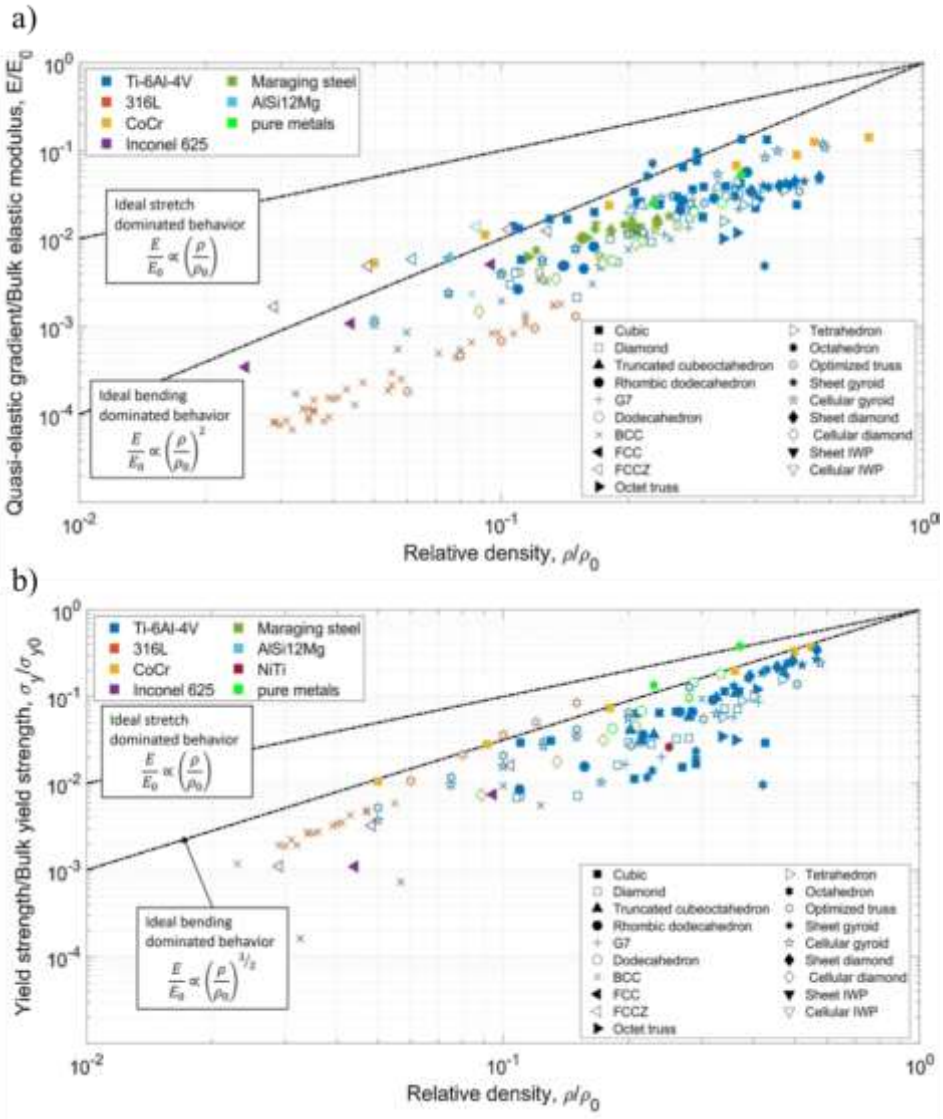

Figure 28 - (a) Relative quasi static elastic gradient and relative yield strength (b)as a function of relative density for different type of cellular lattice structures [141].

The design of lattice structures is characterised by a dual challenge, the description of microscale behaviour in order to infer the macroscale behaviour. Researchers generally implement finite element models to assess the response of the structure to load conditions. This approach provides a precise characterisation of the interactions between struts and nodes, and a description of the connections between the lattice and the rest of the components [142]. In order to achieve precise results, the finite element analysis (FEA) necessitates an accurate mesh to describe the intricate geometry of a LS, thereby increasing the computational time [143]. As demonstrated by several authors [144,145], the mesh density, in conjunction with the number and type of elements employed for the discretisation of the structure, exerts a significant effect on the accuracy of the elastic properties assessment. In order to overcome these limitations, a range of approaches have been developed for the analysis of the mechanical behaviour of the entire lattice structure. One of the most widely employed approaches

is the Representative Volume Element (RVE). This method is based on the utilisation of a fraction of the volume of the lattice, which is representative of the properties of the entire structure. It is imperative that this element is sufficiently small in order to reduce the complexity of the simulation, whilst also being sufficiently large to properly represent the behaviour requested of the lattice [141]. This method has been employed to analyse different lattice structures, thereby demonstrating its reliability in evaluating the overall linear elasticity constant and overall ultimate failure envelope [146,147]. Moreover, this approach has been shown to reduce significantly the computational cost of simulating lattice structures. However, in cases where the structure is complex or large, the computational cost remains substantial. The problem is exacerbated when the analysis is extended to components integrating lattice structures, due to the requirement of a considerable number of elements to fully describe the mechanical behaviour of the entire structure.

In order to overcome the aforementioned challenges, a variety of methodologies have been developed to analyse the mechanical behaviour of complex components, while maintaining reasonable computational cost. One of the most valuable techniques is multiscale modelling [148]. This approach involves the computational modelling of the mechanical behaviour of small lattice structures or single unit cells through finite element analysis, and the subsequent experimental validation through the use of additive manufactured specimens. Following this, the unit cells space is replaced by a continuum that can be efficiently modelled by finite element [149]. This facilitates the evaluation of the mechanical behaviour of the entire structure. Shojaee et al. [150] corroborated the satisfactory agreement between a multi-scale approach and a full-scale simulation for the characterisation of the mechanical properties of a lattice structures component. In the field of industrial applications, the design strategy is driven by this methodological approach [151,152].

The complex architectures of lattice structures pose a crucial challenge in the manufacturing process. While conventional techniques are not suitable for the production of components with intricate and detailed features, additive manufacturing is unique in its ability to overcome these constraints. Among all the 3D printing technologies nowadays available on the market, Laser Powder Bed Fusion represents the more reliable and well-established technique for the manufacturing of lattice structures [153]. Despite the well-known advantages of LPBF technologies, it is crucial to clearly define the limitations, mostly in term of the presence of defects. As reported by Dallago et al. [154], a wide range of defects can be observed in LPBF-processed components, including porosity, as-built/as-designed morphological deviations, residual stresses and high surface roughness. These defects can markedly affect the mechanical properties of the components. Lattice structure components are distinguished by their large specific surface area, thin struts, and numerous nodal locations. In this scenario, minor defects also become stress raisers. As reported by some authors [134,141], the geometric inaccuracies affecting the real manufactured lattice structures can affect the mechanical behaviour. For instance, these differences can lead to a bending-dominated behaviour with respect to the stretch-dominated behaviour that was predicted. In this field, the mechanical performance is affected not only by the topology and relative density of the lattice structure, but also by printability and manufacturing-induced defects, which must be taken into account [155].

Based on the considerations discussed above, the present chapter is dedicated to the experimental characterisation of lattice structures manufactured by LPBF technology under quasi-static compression tests. The aim of this study is to undertake a comparative analysis of different lattice structures configurations in order to assess the most suitable configuration in terms of stiffness and deformation behaviour. This investigation is driven by the objective of identifying the optimal

architecture for integration into an e-bike frame component, a topic that will be addressed in the following chapters.

3.2 Materials and methodology

In this study, cylindrical specimens with a non-periodic lattice topology were employed. The architectural design is based on a tetrahedral topology. The external surface of the specimens is discretised into a triangular mesh while the internal volume is comprised of tetrahedral cells that are rearranged with a non-periodic topology. The selection of this architecture was made with the aim of achieving macroscopically quasi-isotropic mechanical behaviour. This unit cell type, according to Maxwell's criterion, is expected to promote a stretch-dominated behaviour, making it particularly well-suited for applications requiring high stiffness [156]. Due to the non-periodic arrangement, the unit cells do not exhibit a constant nodal connectivity.

The mechanical behaviour of the lattice structures was investigated by varying the unit cell size (L_{cell}) from 3.0 mm to 3.5 mm and by varying the strut diameters (d_s) between 0.7, 0.85, 1.00, 1.15, 1.30 mm, for a total of ten distinct configurations. The selection of this range was guided by the manufacturer's guidelines to ensure printability, to avoid extreme geometric distortion and to prevent strut collapse during the fabrication process. Adopting this approach ensures that the resulting lattice structures remain representative of configurations that could be realistically integrated into structural components. The specimens were manufactured in three different types to evaluate the effect of specimen size and geometry on the mechanical behaviour:

- Solid cylinder with a height, L_0, and diameter, D_0, of 13 mm
- Solid cylinders with a height, L_0, and diameter, D_0, of 25 mm
- Hollow cylinders with an internal diameter, D_{0_int}, of 7 mm and a height, L_0, and external diameter, D_0, of 13 mm

The specimens were designed with a height-to-diameter ratio of 1 in accordance with the ISO 13314:2011 guideline and were manufactured using AlSi10Mg alloy with laser powder bed fusion (LPBF) technology. The chemical composition of the powder feedstock is reported in Table 9, while the main physical and mechanical properties of the AlSi10Mg alloy employed for the tested specimens are reported in Table 10. The selection of this alloy was driven by its high stiffness, low density and high corrosion resistance. These properties make it a highly suitable material for a wide range of applications in the automotive, aerospace and defence sectors [157].

Table 9 - Chemical composition (wt.%) of the feedstock powder.

Element (wt.%)	Al	Si	Mg	Cu	Mn	Fe	Ti
AlSi10Mg	Bal.	10.3	0.36	< 0.01	< 0.01	<0.15	< 0.01

Table 10 - Physical and mechanical properties of AlSi10Mg alloy [158].

Density ρ_s (g/cm^3)	Ultimate Tensile Strength *UTS* (MPa)	Yield stress σ_{ys} (MPa)	Elongation *A%*	Young Modulus E_s (GPa)

2.67	440 ± 30	240 ± 20	6 ± 3	70

The specimens were fabricated using an EOS M290 Dual Mode LPBF machine with a layer thickness of 30 μm and an argon atmosphere. The fabrication step deployed a heating system that kept the baseplate temperature as high as 165°C throughout the whole process. The samples were manufactured with the base parallel (Z) to the building direction as illustrated in Figure 29, following the manufacturer's expertise in terms of optimal build orientation.

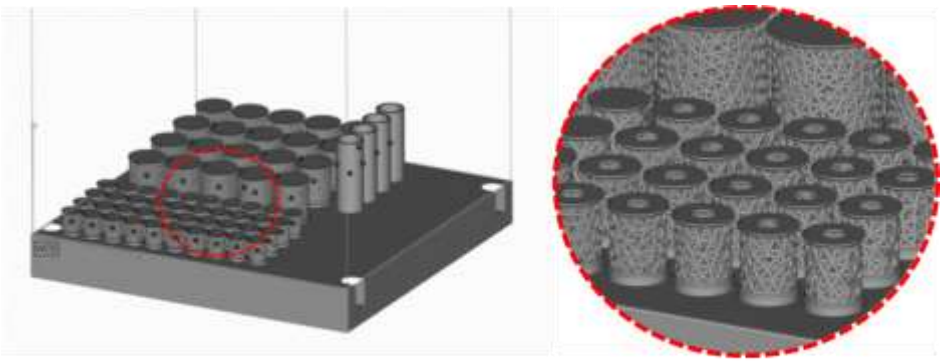

Figure 29 - Build layout of the cylindrical AlSi10Mg specimens.

The mechanical characterisation was conducted through quasi-static compression tests, performed in accordance with the guideline outlined in ISO 13314:2011. These tests were carried out using a servo-hydraulic Instron tensile testing machine operated under displacement control, with a crosshead speed of 0.013 mm/s and an initial preload of 100 N. This ensured proper contact between the specimen and the platens prior to data acquisition. Two specimens per configuration were manufactured and subsequently tested.

The Table 11 summarises the lattice-structure parameters of all specimens manufactured.

Table 11 - Lattice structure parameters of all the specimens manufactured.

Type	**$L_0 = D_0$ (mm)**	**L_{cell} (mm)**	**d_s (mm)**	**Name**	**ρ_{rel}**
Solid	13	3	0.70	S13_3_0.70	0.27
			0.85	S13_3_0.85	0.48
			1.00	S13_3_1.00	0.61
			1.15	S13_3_1.15	0.72
			1.30	S13_3_1.30	0.83
		3.5	0.70	S13_3.5_0.70	0.27
			0.85	S13_3.5_0.85	0.38
			1.00	S13_3.5_1.00	0.49
			1.15	S13_3.5_1.15	0.59
			1.30	S13_3.5_1.30	0.70
Hollow	13	3	0.70	H13_3_0.70	0.27
			0.85	H13_3_0.85	0.48
			1.00	H13_3_1.00	0.61

			1.15	H13_3_1.15	0.72
			1.30	H13_3_1.30	0.83
			0.70	H13_3.5_0.70	0.27
			0.85	H13_3.5_0.85	0.38
		3.5	1.00	H13_3.5_1.00	0.49
			1.15	H13_3.5_1.15	0.59
			1.30	H13_3.5_1.30	0.70
			0.70	S25_3_0.70	0.27
			0.85	S25_3_0.85	0.48
		3	1.00	S25_3_1.00	0.61
			1.15	S25_3_1.15	0.72
			1.30	S25_3_1.30	0.83
Solid	25		0.70	S25_3.5_0.70	0.27
			0.85	S25_3.5_0.85	0.38
		3.5	1.00	S25_3.5_1.00	0.49
			1.15	S25_3.5_1.15	0.59
			1.30	S25_3.5_1.30	0.7

The specimens were grouped according to their type, overall dimensions, unit cell size, and strut diameter. In this notation, for example, the label S13_3_0.70 denotes a solid cylindrical specimen with height, L_0, and diameter, D_o, equal to 13 mm, a unit cell size of 3 mm and a strut diameter of 0.70 mm. The relative density, ρ_{rel}, is evaluated as the ratio between the designed lattice structure volume and the volume of a bulk specimen with the same dimensions.

3.3 Results and discussion

The compression tests were stopped once 40% of the specimens' height was reached, due to extremely high densification, in order to avoid possible undesired buckling effects. Examples of resulting compression curves are demonstrated in Figure 30. All compression curves exhibit the characteristic behaviour of metal lattice structures [140]. The initial linear regime is characterised by the elastic deformation of the struts, while the instability regime is marked by oscillations in the compression force or the presence of a plateau. This region has been demonstrated to be linked to the buckling trigger of struts [134]. Finally, for some more compact configurations, a densification regime linked to the progressive collapse of the struts and to the increase in the compression force is observed.

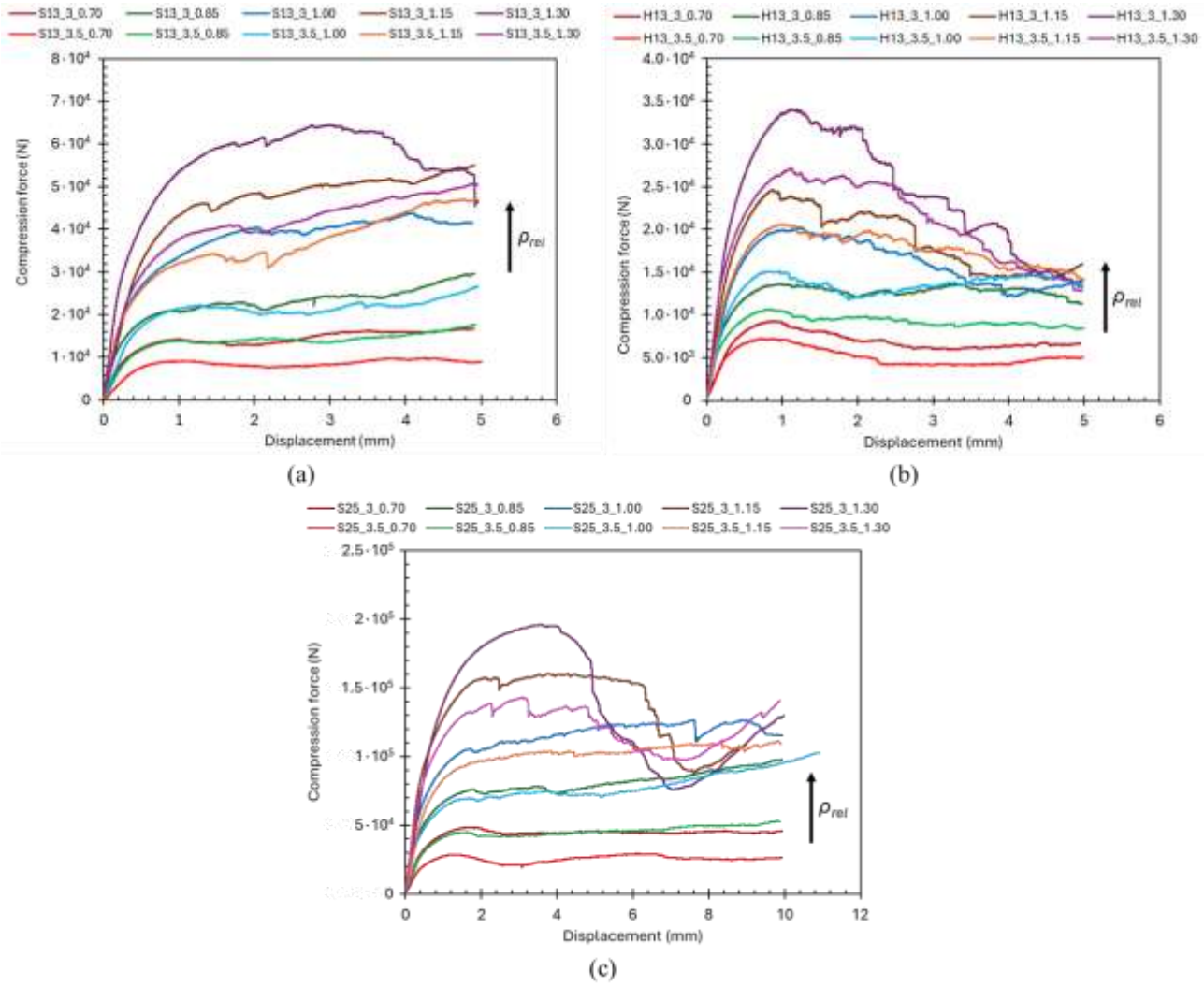

Figure 30 - Compression curves for (a) solid specimens with $L_0=D_0=13mm$, (b) hollow specimens with $L_0=D_0=13mm$ and (c) solid cylinder specimens with $L_0=D_0=25mm$.

In order to compare the different topology of the lattice structures analysed, the following parameters were evaluated. Specific stiffness, stress and strain were evaluated for each lattice series through the following equations:

$$K\left[\frac{N}{mm}\right] = \frac{F}{u} \tag{4.4}$$

$$\sigma[MPa] = \frac{F}{A_0} \tag{4.5}$$

$$\varepsilon\left[\frac{mm}{mm}\right] = \frac{L_0 - L}{L_0} \tag{4.6}$$

Where $F\ [N]$ represents the applied load, $u\ [mm]$ is the displacement, $A_0\ [mm2]$ is the base area of the lattice specimen and $(L_0\text{-}L)$ represents the reduction of the initial length L_0 of the lattice specimen. The elastic modulus is evaluated employing the linear interpolation with a correlation factor almost equal to 1 ($R^2 \geq 0.99$) in the elastic region of σ-ε curve. Thus, the yield stress is calculated in correspondence of a permanent strain ε equal to 0.2% [21]. Table 12 shows the evaluated

mean value of specific stiffness, Young's modulus (E) and yield strength (σ_y) for each tested lattice topology.

Table 12 – Mean values and standard deviation data of mechanical properties and Topological Aspect Ratio (TAR) of lattice specimens.

Type	Name	ρ_{rel}	K (kN/mm)	E (GPa)	σ_y (MPa)	TAR (mm)
Solid	S13_3_0.70	0.27	37 ± 5	3.6 ± 0.5	92 ± 3	12.9
	S13_3_0.85	0.48	71 ± 1	7.0 ± 0,1	133 ± 1	10.6
	S13_3_1.00	0.61	67 ± 15	6.5 ± 2,1	219 ± 20	9.0
	S13_3_1.15	0.72	85 ± 18	8.3 ± 1,8	281 ± 15	7.8
	S13_3_1.30	0.83	135 ± 5	13.3 ± 0,5	310 ± 1	6.9
	S13_3.5_0.70	0.27	22 ± 5	2.2 ± 0,5	63 ± 2	17.5
	S13_3.5_0.85	0.38	31 ± 3	3.1 ± 0,3	93 ± 1	14.4
	S13_3.5_1.00	0.49	50 ± 9	4.9 ± 0,8	138 ± 5	12.3
	S13_3.5_1.15	0.59	89 ± 1	8.7 ± 0,1	192 ± 1	10.7
	S13_3.5_1.30	0.70	129 ± 21	12.6 ± 6,8	264 ± 38	9.4
Hollow	H13_3_0.70	0.27	22 ± 2	3.0 ± 0,4	90 ± 2	12.9
	H13_3_0.85	0.48	43 ± 1	5.9 ± 0,1	124 ± 1	10.6
	H13_3_1.00	0.61	51 ± 8	7.0 ± 1,0	182 ± 8	9.0
	H13_3_1.15	0.72	78 ± 25	10.8 ± 3,5	218 ± 13	7.8
	H13_3_1.30	0.83	99 ± 33	13.7 ± 4,6	279 ± 21	6.9
	H13_3.5_0.70	0.27	31 ± 11	4.2 ± 1,5	55 ± 22	17.5
	H13_3.5_0.85	0.38	50 ± 5	6.9 ± 0,7	92 ± 1	14.4
	H13_3.5_1.00	0.49	48 ± 8	6.7 ± 1,1	138 ± 6	12.3
	H13_3.5_1.15	0.59	52 ± 4	7.1 ± 0,5	189 ± 2	10.7
	H13_3.5_1.30	0.70	79 ± 3	10.9 ± 0,4	225 ± 2	9.4
Solid	S25_3_0.70	0.27	85 ± 6	4.4 ± 0,3	76 ± 3	12.9
	S25_3_0.85	0.48	148 ± 2	7.5 ± 0,1	111 ± 1	10.6
	S25_3_1.00	0.61	187 ± 3	9.5 ± 0,1	158 ± 7	9.0
	S25_3_1.15	0.72	228 ± 7	11.6 ± 0,7	221 ± 2	7.8
	S25_3_1.30	0.83	173 ± 15	8.8 ± 1,4	283 ± 1	6.9
	S25_3.5_0.70	0.27	54 ± 3	2.7 ± 0,2	48 ± 2	17.5
	S25_3.5_0.85	0.38	82 ± 12	4.2 ± 0,6	73 ± 5	14.4
	S25_3.5_1.00	0.49	139 ± 16	7.1 ± 0,8	104 ± 3	12.3
	S25_3.5_1.15	0.59	164 ± 24	8.4 ± 2,2	150 ± 3	10.7
	S25_3.5_1.30	0.7	218 ± 9	11.1 ± 0,5	193 ± 1	9.4

As illustrated in Figure 31, the stress-strain curves demonstrate the effect of varying the parameters L_0 and D_0 on the behaviour of the solid cylinder. It has been observed that, with the maintenance of the unit cell size, an increase in the strut diameter is associated with an increase in the relative density. This rise is directly correlated with an enhanced slope of the linear phase, suggesting elevated stiffness, as demonstrated in Figure 31 and Table 12. This monotonic and well-defined trend is also observed in the case of Young's modulus and yield strength, indicating that relative density is a dominant parameter in controlling the mechanical performance of a lattice

structure. It is evident from the stress-strain curves depicted in Figure 31 that an increase in the relative density of the lattice also affects the mechanical behaviour of the structure. In the case of structure with low relative density, a σ-ε curve is observed that suggests a bending-dominated behaviour, characterised by an almost constant plateau after yield. Conversely, with increasing strut diameter, and consequently relative density, a transition to a more stretch-dominated behaviour is evident, characterised by higher stiffness and post-yield softening. Kechagias et al. [138] reported analogous results, thereby confirming that an increase in relative density can lead to a transition from bending- to stretch-dominated behaviour for non-periodic lattice structures. A further parameter that exerts an impact on relative density is the unit cell size. It is evident from Figure 31 that increasing the size of the unit cell while maintaining the strut diameter results in a reduction of the relative density of the lattice structures, which consequently leads to a reduction in mechanical properties. As reported by Pollara et al. [159] a larger lattice architecture offers a smaller number of load-bearing members within the same volume.

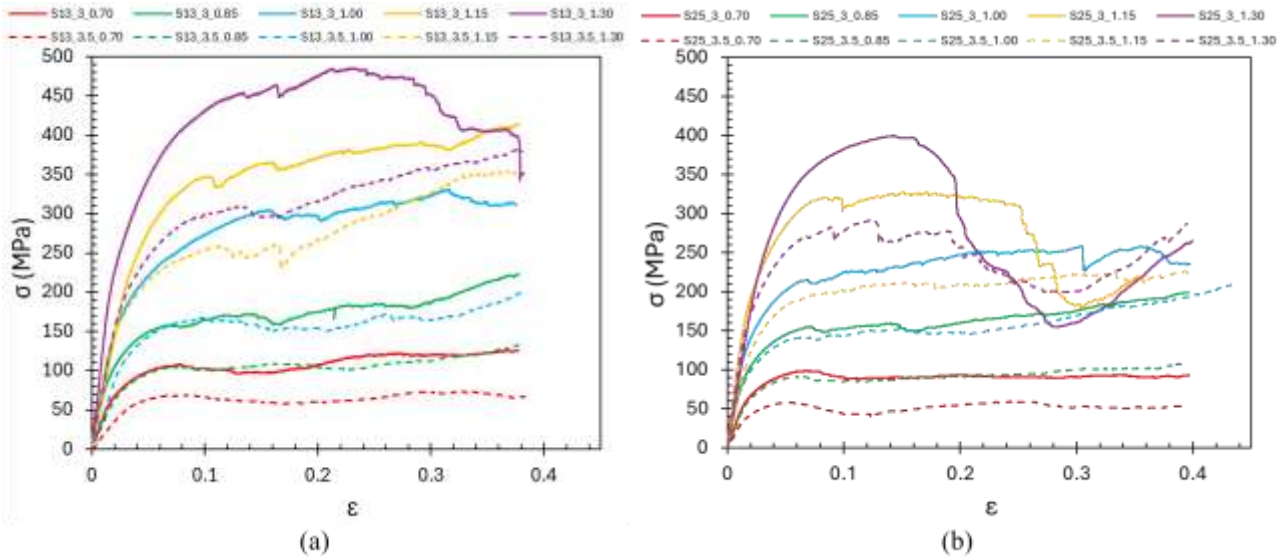

Figure 31 - Stress-strain curves for solid cylinder with (a) $L_0 = D_0 = 13\ mm$ and (b) $L_0 = D_0 = 25\ mm$.

It is evident that by increasing the overall size of the specimens, whilst maintaining the unit cell size and strut diameter constant, lattice structures with identical relative density but a different number of unit cells are obtained. Therefore, it can be theorised that this could affect their mechanical properties. Xu et al. [160] introduced the concept of "node weight" to quantify the mechanical contribution associated with each node in a lattice structure as a function of the number and orientation of converging struts. From a macroscopic view, the overall mechanical response is driven by the statistical distribution of these load-bearing nodes. Increasing the number of unit cells enhances the load-transferring capacity of the lattice structure, resulting in increased stiffness. However, this also led to an enhancement in the number of highly stressed nodes and struts, as well as the probability of geometric irregularities and manufacturing-induced defects inherent in the LPBF process. It is well established in the literature that the onset of failure in lattice structures could be driven by the weakest local feature, resulting in a potential premature rupture [161]. As demonstrated in Figure 32a, an enhancement in Young's modulus is associated with a decrease in the apparent yield strength as the sample size increases (Figure 32b). While an increased number of nodes contributes to greater

stiffness in the linear elastic regime, as also confirmed by Yang and Park et al. [162,163], the increased probability of critically stressed or faulty nodes results in an earlier onset of collapse. In view of the limited number of specimens analysed and the low dispersion observed in these results, further experimental and numerical investigations would be necessary to fully quantify the influence of the number of unit cells on the mechanical properties of these lattice structures.

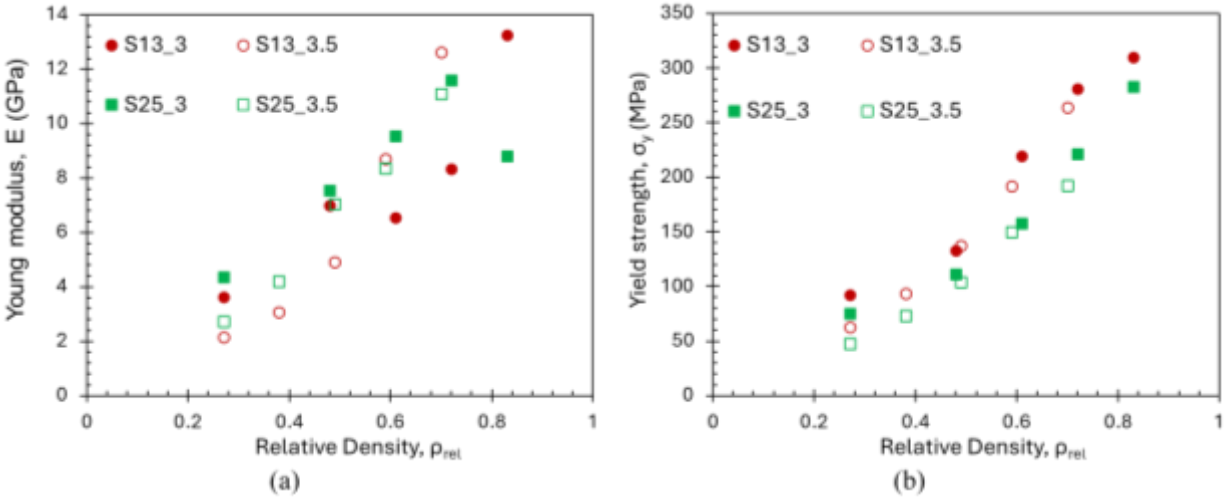

Figure 32 – Effect of relative density, unit cell size and specimen geometry on (a) Young modulus and (b) yield strength of the lattice structures.

Figure 33 presents the σ-ε curves for specimens S13 and H13. It is evident that the different geometry used for the H13 configuration results in a pronounced reduction in mechanical properties. This assertion is corroborated by the values of stiffness, Young's modulus and yield strength reported in Table 12. These differences further confirm that the geometry of the specimens has a significant impact on the propagation of local instabilities within the structure and the redistribution of load within the lattice. In the specimens analysed, the reduction in the volume occupied by the lattice structure, while maintaining constant unit cell size and strut diameter, is in accordance with the "weight node theory" introduced by Xu et al. [160]. The employment of cylindrical specimens, wherein the lattice structure is confined within a circular crown with thickness of 3 mm, results in a substantial reduction in the number of load-bearing nodes and struts that contribute to the mechanical response. Consequently, the macroscopic stiffness of the structure is significantly reduced. This effect is particularly evident in the second stage of deformation, referred to as the plateau regime [131]. Once yielding occurs in the struts, the number of elements effectively working against the compression load is significantly lower in the H13 specimens than in the S13 configurations. This leads to a faster collapse and a more pronounced decrease in compressive stress. Figure 33 clearly shows that, even for the H13 architecture as observed for the S13 and S25 specimens, an increase in relative density strongly affects the mechanical behaviour of the structure, promoting a transition from predominantly bending-dominated behaviour to a predominantly stretch-dominated behaviour.

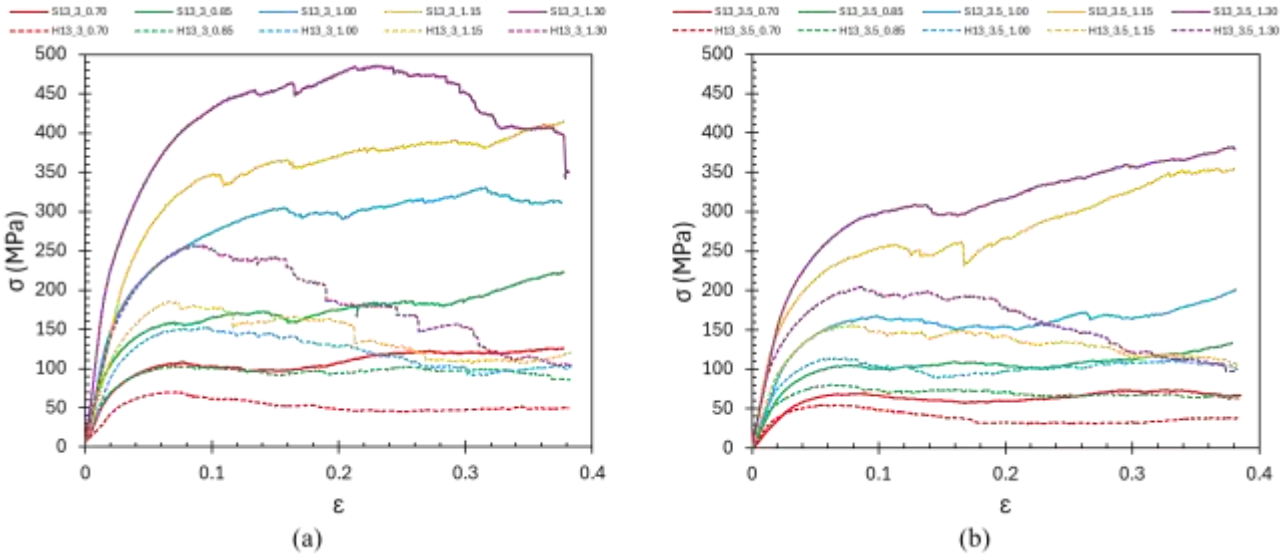

Figure 33 - Stress-strain curves for solid and hollow cylinder with unit cell size (a) L_{cell} = *3 mm* and (b) L_{cell} = *3.5 mm*.

The experimental results obtained in this study provide evidence that the mechanical behaviour of the tested lattice structures is primarily driven by the relative density and specimen geometry. Among these parameters, relative density has been identified as the primary driver of stiffness, Young's modulus and yield strength. The relative density is linked to the geometrical parameters of the lattice structure expressed in terms of unit cell size and strut diameter. In order to better analyse the effect of these geometrical features on the mechanical properties, the experimental results were further analysed using the Topological Aspect Ratio (TAR), as reported in [133]. The TAR parameter is defined as follows:

$$TAR\ [mm] = \frac{A_{cell}}{d_s} = \frac{L_{cell} \cdot L_{cell}}{d_s} \tag{4.7}$$

As presented in Table 12, the evaluated *TAR* for each configuration of lattice structures is provided, thus offering a geometrical descriptor of the lattice architecture. In the context of structural analysis, the relative density of a material is defined as a quantitative parameter that quantifies the solid material within a structure. The *TAR* method has been demonstrated to effectively describe the slenderness of load-bearing elements, thereby facilitating a comprehensive understanding of the mechanical behaviour of the structure. As demonstrated in Table 12, this parameter could represent a reliable alternative to relative density in order to describe the mechanical performance. Specimens with identical relative density may exhibit different *TAR* value. As shown in Figure 34, the normalised Young's modulus (E/E_s) and normalised yield strength (σ_y/σ_{ys}) are presented as a function of the *TAR* parameter. The values of the elastic modulus and yield strength, obtained for each configuration of the lattice structure, have been normalised with respect to the modulus of elasticity (E_s) and yield strength (σ_{ys}) of the AlSi10Mg alloy, as reported in Table 10. For all the configurations analysed, the mechanical properties exhibited a decreasing trend as *TAR* increased. As illustrated in Figure 34a, the relationship between E/E_s and *TAR* displays a coefficient of determination (R^2) ranging from 0.72 to 0.94. This finding suggests that this parameter effectively captures the geometric features that govern the mechanical behaviour of these lattice structures. It has been demonstrated that the reduction in the Young's modulus of the lattice structures, with an increase in the TAR, can be attributed to the

enhanced slenderness of the struts in comparison to the dimensions of the unit cell. Pirinu et al. [133] corroborated that a low *TAR* is indicative of a structure characterised by elevated stiffness and mechanical resistance, and a greater tendency for stretch-dominated behaviour, whilst a higher *TAR* is representative of a greater propensity for bending-dominated behaviour. As demonstrated in Figure 34b, a similar trend is evident in σ_y/σ_{ys}, exhibiting a stronger correlation ($R^2 > 0.89$). This finding indicates that the slenderness of the load-bearing elements, as characterised by the *TAR*, is a pivotal factor in the onset of yielding in the struts and nodes [164].

When comparing different configurations with equal *TAR* values, a dispersion of experimental results can be observed. This underscores the fact that, while the topological aspect ratio can describe the mechanical behaviour of a lattice structure, it is insufficient to fully capture its complexity. The mechanical behaviour of the structure is also affected by parameters such as the number of unit cells and the geometry of the specimen.

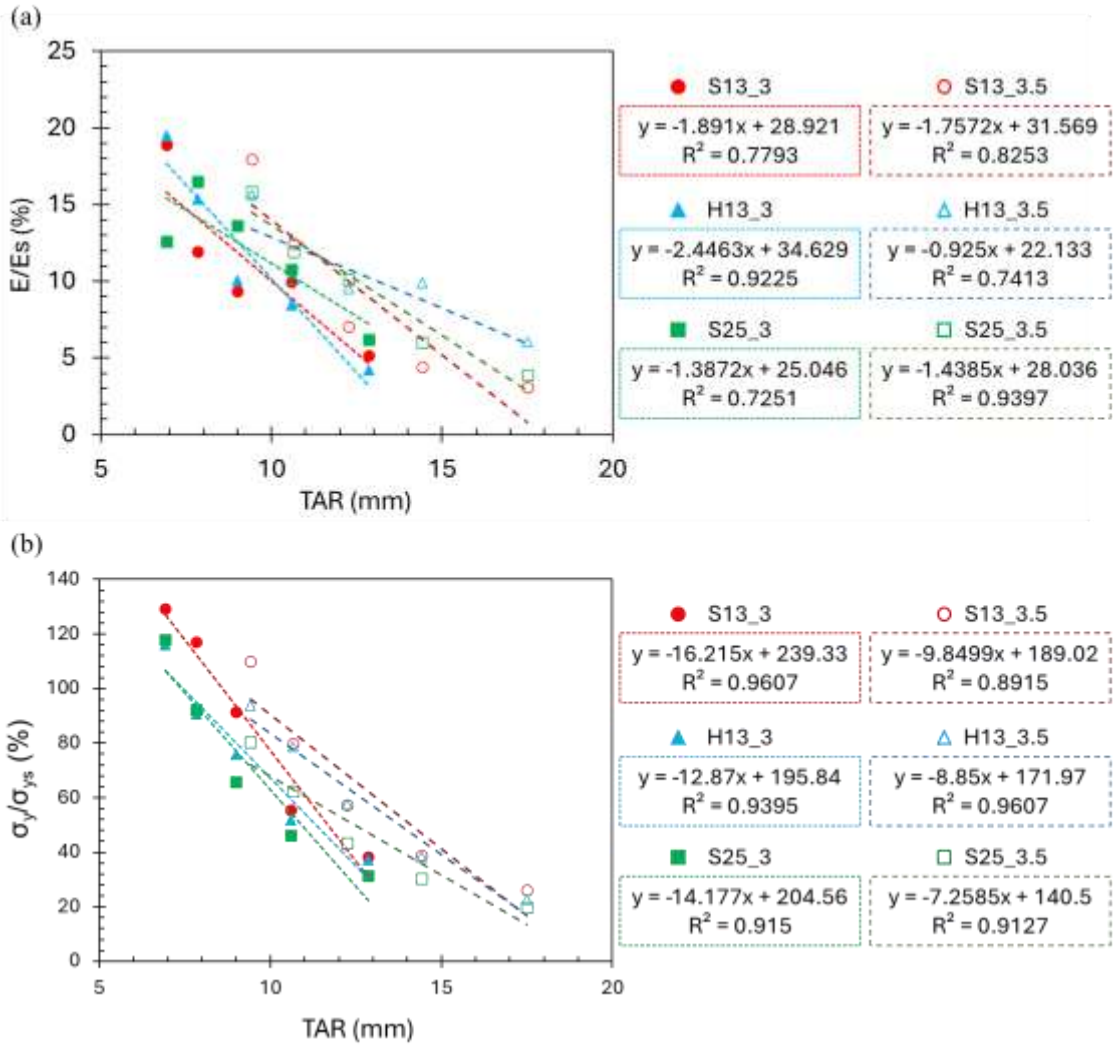

Figure 34 – Normalised (a) elastic modulus and (b) yield strength versus TAR index for all the lattice configurations tested.

Although the topological aspect ratio (*TAR*) describes how the geometrical features affect the mechanical response of non-periodic lattice structures, it does not provide a unique criterion to distinguish between bending-dominated and stretch-dominated behaviour. Therefore, an additional

mechanical analysis based on established models is required. In order to perform a more detailed analysis of these non-periodic lattice structures and distinguish them in stretch- or bending-dominated behaviour, the Gibson-Ashby model was implemented. The experimental data collected for all the configurations were analysed with the Eq. (4.2) and Eq. (4.3), as illustrated in Figure 35. A power regression was performed on the lattice structures' elastic modulus and strength data in order to derive the coefficients and exponents. Subsequently, these parameters were compared with the predictions of the Gibson-Ashby model in terms of bending- and stretch-dominated behaviour. The elastic response, as shown in Figure 35a, demonstrates exponents *n* ranging from approximately 0.8 to 1.9, based on the relative density and specimen geometry. The Gibson-Ashby model shows specimen S13_3 exhibits a stretch-dominated behaviour. An increase in the unit cell size, whilst maintaining a constant strut diameter, resulted in a slenderness of the struts with respect to the cell size and a decrease in the number of unit cells within the lattice volume. This finding aligns with the aforementioned "node weight theory", and it is consistent with the observation that the struts are less able to equilibrate the bending moments at the nodes, resulting in a behaviour that is predominantly governed by bending forces [132,160]. For the S25 configuration, the trend is comparable, however, increasing the unit cell size resulted in a transitional regime between the two ideal deformations. For the H13 configuration, an exponent *n* decrease was observed as the unit cell size increased, thus indicating a deviation from the previously observed trend. Such behaviour, when combined with an exponent $n < 1$, may be associated with geometric weakness or local defects [165]. The yield strength analysis reported in Figure 35b highlights a clear transition from stretch-dominated behaviour ($n=1$) for $L_{cell} = 3\,mm$ to bending-dominated behaviour ($n=1.5$) for $L_{cell} = 3.5\,mm$ across all the investigated configurations.

It has been observed that configurations previously associated with low *TAR* values, characterised by increased density, demonstrate a greater propensity for stretch-dominated behaviour. In contrast, lattices with high *TAR* values are associated with a more bending-dominated behaviour. The Gibson-Ashby model has been proven to align closely with the *TAR*-based model, thereby reinforcing the hypothesis that topological aspect ratio can accurately capture the geometrical features of non-periodic lattice structures. The Gibson-Ashby analysis demonstrates also that the mechanical behaviour of non-periodic lattice structures cannot be described using a single deformation regime. In certain scenarios, the observed behaviour was attributed to a transitional regime, which was found to be influenced by parameters such as the unit cell size, strut diameter, lattice geometry and also geometric irregularities and manufacturing-induced defects.

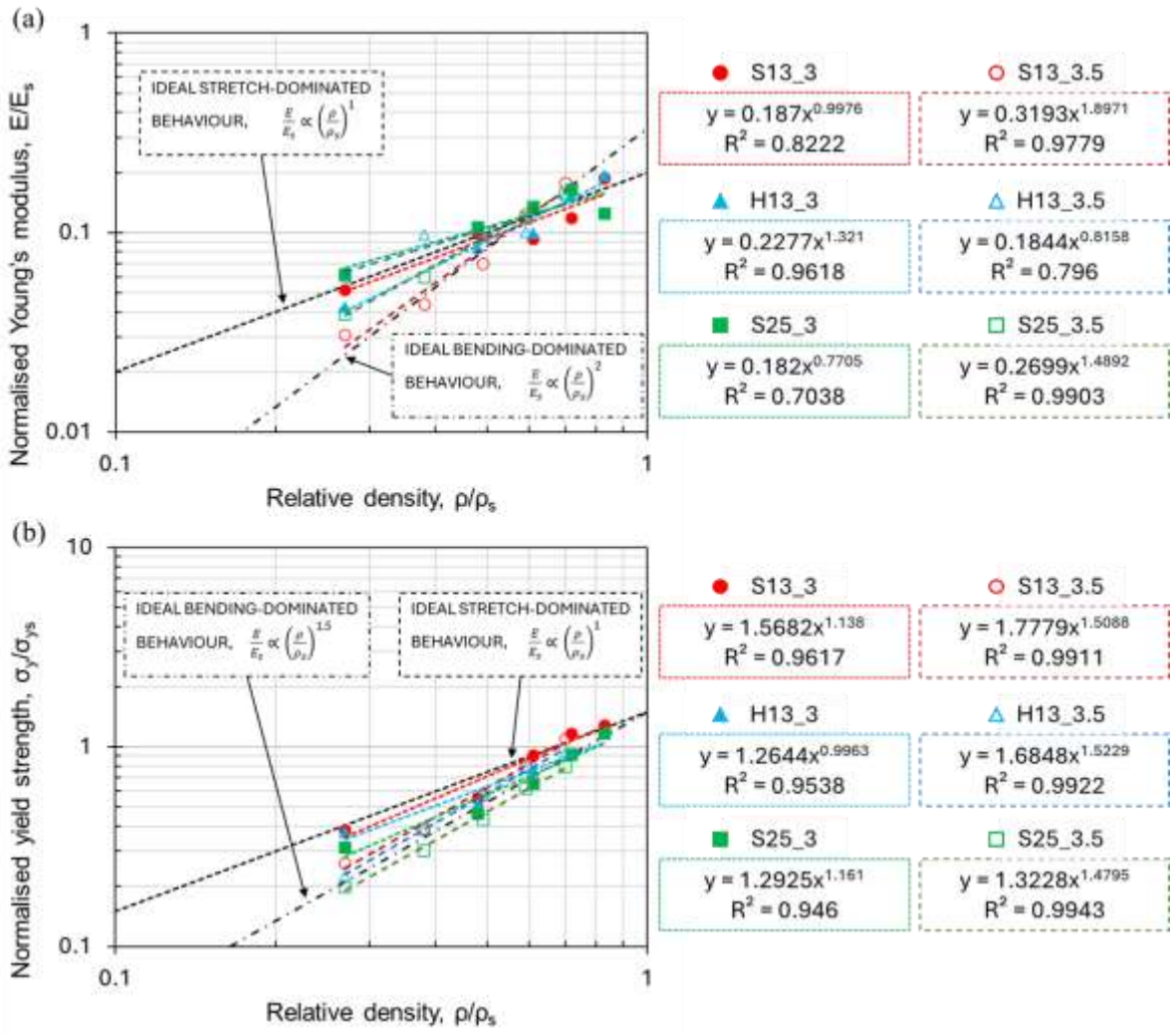

Figure 35 - Normalised (a) elastic modulus and (b) yield strength versus relative density for all the lattice configurations tested.

This study established a robust experimental and analytical basis for understanding the mechanical behaviour of LPBF-processed non-periodic lattice structures. The combined use of relative density, the topological aspect ratio and the Gibson-Ashby model enables a comprehensive interpretation of stiffness, strength and deformation mechanism.

In the course of the present study, a comprehensive analysis of the tested configuration was conducted. The analysis revealed that, tetrahedral cells with a unit cell size of 3 mm consistently led to a lattice structure exhibiting stretch-dominated behaviour, regardless of the specimen size and geometry. From an industrial standpoint, these configurations appear particularly suitable for lightweight structural applications in which high stiffness and strength are the primary requirements [166]. Conversely, an enhancement in the unit cell size resulted in architectures with a predominantly bending-dominated behaviour. From the perspective of energy absorption, such configurations dominated by bending exhibit a more stable plateau regime, which is typically associated with enhanced energy dissipation through progressive strut yielding [167]. Furthermore, this study highlighted the possibility of achieving mixed deformation regimes through appropriate tailoring of the lattice parameters. This aspect is worthy of considerable interest, as, in accordance with specific

functional requirements, lattice structures can be tailored to exhibit a hybrid mechanical behaviour that is specifically suitable for certain applications.

4 Hybrid welding of aluminium alloys

Additive manufacturing is a well-established technology that has found application in numerous industrial sectors, such as aerospace, automotive and biomedical [168]. Among all the additive manufacturing technologies, Laser Powder Bed Fusion is recognised as one of the most promising for industrial applications [169]. Despite its well-known advantages and strategic suitability for specific applications, already discussed in the previous chapters, this technology is not always able to produce large or geometrically complex parts without resorting to conventional manufacturing or joining processes. Furthermore, in specific scenarios, economic or operational constraints require joining processes [170]. In the field of light mobility, the employment of hybrid design strategies integrating AM with wrought aluminium alloys has been shown to yield substantial advantages, including enhanced functionality and weight reduction. However, this hybrid approach involves the development of reliable and suitable welding strategies to ensure mechanical integrity and durability. In order to overcome these limitations, it is crucial to develop the technological capability to join components fabricated via both traditional and additive manufacturing methods.

Recent studies have focused on the welding of additively manufactured aluminium alloys, particularly the combination of 3D-printed and wrought materials in joints [171,172]. Potential solutions explored include fusion welding processes and solid-state techniques. Although well-established in the bike frame industry, fusion welding processes can result in microstructural problems and defects [173]. Solid-state processes may circumvent some issues by avoiding melting. However, poor welding parameters can reduce the mechanical properties of the weld [174].

Despite the findings reported in recent studies, there remains a significant lack of information regarding the microstructural evolution and its direct influence on the mechanical and corrosion behaviour of hybrid-welded joints, particularly those involving Al alloys. In order to support the development of cost-effective, geometrically complex, and functionally tailored hybrid structures, further in-depth investigations are required.

The objective of this chapter is to analyse hybrid welded joints between LPBF AlSi10Mg and wrought aluminium alloys 6061 and 6082, produced using both fusion and solid-state welding processes. The present study investigates the resulting microstructural features and evaluates the mechanical and corrosion behaviour, with the aim of identifying the key factors governing the structural integrity and durability of the hybrid joints.

4.1 Welds of aluminium alloys

Aluminium and its alloys are widely used in welding industries due to economic advantages, such as good strength-to-weight ratio, good corrosion resistance and easy recyclability [175]. Despite these advantages, aluminium alloys are also well-known for their welding challenges mainly related to thermal properties and the presence of some alloying elements that might evaporate during the welding process [176]. Its high thermal conductivity, approximately 237 W/(m·K), results in rapid dissipation of heat and subsequent negative effects on the control of thermal processes during fusion

welding [177]. In addition, the higher coefficient of thermal expansion leads to the formation of residual stresses during the solidification process, which could result in hot cracking [178].

The main challenge in applying most joining technologies to aluminium is the presence of its stable and refractory aluminium oxide layer (Al_2O_3) on the material surface [179]. The alumina layer exhibits reduced electrical conductivity and elevated melting temperature (2070°C) in comparison to aluminium alloys (600°C) [180]. This difference requires prior cleaning of the surface to be welded to remove excess of oxide. This alumina layer has the potential to hinder the formation of a cohesive weld bead if it is not adequately addressed prior to the welding process.

A defect that drastically reduces the weld quality and its mechanical properties is porosity. Regardless of whether the discussion concerns the welding of conventional aluminium alloys or those produced through additive manufacturing processes, it is generally assumed that the reason for porosity formation within weld beads is the presence of hydrogen. Significant sources of hydrogen can be attributed to the presence of surface contamination in both the base metals. As reported by Mazur et al. [181], this contamination typically manifests in the form of hydroxides, hydrocarbons or oxides, in conjunction with adsorbed moisture. An additional source of hydrogen can be attributed to impurity in the shielding gas as a consequence of erroneous procedures. The pronounced tendency of aluminium to form porosity is related to the hydrogen solubility. As reported by Mathers et al. [182], the hydrogen solubility in molten aluminium is approximately 20 times higher than that of solid aluminium. As the temperature of the melt decreases rapidly, the insoluble hydrogen is unable to escape the molten bath and remains trapped. This results in a marked tendency of porosity formation. When considering welding of additively manufactured aluminium alloys, the issue of hydrogen presence is of particular concern. The hydrogen content of the AM component is found to be seven times higher than that of the cast or wrought aluminium parts [183]. The elevated hydrogen content may be attributed to the powder and its processing from the atomisation to the finished AM component. Throughout the procedure, the powder is exposed to the ambient atmosphere on multiple occasions. Since the powder has a surface area that is substantially larger than that of a compact component, it exhibits a greater tendency to moisture adsorption from the environment [184]. Following the dissolution of moisture and hydrogen in the powder, the process of removal becomes extremely challenging. The outcome of this phenomenon is the formation of porosity during the printing process, as well as the potential for subsequent porosity formation during welding processes. Techniques to reduce the porosity level and to improve the mechanical properties of joints have been reported in literature, such as heat input control [185], pre-heating [186], optimised process parameters [187], laser cleaning of the parts to be welded prior to welding [188]or use shielding gas with CO_2 and He [189].

From a metallurgical standpoint, the weldability of aluminium alloys is significantly influenced by their chemical composition and strengthening mechanism. As reported by Olabode et al. [190], the presence of alloying elements has been demonstrated to directly impact the weldability of materials. Specifically, the addition of silicon and magnesium has been shown to enhance weldability, while the presence of copper and Zinc has been observed to impede this process, thereby favouring the formation of weld defects. Non-heat-treatable alloys have been shown to exhibit good weldability and retain satisfactory mechanical properties after welding. For instance, AlSi10Mg is an additive manufacturing alloy with a chemical composition similar to 4xxx Al-Si alloys, to which magnesium has been added to introduce some precipitation hardening, through Mg_2Si precipitates, at the expense of a slight reduction in weldability [182]. Heat-treatable alloys demonstrate a significant decrease in

mechanical properties after the welding process. Alloys of the 6xxx series have been observed to exhibit a higher susceptibility to hot cracking in the weld bead and over-ageing in the regions adjacent to the weld bead [191]. The presence of silicon and magnesium in these alloys provides good weldability, but the marked deterioration of mechanical properties requires post-weld heat treatments to restore strength, thus constraining their use in certain applications.

Joining methods for aluminium alloys can be generally divided into fusion welding and solid-state welding techniques, which differ fundamentally in their joining mechanisms and thermal histories.

The most reported fusion welding process in literature is gas tungsten arc welding (GTAW). In this method, a non-consumable tungsten electrode, an arc column and a filler metal are used to melt the material and form the joint, as illustrated in Figure 36. An inert shielding gas, typically argon or helium, is also used to protect the electrode and the molten pool from atmospheric contamination [192].

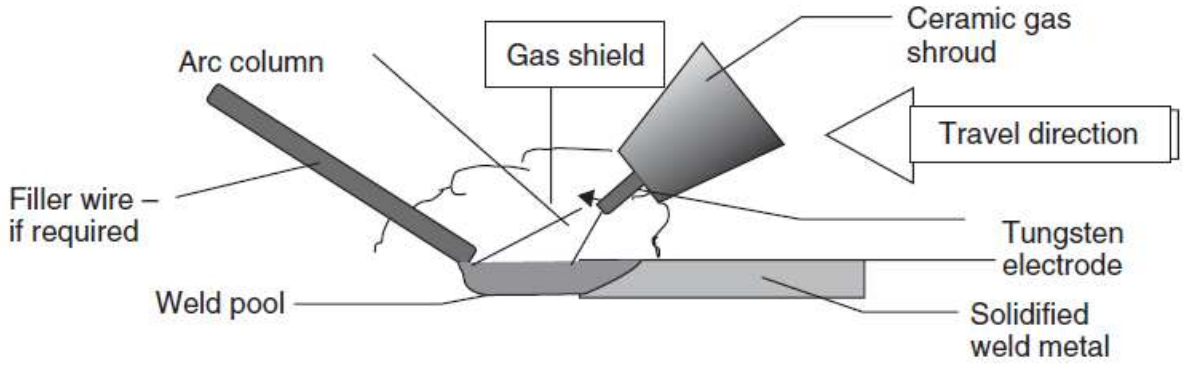

Figure 36 - Schematic representation of GTAW process [182].

Based on microstructural features, GTAW welded joints are typically divided into three main regions: the weld zone (WZ), the heat-affected zone (HAZ) and the base material (BM) [193]. This heterogeneity strongly affects the mechanical behaviour of the joint and is often the primary criterion for assessing its in-service performance. In the WZ, the weld metal is in as-cast structure, consisting of a mixture of the filler metal and the base metal. The property of this zone depends on the chemical composition of base metal and filler metal, the quality of the welding process and the rate of solidification. According to Mathers et al. [182], in welding conventional aluminium alloys the WZ will match the parent metal properties only when they are in as-cast or annealed condition. If the base metals are precipitation-hardening alloys, a post-weld heat treatment can be carried out in order to increase the strength of the WZ, but the effectiveness of this post-weld heat treatment is strongly related to the filler metal composition and dilution [194]. This behaviour can be extended to the HAZ, in heat-treatable aluminium alloys, such as those belonging to the 6xxx series, the heat generated during the welding process can lead to precipitates dissolution and over ageing phenomena. This, in turn, results in a decline in the mechanical properties of the heat-affected zone [195]. In the context of additive manufactured aluminium alloys, the aforementioned behaviour is amplified by the intrinsic microstructural features of LPBF parts. Nahmany et al [196], shown that the WZ of LPBF AlSi10Mg exhibits a cast-like Al-Si eutectic morphology whit columnar/equiaxed dendrites, whereas the LPBF base material displays a much finer cellular-dendritic solidification structure. This microstructural mismatch strongly affects the mechanical response. In AM components the fast solidification rate led to very fine microstructure and significant solid-solution strengthening, while the slower solidification rate during welding produces a coarser microstructure with reduced

strengthening and lower mechanical properties, as observed by Zhang et al. [197] for GTAW of LPBF AlSi10Mg.

The microstructural heterogeneity across BM, HAZ and WZ also manages the corrosion behaviour of aluminium welds. As reported by Zhu et al. [193], the HAZ of GTAW-welded AA2219 exhibits an increased content of Cu-rich precipitates along the grain boundaries, leading to the formation of precipitate-free zones adjacent to the grain boundaries. This microstructural condition promotes the intergranular corrosion within the HAZ. Fahimpour et al. [198], reported analogous observation concerning GTAW joints in AW6061 plates, thereby confirming the need for post-weld heat treatment to enhance the corrosion and mechanical performance of weld bead.

In addition to porosity and microstructural heterogeneity, other factors such as cracks, residual stresses, and filler metal composition can also have a substantial impact on mechanical and corrosion behaviour of fusion-welded aluminium alloys [199]. Despite these disadvantages, GTAW has been widely adopted in industrial applications, such as bike frame production, due to its versatility and easy to carry equipment [200].

Friction stir welding (FSW) is the most widely used solid-state welding method. FSW is distinguished from conventional fusion welding by avoiding the melting of the base materials. The joint is formed through an intense plastic deformation and frictional heating generated by a rotating tool pressed against the surface of two abutting plates, as illustrated in Figure 37. In the process of friction stir welding the most relevant feature is the asymmetry between the advancing and retreating side. This asymmetry exerts a significant influence on material flow, microstructural evolution, defect formation and, therefore, on mechanical properties. The advancing side is characterised by more severe thermal and mechanical conditions and represents the most critical region for bonding quality. In contrast, the retreating side often provides a more stable contribution to the nugget zone.

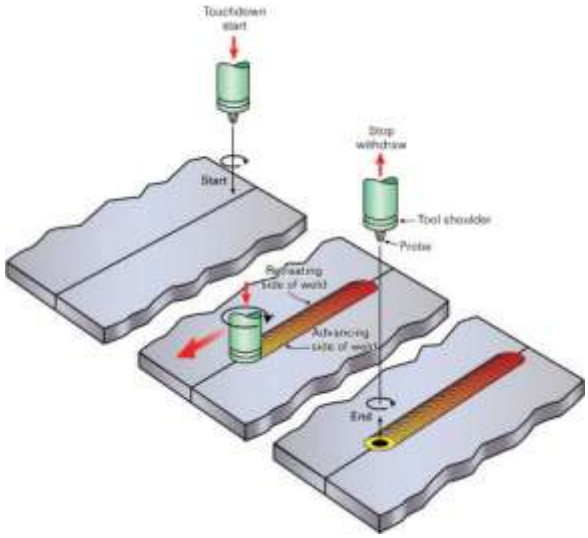

Figure 37 - Schematic representation of FSW process [201].

FSW joints are characterised by four distinct regions: the nugget zone (NZ), where the plastic deformation and heat generated by the FSW tool induce a recrystallisation resulting in the formation of refined equiaxed grains within the stir zones [202]; the thermo-mechanically affected zone (TMAZ), where in the case of aluminium alloys, the rotating tool generates considerable plastic deformation without recrystallisation [201]; the heat-affected zone (HAZ), where, as in the case of GTAW process, the heat generated by the welding process can modify the microstructure; and the base material (BM). The FSW process has been shown to minimise problems typically associated

with aluminium welding, such as hot cracking, porosity, and excessive residual stress [203]. Notwithstanding the aforementioned advantages, the weld bead is significantly affected by process parameters, including tool geometry, rotating speed, and travel speed. Improper parameters may result in inadequate material mixing or defects within the weld bead. The most significant defects impacting the mechanical properties of FSW joints are those which result from voids and joint line remnants. The formation of voids is observed to occur preferentially in the advancing side of the weld or near the base of the pin. This phenomenon has been found to be related to high travel speed, low tool rotation speed or inadequate joint gap [204]. The term "joint line remnant" refers to a feature that extends from the weld root through the weld. The presence of this defect is attributable to inadequate removal of aluminium oxide from the surfaces of the butting plates [205]. The presence of these defects has been shown to have a significant impact on the mechanical properties of the joints, thereby promoting the occurrence of mechanical failure within the weld bead. Inadequate process parameters have also been demonstrated to exert an effect on the microstructural features that are present within the joints and adjacent regions. In the case of 6xxx aluminium alloys, for example, an increase in tool rotation speed, with the subsequent higher thermal input, can lead to a significantly increased dissolution of hardening precipitates, with the consequent reduction in the tensile strength [202]. From a corrosion perspective, given the specific aluminium alloys and the process parameters, the corrosion may occur preferentially in the TMAZ, HAZ or NZ. Jariyaboon et al. [206] established that, for AA2024, a low heat input results in the TMAZ being most affected by corrosion attacks in comparison to the adjacent zone. However, with increasing heat input the HAZ becomes significantly more affected. Fahimpour et al. [198] reported that the nugget zone of AW6061 joints exhibited fine-grain structures in comparison to the adjacent zone. This was accompanied by a higher susceptibility to corrosion due to the presence of FE- and Si-rich precipitates along the grain boundaries.

4.2 Dissimilar welding of aluminium alloys

The integration of components manufactured from different aluminium alloys is often a prerequisite for the use of aluminium alloys in industrial applications. Consequently, it is imperative to distinctly differentiate between dissimilar and hybrid welding methods.

In this scenario, the welding of different aluminium alloys, referred to as dissimilar joints, involves materials characterised not only by mismatch in chemical composition but also by profound differences in microstructural features and processing history. Hybrid welding can be regarded as a specific subclass of dissimilar welding, referring in particular to the joining of materials produced through different manufacturing processes. Within this framework, the present chapter discusses both fusion and solid-state welding process applied to joints between conventionally manufactured and additively manufactured aluminium alloys.

When dissimilar aluminium alloys are joined by fusion welding processes, the selection of suitable welding parameters and filler metal plays a crucial role in obtaining sound welded joints. Differences in chemical composition give rise to variations in thermo-physical and mechanical properties, such as thermal conductivity and melting point [207]. As reported by Luijendijk et al [208], for GTAW joints the heat produced by the arc will flow more easily in material with larger thermal conductivity, leading to possible lack of fusion in this material or excessive melting in the material with lower thermal conductivity.

The selection of filler metal represents another crucial factor in the performance of dissimilar joints [178]. Yelamasetti et al [209], reported that the employment of ER4043 as filler metal instead of ER5356 resulted in weld beads that exhibited a reduced defects density and enhanced mechanical properties. However, only few guidelines or published literatures are available to select the most suitable filler metal. The corrosion behaviour of dissimilar aluminium alloy welds is also significantly affected by the selection of filler metal and the subsequent microstructural heterogeneity. As reported by Gadallah et al. [210], differences in alloy composition between BM, WZ and HAZ can promote the formation of local galvanic couples. The use of an inadequate filler metal can amplify the electrochemical differences across the joint, resulting in enhanced corrosion phenomena.

Friction stir welding is also one of the most frequently employed techniques for dissimilar welds. Welding aluminium alloys with different chemical composition introduces further challenges, mainly due to the fact that the two base materials can have different plastic deformation behaviour, different thermal conductivity and different material flow kinematics during the stirring phase. These differences lead to significant microstructural and mechanical asymmetry between advancing side and retreating side [201]. Furthermore, numerous studies have been conducted that demonstrate the absence of effective alloying mixing within the weld bead, regardless of the process parameters employed. Larssoon et al. [211], reported that an EDS scan across the nugget zone of FSW joints between 5083 and 6082 aluminium alloys shows no evidence of regions with an intermediate composition. From a corrosion perspective, despite the chemical mismatch between the base materials, several studies have demonstrated that the nugget zone frequently exhibits greater corrosion performance in comparison with both the base metals [212,213].

These challenges are expected to be further amplified when one of the joined materials is produced by additive manufacturing. In such instances, the welding process, designated as hybrid welding, encounters not only a chemical mismatch, but also microstructural and stress residual differences. These aspects contribute to an enhancement in the overall complexity of the welding process, affecting repeatability and achievable weld quality.

In the context of fusion welding processes, such as GTAW, the main challenge influencing the mechanical performance of hybrid joints is linked to the markedly elevated susceptibility to porosity exhibited by additively manufactured components in comparison to conventional wrought alloys. It has been reported in several studies that aluminium alloys commonly processed by LPBF exhibit this behaviour, with a significantly higher pore density observed within the weld zone, particularly in the region adjacent to the AM material in hybrid welds [43,183,197,214].

Solid-state welding techniques, such as FSW, have been shown to reduce fusion-related defects, particularly porosity within the weld bead. However, hybrid solid-state welding has been observed to emphasise the microstructural and mechanical asymmetry between the advancing side and the retreating side [215]. Moreover, as was also observed in dissimilar welding, incomplete material mixing between the additively manufactured alloy and the conventionally produced alloy within the weld zone plays a pivotal role in governing both the mechanical performance and the corrosion behaviour of the joint [216].

4.3 Hybrid welding between LPBF AlSi10Mg and wrought 6xxx alloys

This work has been developed within the framework of the MOST (National Centre for Sustainable Mobility) project, which aims to explore the application of advanced materials and

additive manufacturing (AM) in the development of lightweight and modular components for light electric vehicles. The present study originates from the need to evaluate the mechanical integrity and corrosion resistance of hybrid joints. It specifically investigates the welding behaviour between AlSi10Mg produced by laser powder bed fusion (LPBF) and conventionally wrought AW6061 and AW6082 T6 by gas tungsten arc welding (GTAW) and friction stir welding (FSW). Tests were performed on specimens in the as-built (AB) condition and after heat treatment, analysing different welding techniques to better understand the influence of welding parameters on mechanical properties and corrosion resistance. The results contribute to the broader goal of enabling the application of AM-fabricated components in structural parts of lightweight vehicles, with particular attention to durability and safety.

4.3.1 Fusion welding of LPBF AlSi10Mg to AW6061

4.3.1.1 Materials and methodology

The additive manufactured specimens were fabricated using an EOS M290 LPBF machine to process EOS aluminium AlSi10Mg powders, in collaboration with the industrial partner Aidro. The powders were characterised by a particle size range of 27 - 76 μm and the nominal compositions of the additively manufactured alloy powders are shown in Table 13. The fabrication step employed a heating system that kept the baseplate temperature as high as 165°C. The AlSi10Mg specimens were printed with a cylindrical shape, measuring 30 mm in height, 20 mm in external diameter and a width of 1.20 mm. The printing direction was parallel to the cylinder axis. The AW6061-T6 specimens were plate-shaped, with dimensions of 50 x 50 x 4 mm. Table 13 illustrates the mechanical properties of the AlSi10Mg alloy and AW6082-T6. The welding process was carried out using Gas Tungsten Arc Welding (GTAW) with three different welding techniques: continuous GTAW, pulsed GTAW at 80 Hz and 100 Hz. The initial peak current was set to 140 A. However, since the welding process was performed manually using a foot pedal, the current was dynamically adjusted by the operator during the joining process. Subsequent to the initial arc ignition, at which point the current typically reached values between 120 - 140 A, a gradual reduction occurred as the weld progressed. This manual modulation of the input resulted in an estimated average current of 90 - 100 A along the weld bead. The GTAW process was conducted using argon as the shielding gas and ER5356 as the filler metal, chemical composition reported in Table 13, obtaining specimens with the shape shown in Figure 38.

Table 13 - Chemical composition (wt.%) of the base materials (AlSi10Mg, AW6061) and filler alloy (ER5356).

Elements (wt.%)	Al	Si	Mg	Fe	Cu	Mn	Zn	Cr	Ti
LPBF AlSi10Mg	bal.	10.3	0.36	< 0.55	< 0.05	< 0.45	< 0.10	-	< 0.15
ER5356	bal.	< 0.25	4.5 – 5.5	< 0.40	< 0.10	< 0.20	< 0.10	< 0.20	< 0.20
AW6061-T6	bal.	0.4 – 0.8	0.8 – 1.2	< 0.70	0.15 – 0.40	< 0.15	< 0.25	< 0.35	< 0.15

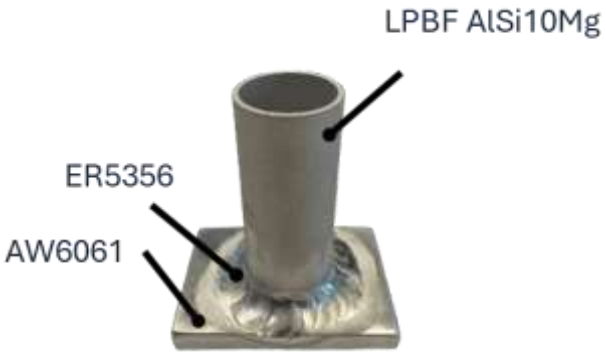

Figure 38 - GTAW specimen geometry.

The LPBF AlSi10Mg specimens were tested in the as-built condition (NT) and after a solution heat treatment at 530 °C for 6 hours (HT) performed before the welding process. Table 14 illustrates the classification of the samples analysed.

Table 14 - Classification of the welded specimens by heat treatment condition and GTAW techniques.

		GTAW technique		
		Continuous	Pulsed at 80 Hz	Pulsed at 100 Hz
Specimen conditions	As-built	Cont NT	80Hz NT	100 Hz NT
	Solution heat treatment	Cont HT	80 Hz HT	100 Hz HT

In view of the restricted number of samples available for this study, it was only possible to perform a single test for each condition (NT and HT) and for each GTAW parameter in use. In order to address this, the test pieces were cut vertically, with one half of each specimen utilised for microstructural analysis and hardness testing, and the other half for corrosion testing. Thermal desorption analysis was performed on the LPBF AlSi10Mg specimens using a commercial Leco instrument to quantify hydrogen content. The test was carried out at a constant temperature of 1800 °C until the hydrogen signal dropped below 1% of the maximum peak value detected.

Microstructural analysis was performed on cross sections, in order to obtain a surface finishing suitable for micrographic analysis, the specimens were mechanically polished with SiC papers up to 4000 grit and then with a 1 μm diamond suspension. The microstructures were revealed by chemical etching with Keller and Weck reagent, analysed using digital-optical microscope Keyence VHX-7100 and a Gemini Sigma 300 field emission scanning electron microscope (FESEM), equipped with an Oxford x-act probe for energy-dispersive X-ray spectroscopy (EDS).

The geometry of the weld mock-ups precludes the samples from being subjected to tensile testing. Accordingly, the mechanical behaviour was investigated through Vickers hardness tests, in accordance with UNI EN ISO 6507-1, utilising a load of 0.1 kg and a loading time of 10 s. To evaluate the mechanical properties of the weld beads, the section of the weld bead of each test piece was mapped.

Intergranular corrosion tests were performed in accordance with the EN ISO 11846 standard (Method B). It is evident that, owing to the specimen's geometry, no mechanical grinding was performed prior to testing. Consequently, the specimens were evaluated with a surface roughness that was as-built. The samples were degreased with acetone, immersed for 3 minutes in a sodium hydroxide solution (8% by weight at 55 ± 2 °C), rinsed in water, immersed for 2 minutes in

concentrated nitric acid, rinsed in distilled water and dried. Subsequently, the specimens were immersed in the test solution, containing 30 g/L sodium chloride and 10 mL/L concentrated hydrochloric acid, at room temperature for 24 h. The temperature of the test solution was maintained within a range of 21 - 25 °C. Afterwards, the samples were rinsed in distilled water and dried. Corrosion products were removed with a non-metallic brush, followed by a systematic rinsing in distilled water, immersed for 30 seconds in concentrated nitric acid, then immersed in an ultrasonic bath of acetone and subsequently allowed to dry. A metallographic section perpendicular to the exposed surface was evaluated in order to determine the presence and depth of the attacks.

4.3.1.2 Results and discussion

Microstructural analysis

The cross-section of the hybrid weld bead obtained with different welding parameters is shown in Figure 39, AlSi10Mg is in the upper part of the welded specimens while the AW6061-T6 is in the lower part. Similar microstructural features were observed across all analysed specimens. However, for the sake of clarity, only representative samples are discussed in the following sections. While the exact distribution and extent of the microstructural regions may vary slightly among the specimens, the reported features capture the main trends consistently observed throughout the investigation.

As illustrated in Figure 39, the analysis of the cross-sections of all specimens revealed the presence of welding defects in the lower region of the weld bead. The defects observed are likely attributable to the specimen geometry and the welding configuration, given that the welding process was executed from the outer side of the components. Consequently, the internal surface of the joint, in the transition region between the LPBF AlSi10Mg and the AW6061-T6, exhibits an irregular bead morphology. In this area, a local lack of fusion can be observed, resulting in an irregular bead morphology characterised by insufficient penetration at the LPBF AlSi10Mg - AW6061-T6 interface. The presence of this lack of fusion at the weld root may be ascribed to insufficient heat input, which results in a shallow molten pool unable to fully melt the joint interface [217]. The cross-sections of the specimens welded, illustrated in Figure 39, revealed also a higher amount of pores within the weld zone. Wu et al. [218] obtained analogous results suggesting that the round shape is related to gas pores. As aforementioned in the previous chapters, the underlying causes of the porosity formation within the weld bead may be ascribed to various factors, the hydrogen trapped within the LPBF component [219], the presence of surface oxides or incorrect welding procedure [181]. As reported by some authors [43,214], the formation of areas with elevated porosity within joints is particularly observed in hybrid welding. This zone, evident in Figure 39, is called the pore belt. Heterogeneous nucleation and the action of the filler material result in the movement of porosity towards the periphery of the weld bead. This process consequently creates a denser zone of porosity, thereby promoting the formation of the pore belt [197]. The redistribution of porosity towards the periphery of the weld bead may be further promoted by Marangoni convection flows, driven by temperature-dependent surface tension gradients, which influence fluid circulation and gas bubble movement within the molten pool [220].

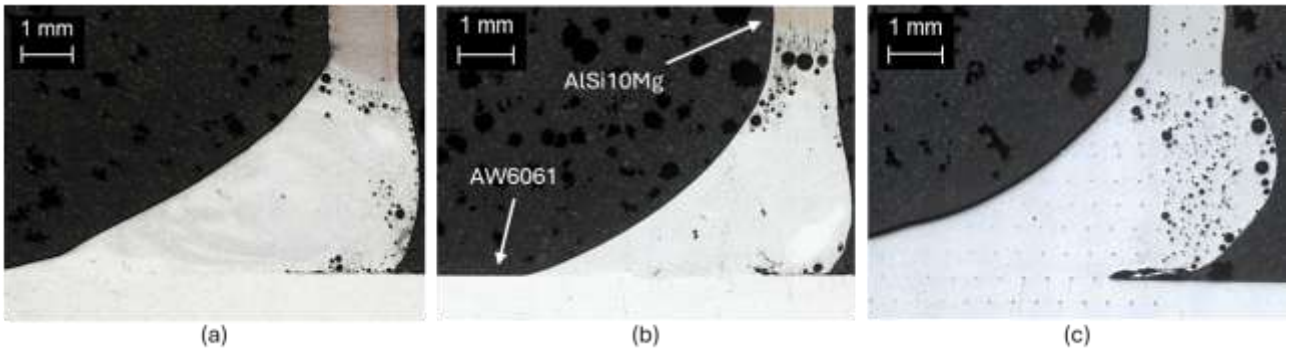

Figure 39 - Cross-sections of specimens welded with (a) continuous GTAW, (b) pulsed GTAW at 80 Hz and (c) 100 Hz.

The welding technique employed can also influence the formation of porosity within the weld bead. Nunes et al [221] highlight how arc welding produces a wider molten zone and greater heat dissipation to adjacent areas in comparison to alternative techniques. This results in longer solidification times, which promote the nucleation and coalescence of porosity. This porosity tends to accumulate in the upper part of the molten zone. The analysis of the cross-sections of the welds suggests that continuous and pulsed TIG welding at 80 Hz results in less porosity in the joint when compared with pulsed welding at 100 Hz. This difference may be ascribed to the manual execution of the welding process, which inherently involves variations in the feed rate along the bead. These variations have the capacity to affect the solidification times, and consequently, the formation of defects.

In order to address the issue of porosity, the LPBF AlSi10Mg samples underwent a solubilisation heat treatment at 530°C for 6 hours before the welding process. Analysis of the hydrogen content of the AM specimens showed a decrease from 64 ± 7 ppm to 49 ± 5 ppm, confirming the treatment's effectiveness in promoting the material's degassing. The cross-section analysis of the hybrid heat-treated weld bead, illustrated in Figure 40, revealed a porosity reduction. This is linked to the reduction in hydrogen content within the AM component following the heat treatment and microstructural modification. As reported by Yi et al. [222], exposure to high temperature promotes pore nucleation and coalescence. In some cases, it also allows hydrogen to diffuse outwards due to its increased solubility in aluminium's solid phase. However, the reduction in hydrogen content by around 15 ppm suggests the heat treatment was only partially effective, potentially due to the presence of surface oxide. Song et al. [223] highlighted that the Al_2O_3 oxide film that forms on the surface of aluminium alloys represents a highly effective barrier to hydrogen diffusion, drastically reducing its permeability.

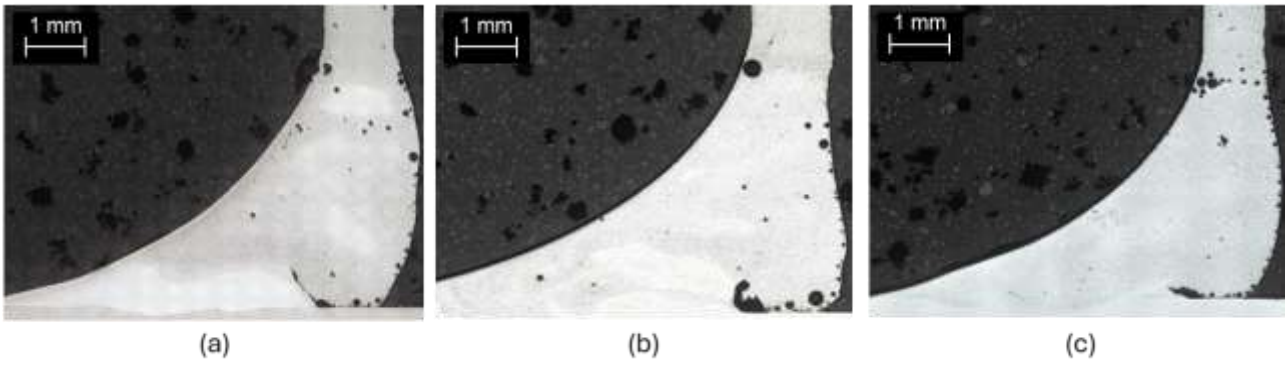

Figure 40 - Cross-sections of heat-treated (HT) specimens welded with (a) continuous GTAW, (b) pulsed GTAW at 80 Hz and (c) 100 Hz.

The microstructural analysis of the cross-sections, illustrated in Figure 39 and Figure 40, highlighted a clear heterogeneity within the joints. This heterogeneity may be attributed to the welding speed, the heat input during the process and to an inhomogeneous mixing between the base material and the filler metal during the welding process. The manual execution of the welding, which inherently involves variations in welding speed along the bead, may have played a key role in promoting such microstructural irregularities.

The high thermal conductivity of aluminium resulted in substantial microstructural modifications, even in regions distant from the weld bead, as illustrated in Figure 41. As demonstrated in Figure 41a, the external region of the LPBF AlSi10Mg base material underwent a significant alteration of the as-built microstructure as a result of the heat input associated with welding. In particular, the thermal exposure led to the dissolution of the characteristic Si-rich eutectic network, while the slow cooling rate resulted in the coarsening of both the α-Al matrix and the Si-rich precipitates, as illustrated in Figure 41c,e. In the inner region (Figure 41d), a cellular-like microstructure remains evident. However, the continuity of the eutectic network, as observed in the as-built condition, is evidently disrupted. This microstructural evolution is attributed to the prolonged exposure at elevated temperatures during the welding process and is consistent with microstructures reported for LPBF AlSi10Mg subjected to stress-relief heat treatments in the range of 300-350°C [77,112]. Vickers hardness measurements performed in this region revealed a significant reduction compared to the as-built condition, with hardness values of 66 ± 2 HV1 versus 113 ± 9 HV1 for the as-built material. Furthermore, hardness profiling along the LPBF AlSi10Mg BM demonstrated that even in the upper part of the specimen, approximately 25 mm away from the weld bead, the material exhibited a hardness value of 70 ± 3 HV1. In this region, the microstructure still displays the typical melt pool macrostructure, as illustrated in Figure 42a. However, the thermal input associated with welding effectively subjected the material to an over-ageing treatment, promoting the coarsening of Si-rich precipitates (Figure 42b), the loss of their coherency with the α-Al matrix and the following decrease in hardness [51]. The results obtained demonstrate that the HAZ extends well beyond the immediate vicinity of the weld bead, reaching the upper part of the specimens and potentially affecting both mechanical and corrosion performance. Analogous trends were observed for all the non-heat-treated specimens analysed, underscoring the profound impact of welding parameters on microstructural characteristics and, consequently, on the mechanical and corrosion behaviour of fusion-welded hybrid joints.

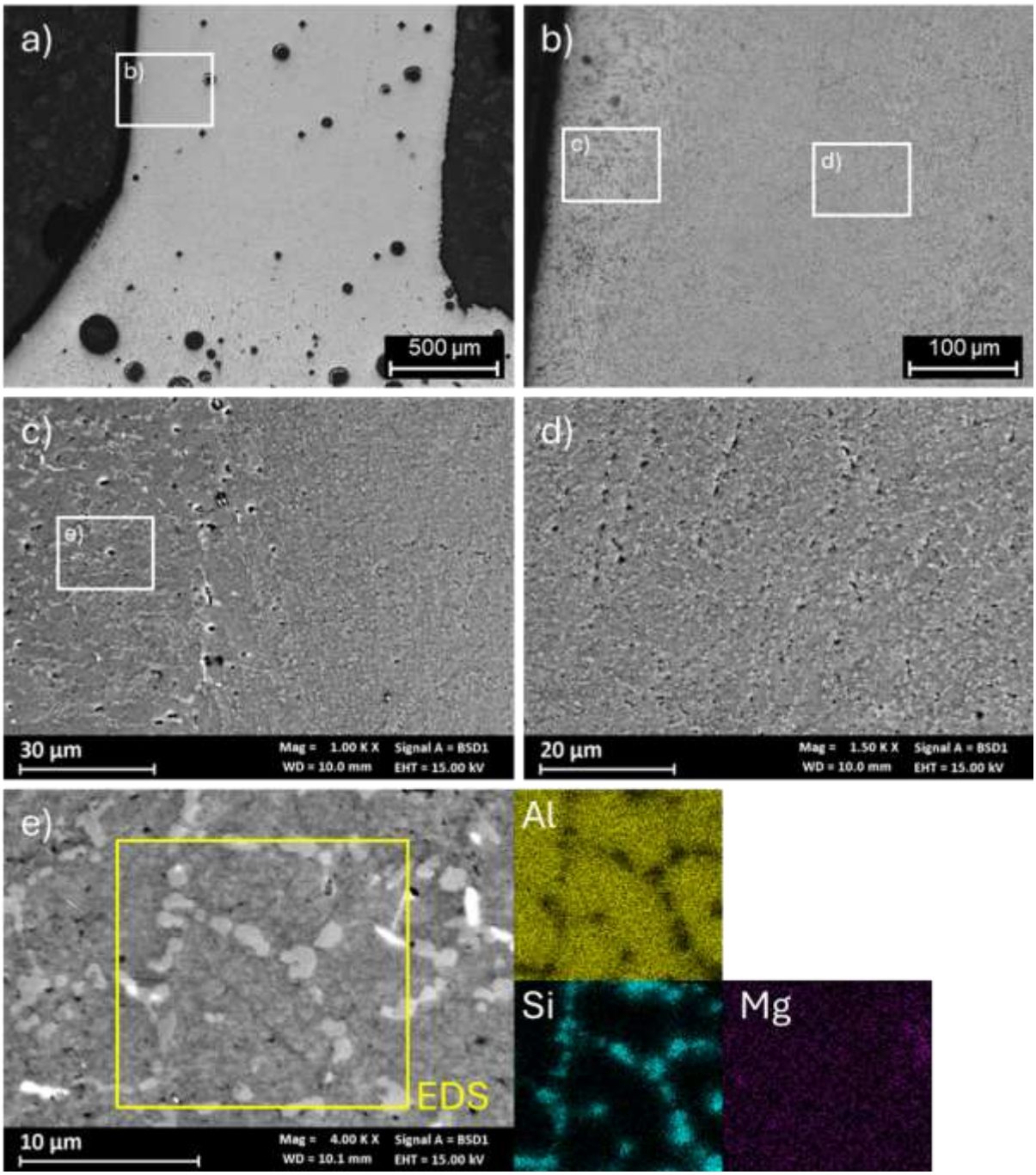

Figure 41 – (a, b) Optical microscope images of the transition region between LPBF AlSi10Mg base material and the weld zone in the 100 Hz NT specimen; FESEM micrograph of the (c) outer and (d) inner region of the area marked in (b); (e) High-magnification FESEM image and corresponding EDS elemental maps of the outer region marked in (c).

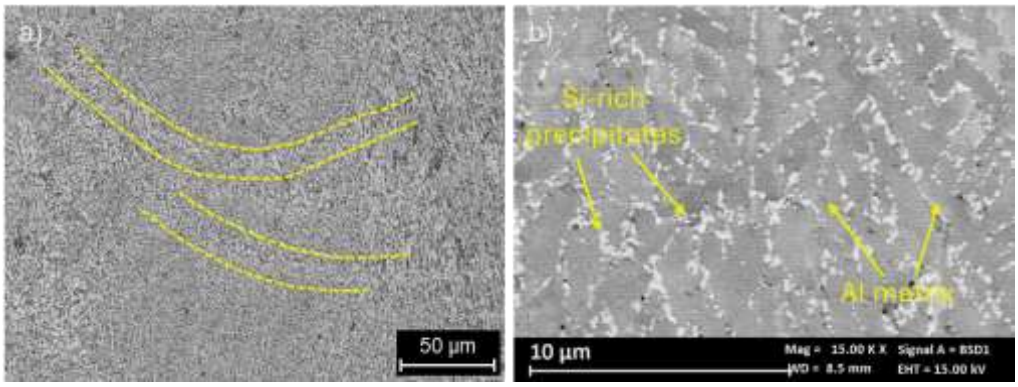

Figure 42 – (a) Optical microscope image highlighting the melt pool macrostructure and (b) high-magnification FESEM image of microstructure in LPBF AlSi10Mg base material.

The microstructural analysis of the pre-weld heat-treated specimens (Figure 43) revealed that the typical melt pool macrostructure was completely replaced by coarsened Si particles and needle-like Fe-rich precipitates, leading to a further reduction in hardness. In the upper region of the pre-weld heat-treated LPBF AlSi10Mg BM, Vickers hardness measurements showed values of approximately 63 ± 5 HV1 for all the heat-treated specimens. These findings are in agreement with literature data [44,116], where prolonged high-temperature solubilisation treatments were reported to cause a significant degradation of the mechanical properties of LPBF AlSi10Mg due to microstructural coarsening and dissolution of strengthening features.

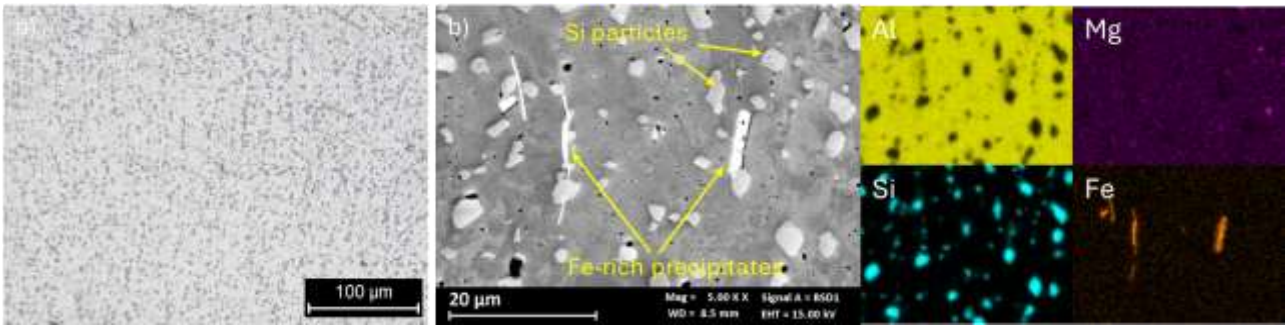

Figure 43 – (a) Optical microscope image of microstructure in the pre-weld heat-treated LPBF AlSi10Mg base material and (a) high-magnification FESEM image and corresponding EDS maps.

In the transition region between the LPBF AlSi10Mg to the weld bead, two zones with different microstructures can be detected. As illustrated in Figure 44, the difference in cooling rate at different depths in the weld resulted in different microstructures being present along the partially melted zone (PMZ). This PMZ is an intermediate zone between the HAZ and WZ, where the temperature exceeds the solidus but remains below the liquidus, so that the low-melting constituents, such as Si-rich phases, melt while the α-Al matrix remain solid [224]. Figure 44b illustrates the microstructure in the PMZ closer to the outer surface of the joints, where the cooling rate was higher resulting in equiaxed grains surrounded by Si-rich precipitates. In the inner zone of the joints, as illustrated in Figure 44a, the cooling rate is lower, leading to a PMZ characterised by columnar grains aligned with the centre of the weld. Similar results were reported by Nahmany et al. [196], which identified a transition from narrow columnar-eutectic to equiaxed-eutectic microstructure within the PMZ.

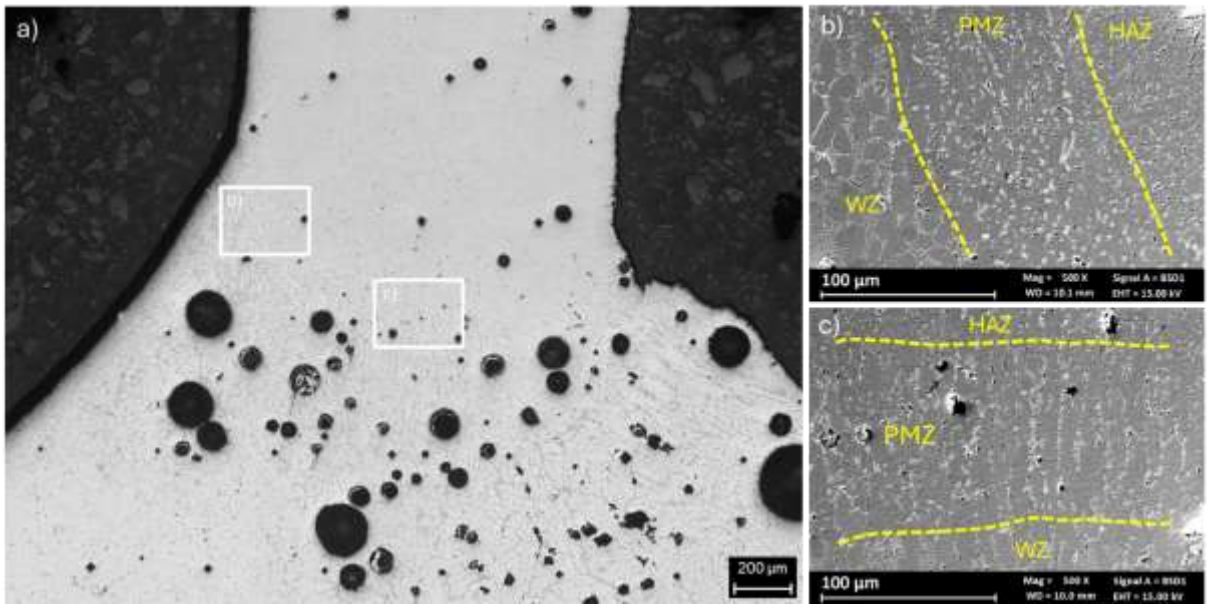

Figure 44 – (a) Optical microscope image of the transition region between LPBF AlSi10Mg base material and the weld zone in the 100 Hz NT specimen; FESEM micrograph of PMZ in the (b) outer and (c) inner region of the joint.

As demonstrated in Figure 45, the central region of the weld bead displays an equiaxed-eutectic morphology, exhibiting discernible differences between the outer and the inner region of the joint. The outer region, in closer proximity to the welding arc (Figure 45a,c), is characterised by the presence of equiaxed α-Al grains, which are surrounded by thin eutectic regions and very fine Mg-rich precipitates. In contrast, the inner region, adjacent to the LPBF AlSi10Mg substrate (Figure 45b,d), shows equiaxed α-Al grains surrounded by thicker eutectic regions and coarser Mg-rich precipitates.

In order to achieve a more detailed comprehension of the nature of these microstructural discrepancies, EDS analyses were conducted along the weld cross-sections, as illustrated in Figure 45e. The corresponding chemical profiles reported in Figure 45f revealed that the observed microstructural variations are closely related to local compositional differences within the weld bead. The outer region exhibits a low silicon content, approximately around 1 wt.%, whereas the inner region shows a significantly higher Si concentration, reaching values close to 8 wt.%. Conversely, magnesium displays an opposite trend, its content is approximately 4 wt.% in the outer region and decrease to about 1 wt.% in the inner region.

It is noteworthy that the chemical composition of the outer region is more closely aligned with that of the ER5356 filler metal, as reported in Table 13, while the inner region exhibits a composition that is more comparable to the LPBF AlSi10Mg. The microstructural and compositional gradients within the weld bead indicate a heterogenous mixing process between the filler metal and the LPBF AlSi10Mg.

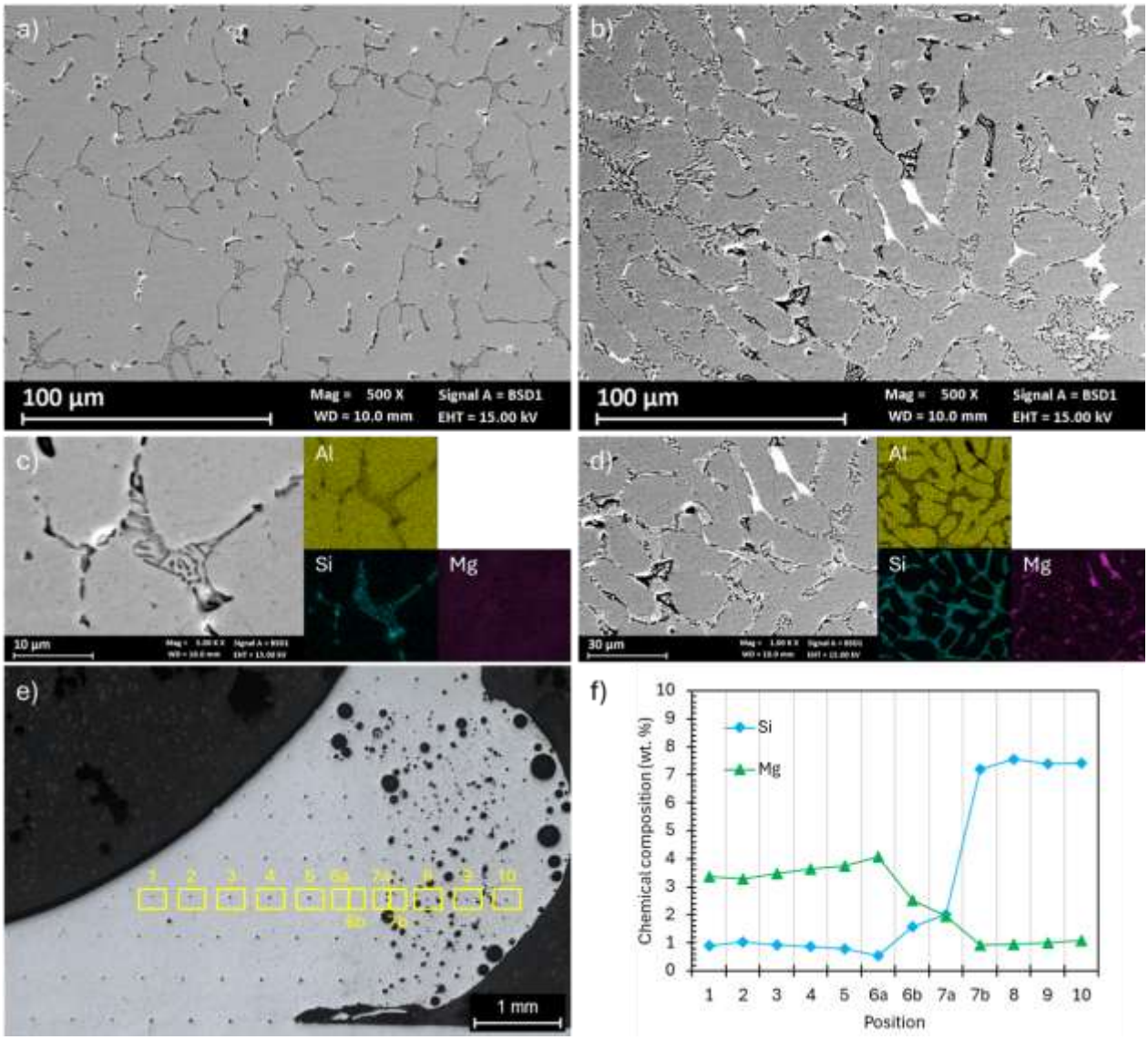

Figure 45 – Low- and higher-magnification FESEM micrographs and corresponding EDS elemental maps of the microstructure in the (a,c) outer and (b,d) inner regions of the weld bead in the 100 Hz NT specimen; (e) location of the EDS scans performed and (f) variations of Si and Mg content along the analysed cross-section.

The analysis of the weld bead cross-sections, under both NT and HT conditions, revealed a discernible correlation between porosity distribution and the local microstructural features of the material. Taking into account the microstructural heterogeneity arising from the non-uniform mixing between the base materials and the filler metal, the distribution of porosity within the weld bead can be further analysed. As demonstrated in Figure 46a,b, pores exhibit a marked preferential accumulation in regions characterised by α-Al grains surrounded by eutectic areas that are significantly richer in silicon than in magnesium.

These findings may be considered in contrast with the assumption reported by Xu et al. [225], whereby a higher content of Si facilitates the reduction of pores density. The observed behaviours can be explained by taking into account the synergistic effect between the local chemical composition, the fluid dynamics of the molten bath and the solidification kinetics. The LPBF component acts as the primary source of hydrogen, which is released into the molten bath during the welding process

and transported by convection induced by the thermal and compositional gradient. The addition of filler and the consequent surface tension gradients engender a Marangoni motion that facilitates the movement of gas bubbles towards the AlSi10Mg side, where they tend to accumulate in a “pore belt” in proximity to the interface [197,220]. Furthermore, the microstructure that develops in this area is characterised by α-Al grains surrounded by a eutectic that is rich in silicon and relatively depleted in magnesium. The aluminium matrix solidifies more rapidly , while the residual eutectic liquid remains at the grain boundaries during the final stages of solidification [113]. This results in the formation of discontinuous liquid films that do not constitute an efficient network of Mg_2Si-rich pathways for hydrogen evacuation [226].

The combination of bubble accumulation due to the Marangoni effect and a eutectic morphology that is deleterious to gas evacuation means that the bubbles that have already nucleated are unable to escape from the molten bath before complete solidification, remaining trapped and assuming an internal morphology that follows the contour of the eutectic microstructure [225,227], as reported in Figure 46c-e. In contrast, regions of the weld exhibiting elevated local Mg content and a greater proportion of finely dispersed Mg_2Si phases within the matrix exhibit conditions more advantageous to hydrogen drainage towards the surrounding bath, consequently resulting in a reduced pore density. Overall, the porosity in the hybrid joints considered in this study is governed by a close interaction between the hydrogen content in LPBF components, an optimised mixing between filler metal and base materials, the convective flows induced by the filler metal and the solidification kinetics.

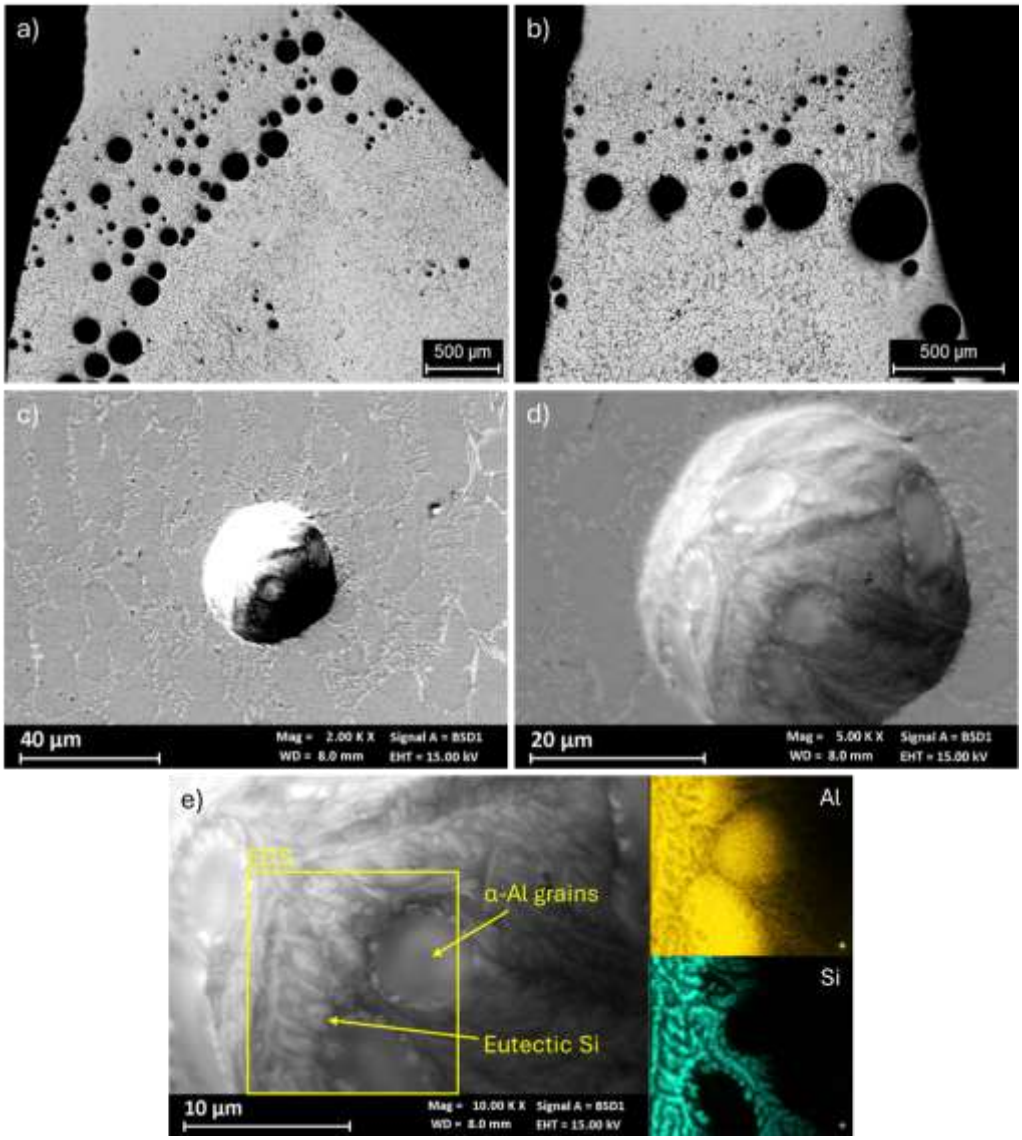

Figure 46 - Optical micrographs showing the porosity-enriched regions within the weld bead of the (a) Cont NT and (b) 80 Hz NT; (c) low- and (d,e) high-magnification FESEM images of a representative pore, highlighting the microstructural features inside a pore and (e) corresponding EDS elemental map.

As illustrated in Figure 47a,b, the microstructural analysis of the cross-sections of the 80 Hz HT specimen reveals the presence of marked microstructural heterogeneities within the weld bead, even for joints welded using different GTAW techniques. In particular, the central region of the weld bead (Figure 47b,c) exhibits a distinct microstructural zone characterised by columnar α-Al dendrites surrounded by Si-and Mg-rich interdendritic regions, as confirmed by the EDS elemental maps reported in Figure 47d. The chemical composition analysis revealed silicon and magnesium contents of approximately 0.54 wt.% and 0.63 wt.%, respectively. This composition is more similar to that of the AW6061-T6 alloy, whereas the surrounding regions of the weld bead exhibit a microstructure and chemical composition that is comparable to those observed in the equiaxed-eutectic regions shown in Figure 45a,c.

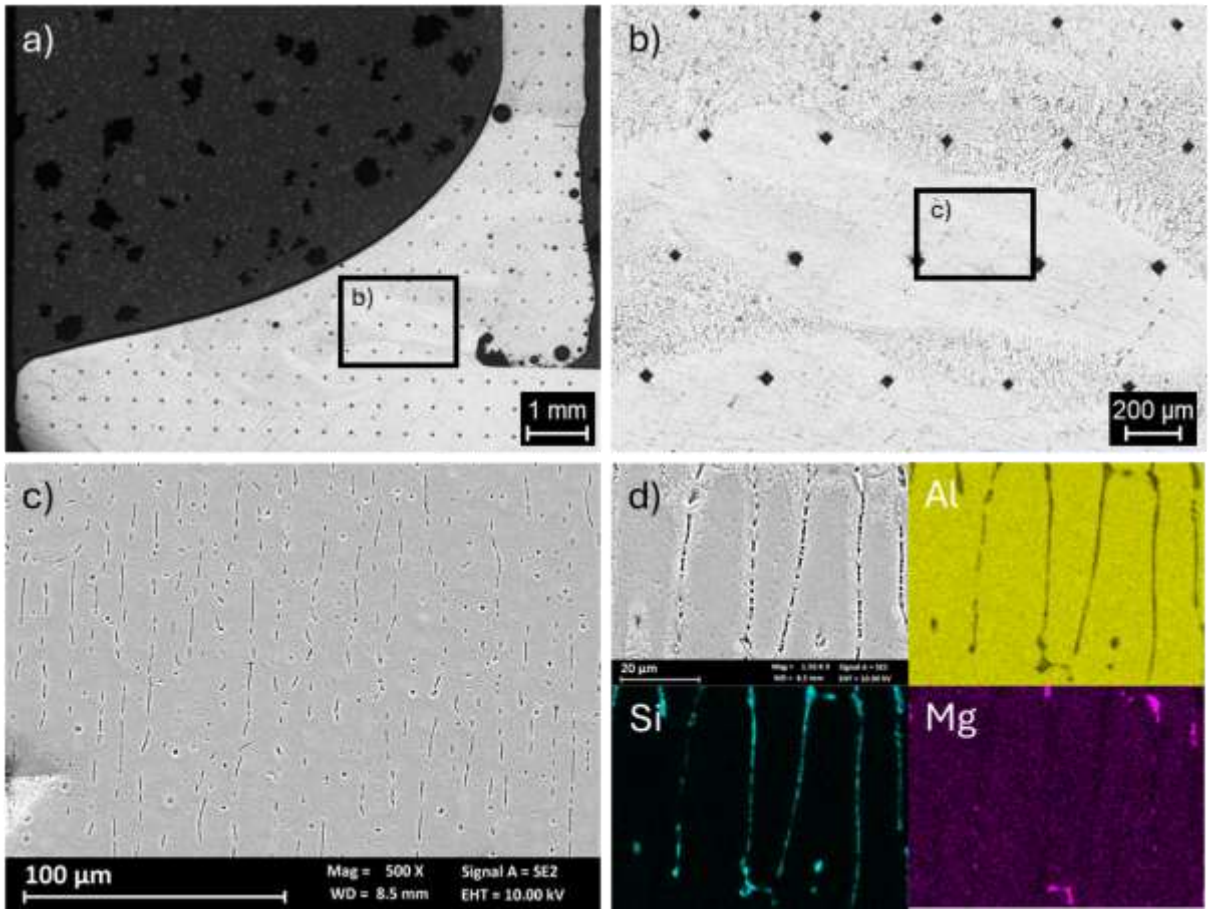

Figure 47 – Optical micrographs of the 80 Hz HT specimen showing (a) the weld bead cross-section and (b) a magnified view of the central region; (c) low- and (d) higher-magnification FESEM micrographs and corresponding EDS elemental maps of the microstructure in the central regions of the weld bead.

As illustrated in Figure 48 the PMZ and HAZ are observed in the cross-sections of the 100 Hz NT and Cont HT specimens. In both cases, the weld zone exhibits a microstructure characterised by α-Al dendritic structures surrounded by Al-Si eutectic regions, in agreement with previous observations reported for GTAW joints of AW6061-T6 aluminium alloy welded using 5xxx-series filler metal [228]. The partially melted zone is characterised by the presence of elongated columnar grains aligned with the thermal gradient during the process of solidification. These grains originate by epitaxial nucleation [229], whereby partially melted base metal grains along the fusion line act as crystallographic substrates, transferring their crystallographic orientation to the solidifying weld metal [230]. Adjacent to the PMZ, the heat affected zone is identified as a fully solid region in which the peak temperature remains below the solidus. This region is characterised by the presence of coarser equiaxed α-Al grains, which are the result of grain growth and recovery phenomena induced by the welding thermal cycle, without the occurrence of melting.

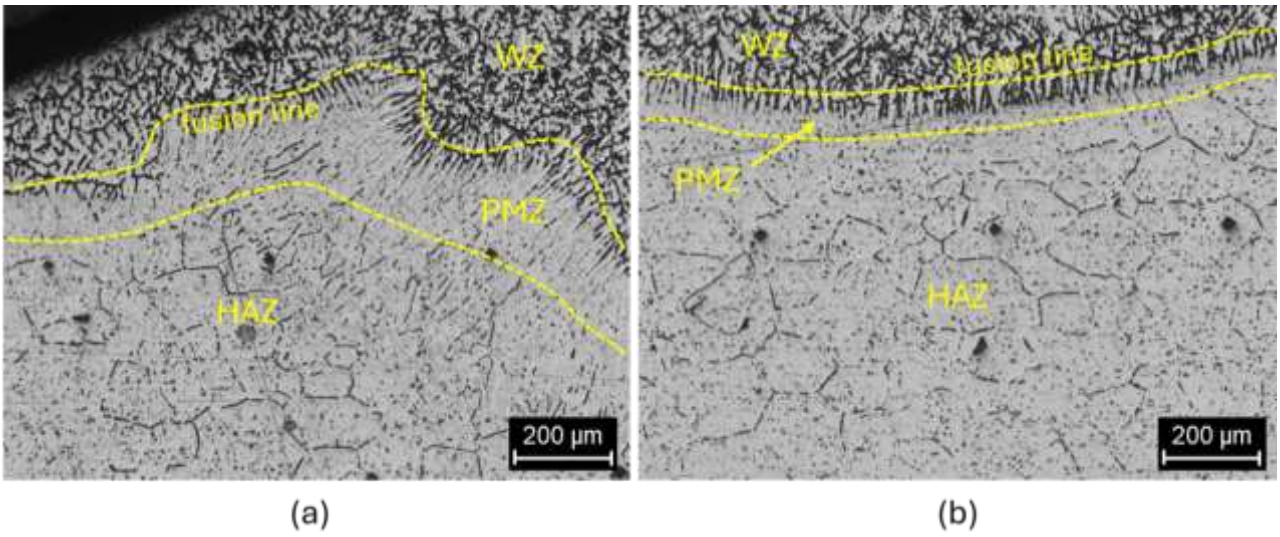

Figure 48 – Optical micrographs of the (a) 100 Hz NT and (b) Cont HT specimens showing the WZ, PMZ and HAZ of AW6061.

Mechanical behaviour

These aforementioned microstructural heterogeneities observed within all the specimens analysed may also affect the mechanical behaviour of the joints. As illustrated in Figure 49, the results of the Vickers microhardness mapping performed across the weld bead, the heat-affected zone and the base material demonstrate that the hardness distribution is significantly influenced by local microstructural variations.

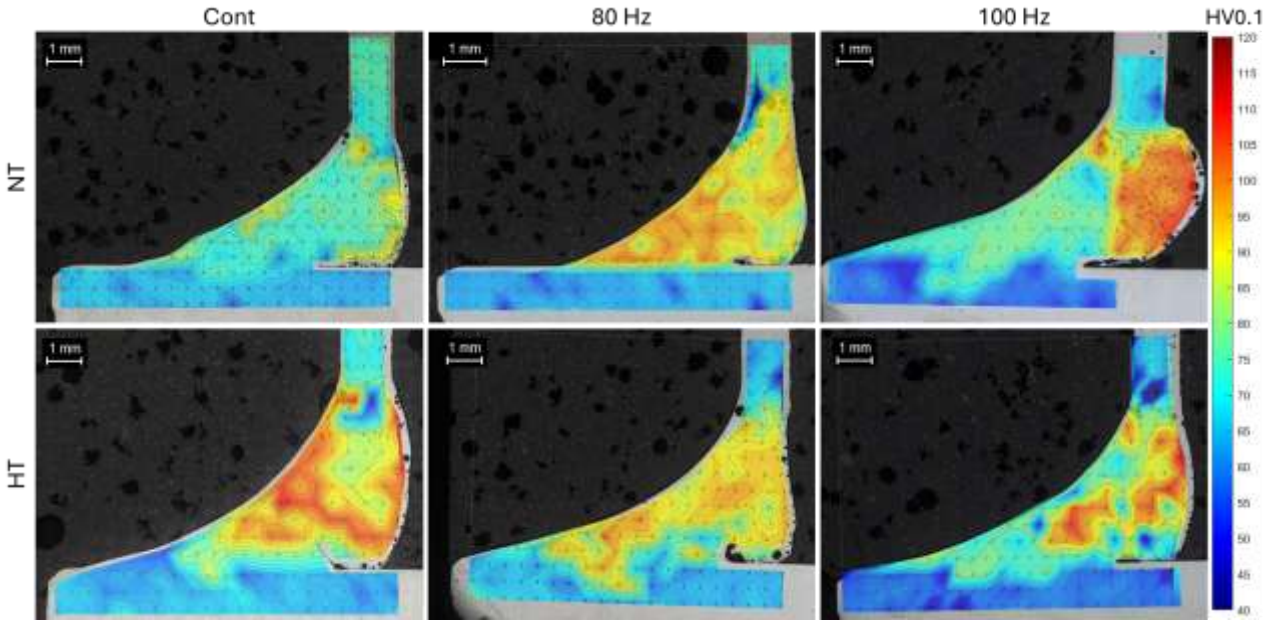

Figure 49 – Microhardness distribution maps (HV0.1) across cross-sections of hybrid welds in non-heat-treated (NT) and heat-treated (HT) conditions, obtained with different GTAW techniques: continuous (Cont), pulsed at 80 Hz and 100 Hz.

Particularly, the regions richer in silicon content characterised by equiaxed α-Al grains surrounded by thicker eutectic regions and coarser Mg-rich precipitates, as illustrated in Figure 45b, exhibit

higher hardness values, approximately around 100-110 HV0.1 (Figure 50a,b). Conversely, the regions richer in magnesium and depleted in silicon characterised by equiaxed α-Al grains surrounded by thin eutectic regions and very fine Mg-rich precipitates, as illustrated in Figure 45a, exhibit lower hardness values, approximately around 75-80 HV0.1 (Figure 50c,d). The regions where the chemical composition is more aligned with the chemical composition of the AW6061-T6, characterised by columnar α-Al dendrites surrounded by Si-and Mg-rich interdendritic regions, as illustrated in Figure 24, also exhibit very low hardness values, around 65-70 HV0.1.

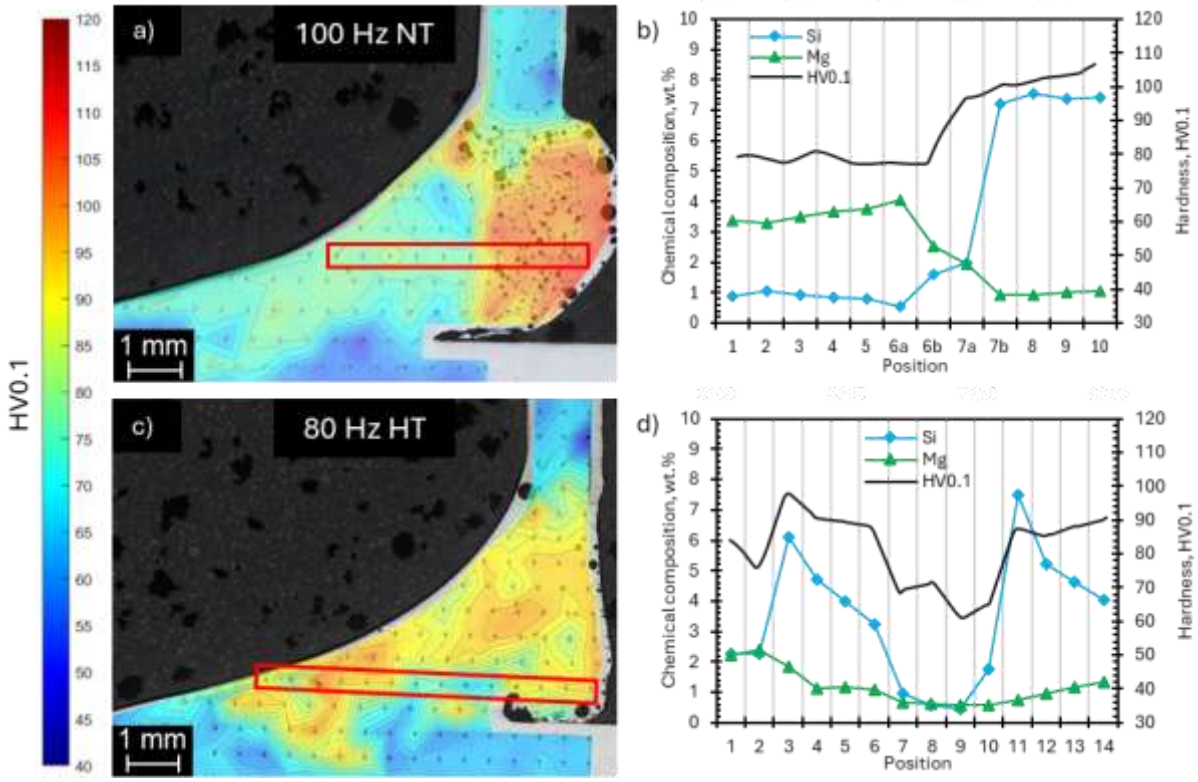

Figure 50 – (a,c) Vicker microhardness maps and (b,d) corresponding chemical composition and hardness profiles measured along the red-marked paths in the cross-sections of the 100 Hz NT and 80 Hz HT specimens.

As illustrated in Figure 49, the hardness maps provide a clear representation of the impact of the various GTAW techniques. In the Cont specimens, the greater variation in hardness is observed between the NT and HT conditions. However, the weld beads demonstrate a comparatively uniform hardness distribution, indicative of effective mixing between the filler metal and the base materials. The primary distinction between NT and HT lies in the pre-weld heat treatment process. Nevertheless, the manual execution of welding is likely to introduce local variations in feed rate and travel speed, which can influence solidification time, defect formation and mixing efficiency along the weld bead. It is evident that this aspect constitutes a primary factor in the determination of the quality of the weld. For the continuous GTAW specimens, the intrinsically higher thermal input of this technique leads to an extended HAZ with significantly reduced hardness values, approximately of 65 - 70 HV0.1, as expected for longer thermal cycles and enhanced grain growth [231].

The 80 Hz NT and HT joints (Figure 49) have comparatively uniform weld beads characterised by higher and more evenly distributed hardness than those obtained with continuous GTAW. This behaviour is primarily linked to the ability of pulsed GTAW to reduce the average heat input while

increasing the instantaneous power density during the current peaks and thus promoting faster solidification and finer microstructure in the weld zone [232]. Despite the lower nominal heat input, the HAZ remains quite extensive, consistent with the previously discussed microstructural observations. This may be attributed to the high thermal conductivity of aluminium alloys and potentially to an incorrect welding speed.

Joints welded using pulsed GTAW at 100 Hz exhibit the highest hardness values within the weld bead of all the investigated conditions. However, these hard regions are more localised, indicating less uniform mixing of the filler metal and base materials. Using a higher pulsing frequency increases the effective thermal input compared to lower frequency GTAW due to the more frequent repetition of high-current peaks and stronger arc constriction [233]. Consequently, the HAZ in the 100 Hz specimens exhibits hardness values of approximately 50 - 55 HV0.1, which is lower compared to 80 Hz condition. This is coherent with the more pronounced grain growth and recovery phenomena induced by the higher thermal load during welding [229].

Corrosion behaviour

The analysis of the cross-sections of the hybrid joints after the intergranular corrosion test highlighted a variable susceptibility to corrosion phenomena within the weld bead, Figure 51. The 100 Hz NT specimen, during the preparation phase, was damaged and it was not possible to subject this specimen to the corrosion test.

As for the mechanical performance, the corrosion behaviour of the hybrid joints analysed seems to be strongly affected by microstructural features.

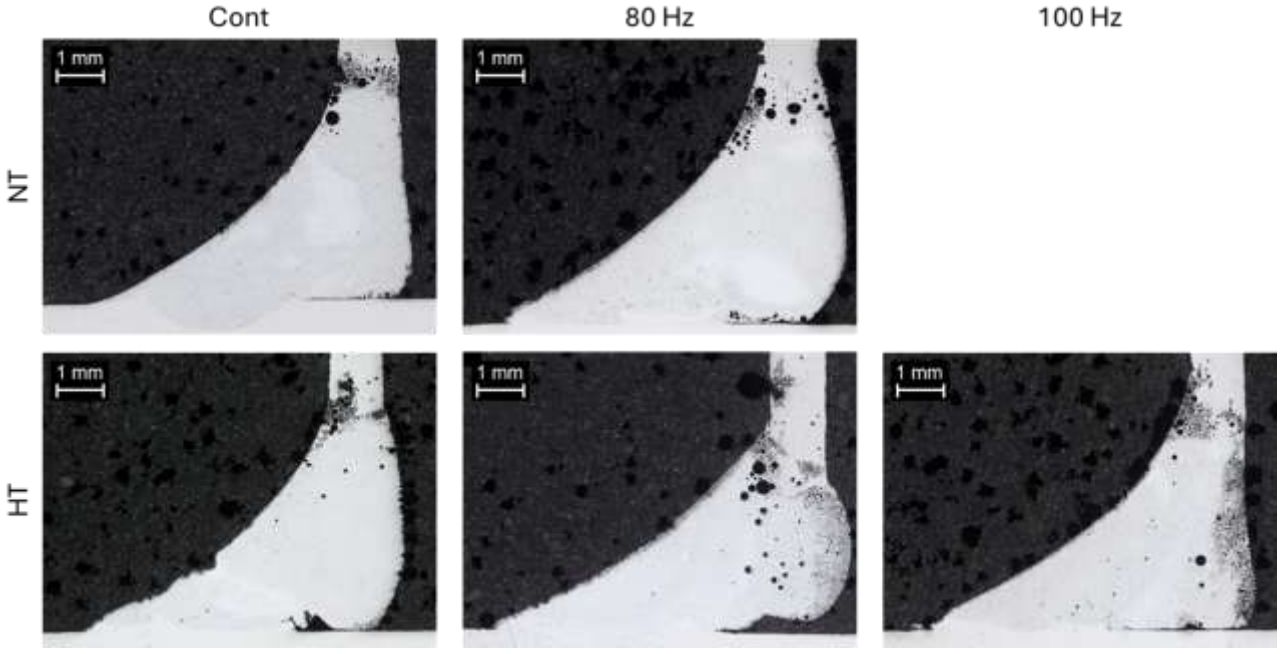

Figure 51 - Cross-sections of hybrid welds in non-heat-treated (NT) and heat-treated (HT) conditions, obtained with continuous GTAW (Cont), pulsed GTAW at 80 Hz and at 100 Hz after intergranular corrosion test.

As shown in Figure 51, all the joints analysed exhibited a corrosion susceptibility strongly linked to the microstructural features observed within the weld bead. Similar microstructural features were observed across all analysed specimens. However, for the sake of clarity, the reported features capture the main trends consistently observed throughout the investigation.

As extensively reported in the scientific literature, the selective corrosion behaviour of LPBF AlSi10Mg is strongly associated with the melt pool macrostructure and with the distribution of second phases, particularly along the melt pool boundary [53,54,77]. As stated by Zhang et al. [234], the application of direct ageing treatments to this alloy promotes silicon precipitation, leading to enhanced mechanical properties while simultaneously reducing corrosion resistance. It has been demonstrated that when elevated ageing temperatures or prolonged exposure times are employed, the alloy undergoes over-ageing, resulting in the coarsening of Si-rich precipitates within the microstructure [77].

As previously discussed, the non-heat-treated LPBF AlSi10Mg in regions far from the weld bead was nevertheless subjected to an over-ageing condition induced by the welding thermal cycle. This resulted in a melt pool macrostructure characterised by an increased amount of Si particles dispersed within the aluminium matrix, particularly along the melt pool boundaries [235]. Furthermore, the occurrence of Si precipitates within the melt pool centre was observed, resulting from the thermal input associated with the welding process. This phenomenon can be attributed to the enhanced diffusion and redistribution of silicon within the aluminium matrix [117]. This microstructural evolution promotes more severe localised corrosion attacks, resulting in the characteristic melt pool dropping morphology observed in Figure 52a,b. In this condition the corrosion mechanism is governed by micro-galvanic coupling between the α-Al matrix and the Si-rich precipitates, as observed in the as-built condition [234].

Moving closer to the weld bead, the increased thermal input associated with the FSW process induces more pronounced microstructural modifications. Consequently, the corrosion morphology gradually evolves towards a more widespread attack, as demonstrated in Figure 52c,d. This is indicative of reduced microstructural contrast and the partial homogenisation of the Si distribution within the aluminium matrix.

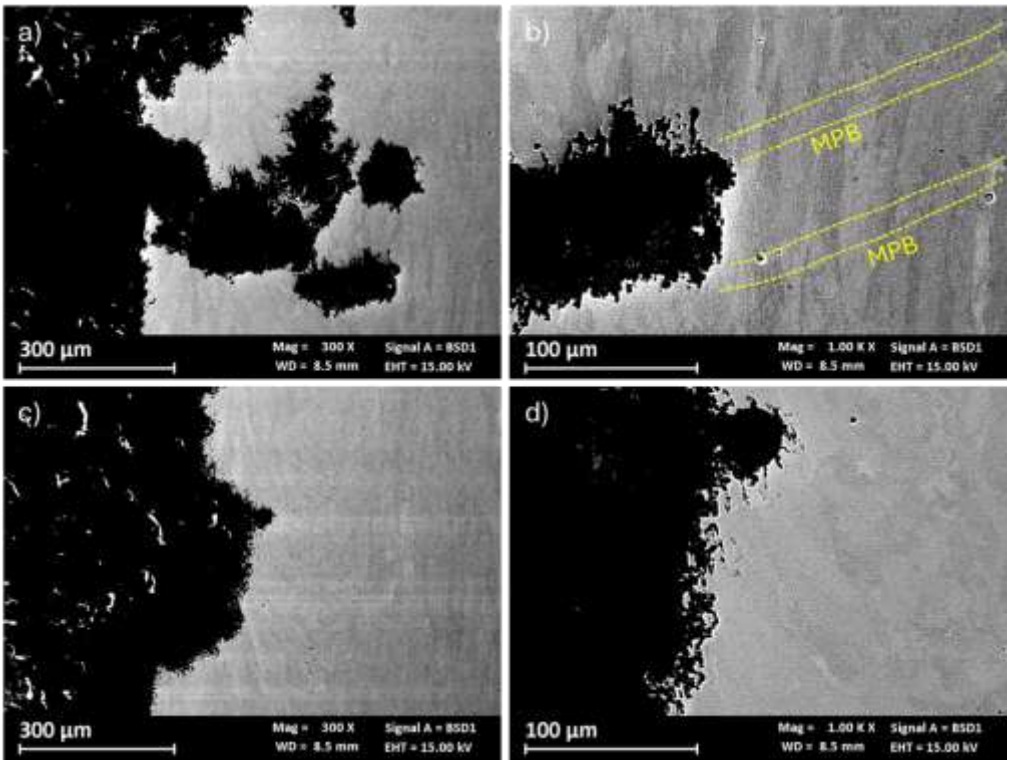

Figure 52 – Low- and high-magnification FESEM images of corrosion attacks observed in the (a,b) base material far from the weld bead and in the (c,d) HAZ in proximity of the weld metal of LPBF AlSi10Mg.

In the heat-treated specimens, as previously discussed, the LPBF AlSi10Mg component underwent a solubilisation treatment at 530 °C, resulting in a microstructure characterised by α-Al grains and coarsened Si particles (Figure 43) with significantly reduced mechanical properties. This heat treatment has also been demonstrated to affect the corrosion behaviour of LPBF AlSi10Mg. As illustrated in Figure 53a, the microstructural modification imposed by the heat treatment modified the corrosion behaviour of LPBF AlSi10Mg in comparison with the as-built condition, leading to a generalised corrosion morphology, in agreement with those reported by Cabrini et al. [65]. Proceeding towards the weld bead, the impact of elevated welding thermal input amplifies the susceptibility to selective corrosion, with pronounced attacks penetrating an average depth of 362 ± 34 µm for all specimens analysed, with a maximum depth of approximately 577 µm, as illustrated in Figure 53b. Figure 53c,d clearly reveal the intergranular morphology of the corrosion process, driven by the galvanic coupling between the α-Al grains and the coarser Si-rich precipitates [59].

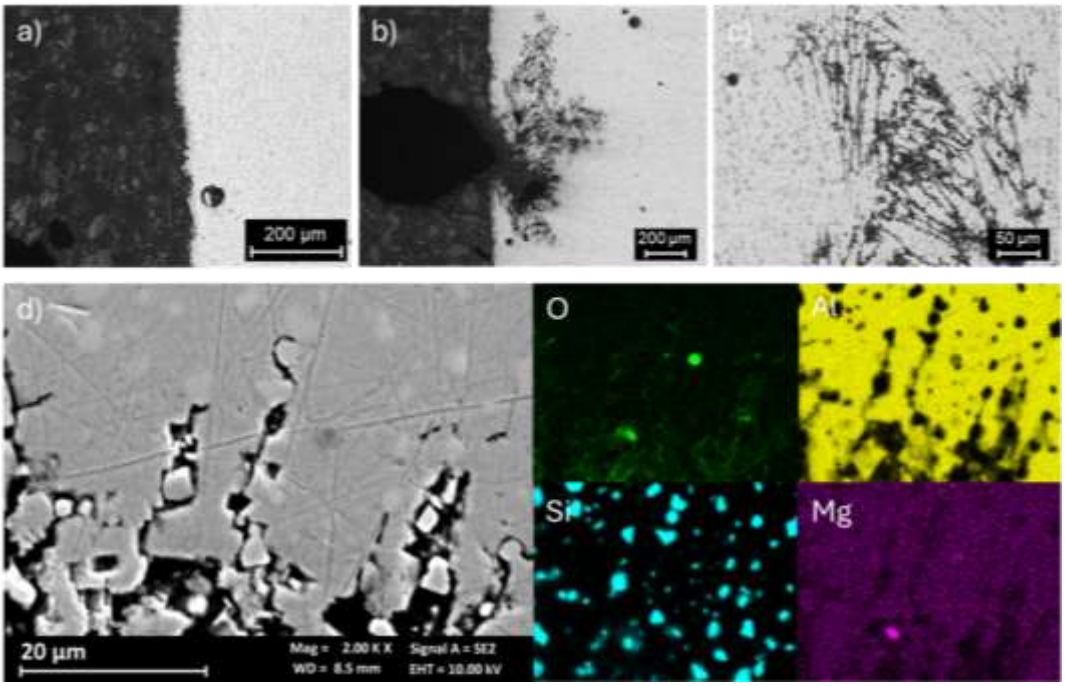

Figure 53 – Optical micrographs of corrosion attack in the 80 Hz HT specimen; (a) generalised corrosion in the HAZ far from the weld zone; (b,c) low-magnification images and (d) high-magnification FESEM image with corresponding EDS elemental map showing selective corrosion attacks in HAZ adjacent to the weld bead.

According to Figure 54a, the corrosion attack appears to occur initially in the weld metal close to the LPBF AlSi10Mg side and then to extend into the adjacent HAZ. In the HAZ, the corrosion mechanism is consistent with the previously described process, characterised by the preferential dissolution of the Al matrix along the over-aged eutectic regions. In the upper part of the weld zone, corrosion propagates along the Al-Si-Mg eutectic network, Figure 54b. As observed in Figure 54c, Al in the eutectic phase is selectively dissolved by micro-galvanic coupling with Si-containing intermetallics. Mg-bearing phases, such as Mg_2Si, act as sacrificial anodes and affect the morphology and extent of the local attack [236]. This corrosion attack, which was consistently observed in the same region for all specimens that were tested, penetrate deeply into the weld metal, reaching an average depth of 720 ± 108 µm. EDS analysis carried out in this area indicate an average local composition of approximately 9 wt.% Si and 1 wt.% Mg for the region exhibiting this corrosion morphology.

The aforementioned observations are consistent with the hypothesis proposed by McCloy et al. [237] for similar SLM AlSi10Mg-AA6082 joints, where the weld metal region adjacent to the SLM component exhibits a mixed Al-Si-Mg chemistry. McCloy et al. further hypothesised that the compositional gradient between the SLM HAZ and the weld metal is expected to enhance local micro-galvanic interactions and to promote the localisation of corrosion in this specific region of the weld bead.

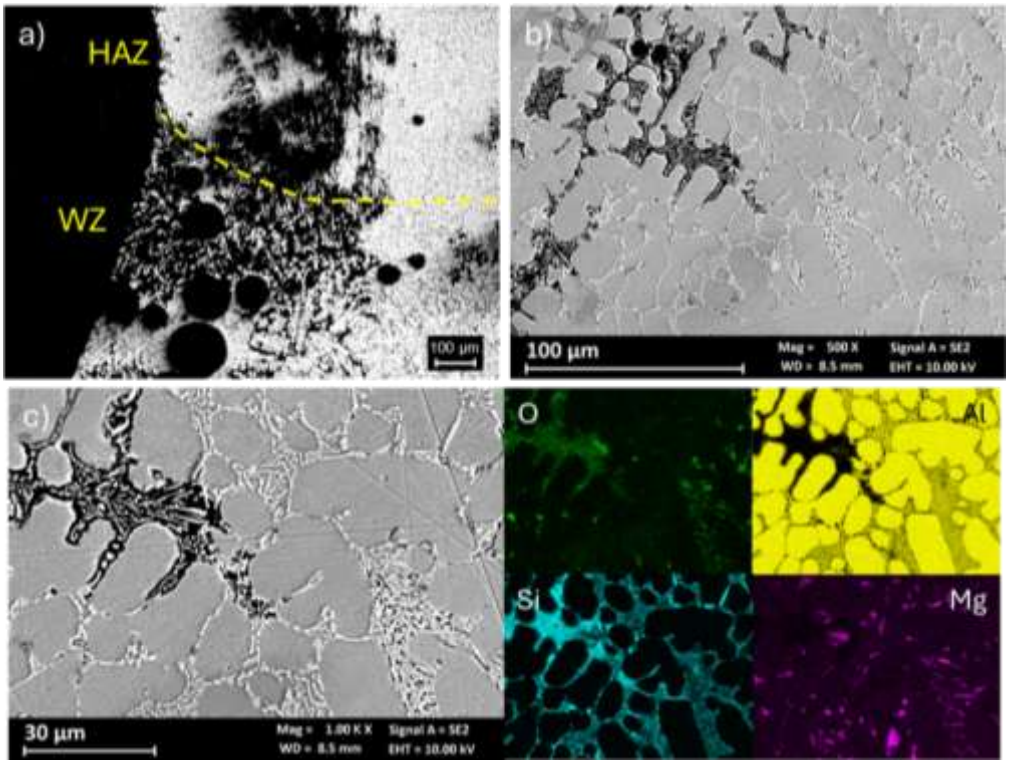

Figure 54 – (a) Optical micrograph of the corrosion attacks in the weld zone on the LPBF AlSi10Mg side of Cont HT specimen; (b) low-magnification FESEM image of corrosion attack within the weld bead; (c) high-magnification FESEM image and corresponding EDS elemental maps of the selective corrosion attack.

Proceeding towards the central region of the weld bead, in the proximity of the weld spot, the corrosion exhibits significant deviation from the previously described patterns, Figure 55a. As illustrated in Figure 55b, the exposed surface of the Cont HT specimen exhibits a microstructure characterised by equiaxed α-Al grains, surrounded by thin eutectic films and Mg-rich precipitates. In this region, corrosion is predominantly superficial and manifest as an interdendritic attack [237], controlled by micro-galvanic coupling between eutectic Al and Si-containing precipitates, Figure 55c. the presence of Mg-rich phases still results in a slight enlargement of the affected area. Across all specimens, regions exhibiting this morphology demonstrate an average penetration depth of 105 ± 15 µm, and EDS analyses indicate an average local composition of approximately 5 wt.% Si and 1.5 wt.% Mg. this composition demonstrates a more homogeneous mixing of the ER5356 filler and the LPBF AlSi10Mg, with Si and Mg contents that correspond to those od the base materials. The enhanced mixing of the weld is therefore associated with a substantial reduction in the susceptibility to deep intergranular corrosion.

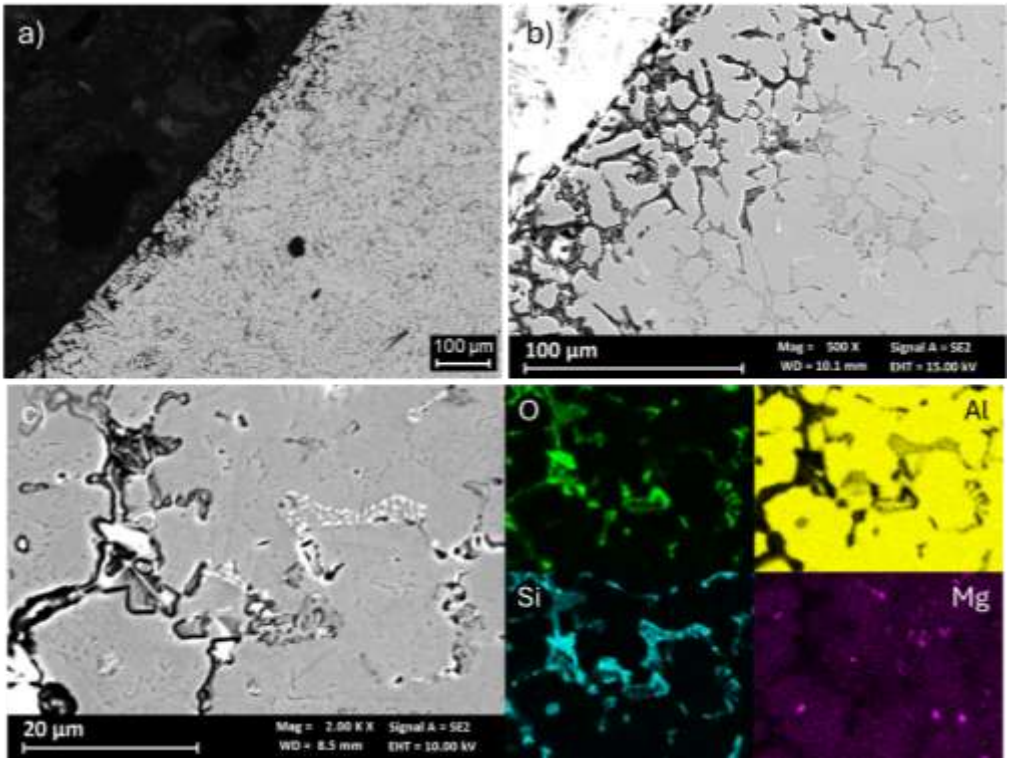

Figure 55 - (a) Optical micrograph of the corrosion attacks in the cental region of weld zone in the Cont HT specimen; (b) low-magnification FESEM image of corrosion attack penetrating into the weld metal; (c) high-magnification FESEM image and corresponding EDS elemental maps of the selective corrosion attack.

In the Cont HT specimen, Figure 56a, a third region was identified within the weld bead with a corrosion behaviour completely different from those described above. In this area, the attacks penetrate to a greater depth than in the adjacent regions, with an average depth of approximately 363 ± 17 µm. The microstructure observed in Figure 56b is different and the chemical composition analysis reveal an average content of 0.5 wt.% Si and 7 wt.% Mg, values that closely approximate the composition of the ER5356 filler metal. The position of the region in proximity to the weld spot suggest limited mixing between filler and base materials. The EDS maps in Figure 56C suggest a microstructure consisting of α-Al grains surrounded by fine Si-rich precipitates and a high concentration of Mg accumulated along the grain boundaries. Wei et al. [238], reported that, in welds with Al-Mg filler metals such as ER5356, the corrosion resistance of the weld zone is strongly dependent on the amount and distribution of β-Al_8Mg_5/Mg-rich phases at the grain boundaries. More dispersed precipitates lead to surface pitting, while almost continuous networks facilitate the transition to deeper intergranular attacks. In the AlSi10Mg–AA6082 SLM system analysed by McCloy [237], welds made with ER5356 show very high mass loss and intergranular morphologies, attributed to the higher Mg content of the filler and the possibility of forming sensitised microstructures. In the region of the weld dominated by the chemistry of 5356, the presence of continuous Mg-rich precipitates along the grain boundaries lead to micro-galvanic coupling, favouring the preferential dissolution of α-Al and Mg-rich phases. This allows intergranular attack to propagate deep into the weld metal, as evidenced by the attacks observed in Figure 56c.

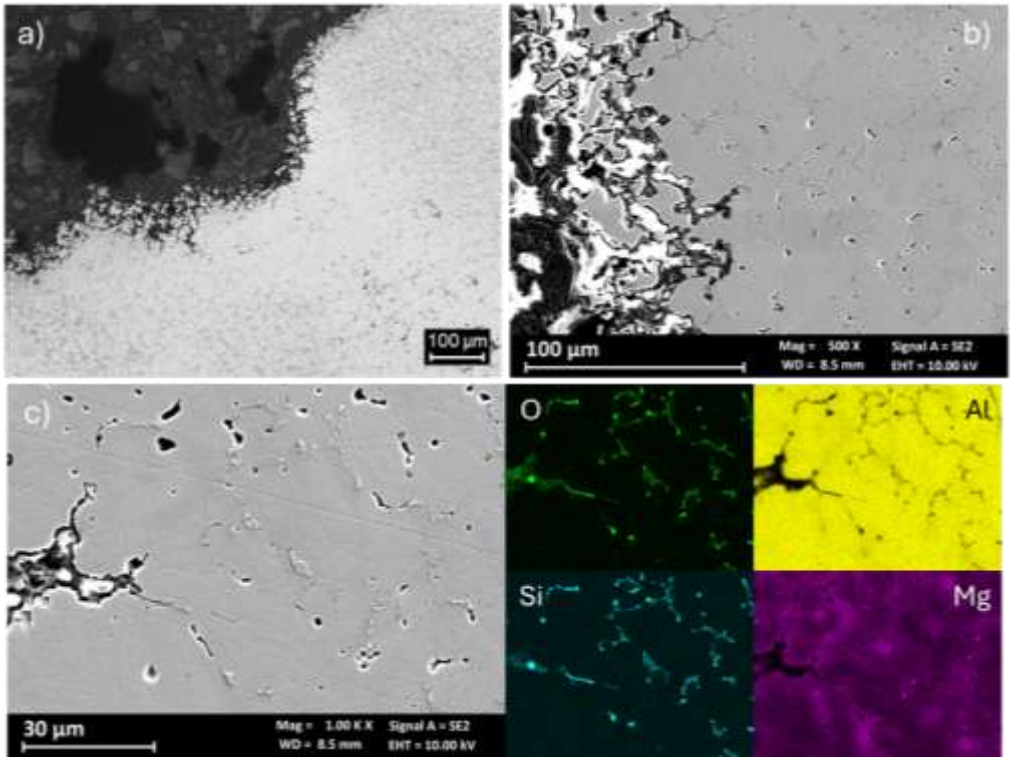

Figure 56 - (a) Optical micrograph of the corrosion attacks in the weld zone of the Cont HT specimen; (b) low-magnification FESEM image of corrosion attack penetrating into the weld metal; (c) high-magnification FESEM image and corresponding EDS elemental maps of the selective corrosion attack.

Table 9 presents the average depth of corrosion attacks measured in the regions of hybrid joints mentioned above, together with the values obtained for the LPBF AlSi10Mg alloy in its as-built condition [60]. In the regions distant from the weld bead, both in the untreated specimens, NT, and in those subjected to pre-weld heat treatment, HT, there was a generalised corrosion over the entire surface, Figure 52 and Figure 53. Consequently, it was not possible to define a representative penetration depth. However, the as-built material exhibited a substantially deeper level of attack, consistent with the recognised susceptibility to selective corrosion of the cellular microstructure characteristic of LPBF AlSi10Mg [77], as illustrated in Figure 57. Moving towards the weld bead, the NT HAZ displays a significant reduction in penetration depth compared to as-built condition, while preserving the same Si/Mg ratio. This finding suggest that the thermal cycle imposed by welding alone is sufficient to modify the LPBF microstructure in a way that mitigates selective corrosion, as discussed in the preceding sections. In specimens subjected to pre-weld heat treatment, the HAZ demonstrates higher penetration values in comparison to the NT HAZ, while remaining lower than the as-built. This observation suggests that further coarsening and the formation of secondary phases at the grain boundaries can locally augment susceptibility [67].

Table 15 – Local Si and Mg content, Si/Mg ratio and average corrosion depth measured in the different regions of the hybrid joints.

	Si (wt. %)	Mg (wt. %)	Si/Mg (wt. %)	Average depth (µm)
AlSi10Mg AB	10.3	0.36	28.6	539 ± 271
AlSi10Mg NT	10.3	0.36	28.6	-
AlSi10Mg NT HAZ	10.3	0.36	28.6	147 ± 17

AlSi10Mg HT	10.3	0.36	28.6	-
AlSi10Mg HT HAZ	10.3	0.36	28.6	362 ± 34
AW6061-T6	0.6	1	0.6	0
Zone 1	9	1	9.0	804 ± 161
Zone 2	5	1.5	3.3	119 ± 25
Zone 3	0.5	7	0.1	363 ± 17

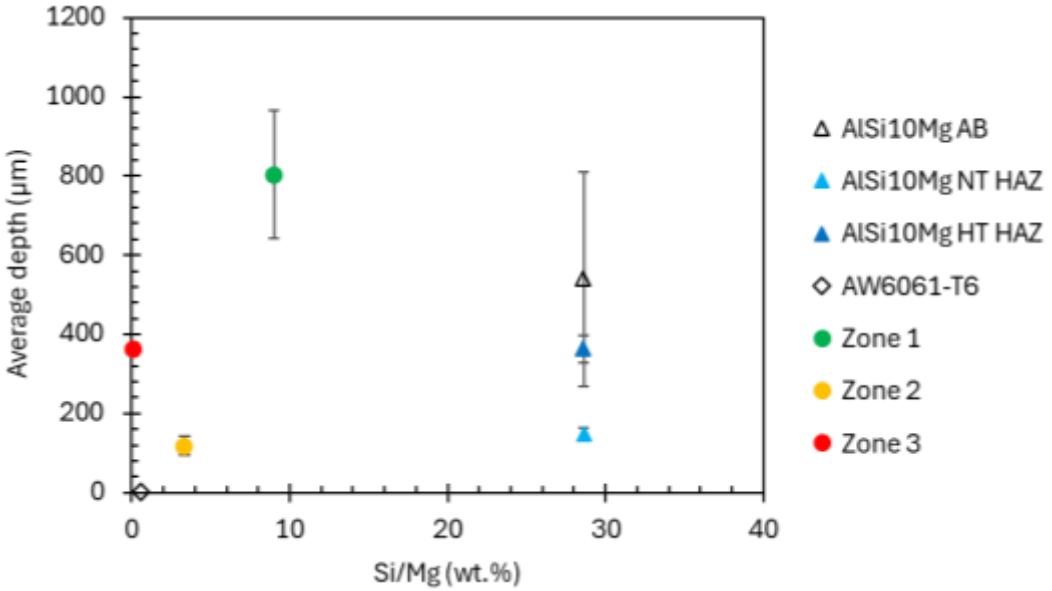

Figure 57 – Average corrosion depth versus Si/Mg ratio for the different regions of the LPBF AlSi10Mg – AW6061-T6 hybrid joints.

When considering the central region of the weld, three characteristic zones were identified, each exhibiting a distinct local chemistry and corrosion response. Zones 1, located on the LPBF AlSi10Mg side, correspond to the region shown in Figure 54 and exhibited the highest penetration depth, despite a decrease in the Si/Mg ratio. This behaviour suggests that, in this region, the combined effect of local compositional gradients and microstructural features promotes intense micro-galvanic activity and deep attack. Zone 2 (Figure 55), in closer proximity to the dead centre, exhibited a higher contribution from ER5356 filler metal, consequently resulting in a lower Si/Mg ratio. In this area, the penetration depth was significantly reduced, suggesting that a more balanced local chemical composition and a more homogeneous eutectic morphology result in a comparatively lower corrosion susceptibility. Zone 3 (Figure 56) demonstrated the lowest Si/Mg ratio within the weld bead. Nevertheless, the penetration depth exhibited an increase once more. This emphasises the deleterious role of Mg-rich precipitates along the grain boundaries in promoting selective corrosion when the weld chemistry shifts locally towards the filler metal.

This study has investigated the corrosion behaviour of GTAW hybrid joints. The investigation revealed that the behaviour is governed by a strong interplay between local chemical composition, microstructural architecture and the degree of mixing between the filler and base materials. From a processing perspective, both continuous and pulsed GTAW conditions resulted in weld beads exhibiting compositional heterogeneity. These findings suggests that further optimisation of welding

parameters and, potentially, filler metal selection is necessary to enhance the uniformity of mixing and, consequently the mechanical corrosion performance joints.

4.3.2 Solid-state welding of LPBF AlSi10Mg to AW6082 T6

4.3.2.1 Materials and methodology

The additive manufactured specimens were fabricated using the same printing machine, parameters and alloy powder used in the manufacturing process of the mock-ups for GTAW hybrid joints, previously discussed. The LPBF AlSi10Mg sheets were printed with dimensions equal to 150 x 50 x 4 mm. The AW6082-T6 samples were plate-shaped, with dimensions of 150 x 50 x 4 mm. Their chemical composition and mechanical properties are reported in Table 16 and Table 17.

Table 16 - Chemical composition (wt.%) of the base materials LPBF AlSi10Mg and AW6082-T6.

Elements (wt.%)	Al	Si	Mg	Fe	Cu	Mn	Zn	Cr	Ti
AlSi10Mg	bal.	10.3	0.36	< 0.55	< 0.05	< 0.45	< 0.10	-	< 0.15
AW6082-T6	bal.	1.01	0.88	0.30	0.05	0.55	0.02	0.01	0.01

Table 17 - Mechanical properties of AlSi10Mg and AW6082-T6.

Material	Ultimate Tensile Strength UTS_s (MPa)	Yield stress σ_{ys} (MPa)	Elongation $A\%$	Young Modulus E_s (GPa)
AlSi10Mg	440 ± 30	240 ± 20	6 ± 3	70
AW6082-T6	349	304	14	70

The solid-state welding process was performed using a Famup MC60 Evolution CNC machine, where the sheet metal pieces were mounted, clamped, and subsequently welded by friction. The welding process takes place with the sheet securely fixed on a plate inclined at 3° to ensure the tilt angle. The geometry of the conventional tool (Figure 58a) includes a shoulder with a diameter of 16 mm and a height of 20 mm, while the pin has a truncated conical shape with a base diameter of 6 mm and a smaller diameter of 4 mm. The process was carried out with a constant travel speed (F) equals to 60 mm/min and two different rotation speeds (S) equal to 1000 rpm (low heat input) and 2000 rpm (high heat input). In this study, similar and hybrid FSW joints were analysed. For the hybrid joints, the relative positions of both the alloys were varied, i.e AlSi10Mg alloy plates were placed interchangeably on the advancing side of AW6082-T6 alloy for both rotational speeds. The FSW conditions for different welded joint are shown in Table 18.

Subsequent to the welding process, specimens for tensile testing, hardness, corrosion and microstructure analysis were prepared, as shown in Figure 58b. The specimens were tested in the as-built condition (NT).

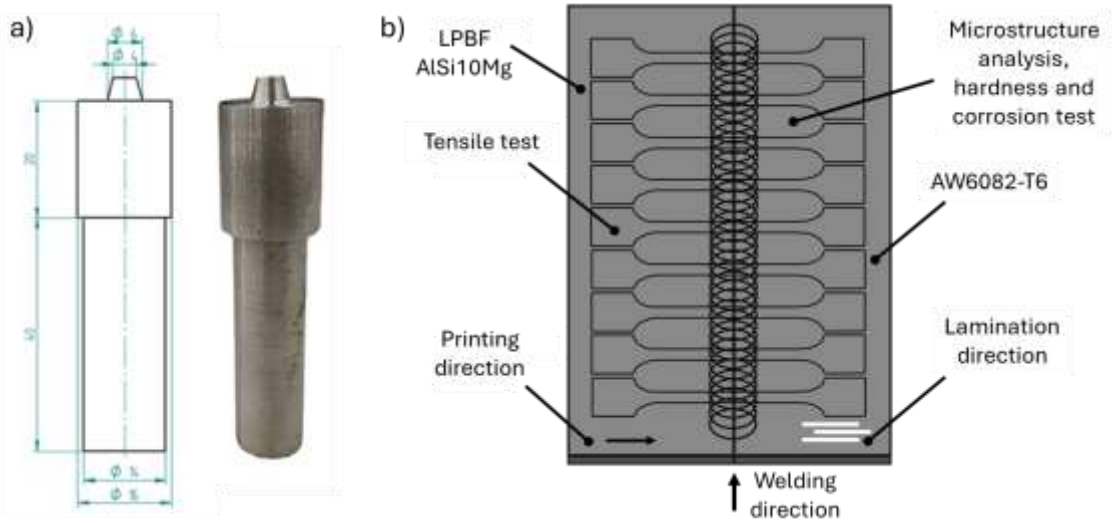

Figure 58 – (a) Traditional C40 tool geometry and (b) specimen layout on FSW welded sheet.

Table 18 - FSW parameters used for the similar and dissimilar joining of AlSi10Mg and AW6082-T6 alloy.

Designation	Joint configuration	Process condition	Material positioning		Rotational speed, S (rpm)	Travel speed, F (mm/min)
			Advancing side, AS	Retreating side, RS		
FSW AW6082-T6 (L)	Similar	Low heat input	AW6082-T6	AW6082-T6	1000	60
FSW AW6082-T6 (H)	Similar	High heat input	AW6082-T6	AW6082-T6	2000	60
FSW AlSi10Mg (L)	Similar	Low heat input	AlSi10Mg	AlSi10Mg	1000	60
AW6082-T6 /AlSi10Mg (L)	Hybrid	Low heat input	AW6082-T6	AlSi10Mg	1000	60
AlSi10Mg/ AW6082-T6 (L)	Hybrid	Low heat input	AlSi10Mg	AW6082-T6	1000	60
AlSi10Mg/ AW6082-T6 (H)	Hybrid	High heat input	AlSi10Mg	AW6082-T6	2000	60

Microstructural analysis was performed on cross sections perpendicular to the welding direction. In order to obtain a surface finishing suitable for micrographic analysis the specimens were mechanically polished with SiC papers up to 4000 grid and then with a 1 μm diamond suspension. The microstructures were revealed by chemical etching with Keller and Weck reagent, analysed using digital-optical microscope Keyence VHX-7100 and a Gemini Sigma 300 field emission scanning electron microscope (FESEM), equipped with an Oxford x-act probe for energy-dispersive X-ray spectroscopy (EDS).

To evaluate the mechanical properties of the joints, tensile tests were carried out using dog-bone-shaped specimens with a 32 mm^2 cross section, 43 mm parallel length, and 32 mm gauge length, compliant with the ISO 6892-1 standard. The specimen geometry was obtained by machining transverse to the welding direction, as schematically represented in Figure 58b. The tensile tests were

carried out using a Galdabini Sun 5 universal testing machine equipped with a 50 kN load cell. These tests were performed in laboratory environment conditions under displacement control, adopting a cross-head speed corresponding to a nominal strain rate of $2.5 \cdot 10^{-4}\ s^{-1}$. A preliminary preload of 200 N was applied in order to ensure correct alignment and elimination of slack in the gripping system before starting the data acquisition. For each welding condition, at least two specimens were tested, recording load and displacement data up to failure. Vickers microhardness tests were performed in accordance with UNI EN ISO 6507-1, utilising a load of 0.1 kg and a loading time of 10 s in order to evaluate the hardness distribution within the joints.

Intergranular corrosion tests were performed in accordance with the EN ISO 11846 standard (Method B). The specimens were mechanically ground with SiC papers up to 2400 grit. The specimens were then degreased with acetone, immersed for 3 minutes in a sodium hydroxide solution (8% by weight at 55 ± 2 °C), rinsed in water, immersed for 2 minutes in concentrated nitric acid, rinsed in distilled water and dried. Subsequently, the specimens were immersed in the test solution, containing 30 g/L sodium chloride and 10 mL/L concentrated hydrochloric acid, at room temperature for 24 h. The temperature of the test solution was maintained within a range of 21 - 25 °C. Afterwards, the samples were rinsed in distilled water and dried. Corrosion products were removed with a non-metallic brush, followed by a systematic rinsing in distilled water, immersed for 30 seconds in concentrated nitric acid, then immersed in an ultrasonic bath of acetone and subsequently allowed to dry. A metallographic section perpendicular to the exposed surface was evaluated in order to determine the presence and depth of the attacks.

4.3.2.2 Experimental strategy and parameter selection

The experimental campaign was designed to progressively transfer an already validated parameter window from similar to hybrid joints, as evidenced by the available literature of FSW of 6xxx alloys and additively manufactured AlSi10Mg. The parameters that have the strongest impact on the mechanical properties of FSW joints are rotational speed and travel speed. For FSW of 6xxx alloys, numerous studies have been reported that analyse different configurations of rotational speed and travel speed and their effect on mechanical properties [201,239–241]. In order to analyse this dual effect, many authors introduce the S/F ratio to compare different parameters. This ratio thus serves as an indirect measure of the thermomechanical energy introduced per unit of welding length [242]. It has been established that an elevated ratio is associated with elevated thermal input and augmented stirring effect within the nugget. However, this is concomitant with an augmented risk of defects and the softening of the weld [243]. Conversely, a lower ratio may be indicative of insufficient energy and problems related to lack of mixing or tunnel defects [244]. Therefore, this S/F ratio is highly useful during preliminary assessment and comparison of welding parameters when the tool geometry and welding configurations are maintained constant.

A survey of welding parameters reported in the literature for friction stir welding of aluminium alloys highlights distinct trends depending on the material system. In the case of analogous joints involving 6xxx series alloys, the majority of studies adopt S/F ratios of a relatively low to intermediate value, typically below 20, with the aim of minimising excessive heat input and avoiding pronounced softening associated with precipitate dissolution in the heat-affected zone [204,243,245]. In the case of similar LPBF AlSi10Mg joints, the reported welding conditions generally shift towards intermediate S/F ratios. This is indicative of the necessity for elevated thermomechanical input in comparison to wrought alloys, with the objective of facilitating effective material flow, disrupting the

Si-rich eutectic network that is characteristic of additively manufactured microstructures, and ensuring adequate joint consolidation [174,202,203]. The existing literature demonstrates a wider dispersion of welding parameters for hybrid joints between LPBF AlSi10Mg and conventional aluminium alloys. A number of studies have explored intermediate-to-high S/F ratios, suggesting that increased heat input and stirring intensity may be required to accommodate the strong microstructural and mechanical asymmetry between the additively manufactured and wrought materials, and to enhance mixing across the joint interface [215,216].

This study has selected two representative S/F regimes, an intermediate and a higher ratio, as candidate parameter windows for experimental investigation, on the basis of prevailing literature trends. The experimental activity first assessed similar AW6082-T6 welds at two rotational speeds ($S = 1000 - 2000\ rpm$) and constant travel speed ($F = 60\ mm/min$), corresponding to S/F ratio of 16.7 and 33.3, respectively. Based on the findings derived from the experimental analysis of the wrought alloys, the welding condition that was identified as the reference parameter set was determined to be characterised by a rotational speed of 1000 rpm and a travel speed of 60 mm/min. This condition was then applied to similar LPBF AlSi10Mg joints to evaluate whether the $S/F = 16.7$ identified for AW6082-T6 could also ensure satisfactory welding efficiency when applied to an additively manufactured material, characterised by a markedly different microstructure.

Subsequent to this validation step, the same welding parameters were applied to hybrid LPBF AlSi10Mg – AW6082-T6 joints. In this instance, the advancing and retreating side configuration was defined in accordance with established literature guidelines on material flow and heat input control in dissimilar FSW. Following mechanical screening, the configuration characterised by a rotational speed of 1000 rpm and a travel speed of 60 mm/min was identified as the most promising for hybrid joints. Consequently, the detailed investigation of microstructure-property relationships was focused on this condition, including microstructural analysis across the weld zones, hardness mapping, intergranular corrosion testing and local electrochemical measurements using a microcell.

4.3.2.3 Results and discussion

The engineering stress-strain curves obtained for similar and hybrid FSW welded joints are shown in Figure 59. The performance were evaluated based on ultimate tensile strength (UTS), 0.2 % yield strength (σ_y) and joint efficiency, illustrated in Table 19. The joint efficiency was evaluated based on the ratio between the ultimate tensile strength of FSW joint and the UTS_s related to the base material (Table 17). For hybrid joints it was used the lower value between the two different aluminium alloys, thus the ultimate tensile strength of the AW6082-T6.

Starting from the similar FSW joints between AW6082-T6, from Figure 59 and Table 19 it can be seen that both FSW joints exhibit comparable mechanical properties, joint efficiency (62 %) and a fracture located in the TMAZ/HAZ of the retreating side. In the case of 6xxx alloys in T6 condition, a thermal input, like those generated during the welding process, promote the dissolution and coarsening of strengthening precipitates [246]. This led to a softening within the TMAZ and HAZ of the FSW joints, while the intrinsically thermal asymmetry related to FSW process contribute to localise this minimum-strength zone into the retreating side [247]. Despite the different S/F ratios, both parameter sets produced comparable softening in both joints. As reported by Ma et al [248], increasing the rotational speed led to a higher thermal input and an expected further reduction of the mechanical properties, but if the heat input is sufficient to induce extensive precipitate dissolution and coarsening, further increases in the welding parameters affecting the thermal input do not

necessarily result in a proportional reduction in tensile strength. Based on this consideration, in order to reduce the risk of defects related to heat-input and excessive softening in the HAZ/TMAZ and to provide a more energy-efficient process [201], the S/F = 16.7 was identified as the possible best solution also for the hybrid welds.

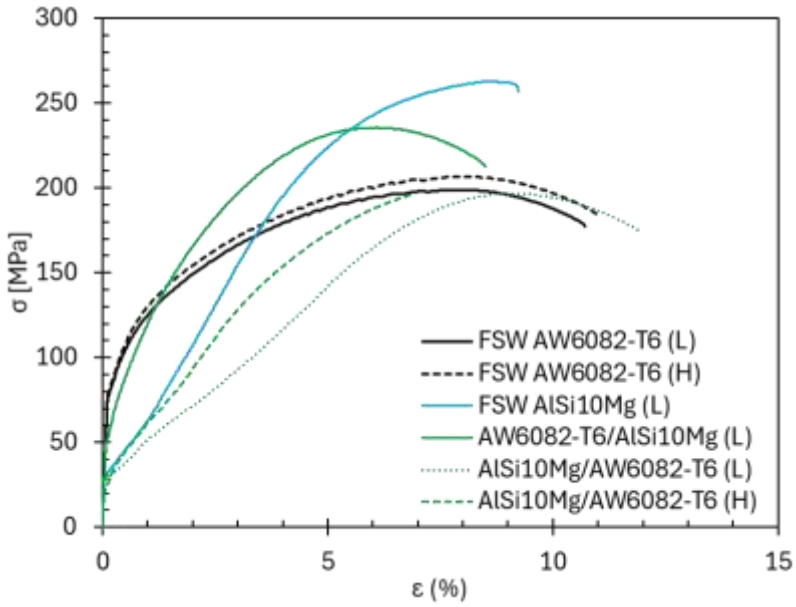

Figure 59 - Engineering stress-strain curves for similar and hybrid FSW joints.

Table 19 - Tensile properties, joint efficiency and fracture location of similar and hybrid FSW joints.

Designation	**S/F**	**σ_y (MPa)**	**UTS (MPa)**	**A %**	**Joint efficiency (%)**	**Fracture location**	
						AS/RS	Zone
FSW AW6082-T6 (L)	16.7	84 ± 9	201 ± 2	11.0 ± 0.3	62 ± 1	RS	TMAZ/HAZ
FSW AW6082-T6 (H)	33.3	80 ± 20	200 ± 4	11.7 ± 0.5	62 ± 1	RS	TMAZ/HAZ
FSW AlSi10Mg (L)	16.7	37 ± 2	260 ± 2	10.5 ± 1	74 ± 1	Weld centre	SZ
AW6082-T6 /AlSi10Mg (L)	16.7	55 ± 8	235 ± 4	8.7 ± 0.2	72 ± 1	AS	HAZ
AlSi10Mg/ AW6082-T6 (L)	16.7	41 ± 9	214 ± 4	9.3 ± 1.7	59 ± 1	RS	HAZ
AlSi10Mg/ AW6082-T6 (H)	33.3	37 ± 3	190 ± 9	7.1 ± 0.4	56 ± 3	Weld centre	SZ

Based on the results reported in Figure 59 and Table 19, a rotational speed of 1000 rpm and travel speed of 60 mm/min, with a S/F ratio of 16.7, could represent a good solution, leading to a quite high joint efficiency (74%). In accordance with the literature [249,250], in the case of similar FSW joints

between LPBF AlSi10Mg alloy, the weakest region within the weld is the stir zone due to the dissolution of the as-built Si-rich network and the promotion of coarsening and re-distribution of Si particles. For LPBF AlSi10Mg alloy the use of a rotational speed (S) approximately of 750-1200 rpm and a travel speed (F) in a range of 40-80 mm/min could represent the best suitable conditions to obtain good mechanical properties and joint efficiency, avoiding excessive softening in HAZ and weld defects [250,251].

Subsequent to the validation steps performed on similar AW6082-T6 and LPBF AlSi10Mg joints, the selected welding parameter sets were applied to hybrid joints. As previously discussed, the mechanical behaviour of friction stir welded joints is significantly influenced by the inherent process asymmetry between the advancing side (AS) and the retreating side (RS). This aspect assumes particular significance in the case of hybrid joints, where the two base materials exhibit markedly different mechanical and microstructural characteristics. Therefore, for the welding condition identified as the most suitable for the present study (S/F = 16.7), both material configurations were analysed. In this instance, the LPBF AlSi10Mg alloy was positioned on the advancing side and on the retreating side. This approach enabled the direct assessment of the influence of material positioning on joint performance under identical welding conditions. The analysis was also extended to the welding condition characterised by a higher S/F ratio (S/F = 33.3). In this instance, due to the limited number of available specimens, only one material configuration was investigated, with the LPBF AlSi10Mg alloy positioned on the advancing side. This choice was guided by the results reported by Thakur et al. [215], who demonstrated that, under high heat input conditions (S/F = 30), positioning the LPBF material on the advancing side leads to improved joint efficiency compared to configurations with the additively manufactured alloy placed on the retreating side. The tensile test results presented in Figure 59 and Table 19 demonstrate that the welding condition characterised by an S/F ratio of 16.7 provides superior mechanical properties in comparison to the higher S/F configuration, irrespective of material positioning. These findings provide further support for the selection of S/F = 16.7 as the optimal parameter window for hybrid FSW joints in the present study.

The tensile tests highlighted that the specimen AW6082-T6/AlSi10Mg (L), with AlSi10Mg on the RS side, the well-known weakest region, results in the best mechanical performance, with a UTS equal of 235 ± 4 MPa and a joint efficiency of 72 ± 1. Despite the position of AlSi10Mg or AW6082-T6 within the joints, the fracture was located in the AW6082-T6 side, within the HAZ, as illustrated in Figure 60.

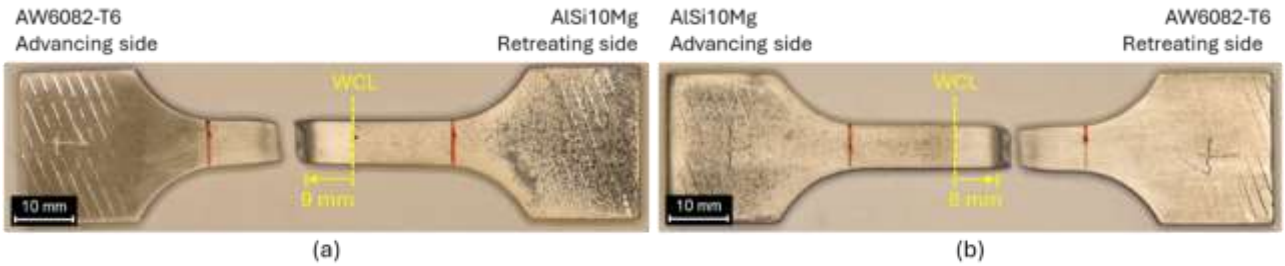

Figure 60 - Fractured location of (a) AW6082-T6/AlSi1Mg (L) and (b) AlSi10Mg/AW6082-T6 (L) hybrid joints.

As demonstrated in Figure 61, the microstructural analysis and microhardness mapping of the AW6082-T6/AlSi10Mg (L) cross-section offer a more profound understanding of the microstructural

characteristics that govern the observed mechanical behaviour. A notable outcome of this analysis is the complete absence of gas porosity within the weld bead, which is consistent with the solid-state nature of the FSW process, as no melting or gas entrapment occurs during the joining process. Moreover, the observation of a lack of welding defects within the stir zone serves to corroborate the hypothesis that the selected welding parameters are well suited to this specific joint configuration.

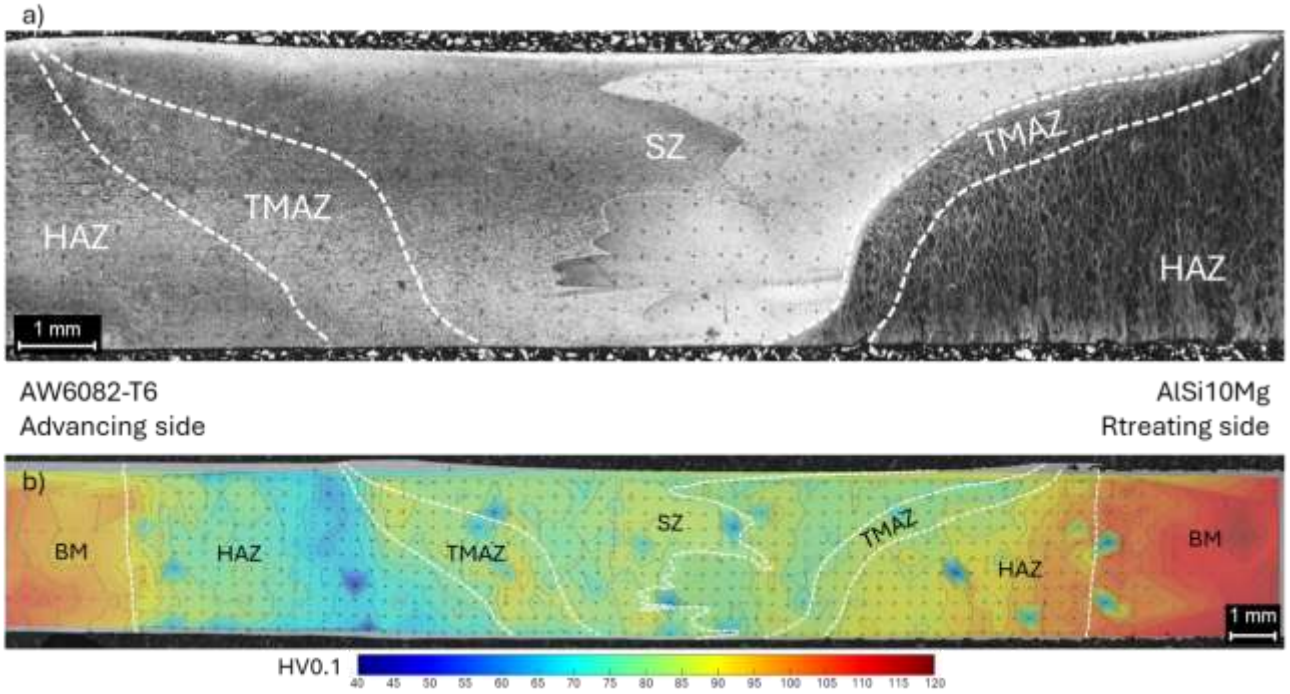

Figure 61 – (a) Optical cross-section macrograph of AW6082-T6/AlSi10Mg (L) specimen and (b) relative microhardness map.

As previously discussed, the HAZ on the AW6082-T6 side exhibits a microstructure characterised by grain coarsening and precipitate dissolution, Figure 62a. This effect becomes increasingly pronounced when approaching the TMAZ, as a consequence of the progressively higher thermal input experienced during the welding process. The hardness values presented in Figure 61b corroborate the softening of the HAZ relative to the base material, emphasising a substantial reduction in hardness at the transition with the TMAZ. The systematic localisation of fracture within the HAZ of the AW6082-T6 side is consistent with the results reported by Thakur et al. [112], who demonstrated that joint failure in dissimilar FSW joints is governed by the locally softened region of the wrought alloy. In this context, precipitate dissolution and coarsening induced by the welding thermal cycle represent the primary factors responsible for this behaviour.

The TMAZ is subjected to both intense plastic deformation and thermal exposure, resulting in a partially recrystallised microstructure characterised by locally refined grains (Figure 62b) due to partial dynamic recrystallisation (DRX). As demonstrated in Figure 61b, the hardness increases progressively due to reduced precipitate coarsening and partial dissolution in comparison to the HAZ [252].

As illustrated in Figure 61a and Figure 63, within the stir zone a clear distinction between the two base materials is observed in terms of both chemical composition and microstructural features, as also reported for dissimilar FSW joints [201,211]. In the case of the AW6082-T6 side, dynamic recrystallisation results in the formation of fine equiaxed grains, coupled with significant precipitate

dissolution. This phenomenon led to a reduction in hardness with respect to the base material, but higher than those measured in the HAZ, as demonstrated in Figure 61b. In the AlSi10Mg alloy, the stir zone is distinguished by the presence of fine equiaxed α-Al grains and a relatively homogeneous distribution of Si-rich precipitates, as illustrated in Figure 62d. Despite the evident refinement of the grain, the disruption of the original Si-rich eutectic network results in a substantial reduction in hardness when compared to the LPBF base material.

The fine-grained microstructure that develops within the stir zone on both sides of the joint plays a pivotal role in the enhanced mechanical performance observed for the AW6082-T6/AlSi10Mg (L) configuration in comparison to the AlSi10Mg/AW6082-T6 (L) specimen. During the process of FSW, the advancing side (AS) is subjected to a slightly higher thermal input and more intense plastic deformation compared to the retreating side (RS) [253]. This condition has been shown to promote a marginally higher degree of grain refinement on the AS, both within the stir zone and in the adjacent regions [254]. In accordance with the Hall-Petch strengthening mechanism [255], the presence of finer equiaxed grains in the HAZ on the AW6082-T6 side, which constitutes the weakest point, resulted in an increase in tensile strength. The enhanced mechanical performance observed when the AlSi10Mg alloy is positioned on the retreating side can therefore be attributed to differences in material flow and mixing within the stir zone. Effective mixing between the base materials is a critical factor in promoting mechanical interlocking within the nugget, which in turn facilitates a more homogeneous load transfer across the interface [256].

As demonstrated in Figure 62e, the TMAZ on the AlSi10Mg side displays a microstructure distinguished by re-oriented and deformed grains [215], and most significantly by a Si network that is already markedly disrupted. Within the HAZ on the AlSi10Mg side, as illustrated in Figure 61a and Figure 62f, the melt pool macrostructure typical of the LPBF process is still discernible; however, a partial breakdown of the Si-rich network is observed, resulting in a reduction in hardness compared to the base material, as confirmed by the hardness profile reported in Figure 61b.

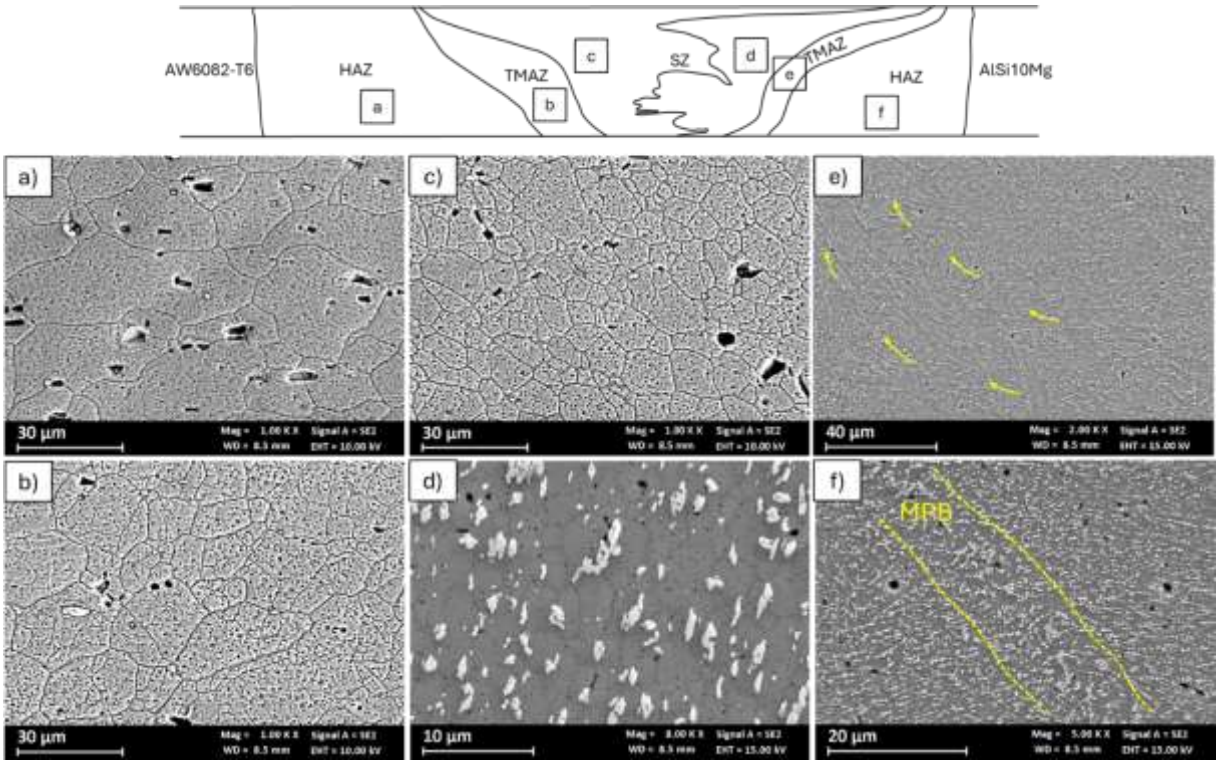

Figure 62 – Schematic representation of the cross-section of the AW6082-T6/AlSi10Mg (L) specimen and FESEM micrograph of the representative microstructure: (a-c) microstructure of BM, HAZ, TMAZ and SZ, respectively, in the AW6082-T6 side; (d-f) microstructure of BM, HAZ, TMAZ and SZ, respectively, in the AlSi10Mg side.

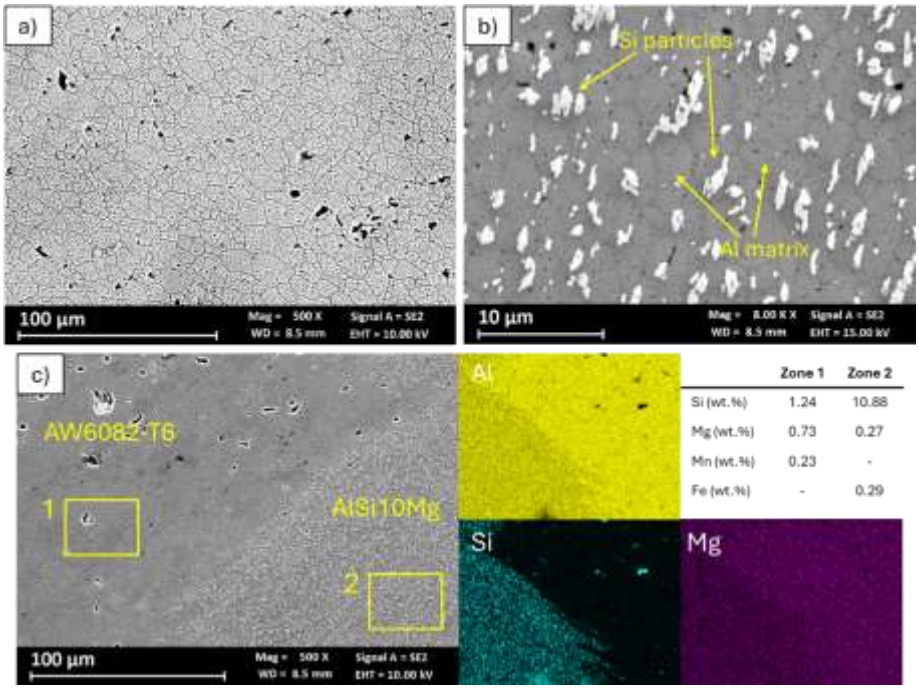

Figure 63 – FESEM macrograph of (a) the stir zone on the AW6082-T6 side, (b) the stir zone on the AlSi10Mg side and (c) the transition zone across AW6082-T6/AlSi10Mg interface, with EDS elemental maps.

The microstructural heterogeneity within the joints exerts a significant influence on both their mechanical response and their corrosion behaviour. To selectively investigate the electrochemical

behaviour of the different regions within the joints, local potentiodynamic polarisation tests were performed using an electrochemical microcell in collaboration with the research group of Prof. Francesco Andreatta (University of Udine). The subsequent surface analyses (Figure 45) enable a direct correlation between local electrochemical response and metallurgical features [257].

As illustrated in Figure 64, the potentiodynamic curves measured in the various regions of the joints demonstrate significant variations. For both alloys, a typical Al-Si-Mg response is observed, with an anodic branch characterised by a more or less extended passive region and, at higher potentials, by a sharp increase in current density associated with pit initiation on the exposed surface [55]. In the case of the AW6082-T6 alloy, the base material exhibits a more stable passive range than the HAZ, TMAZ, SZ. This behaviour can be associated with a gradual loss of passivating capability as the distance from the weld centreline decreases. This variation in behaviour is particularly evident in the AlSi10Mg alloy. The base material displays a broad passive region, with the current density increase being related to pitting initiation only at potentials exceeding 1 V vs SCE. As the specimen moves towards the weld centre, the extent of the passive domain decreases, indicating a progressive reduction in the stability of the alumina film covering the surface [45].

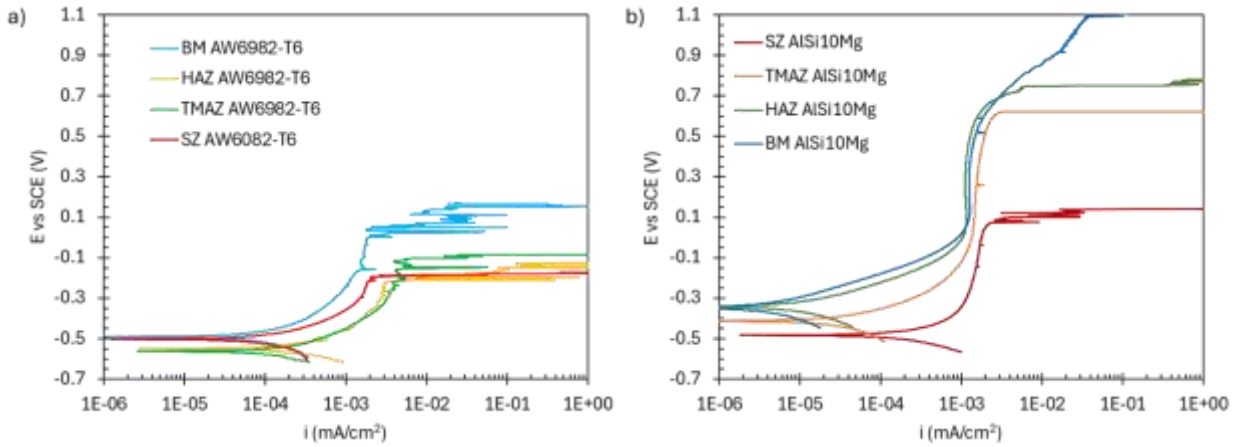

Figure 64 – Polarisation curves of (a) AW6082-T6 side and (b) AlSi10Mg side evaluated on the upper surface of the AW6082-T6/AlSi10Mg (L) specimen.

As demonstrated in Figure 65a, the corrosion potential exhibits moderate variations between the distinct regions of the joint on the AW6082-T6 side, in accordance with the findings reported for FSW welded 6xxx alloys [198]. The current density also remains of the same order of magnitude along the weld, with a slight increase at the HAZ and TMAZ, Figure 65b. This suggests that susceptibility to generalised corrosion is only slightly accelerated in these regions, where over-precipitation and free-precipitation zones along the grain boundaries increase anodic reactivity [258]. The pitting potential, E_{pit}, exhibits a decreasing trend from the BM towards the SZ, as illustrated in Figure 65c. This suggests that the initiation of localised corrosion is facilitated by the co-existence of coarse precipitates and finer grains, which reduce the stability of the oxide film [258,259].

A qualitatively similar behaviour is observed for the AlSi10Mg alloy, but with more marked variations from BM to SZ, Figure 65. The variation in E_{corr} remains negligible, while the current density increases by approximately one order of magnitude between the BM and the SZ. As reported by Cabrini et al. [260], an increase in temperature and the consequent coarsening of the Si network led to the expulsion of Si from the supersaturated matrix and the formation of coarse Si-rich

precipitates along the grain boundary. This, in turn, reduces the stability of the passive film, intensifies the galvanic stimulation of the aluminium matrix corrosion and decreases the resistance to pitting initiation, as confirmed by the reduction in E_{pit}, Figure 65c.

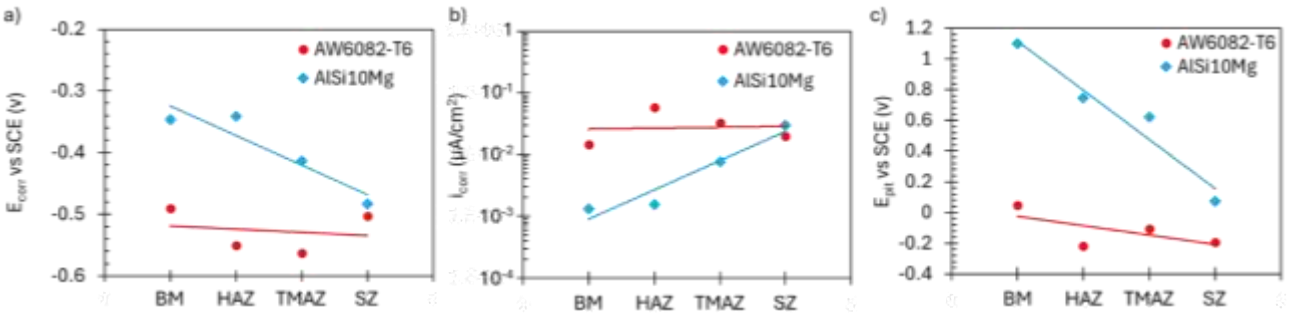

Figure 65 – (a) Corrosion potential (E_{corr} vs SCE), (b) corrosion current density (i_{corr}) and (c) pitting potential (E_{pit} vs SCE) in the different region of the AW6082-T6/AlSi10Mg (L) specimen.

The analysis of corrosion attacks in different areas of the weld bead confirms the results of the electrochemical tests. As illustrated in Figure 66a-d, the morphology of the pits identified on the AW6082-T6 alloy confirms the propagation of corrosion along the grain boundaries, an effect that becomes more visible when moving from the BM to the SZ.

In the case of the AlSi10Mg alloy, the morphology of the corrosion attack corroborates the impact of the microstructure on the corrosion behaviour in different areas of the joint. As illustrated in Figure 66e, in the BM, corrosion is driven by the melt pool macrostructure and, particularly, by the lower stability of the oxide film along melt pool boundaries [260]. As the attack progresses towards the HAZ, TMAZ and SZ, an intensification of penetration is observed, aligning with the trend previously identified in E_{pit} and i_{corr}.

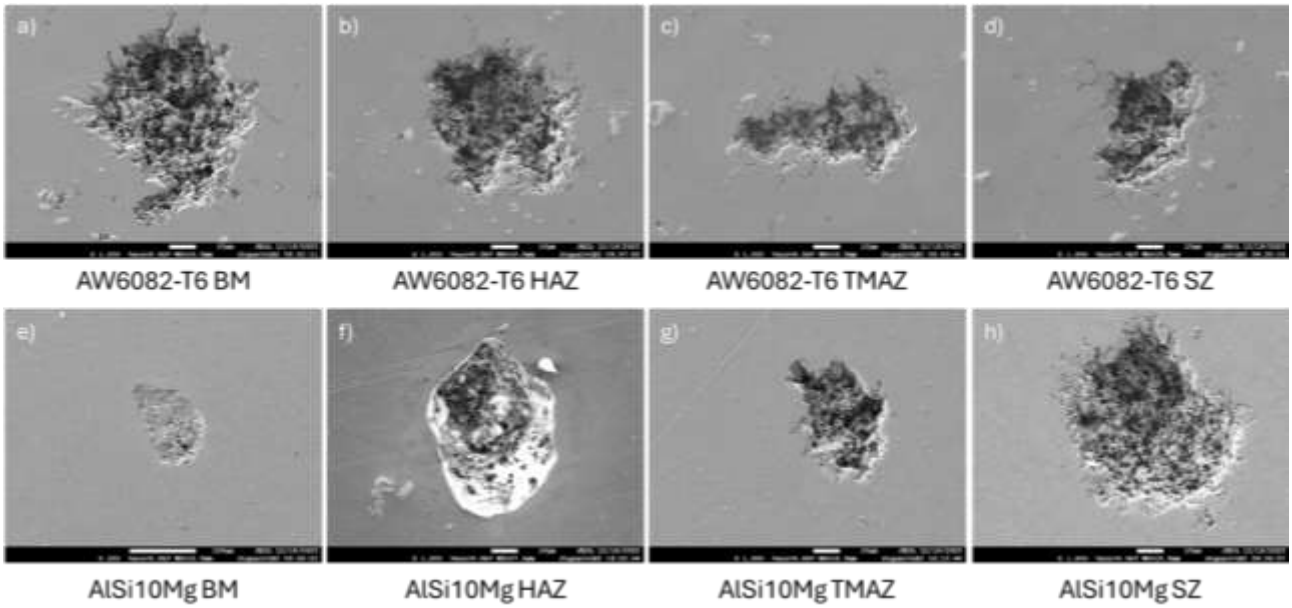

Figure 66 – Morphology of corrosion after potentiodynamic tests in BM, HAZ, TMAZ and SZ performed on (a-d) AW6082-T6 side and (e-h) AlSi10Mg side for the AW6082-T6/AlSi10Mg (L) specimen.

Intergranular corrosion tests performed on FSW joints enabled the identification of any preferential attack paths related to microstructural changes induced by the welding process. No significant intergranular attack was detected on the AW6082-T6 alloy, in line with the known good IGC resistance of Al-Mg-Si alloys [261], while on the AlSi10Mg alloy, variable susceptibility was observed within the weld, both in terms of morphology and depth of attack.

As demonstrated in Figure 67a and Figure 68, the BM AlSi10Mg displays the characteristic inter-melt-pool morphology, which is notably aggressive and deeply penetrating. In this morphology, corrosion occurs in the regions adjacent to the melt pool border and is driven by the galvanic coupling between the α-Al matrix and the Si-rich network along these areas, where the network is more discontinuous [53]. In the HAZ, inter-melt-pool attacks are still observed, with reduced average penetration (Figure 68), but the partial breakage of the Si network and the precipitation of Si-rich phases favour an extension of the attack towards the centre of the melt pools, as illustrated in Figure 67b. In the TMAZ, where the microstructure has been modified by partial dynamic recrystallisation and heat input from welding, the attacks identified show an even lower average penetration and a morphology that evolves from inter-melt-pool to a more similar pitting/localised attack, as demonstrated in Figure 67c. This morphological evolution is consistent with the progressive fragmentation of the eutectic network and with the decrease in the continuity of the galvanic paths along the edges of the melt pools [59].

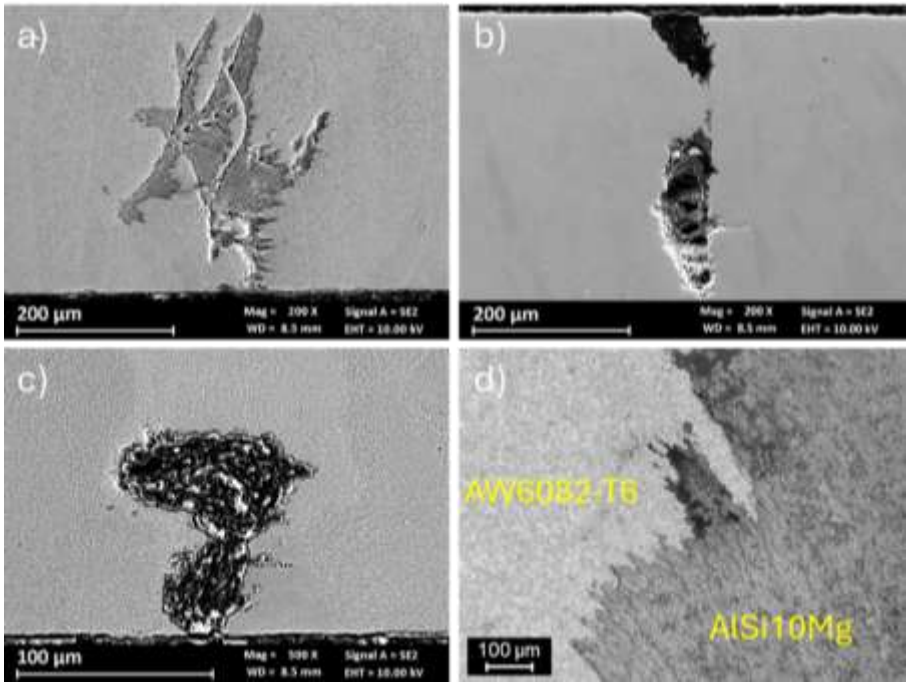

Figure 67 – Low-magnification FESEM images of corrosion attacks in (a) BM, (b) HAZ, (c) TMAZ and (d) optical image of corrosion attack located in the bottom of the SZ on the AlSi10Mg side of the AW6082-T6/AlSi10Mg specimens after IGC test.

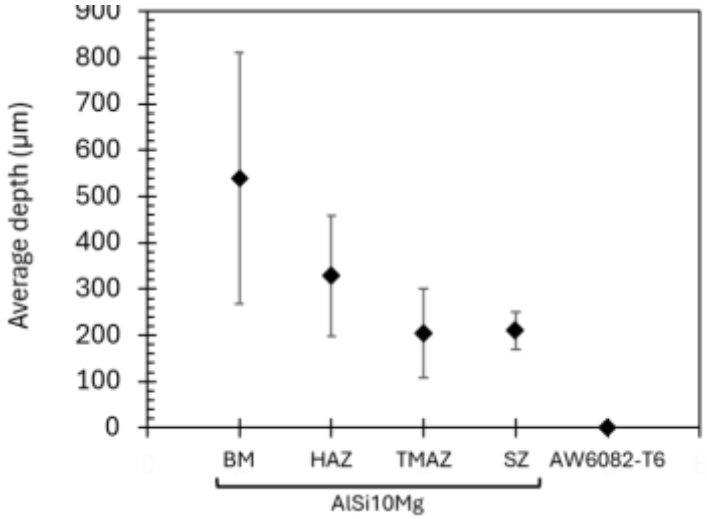

Figure 68 – Average penetration depth of corrosion attacks measured after the IGC test in different zones of the AW6082/AlSi10Mg (L) specimens.

Within the stir zone, severe and deeply penetrating corrosion attacks were observed at the interface with the AW6082-T6 alloy, particularly on the bottom side of the weld, Figure 68. As illustrated in Figure 67d, the weld root surface exhibits a corrosion attack at the interface between AW6082-T6 and AlSi10Mg. Figure 69 presents the cross-section corresponding to the corrosion attack depicted in Figure 67d. It is evident that the occurrence of corrosion has been facilitated by the preferential dissolution of the α-Al matrix, driven by galvanic coupling with the Si-rich precipitates that are characteristic of the microstructure of the SZ on the AlSi10Mg side.

FSW welding has been shown to generate a compression and tensile residual stress field within the weld, both along the welding direction and in the transverse direction, with maximum tensile stresses located in the SZ region [262,263]. As demonstrated by Turnbull et al. [264], in the presence of pits, a tensile stress field has the potential to generate local plastic deformation at the pit boundary, thereby facilitating the transition from a corrosion crater to a small crack. This, in turn results in accelerated growth in an aggressive environment. In accordance with the established principles of stress corrosion cracking [265], where tensile stresses, including residual stresses, have been demonstrated to facilitate environmentally assisted crack initiation and propagation, residual stress fields in welded joints may consequently assume a non-negligible role in the evolution of damage. Similarly, in the case of the FSW welds analysed in this study, it can be hypothesised that the residual stresses present in the nugget contribute, once the corrosive attack has been triggered, to promoting its penetration along the weld. However, in order to clarify the specific role of residual stresses with respect to the microstructure alone, dedicated studies would be necessary. A comparative analysis of the corrosion behaviour of joints in the as-welded state and after appropriate stress-relieving cycles could provide insights into whether and to what extent the relaxation of the internal stress field modifies the extent and depth of selective attack in this region.

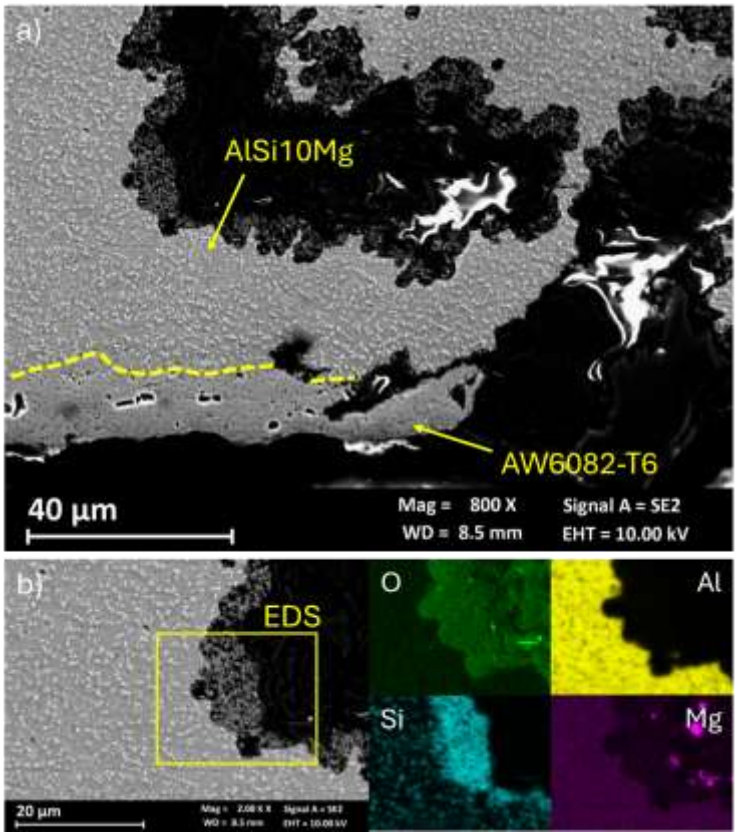

Figure 69 – (a) Low-magnification FESEM image of corrosion attack in the stir zone on the AlSi10Mg side of the AW6082-T6/AlSi10Mg (L) specimen; (b) High-magnification image of the corroded region with corresponding EDS elemental maps.

The present study has demonstrated that friction stir welding is an effective strategy for joining wrought AW6082-T6 and LPBF AlSi10Mg, enabling sound solid-state joints without fusion-related defects such as gas porosity. Furthermore, it has been shown that the adoption of an intermediate S/F ratio results in a relatively high joint efficiency (72%). From a mechanical perspective, the predominant constraint appeared to be the local softening of the wrought alloy. Fracture exhibited a systematic tendency to localise in the AW6082-T6 HAZ/TMAZ region. In this region, the welding thermal cycle has been observed to promote precipitate dissolution, coarsening and a significant decline in hardness. In contrast, the stir zone displayed a refined, equiaxed microstructure on both sides, facilitating load transfer across the nugget and contributing to optimal performance when material positioning enhanced material flow and interlocking. From a corrosion perspective, the joint response was microstructure-controlled: AW6082-T6 exhibited only moderate variations across BM, HAZ, TMAZ and SZ, whereas AlSi10Mg demonstrated a more pronounced loss of passivity and pitting resistance towards the centre of the weld, consistent with the progressive disruption and coarsening of the Si-rich features. Intergranular corrosion tests further indicated that the most critical condition is associated with the AlSi10Mg side, especially in the region near the interface and the weld root within the stir zone. In these areas, micro-galvanic coupling and local heterogeneities can drive deeper attacks. It is evident that, in general, the FSW process is effective in reducing process-induced defects and enhancing joint integrity. However, it is important to note that the mechanical performance of the material is primarily influenced by the softened HAZ of the wrought alloy.

Additionally, the durability of the material may be affected by localised corrosion susceptibility, particularly in the LPBF region and at the interfaces.

5 Prototypes manufacturing

5.1 Design of metal lattice structures for a e-bike frame

In recent years, there has been an increased focus on the integration of lightweight structures in bicycle frame design, driven by the growing demand for high-performance and energy-efficient transport solutions [266]. Lattice structures, particularly those fabricated via additive manufacturing (AM), offer a noteworthy combination of strength, weight reduction, and tunable mechanical properties [267]. These porous architectures offer superior strength-to-weight ratios compared to solid counterparts and are being progressively adopted across the biomedical, aerospace, and automotive sectors [168]. In the cycling industry, research has been conducted into the integration of lattice structures within components such as cranks and forks. The objective of this integration is to enhance the mechanical performance of the components while minimising their weight [268]. However, the integration of this type of structure within a bicycle frame remains restricted. As demonstrated in previous research, the design and the optimization of lattice topologies, such as BCC, FCC, gyroid, and their graded variants, has been investigated, demonstrating the ability to locally tailor stiffness and energy absorption through geometric modifications [267,269].

The present study focused on the design, optimisation and manufacturing of a lattice-structured component integrated into the rear triangle of a bicycle frame. The geometric complexity of the lattice, in conjunction with the inherent limitations of conventional simulation tools, compelled the employment of an approach based on equivalent materials. Modified Young's modulus values were ascribed to the lattice region in order to simulate their expected mechanical properties within the global structural model. The design objective was to achieve a rear dropout displacement that was twice that of the original frame under a standardised loading condition. As discussed in the previous chapters, the AlSi10Mg aluminium alloy was selected for the manufacturing of the integrated component, since it provides an excellent compromise between mechanical properties, corrosion behaviour and strength-to-weight ratio. Furthermore, as the aim of the activity was to produce physical prototypes, it was imperative to select a material that the manufacturing partner could process reliably. AlSi10Mg is one of the most widely used aluminium alloys for additive manufacturing, owing to the consolidation of industrial expertise in its processing [110,270]. Considering these technological constraints and after discussions with the industrial partner, this alloy was selected for the project. The final prototypes were fabricated using LPBF technology in collaboration with Aidro, a company operating in the field of the design and additive manufacturing of aluminium alloy components. This project was conducted within the framework of the GIRO-E flagship initiative, with the objective of designing, developing and integrating structural solutions for two aluminium frames. The primary goal was to enhance the level of comfort and safety through the utilisation of lightweight structures that exhibit a combination of high stiffness and acceptable levels of safety and structural redundancy.

5.1.1 Bicycle frame analysis and design targets

The starting point of this work is a commercial e-bike frame made with aluminium alloy AW6061-T6 used as a reference structure. A finite element analysis (FEA) of this bicycle frame was conducted to understand the deformation mechanisms and stress distribution. The main design goal is to increase the vertical movement of the rear triangle while preserving an adequate safety margin against structural failure. In order to satisfy this goal, during all the FEA simulations the frame was restrained using three types of constraints, reported in Figure 70a. A fixed support at the head tube to restrict all translational and rotational degrees of freedom; a hinge support at the motor and pedal axis to restrict translations while allowing free rotations; and a roller support at the rear axle to permit translation only along the direction parallel to the axle itself. A single loading condition was implemented, comprising two forces of 600 N each, acting on both sides of the rear triangle, Figure 70b.

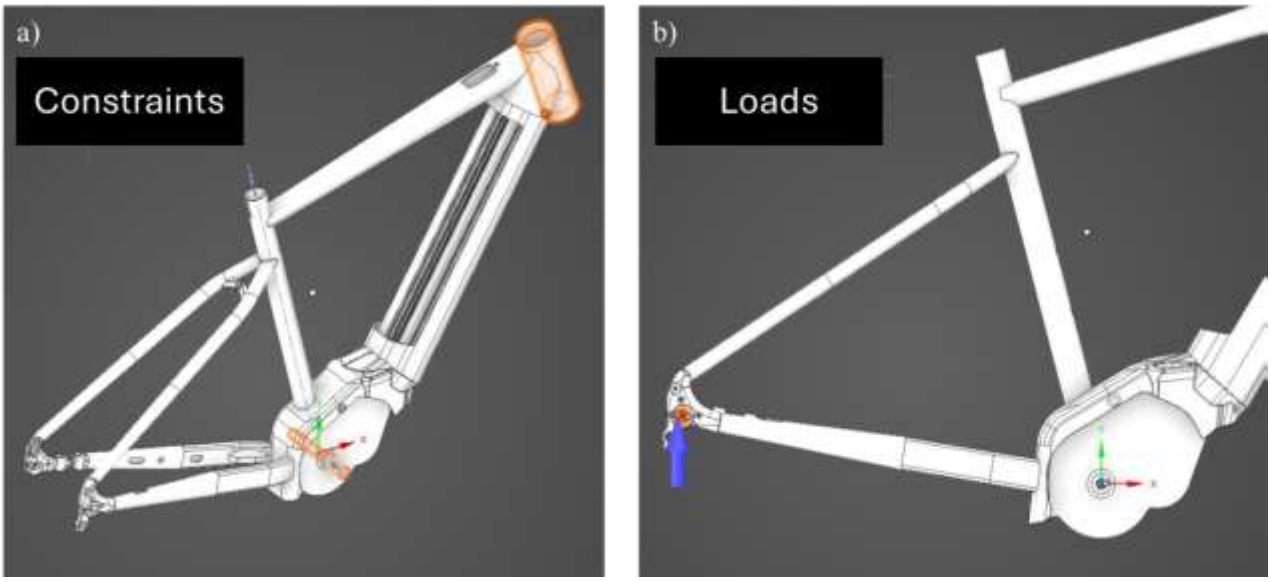

Figure 70 - (a) Constraints and (b) loads setup for the FEA simulations on the original e-bicycle frame.

The results of the finite element analysis, presented in Figure 71, offer a valuable insight into the deformation mechanisms and stress distribution within the frame. The rear hub displays a maximum displacement (δ) at an approximate value of 0.4 mm. Maximum stress concentrations have been observed at the weld joints connecting the rear triangle to the seat tube and to the bottom bracket area, as well as in the proximity of the fastening holes located in the rear wheel hub.

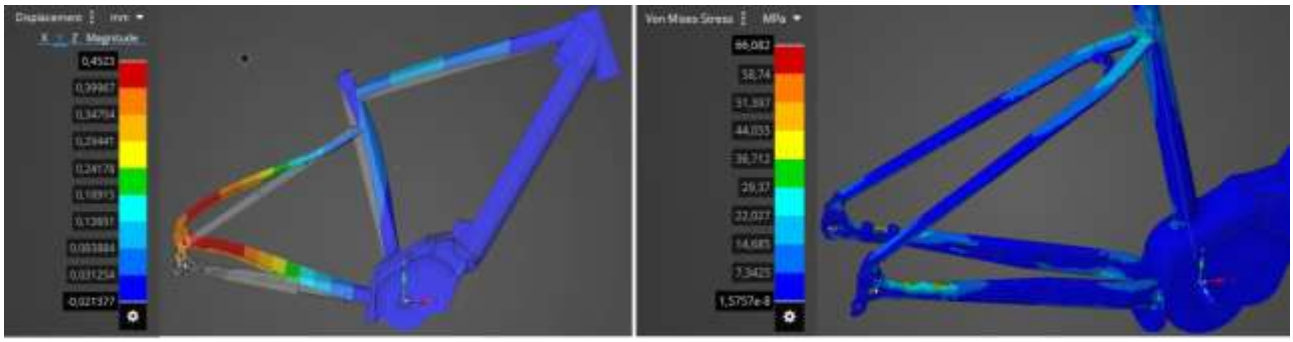

(a) (b)

Figure 71 - (a) Displacement field and (b) Von Mises stress distribution in the original e-bicycle frame.

Considering the findings, the design objective was established to increase the rear hub displacement (target $\delta' = 0.8$ mm) while ensuring the maintenance of acceptable stress levels and a sufficient safety factor. Based on this analysis, a collaborative decision was made to integrate the component with lattice structures within the upper region of the rear triangle, as illustrated in Figure 72.

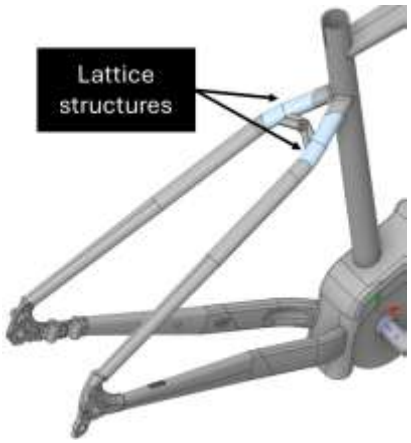

Figure 72 - Detail of the rear triangle highlighting the regions replaced by lattice-structured components.

5.1.2 Lattice structures modelling and material characterisation

Components integrating lattice structures exhibit a highly complex configuration, which necessitates a very fine discretisation and, consequently, a considerable number of finite elements to describe their mechanical properties [155]. Alwattar and Ruiz de Galarreta [142,145] have demonstrated the clear correlation between the mesh density applied and the subsequent error in the predicted elastic properties, with even more pronounced discrepancies when the local stress field is considered. Moreover, the integration of complex lattice-structure models can have a considerable effect on the total computational time. As already discussed in Chapter 3, various approaches have been developed in the literature to overcome the intricate task of fully describing complex geometry while maintaining reasonable computational costs. In this study, an equivalent material approach was adopted in the subsequent FEA simulations. The lattice region, reported in Figure 72, was replaced by a homogenous isotropic material, the effective Young's modulus of which was experimentally

calibrated through mechanical testing of the lattice samples. The FEA performed by Aidro on the original e-bicycle frame revealed a multi-axial and non-uniform stress and strain rate in the rear triangle, with deformation modes that could not be associated with a single dominant load direction. In order to achieve an equivalent mechanical response that is as directionally uniform as possible, a stochastic lattice topology was selected, rather than an ordered structure with struts aligned along specific axes. This particular configuration does not introduce preferred load paths along specific directions and exhibits a mechanical behaviour similar to am isotropic material on a macroscopic scale.

The geometry and topology of the lattice structure were selected in accordance with the findings in Chapter 3. From a technological standpoint, the lattice geometry is constrained by the capabilities of the LPBF process, which require admissible ranges for strut length and strut diameter and, thus, for the achievable relative density and stiffness [271,272]. In the present work, these manufacturing constraints were considered from the design step, so that the lattice geometries explored numerically could be realistically produced. In Chapter 3, several non-periodic lattice geometries were analysed, with particular focus given to architectural configurations representative of the tubes that make up the bike frame. Specifically, cylindrical specimens were produced and characterised, with the lattice structure confined within a circular crown, referred to as H13 specimens. This configuration facilitates the reproduction of the geometry of the tubular components of the frame in a simplified but meaningful way, thereby enabling the analysis of their mechanical behaviour under axial load. The implementation of the Gibson-Ashby model (Figure 35) revealed that, as the unit cell size and strut diameter are subjected to variation, the mechanical behaviour of the lattice structure undergoes a progressive evolution from stretch-dominated regime to a bending-dominated regime. Lattice structures characterised by stretch-dominated behaviour are particularly suitable for applications requiring high structural stiffness, while those with bending-dominated behaviour exhibit a more progressive response, a more stable deformation plateau before densification and greater energy absorption capacity [166].

The aim of this study is to design and manufacture a lattice structure component to be integrated into the frame of an e-bike, with a focus on enhancing user comfort without compromising structural stiffness and safety requirements. In this context, the experimental results obtained on the lattice structures were also analysed within a broader framework for material selection. The mechanical properties of lattice structures tested were mapped onto Ashby diagrams for material selection, as demonstrated in Figure 73. This enabled the positioning of these structures with regard to conventional materials and highlighted their potential as structural solutions. As illustrated in Figure 73a, the configurations analysed exhibit an elastic modulus that is approximately one order of magnitude lower than that of the bulk materials commonly used for the fabrication of bike frames. Conversely, in the strength-density diagram in Figure 73b, the lattice structures analysed are aligned with traditional bulk materials along the strength-to-density design guideline commonly adopted for lightweight design. This finding underscores the capacity of these configurations to maintain a favourable strength-to-weight ratio, comparable to that of conventional materials, despite the observed reduction in elastic modulus. From a design standpoint, using a solution with a lower elastic modulus than conventional materials can be advantageous in the specific case under consideration. It can be assumed that a reduction in stiffness would result in an increase in the vertical travel of the rear triangle. This has the potential to enhance the damping of ground-induced vibrations, thereby improving user comfort, while maintaining structural integrity thanks to adequate mechanical

strength. It is important to note that the introduction of these lattice structures does not seek to replace any existing suspension system but aims to locally adapt the structural response of the frame.

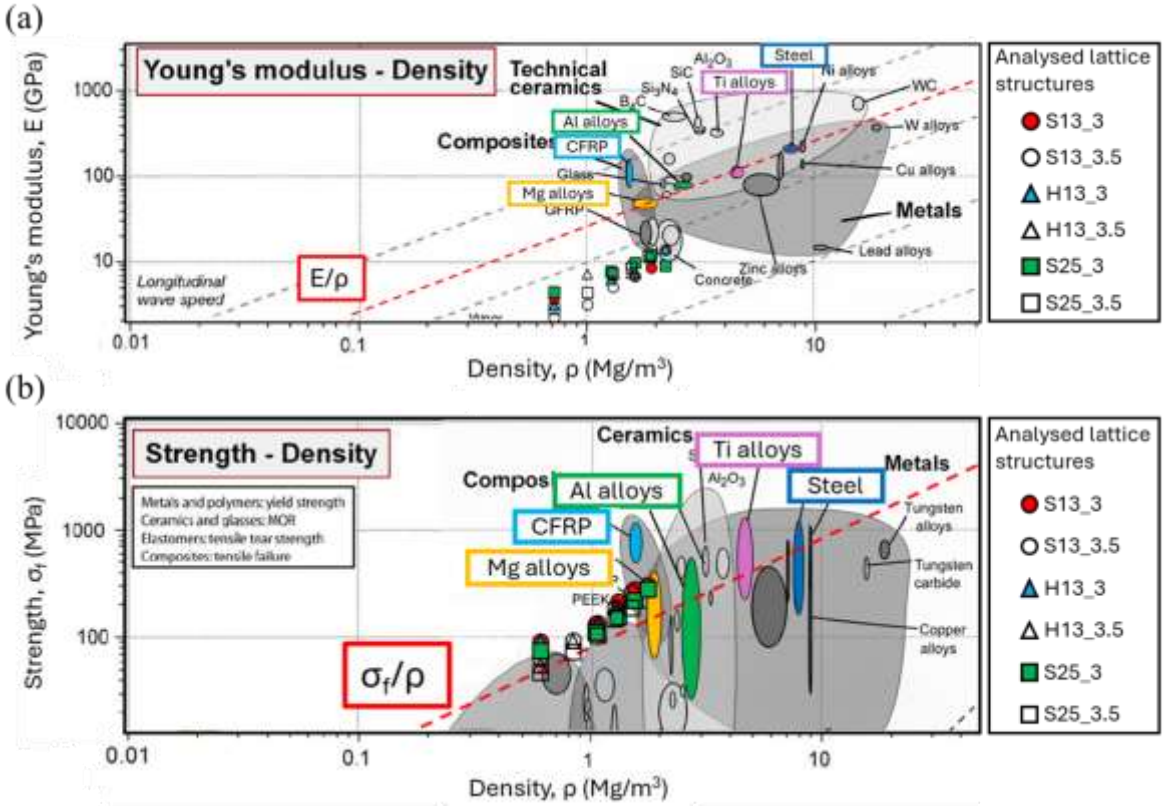

Figure 73 – Ashby charts of (a) elastic modulus, E, and (b) strength, σ, as a function of density for the non-periodic lattice structures compared with bulk materials.

In this study, the Gibson-Ashby model, when combined with Ashby diagrams, was a fundamental tool for understanding the mechanical behaviour of non-periodic lattice structures and for selecting the most suitable configurations based on the requirements of stiffness, strength and structural efficiency in terms of weight reduction.

Considering the aforementioned requirements, a completely stretch-dominated lattice structure would guarantee high stiffness but would be less effective in terms of damping stresses and would demonstrate a lower capacity to sustain damage or collapse. Conversely, a purely bending-dominated lattice structure would offer greater damping capacity, but the overall stiffness of the component would be compromised. Taking these factors into consideration, the lattice structure configuration that has been identified as the most suitable by the analysis described in Chapter 3 is H13_3_0.70, a non-periodic lattice structure characterised by a unit cell size of 3 mm and a strut diameter of 0.70 mm. This configuration has an equivalent elastic modulus of approximately 3.0 GPa and a yield strength of approximately 90 MPa. As demonstrated by the analysis performed with the Gibson-Ashby model (Figure 35), this lattice structure displays mechanical behaviour that is intermediate between stretch-dominated and bending-dominated regimes. This theoretical finding satisfies the requirements of stiffness, damping capacity and safety that are essential for this application.

During the initial design iteration, the lattice integration was confined to the replacement of two tubular segments with a single lattice structure element, whilst preserving the original frame geometry, as reported in Figure 74.

The material model described above was then employed to assign the measured elastic modulus to the lattice region in the finite element model. A new FEA was conducted, employing the same loading and boundary condition that were applied to the “as is” frame. The findings demonstrated an increase in rear dropout displacement in comparison with the original configuration. Nevertheless, the target value of 0.8 mm was not attained, and the overall response of the rear triangle remained overly rigid.

Figure 74 - First design iteration of the lattice structure component.

Given that the lattice parameters could not be subjected to further modification due to technological limitations intrinsic to the LPBF process, and in accordance with the conclusions of Aidro, it was established to act on the component geometry to achieve the desired deformation. The geometry of the lattice component was progressively modified following an iterative FEA-driven approach. Firstly, the length of the lattice region along the rear triangle was increased. The new geometry was defined by following the main load paths identified on the original frame. This consists of two independent lattice sub-regions with different mechanical properties, which are engineered to guide the deformation in the desired direction. This approach involved the introduction of two lattice zones, characterised by distinct relative density and equivalent stiffness, as shown in Figure 75. For the outer region, where the stress level is lower, the same lattice configuration used in the first iteration was maintained. The inner region, located in closer proximity to the main load transfer paths, was designed with a stiffer lattice configuration with the aim of controlling local strains and ensuring sufficient stiffness. In this zone, the lattice structure H13_3_1.00 with strut diameter of 1.00 mm, unit cell size of 3.0 mm, relative density of 0.61, equivalent elastic modulus of 7.0 GPa and yield strength of 182 MPa was adopted. In order to enhance the components compliance, an elliptical notch was introduced on the outer side of the component, as reported in Figure 75b.

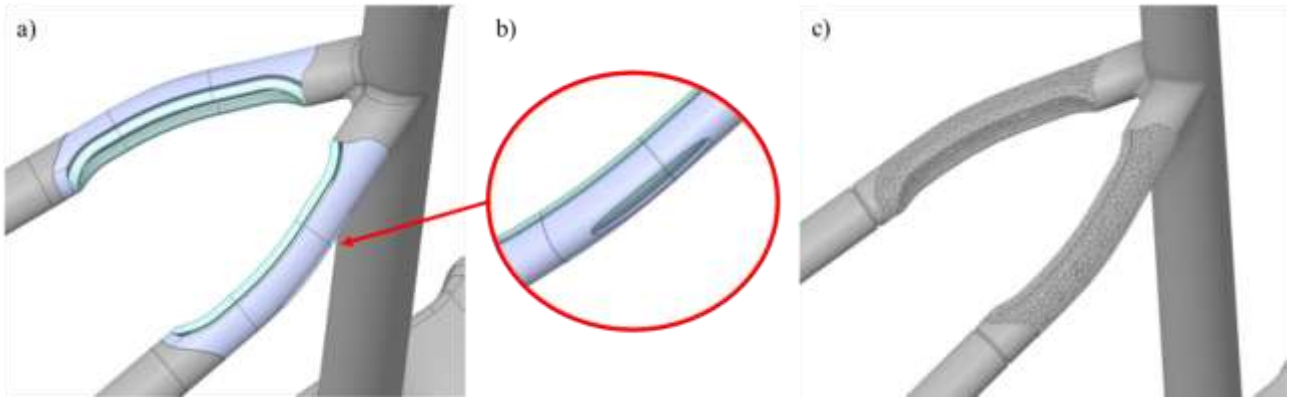

Figure 75 - CAD model of the lattice component: (a) final design with two regions of different stiffness; (b) detail of the external notch; (c) final design with stochastic lattice structures integrated into the component.

The final configuration achieved a rear axle displacement of about 0.8 mm, twice the deformation of the original frame, while keeping the maximum stresses confined within the lattice component, as shown in Figure 76. As demonstrated in Figure 76b, the stresses in the modified rear triangle increase in comparison to the original configuration, with peak Von Mises values of approximately 60 MPa in the outer lattice region and around 80 MPa in the inner region. When these values are compared with the experimentally determined yield strength of the corresponding lattice configurations, safety factors around 1.5 and 2.3 are obtained for the outer and inner regions, respectively, confirming a sufficient margin against yielding.

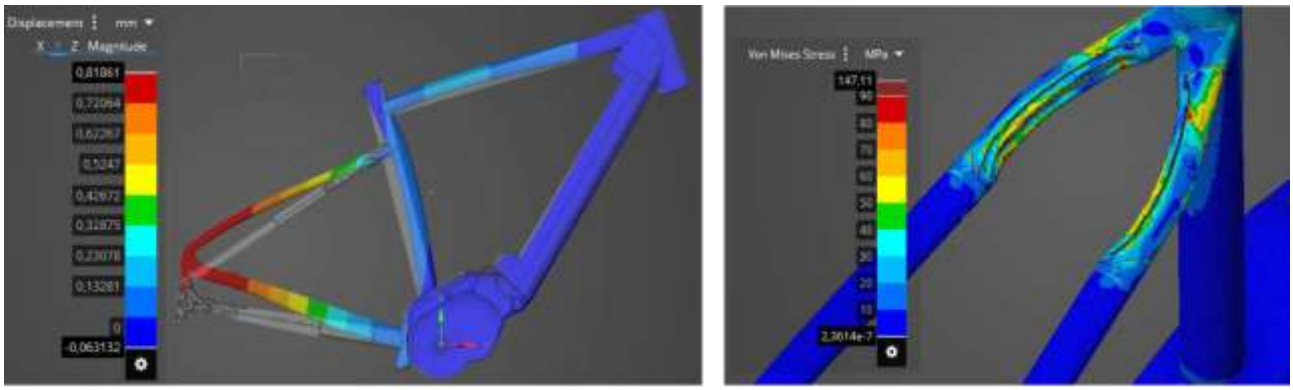

Figure 76 - (a)Displacement field of the frame with the lattice structures integrated and (b) Von Mises stress distribution within the lattice component.

5.1.3 Proof-of-concept manufacturing and experimental validation

The aim of the proof-of-concept phase was to demonstrate the reliability of the manufacturing process for the lattice-integrated component, its successful integration with a conventional aluminium frame, and its operational performance under realistic service conditions. Subsequent to the definition of the final geometry of the lattice element, a series of functional prototypes was produced in AlSi10Mg alloy. The components were manufactured on an EOS M290 Dual Mode LPBF system, employing a layer thickness of 30 µm, an argon atmosphere, and the baseplate was maintained at 165

°C throughout the build in order to limit residual stresses. The chemical composition of the feedstock powder is reported in Table 20.

Table 20 - Chemical composition (wt.%) of the feedstock powders.

Element (wt.%)	Al	Si	Mg	Cu	Mn	Fe	Ti
AlSi10Mg	Bal.	10.3	0.36	< 0.01	< 0.01	<0.15	< 0.01

Figure 77 shows the build layout of the lattice insert and the as-built component after removal from the powder bed.

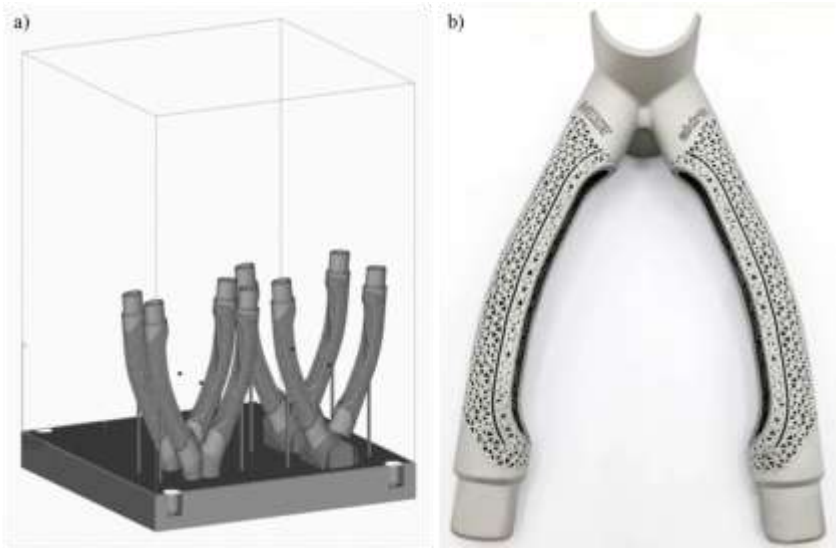

Figure 77 - (a) Build layout of the final lattice-integrated components on the LPBF build plate and (b) as-built AlSi10Mg lattice components.

Subsequent to the availability of the initial lattice components, the focus of the project shifted to their integration into the bicycle frame. Gas Tungsten Arc Welding was selected as the joining process because it is widely used for fabrication of aluminium bicycle frames and was specifically recommended by the frame manufacturer, based on their established experience and existing production practices. In this scenario, the joint does not consist of two conventionally extruded or drawn tubes of the same alloy, but rather a hybrid configuration: an LPBF AlSi10Mg component welded to a frame in AW6061-T6 produced by traditional processes. In order to achieve the maximum benefits of additive manufacturing in structural applications, it is essential to develop a reliable method of joining AM parts to conventionally manufactured components. This hybrid approach enables new design possibilities but also introduces additional metallurgical, mechanical and corrosion-related challenges, due to differences in composition and microstructure between the LPBF and wrought materials. In order to investigate the weldability of LPBF AlSi10Mg component to AW6061-T6 tubes, three full-scale functional prototypes of the lattice structure were produced. The joining process that was adopted was GTAW, using an ER5356 aluminium filler wire. Each functional prototype was utilised to compare three welding strategies: continuous GTAW, pulsed GTAW at 80 Hz, and pulsed GTAW at 100 Hz. The initial peak current was set to 140 A. Since the

welding process was performed manually with a foot pedal, the current was adjusted by the operator during the process. After arc ignition, where the current typically reached 120-140 A, it was progressively reduced along the weld bead, resulting in an estimated average current of 90-100 A. An example of a welded prototype used for hybrid LPBF AlSi10Mg/AW6061-T6 weldability assessment is shown in Figure 78a. To accurately simulate the final frame conditions, the lattice insert was welded to tube segments with the same geometry and thickness as the actual rear-triangle elements.

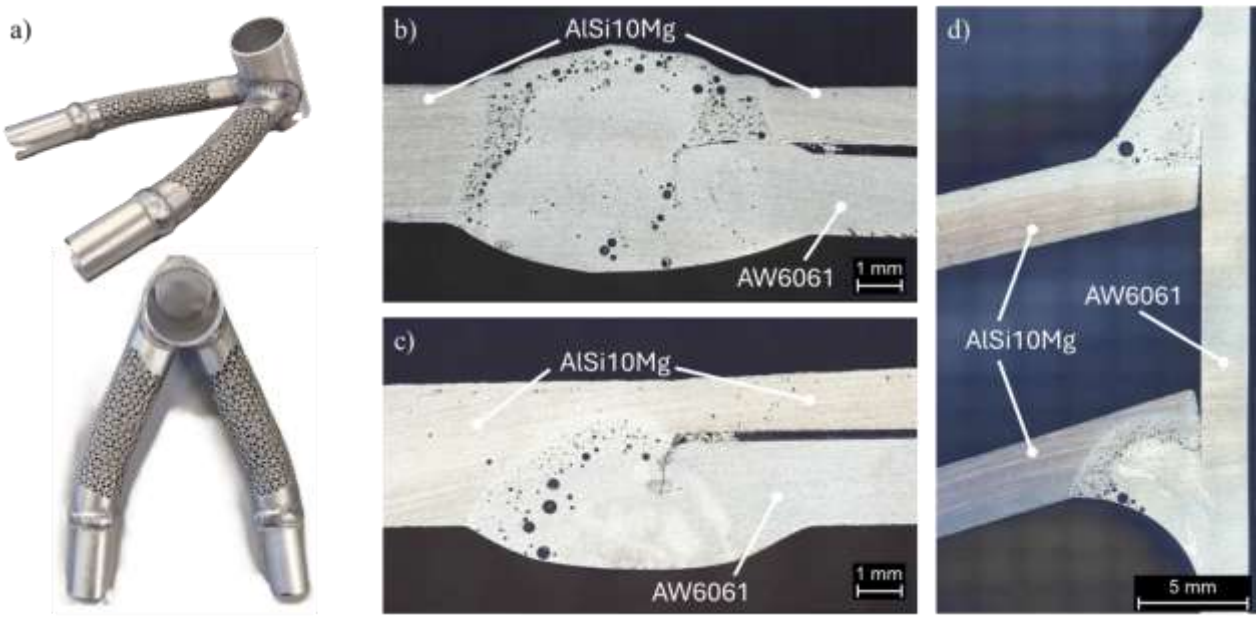

Figure 78 - (a) Prototypes used to assess weldability between LPBF AlSi10Mg components and AW6061 tubes; metallographic cross-sections of the weld bead produced using (b) continuous GTAW, (c) pulsed GTAW at 80 Hz and (d) pulsed GTAW at 100 Hz.

The initial welding campaign revealed a significant issue related to extensive porosity observed within the weld bead. The cross-sections of the weld bead, reported in Figure 11b,c,d, highlighted the presence of porosity in all of the investigated welding techniques suggesting that the combination of alloy pair, process parameters and as-built LPBF microstructure necessitated further optimisation. This pronounced porosity highlighted the need for a more systematic study of hybrid welds between LPBF and conventionally manufactured aluminium alloys. Based on the findings discussed in the Chapter 4.3.1, to reduce the porosity within the weld bead, it was necessary to perform a solution heat treatment at 530°C for 6 h on the AlSi10Mg component. This heat treatment at high temperature led to the reduction of hydrogen content in the AM part, resulting in significantly less porosity in the weld bead. Based on the expertise of the frame manufacturer, the components were integrated into the frame using a pulsed GTAW at 80 Hz. The optimised welding procedure was employed to manufacture one complete frame incorporating a lattice-integrated rear triangle, as illustrated in Figure 79.

Figure 79 - (a) Prototype frame with the lattice structure component integrated into the rear triangle, (b,c) close-up views of the AlSi10Mg insert and (d) presentation of the prototypes during the Giro-E 2024 event.

This prototype was assembled using standard components and presented during the GIRO-E 2024 event, a flagship initiative of the MOST project. The prototype served a dual purpose: firstly, it demonstrated the design concept, and secondly, it was used as test vehicle for preliminary validation in service through road testing in real riding conditions, reaching approximately 60 km. Subsequent to the road test, the lattice structure component exhibited a substantial permanent deformation with respect to the initial profile, as illustrated in Figure 80a. It is particularly evident that the component profile deviates significantly from the original geometry, thus indicating that the structure underwent a severe global plastic deformation. Two damaged regions are visible within the lattice, both located in the outer region of the component, where cracks are clearly detectable by visual inspection, Figure 80b-e. As aforementioned, this outer region corresponds to the least stiff part of the component, which is intentionally designed to provide enhanced local deformability, Figure 75. The upper crack fully intersects the component cross-section, resulting in a through-thickness fracture (Figure 80c,d), whereas the lower crack appears shorter and does not propagate through the entire thickness, Figure 80e. Therefore, it can be reasonably hypothesised that the damage initially occurred in the upper region, where the design stress level is the highest. The progressive loss of stiffness associated with this initial fracture subsequently promoted the initiation of a secondary crack in the lower part of the component.

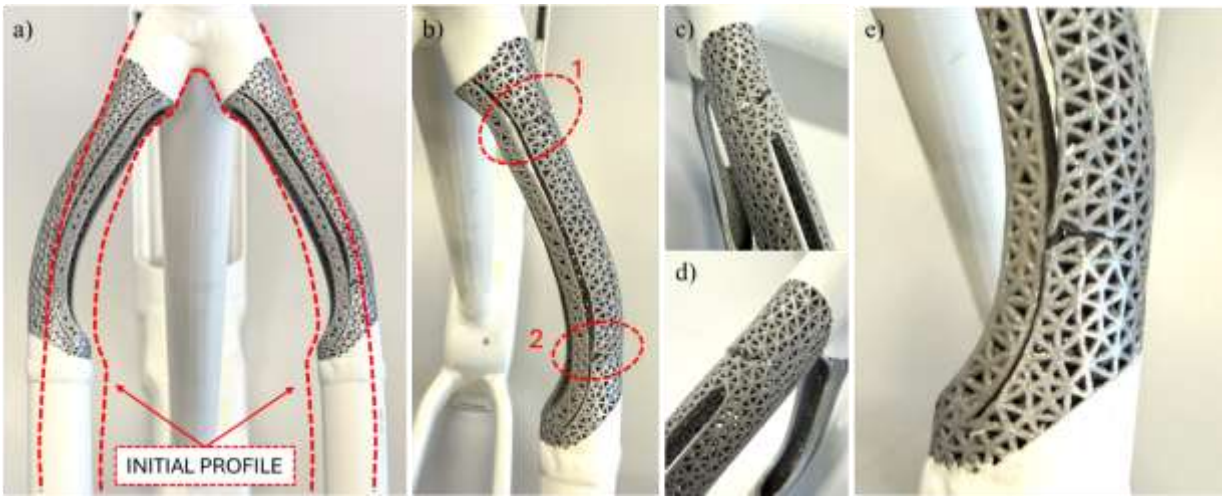

Figure 80 – (a) Bike frame after the road test, showing permanent deformation of the lattice component, (b) damage regions identified in the right rear lattice, (c,d) through-thickness crack in the upper part and (e) non-through crack in the lower region of the component.

In order to investigate the collapse mechanism in more detail, the component was sectioned and removed from the frame, thus allowing the fracture surfaces to be examined by scanning electron microscopy, as illustrated in Figure 81 and Figure 82. These analyses demonstrate that fracture propagated progressively through the struts, along the strut-nodes interface and also through nodes of the lattice. This finding is in agreement with the literature on lattice structures subjected to cyclic or combined loading conditions. Experimental studies on octet-truss lattices demonstrate that, in the presence of an initial defect, damage initially localises in the most highly stressed struts ahead of the crack tip, which fail progressively layer by layer. Furthermore, crack propagation can also involve the nodes when a connection is necessary between regions experiencing high local deformation [273,274]. The precise site of crack initiation remains indeterminate. Following the initial cracking, the frame was utilised for a considerable distance, likely resulting in persistent friction between the fracture surfaces and substantial damage to their original morphology, as illustrated in Figure 82b. However, some relatively intact areas (Figure 82a) exhibit a dimpled morphology, which is consistent with a predominantly ductile fracture mechanism of the struts.

A comparison between the stress field as predicted by the finite element method model (Figure 76b) and the experimentally observed location of the main crack (Figure 81) demonstrates a strong correlation. The through-thickness fracture in the upper part of the component developed precisely in the region characterised by the maximum Von Mises stress within the outer lattice, according to the adopted loading scheme. This finding indicates that the numerical model and the static loading conditions employed during the design phase are capable of realistically depicting the stress distribution under service conditions, despite the fact that the variable and cyclic nature of real road loads is not explicitly reproduced. It is evident from the finite element model that a maximum stress of approximately 60 MPa is obtained in the outer lattice. The experimental investigation, encompassing compression tests on lattice specimens, yielded a yield strength of approximately 90 MPa and an equivalent Young's modulus of about 3 GPa. This resulted in a static safety factor of around 1.5. The experimental observation of fracture thus indicates that the component's actual strength was lower than the estimated value during the design stage. This discrepancy may be attributed to the solution heat treatment applied prior to welding, which has been demonstrated to

markedly reduce the yield strength of AlSi10Mg in comparison to its as-built condition. Bisht et al. [275], demonstrated that a solution treatment carried out at temperatures of approximately 505 °C for a duration of 4 hours resulted in a significantly reduced yield strength, approximately of 140 MPa, compared to 240 MPa of the as-built state. A similar degradation of mechanical properties can therefore be expected for the lattice structure component.

A further critical aspect is the presence of large pores within the struts, which are clearly visible in Figure 81b and Figure 82a. The observed pores have diameters of approximately 100 µm, in comparison to a nominal strut diameter of around 700 µm. Defects of this size, which are compatible with either lack-of-fusion or keyhole porosity, as is typical of LPBF AlSi10Mg, have been shown to significantly reduce both fatigue resistance and local tensile strength [276,277]. The combined effect of reduced load-bearing cross-section and stress concentration around pores thus represents a preferential site for crack initiation.

Furthermore, FESEM observations demonstrate that the external surface of the lattice is fully covered by paint, while the internal surfaces, which were not reached by the coating, exhibit a significantly rougher surface finish (Figure 81). The high surface roughness may have initiated crack formation at geometric notches or surface defects, thereby facilitating progressive damage propagation through the struts and nodes of the lattice structure.

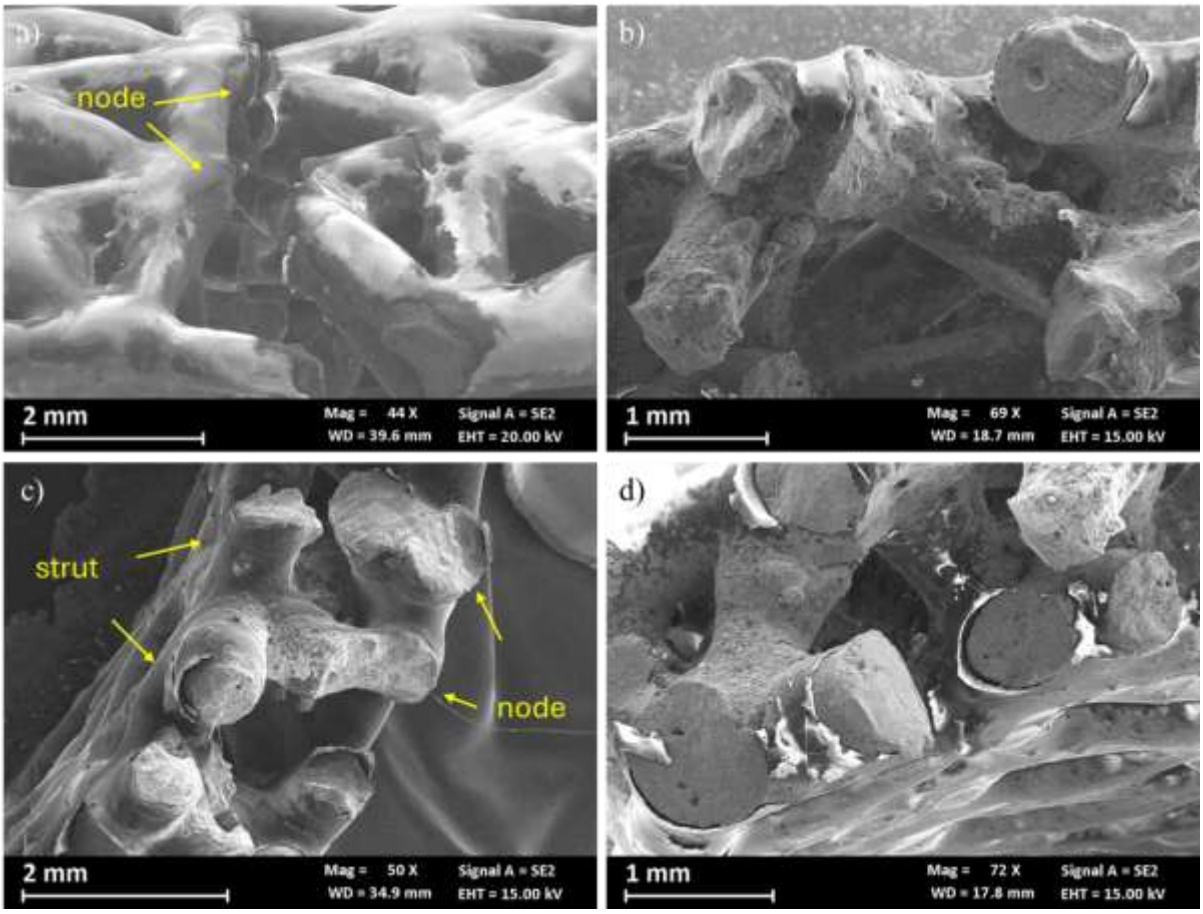

Figure 81 – Low-magnification FESEM images of the fracture surfaces within the lattice.

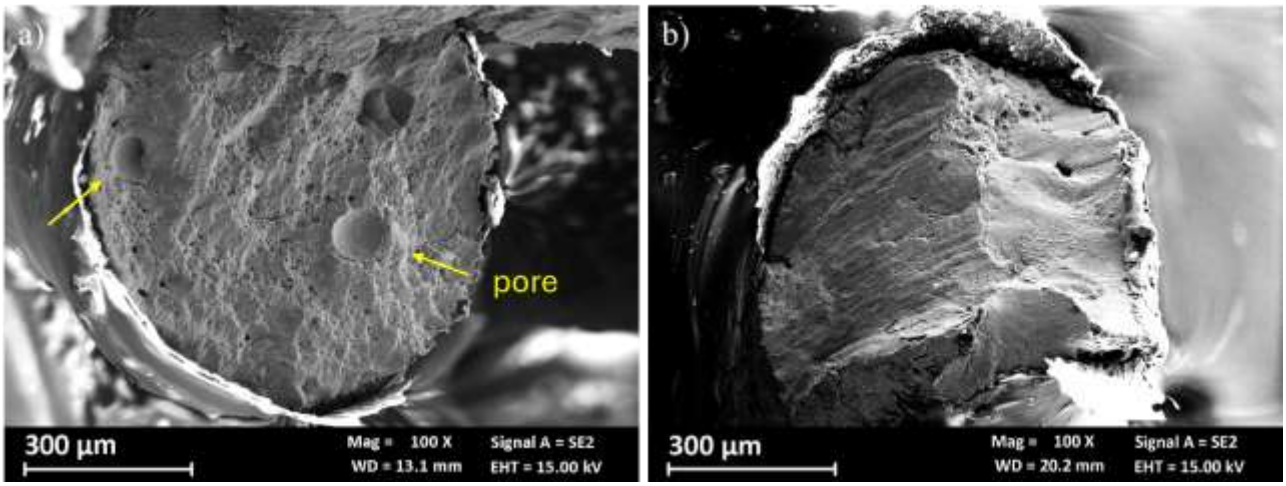

Figure 82 – Low-magnification FESEM images of fractured struts with (a) internal pores and (b) damaged fracture surface.

The present study has confirmed that LPBF lattice structures can be successfully integrated into an aluminium e-bike frame. Furthermore, the equivalent-material design approach has been shown to be capable of reproducing the main deformation mechanisms observed in service, including the localisation of maximum stresses in the outer lattice region. Concurrently, the premature failure of the lattice insert following road testing emphasised the vulnerability of the component to process-induced defects and post-processing treatments, such as solution heat treatment and welding. These treatments have been shown to significantly reduce the strength of AlSi10Mg in comparison to the as-built condition, as highlighted in Chapter 3, and to amplify the detrimental effect of internal porosity and surface roughness. The findings emphasise the necessity of meticulously characterising lattice structures in not only their as-built state but also following the employment of representative thermal cycles and joining processes. This approach is pivotal in ensuring the acquisition of design data that accurately reflects in-service performance.

5.2 Removable functional joints for modular frames

Technological development continues to have a profound impact on the manufacturing sector, with additive manufacturing being a particularly pivotal factor in this transformation. The AM process, which involves the layer-by-layer deposition of material, exhibits significant potential in promoting sustainability. This is due to its ability to facilitate the development of material-efficient designs, the creation of lightweight structures, and the implementation of on-demand production across a range of industrial sectors [17,278]. Among the various AM processes, such as binder jetting, directed energy deposition and material extrusion, Laser Powder Bed Fusion (LPBF) is one of the most widely adopted and versatile, especially when combined with lightweight alloys such as aluminium alloys [22]. New design paradigms, such as Design for Additive Manufacturing (DfAM), generative design and topology optimisation, are fundamental tools to fully exploit the advantages of AM, and in particular of LPBF technology. These approaches facilitate the enhancement of the design process, enabling the creation of complex geometries and sophisticated internal features that would be difficult or impossible to obtain with conventional manufacturing techniques [279,280]. For example, Topology Optimisation (TO) is a numerical method that determines the optimal material distribution within a given design domain, under prescribed loads and boundary conditions. The aim

of this process is to maximise performance while minimising the amount of material used [281–283]. The enabling of highly efficient load paths, in conjunction with the removal of unnecessary material, has been demonstrated to directly support the development of more sustainable components. Consequently, AM technologies such as LPBF, when employed in conjunction with DfAM methodologies, offer a compelling approach to reducing the environmental impact of industrial manufacturing. This is achieved by decreasing material consumption, facilitating part consolidation and prolonging product lifetimes [284,285]. Previous studies in the bicycle sector have demonstrated that the application of DfAM and TO to frame components and accessories results in highly efficient, lightweight structures that meet mechanical and functional requirements while exploiting the freedom of AM processes [19,286,287].

In recent years, in parallel with these design paradigms, the bicycle industry has witnessed a growing demand for vehicles that can be more easily integrated into public and private transport systems, with reduced volume and weight to facilitate intermodal mobility. In urban contexts, intermodal mobility typically combines walking, public transport and active modes such as cycling, enabling door-to-door journeys where bicycles, including folding or separable bikes, act as a flexible solution within a wider public transport network [288]. Currently, the market offers a wide range of solutions, including folding frames with hinges and multi-axis joints, as well as separable frames that can be divided into multiple sections by means of mechanical couplings. These architectures offer several advantages, including compactness, which enhances convenience for domestic storage and ease of transportation on public transport, and reduces the risk of theft, as the bike can be more readily transported within buildings. However, the integration of hinges, couplers and detachable interfaces introduces significant challenges, including an increase in weight due to local reinforcements, potential loss of global frame stiffness and alignment, and additional maintenance requirements for the folding mechanisms. Furthermore, in numerous commercial solutions, the arrangement of electrical wiring and hydraulic brake lines across the joints is managed externally or with limited integration, thereby affecting the overall aesthetics, aerodynamics and ease of assembly/disassembly.

The work presented in this chapter follows a different approach to frame disassembly, based on functional modular joints specifically designed for additive manufacturing. In collaboration with industrial partners specialising in the manufacture of bicycles and metal AM, the activity focuses on the design and production of a frame that can be divided into two sections by means of removable joints in AlSi10Mg produced via LPBF, while maintaining the stiffness and safety levels of the reference monolithic frame. A notable feature of these joints is the implementation of supplementary functionalities that exceed those of conventional commercial couplers. The lower joint is equipped with a hydraulic connector and a electrical interface, allowing for the automatic coupling of the rear brake system and the motor-controller wiring during the frame assembly process. This approach serves to minimise the operational demands for the user, while ensuring the continuity of internal management. The employment of additive manufacturing facilitates the integration of structural and functional characteristics within a singular, optimised component, thereby enabling the development of modular joining systems that overcome the limitations currently exhibited by folding and separable bicycles. This advancement enhances both functionality and aesthetic appeal, while facilitating integration.

5.2.1 Reference frame and joints requirements

The modular joint system was developed for an aluminium gravel frame supplied by one of the partner companies within this project, Dedacciai, an Italian leader in the manufacture of bicycle frames and components. The frame features a conventional gravel frame geometry and is manufactured from AW7020 aluminium alloy (Figure 83a). The division points of the frame were selected with the aim of optimising the size of the two sections and minimising the overall envelope of the disassembled bicycle, thereby ensuring optimal ease of transportation. Figure 83b provides a visual representation of the selected cut locations on the frame, and the corresponding installation of the joint system. This configuration was selected to minimise the packed volume while maintaining the original riding geometry. As demonstrated in Figure 83b, the chosen joints locations allow a reduction of the expected filled volume of the bicycle of about 46%. From a functional standpoint, the joints had to facilitate the rapid disassembly and reassembly of the frame using standard portable tools. The coupling and decoupling operations were required to be intuitive, with a minimal number of steps and no loose components that are not permanently attached to the frame.

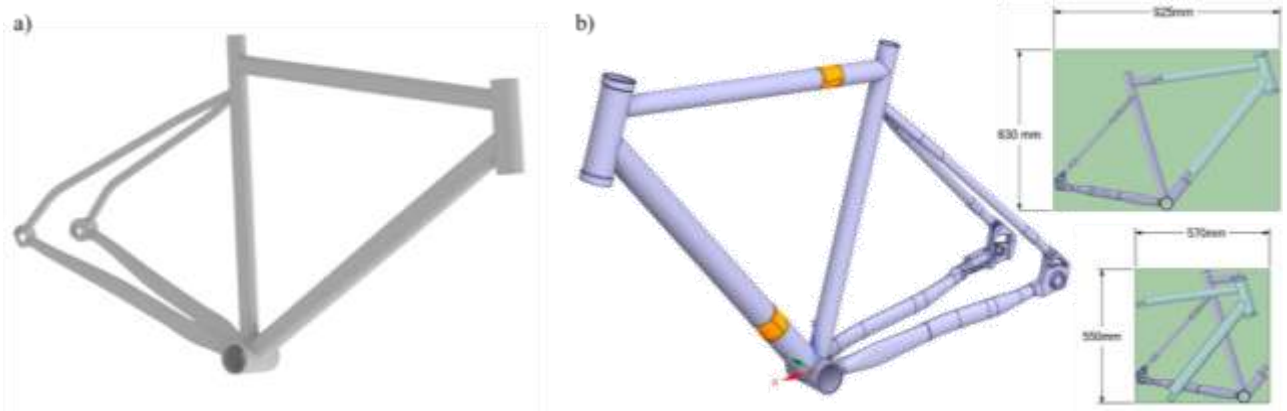

Figure 83 - (a) Original aluminium gravel frame supplied by Dedacciai; (b) frame equipped with the modular joints and corresponding reduction of packed volume.

The joint system was required to ensure the repeatable alignment of the two frame halves, thus preventing movement and noise at the interfaces during riding and preserving the nominal frame geometry after multiple assembly and disassembly cycles.

Moreover, in order to produce a prototype that is legally rideable on public roads, the requirements on the braking systems had to be considered. In accordance with the regulations stated in the Italian Highway Code (art. 68) and its implementing regulation (art. 223), it is mandatory for a bike to be equipped with two distinct brake devices, with one device for each wheel, capable of acting promptly and effectively on the respective wheel. This requirement entails the integration of control and transmission systems that facilitate active braking mechanisms, typically through mechanical or hydraulic connections. In order to comply with this constraint, it is necessary to integrate a hydraulic connector within the joint system. Furthermore, an electrical connector is necessary for the transmission of data and power between the rear hub motor and the handlebar-mounted control unit. Placing a joint on the down tube provides sufficient space for the integration of these connectors while keeping the external diameter aligned with that of the original tube and allow the user to separate and re-connect the frame without bleeding the brake system or handling external cables. From a structural perspective, the joints were engineered to maintain the global stiffness and safety, aiming for equivalent performance to that of the original frame.

5.2.2 Design of the joint system

Subsequent to the selection of the locations of the joining systems on the frame, and in accordance with the frame manufacturer and the company responsible for the design and production of the joints, the geometric constraints associated with their installation were defined. The aforementioned constraints are concerned with the interference-fit diameter, the axial length of this diameter required to facilitate joint installation, and the need to match the outer diameter of the joint with that of the frame tubes.

The joint architecture consists of a vertically dismountable component which is composed of two halves that are clamped together by a bolt acting on inclined contact surfaces. When torque is applied to the bolt, the inclined planes convert the axial preload into a transverse clamping force, as illustrated schematically in Figure 16. This brings the two halves into firm contact, eliminates any clearance at the interface and restores the frame stiffness at the joint location. By addressing the aforementioned functional and structural requirements, the final joint design fulfils all the necessary criteria.

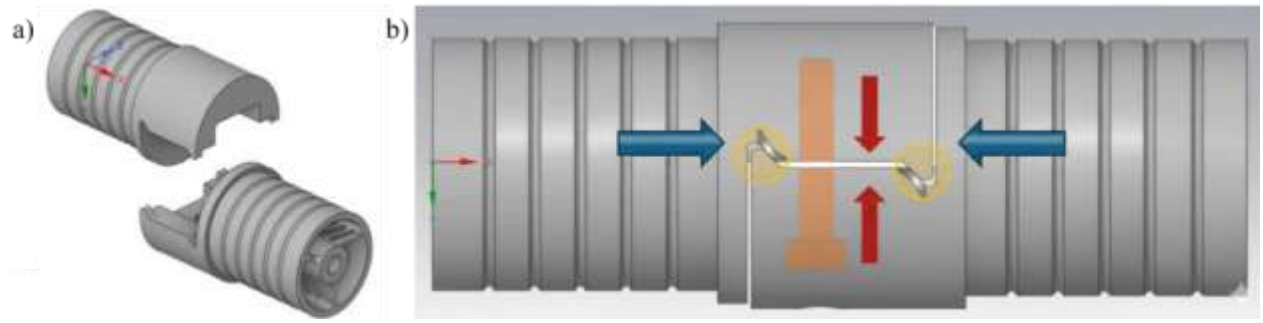

Figure 84 - (a) Vertical disassembly concept and (b) representation of the inclined surfaces that transform the axial force into a transverse clamping action.

The configuration of the hydraulic interface was dictated by the necessity to disengage and then re-engage the frame segments without compromising the integrity of the braking system, whilst simultaneously ensuring the prevention of oil leakage or air infiltration during the repeated cycles. In order to achieve this objective, the female component of the connector was derived from a commercial quick-connect component, whereas the male component was redesigned to be fully integrated into the joint body and compatible with the available space and manufacturing constraints. The electrical connector was positioned alongside the hydraulic path, in a dedicated compartment that ensured proper alignment and shielding, allowing the simultaneous mechanical, hydraulic and electrical coupling of the two frame sections during joint closure.

The design choices result in a modular joint that not only restores the structural continuity of the frame, but also consolidates multiple functions, such as mechanical connection, hydraulic brake continuity and electrical signal transmission, into a single integrated component specifically designed for additive manufacturing.

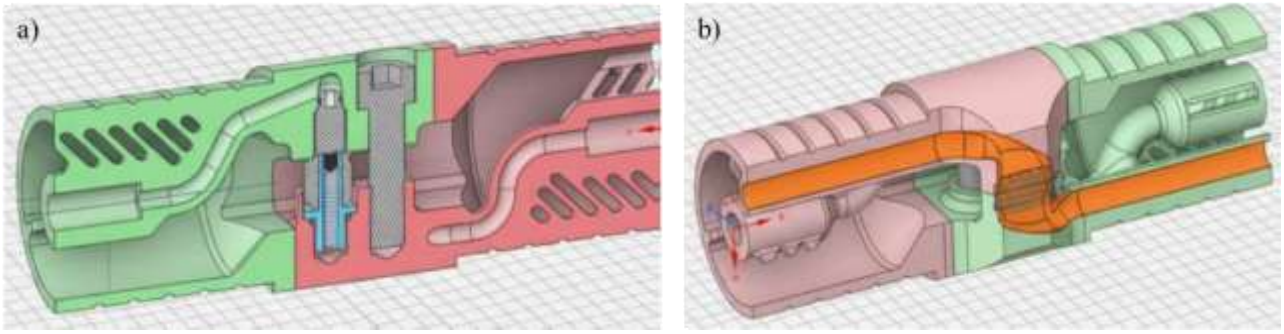

Figure 85 - Cross-section of lower joint showing the internal routing of the (a) hydraulic and (b) electrical connectors.

5.2.3 Finite Element Analysis

The computational design and validation of the joint system was conducted in collaboration with Aidro, which was responsible for the development of the finite element analysis (FEA) and for the execution of the simulations. The University of Bergamo contributed to the interpretation of the numerical results and to the definition of the key parameters to be investigated experimentally.

As previously stated, the aim of the design was to integrate the joints on the frame while ensuring the safety and stiffness of the original configuration. In order to achieve this objective, a preliminary finite element analysis was conducted on the original frame, with the frame virtually cut at the locations designated for the installation of the joints. Two inserts with the same geometry as the original tubes were modelled at these sections, so that the contact pressures along the interfaces between frame and inserts could be evaluated and later used as boundary conditions for designing the real joint (Figure 86a). In order to simulate the behaviour of the frame under load, appropriate boundary conditions were applied at the front and rear wheel axles to reproduce a straight-line riding condition. Constraints were applied to translations and rotations in order to represent tyre-ground contact and bearing supports. The external loads were defined with the aim of simulating the forces exerted by a rider of approximately 90 kg, with partial support on the pedals and partial support on the saddle. A vertical force of 800 N was applied at the bottom bracket to represent the load on the pedals, and a remote vertical force of 1000 N was applied at a virtual point representing the load transmitted through the saddle, which was then transferred to the upper section of the seat tube. The material used in this and all subsequent simulations was the alloy AW7020, which corresponds to the material of the fabricated frames. The results of this preliminary finite element analysis demonstrated a maximum deformation of approximately 0.7 mm in the seat stays of the rear triangle, exhibiting a typical “S-shaped” bending pattern (Figure 86b). The top tube was subjected to a primarily bending load, with the intrados located at the lower side of the tube and the extrados at the upper side. In contrast, the down tube was predominantly subjected to compression. The regions exhibiting the highest levels of stress were identified at the junctions between the rear triangle and the seat tube, and between the top tube and the seat tube, with peak stresses of approximately 60 MPa (Figure 86c).

Figure 86 - (a) As-is frame model with highlighted inserts at the cut sections; (b) displacement field of the as-is frame under load and (c) detail of regions with highest stress concentration.

In order to ensure the correct design of the joint systems, the contact pressures at the cut sections were extracted from the finite element analysis (Figure 87). These pressures were then used to evaluate the corresponding axial forces. Following this, the bolts were then dimensioned to guarantee that the resulting compressive force, generated by their preload, would exceed the separating forces derived from the simulations. The bolt sizing was assessed by considering exclusively the negative contact pressures, given that these are the pressures which tend to open the joint. In contrast, the positive contact pressures are transmitted directly through the contact surfaces of the joint and were thus assessed in subsequent simulations.

For the top-tube joint, the contact pressure distribution was conservatively approximated as uniform over the tube cross section, with an equivalent constant pressure of 18 MPa acting on an annular area of 173 mm^2, which corresponds to the difference between the outer and inner tube diameters. This resulted in an axial separating force of approximately 3.1 kN acting on the joint. Given that the joint relies on inclined surfaces at 45° to transfer the bolt preload into a transverse clamping force, the required bolt preload was set to be twice the axial separating force, i.e. approximately 6.2 kN. To account for load variability and to cover loading scenarios not explicitly simulated, a safety factor of 2 was applied, resulting in a preload of 12.5 kN for the top-tube joint. This can be achieved by two class 12.9 M6×1 screws, with each screw providing approximately 6.9 kN of preload at the specified tightening torque. The employment of two screws enhances redundancy in the event of a fastener becoming loose. An identical approach was employed in the case of the down-tube joint. In this scenario, the equivalent constant pressure from the finite element model was 9 MPa, acting on an annular area of 289 mm^2 and resulting in an axial separating force of approximately 2.6 kN. The employment of the aforementioned relationship for the 45° inclined surfaces resulted in the determination of a preload of 10.4 kN. This requirement can be satisfied by a single class 12.9 M8×1 screw, which is capable of providing a preload of approximately 12.2 kN.

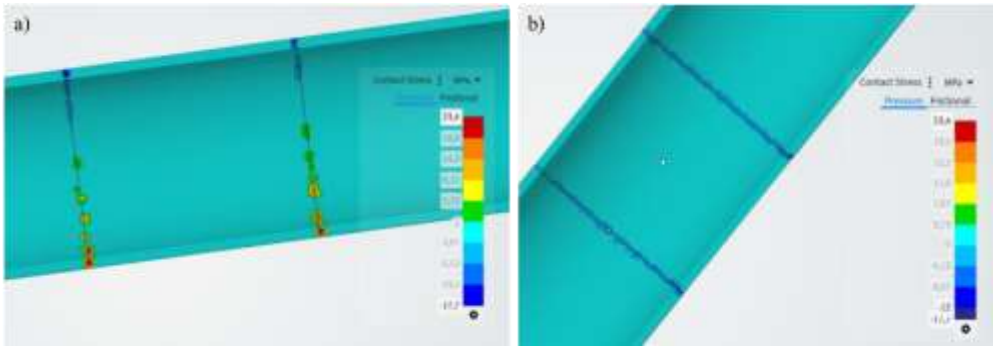

Figure 87 - Cross-sections of the contact stress distribution on the tube surface in the joint region for (a) the top-tube section and (b) the down-tube section.

A finite element analysis was performed on both joint configurations to assess the stress and deformation fields under the bolt preload and contact forces (Figure 88a). The simulations confirmed that the resulting strains and stresses in the joints were within acceptable limits. For the sake of clarity, the main results for the joint located on the down tube are reported below. For the down-tube joint, which integrates the hydraulic connectors and internal fluid passages of the rear brake system, an internal pressure of 200 bar was additionally applied to all wetted surfaces in order to verify sealing and structural integrity under the maximum operating pressure of the braking system. The findings of the simulation illustrated in Figure 88b, highlight that the alignment teeth exhibit the highest deformation with a maximum displacement of approximately 0.15 mm, which is considered within the acceptable range. The stress assessment was conducted according to the acceptance criterion, which was defined on the basis of the mechanical properties of LPBF AlSi10Mg in the as-built condition, reported in Table 21.

Table 21 - Mechanical properties of AlSi10Mg alloy in as-built condition.

Mechanical properties	
Yield strength, $\sigma_{y0.2}$ (MPa)	240 ± 20
Tensile strength, σ_{uts} (MPa)	440 ± 30
Young Modulus, E (GPa)	70
Elongation at break, A%	6 ± 3

Starting from a yield strength equivalent to 240 MPa, a safety factor of 2 was used, leading to a defined limit of 120 MPa. Moreover, the joints were considered to be within acceptable parameters if the Von Mises stresses did not penetrate more than 30% of the wall thickness. The maximum stress observed in the simulations was approximately 110 MPa, restricted to small surface regions and therefore below the admissible limit (Figure 88c).

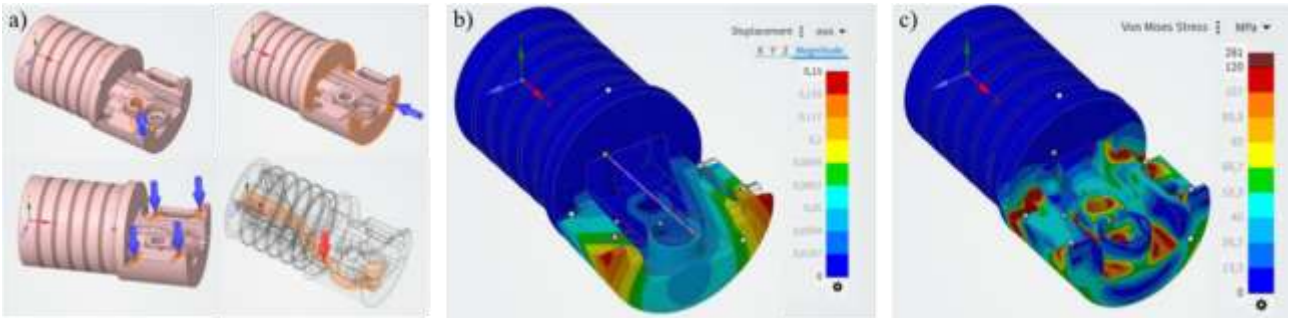

Figure 88 - (a) Load scheme applied to the down-tube joint; (b) displacement field and (c) Von Mises stress distribution in one half of the down-tube joint.

A final FE analysis was performed on the complete assembly, the frame with integrated joints. The boundary conditions and loading scheme employed for the as-is frame were replicated, with the addition of the forces generated by the bolt preloads in the top- and down-tube joints. The findings revealed a maximum deformation of approximately 0.7 mm in the rear triangle, aligning with the original frame, and a stress distribution in the frame tubes that closely resembled the as-is configuration, as illustrated in Figure 89. The only considerable increase in stresses was observed within the joints themselves, due to the preload of the bolts. However, the maximum stress remained below the previously defined limit of 120 MPa, as demonstrated in Figure 90.

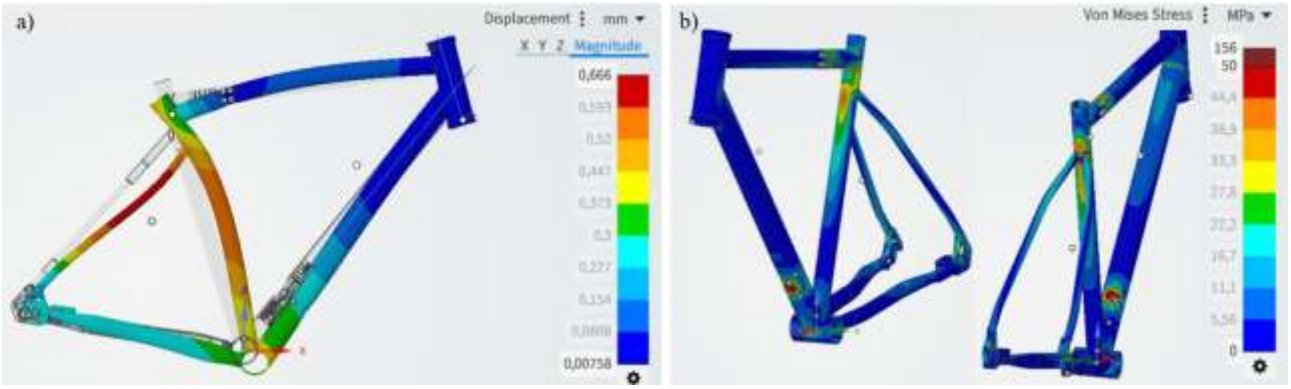

Figure 89 - Results of the FEA on the frame with integrated joints: (a) displacement field and (b) Von Mises stress distribution under the load case.

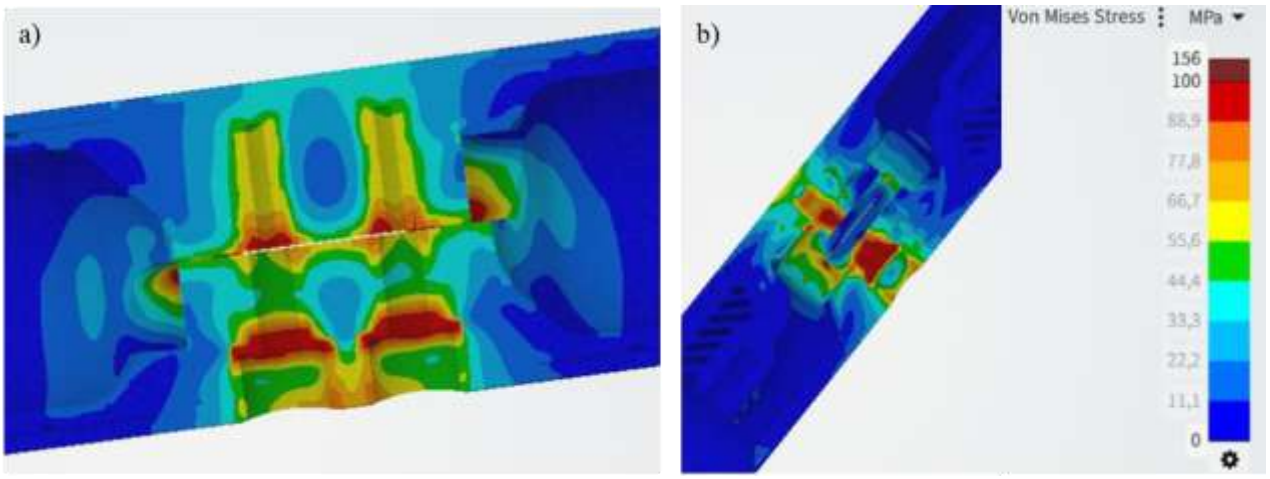

Figure 90 - Detail of the Von Mises stress distribution along the joint cross-sections on (a) the top-tube joint and (b) the down-tube joint.

In conclusion, the FE analyses indicated that the addition of the joints does not significantly alter the stress state of the original frame components, while the stresses in the joints remain within the acceptable range under the simulated load conditions.

5.2.4 Prototype manufacturing and experimental validation

As previously stated, the bicycle frame was manufactured by Dedacciai using an AW7020 aluminium alloy, while the joint system was produced by Aidro in AlSi10Mg alloy. The joints were fabricated on an EOS M290 Dual Mode LPBF machine, with a layer thickness of 30 µm and an argon protective atmosphere. During the fabrication process, the build plate was maintained at an approximate temperature of 165 °C in order to reduce internal residual stresses in the components. The joint halves were constructed in a vertical orientation, with the tube axis aligned with the build direction, thus minimising the requirement for support structures on functional surfaces and enhancing dimensional accuracy in the regions accommodating the hydraulic and electrical connectors (Figure 91a,b).

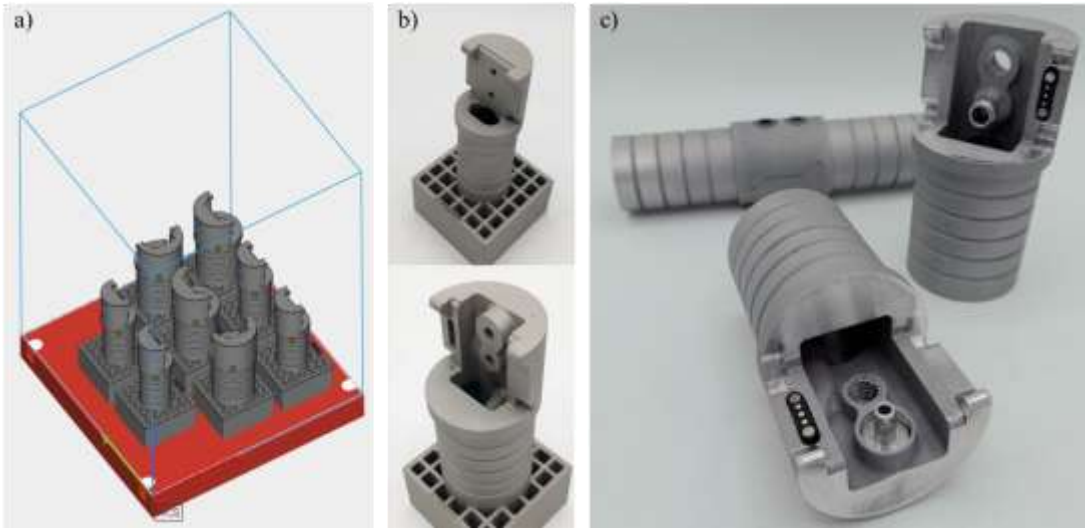

Figure 91 - (a) Arrangement of the joints on the LPBF build plate; (b) joints in the as-built condition before support removal and sandblasting; (c) joints after machining, with the hydraulic and electrical connectors assembled.

Subsequent to the printing phase, the prototypes underwent powder and support removal, followed by manual sandblasting to improve surface roughness. In order to obtain multiple pairs of joints for different test frames and mechanical characterisation campaigns, multiple joint halves were placed on each build plate. In select cases, supplementary machining operations were performed on the external surfaces with the objective of further reducing surface roughness and evaluating its effect on mechanical behaviour and fatigue performance (Figure 91c).

In collaboration with Dedacciai, a number of joining options between the LPBF joints and the AW7020 tubes were evaluated, including fusion welding and adhesive bonding. Gas tungsten arc welding was considered but ultimately dismissed due to concerns regarding porosity and the limited expertise in welding LPBF AlSi10Mg to wrought AW7020 in this particular configuration. A further analysis was conducted on friction stir welding, but it was determined that its implementation in the context of bike frame, characterised by intricate geometries, poses significant challenges with regard to the design of tooling and accessibility. Given the aforementioned constraints, and considering the manufacturer's expertise, the implementation of structural adhesive bonding with epoxy resins was identified as the optimal approach for integrating the joints into the frame. This method ensured a reliable mechanical connection, while concurrently minimising thermal distortion and preserving the properties of both the LPBF joints and the AW7020 tubes. The final design of the manufactured prototypes is illustrated in Figure 92.

Figure 92 - Frame equipped with the joint prototypes in (a) assembled and (b) disassembled configuration; (c) complete bicycle prototype with electric motor and integrated joints.

The fatigue behaviour of the prototype was assessed through a full-frame test performed at Dedacciai, using their internal test protocol for bicycle frames. In this setup, the frame is mounted on two cylinders driven by cams that convert a uniform rotation into a sinusoidal vertical translation with a total stroke of 55 mm and a rotational speed of 300 rpm, corresponding to a loading frequency of 5 Hz. With this configuration, reported in Figure 93, the frame oscillates vertically with the same amplitude. A total mass of 42.25 kg is applied to the bottom bracket shell by means of a central shaft rigidly connected to the shell and carrying several 10 kg and 5 kg discs, distributed asymmetrically between the two sides to generate both vertical loading and a torsional moment on the bottom bracket. Dedacciai employs this particular test to validate the structural integrity of the frames prior to marketing, with the number of cycles the frame undergoes prior to failure serving as the primary criterion. On the basis of long-term experience and historical data, Dedacciai considers frames that withstand more than 250 000 cycles in this test to have an expected 10-year failure rate below 3% in normal service.

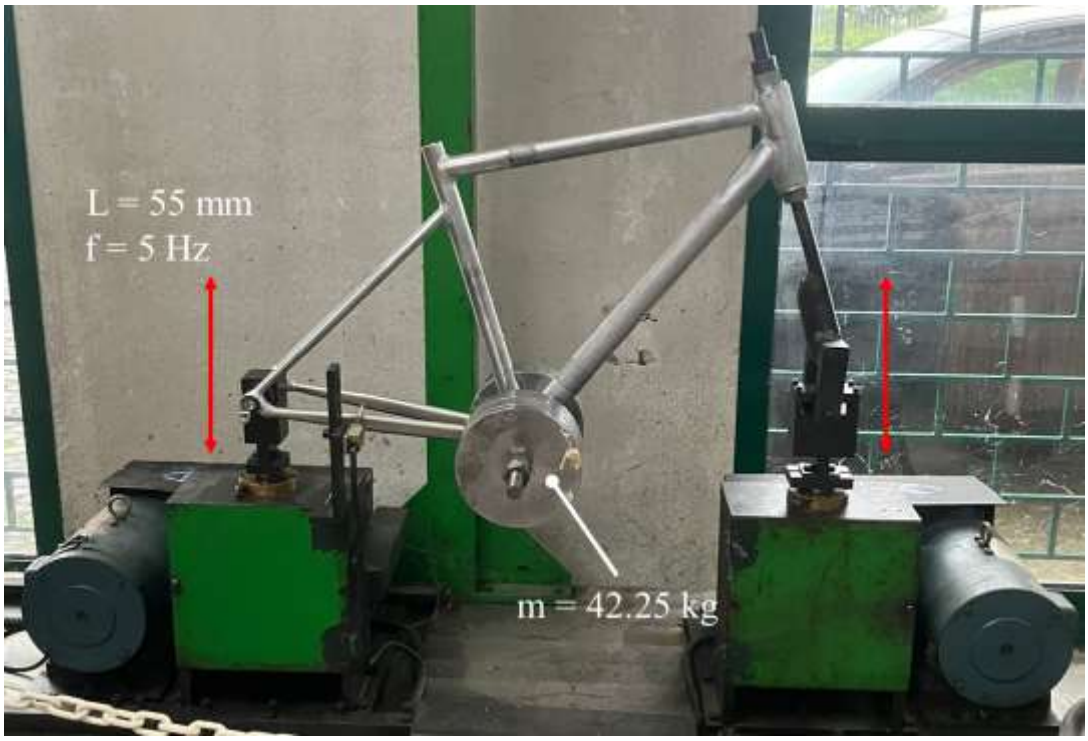

Figure 93 - Fatigue test rig used for frame testing, showing the imposed vertical stroke, loading frequency and total mass applied at the bottom bracket.

Two distinct pairs of joints were examined, characterised by variations in surface roughness and surface finish condition. The first pair was tested in the as-built condition and subjected only to manual sandblasting (SB), resulting in an average surface roughness of $R_a = 14\ \mu m$. The second pair, also in the as-built condition, was further machined (MC) in order to improve the surface finish, achieving a significantly reduced surface roughness of $R_a = 0.8\ \mu m$.

In the first test, the frame was equipped with SB joints. The frame failed after 113 152 cycles, with crack initiation observed in the joint located on the top tube, as demonstrated in Figure 94a,b. As illustrated in Figure 94c,d the fracture developed in one of the most highly stressed regions of the joint, in accordance with the finding of the finite element analysis.

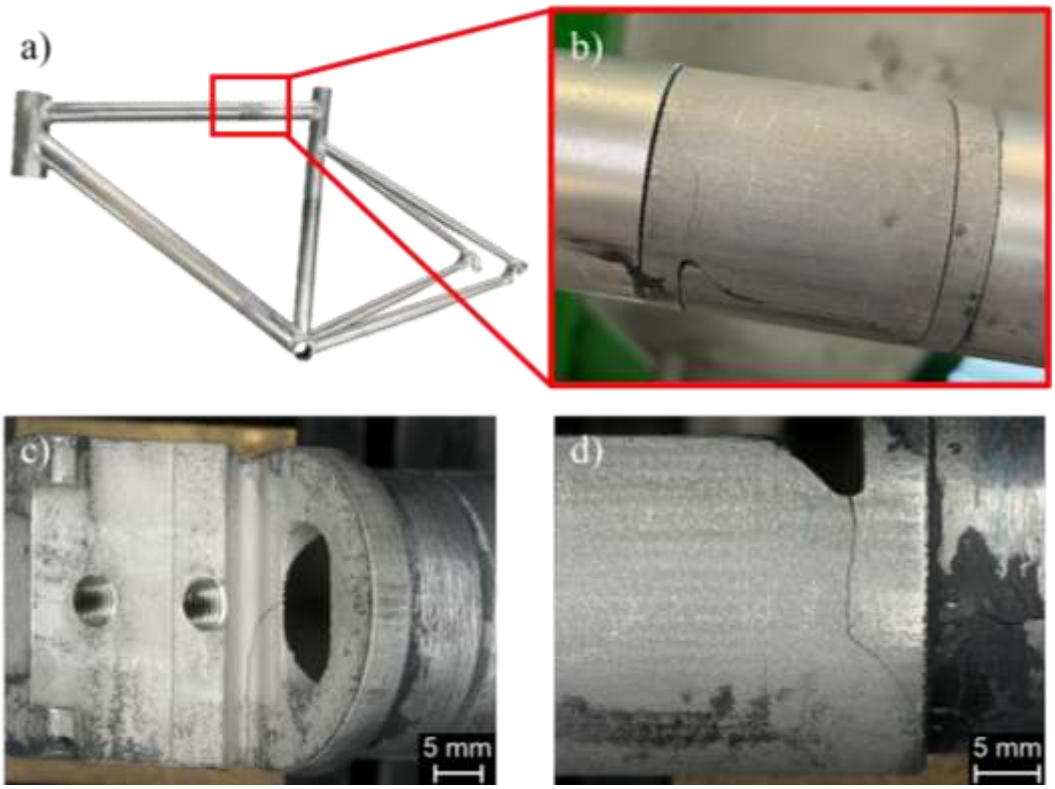

Figure 94 – (a) Frame after fatigue test and (b) crack observed in the top-tube joint; (c) front view and (d) side view of the failed joint showing the crack path.

Subsequent to the fatigue test, the joints were detached from the frame, meticulously cleaned and sectioned to expose and inspect the fracture surfaces. The analysis, conducted using a scanning electron microscope, enabled the identification of the crack initiation zone. As demonstrated in Figure 95b, the fracture surface displays macroscopic ridges that are indicative of the direction of crack propagation. This suggests that the crack nucleates on the outer surface of the joint, in close proximity to the edge, and subsequently propagated towards the interior. As depicted in Figure 95c, the failure was initiated from a single nucleation site, associated with a surface defect. Figure 95d highlights the region of steady crack growth, characterised by a relative planar surface with several shallow ridges. Moving further into the joint, deeper ridges and micro-dimples with dimensions comparable to those of cellular microstructure are observed, suggesting a ductile mechanism of fracture (Figure 95e,f).

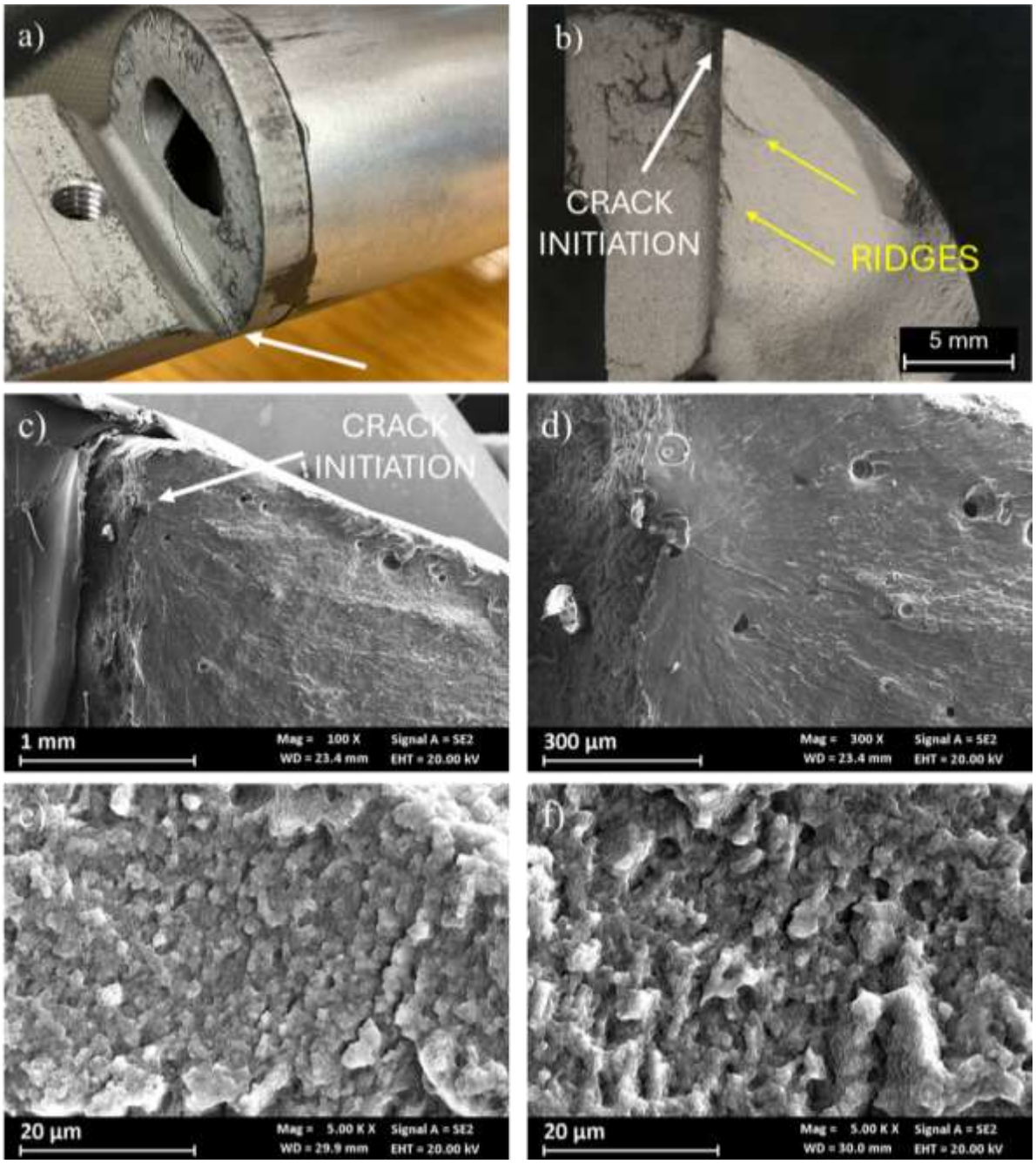

Figure 95 – (a) Macroscopic view of the failed top-tube joint; (b) fracture surface highlighting the crack initiation area and main propagation ridges; (c,d) SEM images showing the single crack nucleation site and the direction of crack growth; (e,f) higher-magnification views of the fracture surface with micro-dimples.

Several studies on LPBF AlSi10Mg have shown that the fatigue behaviour of as-built components is strongly affected by surface and subsurface defects. Imperfections such as porosity, shrinkage cavities, un-melted particles or lack of fusion represent the most common defects [111,289]. The "staircase effect" caused by stepped approximation formed by the layers on curved and inclined surface can also represent a surface defect [34,290]. A sandblasting treatment reduces the macroscopic roughness replacing the LPBF typical features with craters and subsurface porosities attributed to the plastic deformation of the surface and closure of the deep valleys during this treatment [291,292]. The defect located within a few hundreds of micrometres from the surface typically remain active fatigue crack initiators [293]. The fracture features observed on the first joint

are consistent with the aforementioned assumption. The presence of a single nucleation site associated with a surface defect, together with the macroscopic ridges indicating propagation from the outer surface towards the interior, reflects the dominant role of the process-induced defect population in controlling crack initiation in the sand-blasted condition, as reported by Nasab et al. [294]. A review of literature pertaining to the effect of surface finishing on LPBF AlSi10Mg mechanical performance suggests that more aggressive post-processing routes, capable of removing the entire defective surface layer, can strongly enhance fatigue life compared to as-built or sandblasted components [108,289,295]. In this scenario, the relatively low fatigue life measured for the first joint, in conjunction with the established crack initiation mechanism, offers a robust basis for the subsequent joint configurations. A machining was applied to mitigate the effect of surface and subsurface defects in order to achieve a frame with a fatigue behaviour closer to that of conventionally bicycle frame.

In the second test, the frame was equipped with MC joints. Based on the findings achieved in the first test and in agreement with Aidro, it was decided to machine the most highly stressed regions of the joints. In particular, the contact surfaces between the two joint halves, such as the alignment teeth and the inclined surfaces, were machined to remove any surface and subsurface defects generated during the LPBF process, as highlighted in Figure 96.

Figure 96 – Second configuration of joints with machined contact surfaces (indicated by arrows).

With this second configuration, the frame failed after 171 1437 cycles, with crack initiation observed at the joint located on the down tube, as shown in Figure 97a,b. As illustrated in Figure 97c,d, fracture propagation still occurred along the contact region with the alignment teeth of the coupling half of the joint system. As demonstrated by FEA simulations reported in Figure 88c, this region is subjected to the highest stress levels under the applied loading conditions. As reported by other authors [293,294,296], machining operations aimed at improving surface roughness can lead to a significant increase in the fatigue performance of LPBF component. However, fatigue crack initiation remains strongly influenced by the presence of pores or printing defects that may be exposed on the component surface as a result of machining. The presence of internal porosity in LPBF components is an intrinsic feature of the technology, which can be mitigated by optimizing process parameters or by applying specific post-processing treatments, such as hot isostatic pressing.

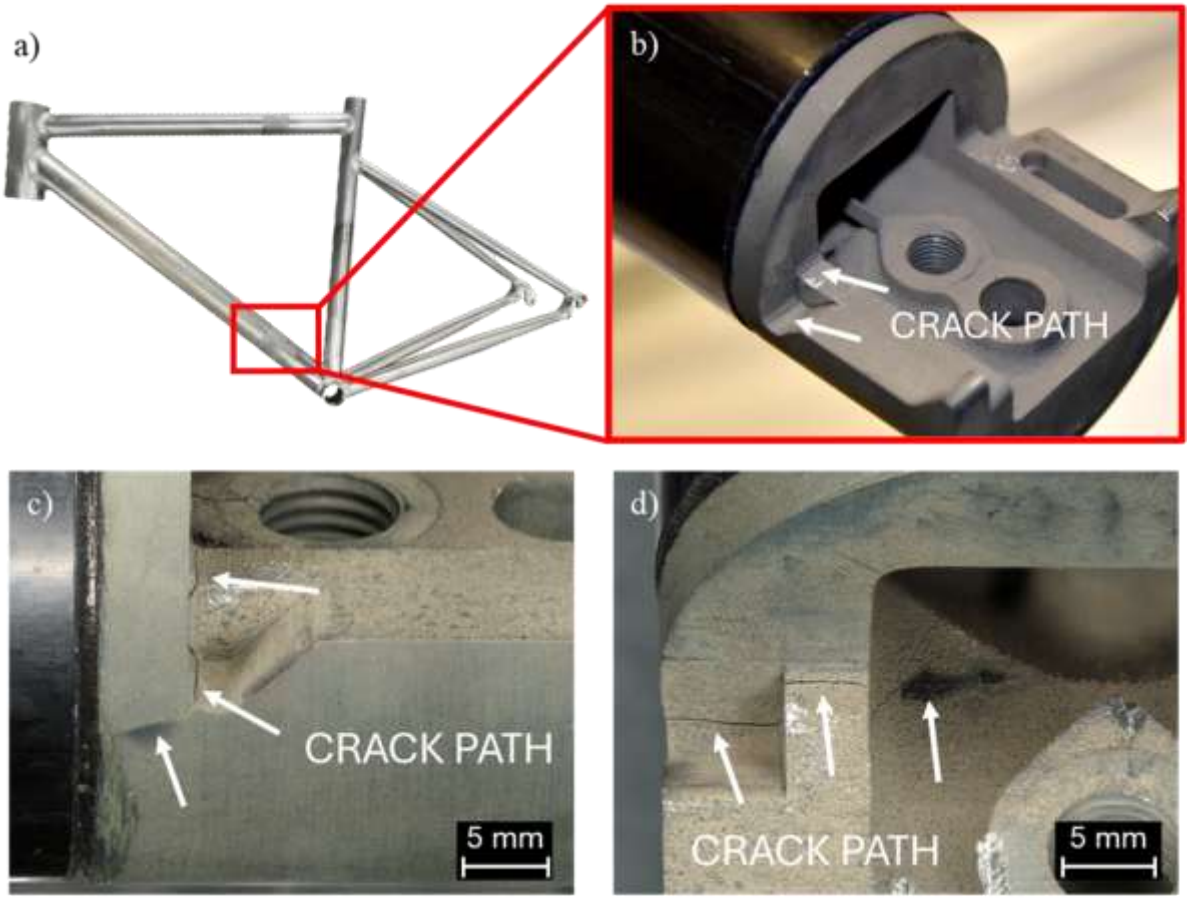

Figure 97 – (a) Frame after fatigue test and (b) crack observed in the down-tube joint; (c) side view and (d) front view of the failed joint showing the crack path.

Subsequent to the fatigue test, the second joint was erroneously subjected to an anodising treatment, which severely damaged the fracture surfaces. As demonstrated in Figure 98, the chemical bath employed for anodising penetrated the crack, thereby producing an etching effect that exposed the microstructure. Consequently, it was unfeasible to conduct a comprehensive fractographic investigation, hindering the precise identification of the crack initiation site and the associated failure mechanisms.

Notwithstanding this constraint, on the basis of previous studies on the fatigue behaviour of LPBF AlSi10Mg and on the effects of surface finishing treatments, it can be reasonably assumed that, in the MC sample, the original LPBF surface features were effectively removed by machining [295–299]. In this configuration, the joints are expected to fail from a single defect corresponding to an occasional bulk pore that became exposed at the surface as a consequence of the machining operation, in agreement with the findings reported by other authors.

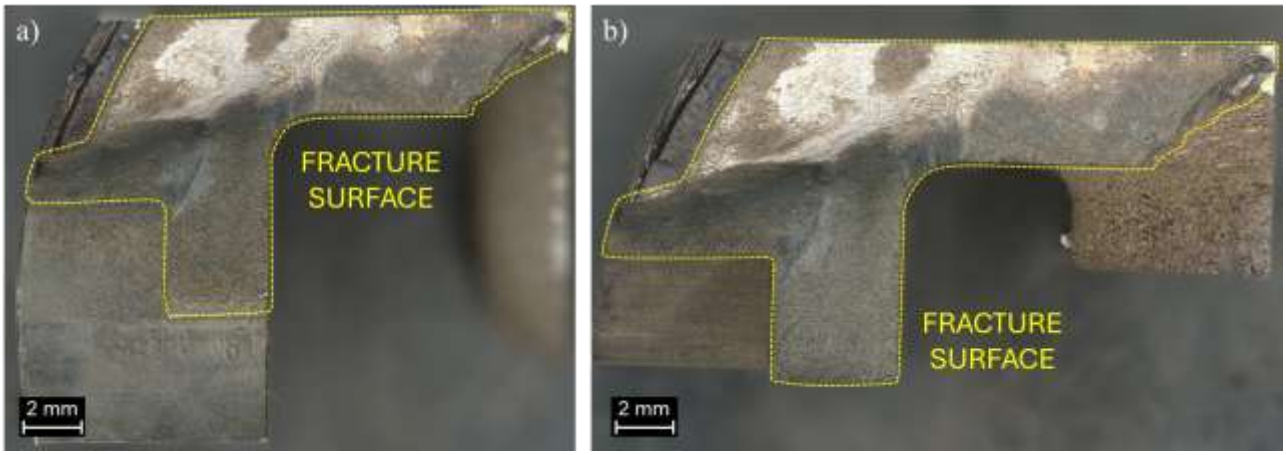

Figure 98 - fdgerg

While these local analyses explain how the joints failed, the design of a safe modular frame also requires an understanding of how frequently such failures are expected to occur in service. For this reason, the experimental fatigue lives measured on the modular frames were interpreted within a probabilistic framework, using a Weibull model calibrated on the manufacturer's historical data. In industrial practice, a single fatigue test result does not directly translate into a guaranteed service life, since fatigue is inherently a stochastic phenomenon and a significant scatter in fatigue life can be observed even among nominally identical frames [297]. Fatigue performance is therefore typically evaluated within a probabilistic framework in which experimental fatigue lives are translated into a probability of failure over a specified service period. In accordance with this approach, the fatigue performance measured on the modular frames were analysed using a probabilistic model calibrated on the long-term experience of the industrial partner. Over the past several decades, the manufacturer has built up an extensive database. This database consists of full-frame fatigue tests that have been conducted in accordance with standardised laboratory protocols, as well as field failure statistics that have been collated during the course of service. From the dataset, an empirical relationship was established between the number of cycles to failure, N_i, and the corresponding 10-year failure rate of commercial frames, F_i. The discrete data provided by the manufacturer are reported in Table 22.

Table 22 - Estimated 10-year failure probability as a function of fatigue life for the traditional frames.

Cycles to Failure, N_i	**Estimated 10-year frame failure rate, F_i (%)**
500 000	< 0.1
250 000	< 3
150 000	< 10
100 000	< 30
50 000	> 80

These data were used as experimental points of the cumulative distribution function F(N) of fatigue life, where F(N) represents the probability that a frame fails within 10 years of service, corresponding to a fatigue life in the laboratory test lower than or equal to N. This interpretation aligns with established reliability approaches for mechanical components. Within these methods, fatigue life distributions are used to link laboratory test result with in-service failure probabilities

[298]. The fatigue life distribution was described in continuous form using a two-parameter Weibull distribution. The Weibull distribution is a frequently employed tool in the fields of fatigue and reliability analyses due to its flexibility, physical interpretability [299]. The probability density function (PDF) for a two-parameter Weibull distribution is defined as:

$$F(N) = 1 - \exp\left[-\left(\frac{N}{\eta}\right)^{\beta}\right] \tag{3.1}$$

$$1 - F(N) = \exp\left[-\left(\frac{N}{\eta}\right)^{\beta}\right] \tag{3.2}$$

Where η is the scale parameter and β is the shape parameter, which reflects the scatter of fatigue life. In order to evaluate η and β, the Weibull cumulative distribution function was linearised. The failure rates supplied by the manufacturer, expressed in percent, were first converted into fractions according to:

$$F(N_i) = \frac{F_i(\%)}{100} \tag{3.3}$$

And the transformed variables were introduced:

$$X_i = \ln(N_i) \tag{3.4}$$

$$Y_i = \ln[-\ln(1 - F_i)] \tag{3.5}$$

By taking the natural logarithm of Eq. (3.2) and substituting Eq. (3.4) and Eq. (3.5), the Weibull distribution reduces to a linear relationship:

$$\ln[-\ln(1 - F_i)] = \beta \ln N_i - \beta \ln \eta \tag{3.6}$$

$$Y_i = \beta X_i - \beta \ln \eta \tag{3.7}$$

The experimental points (X_i, Y_i) can be fitted by a straight line whose slope and intercept provide the value of η and β. The linear regression of the manufacturer's data yields the interpolating line:

$$Y_i = -3.1396 \cdot X_i + 34.911 \tag{3.8}$$

with a coefficient of determination $R^2 = 0.966$, indicating a very good agreement between the Weibull model and the historical fatigue data. From the slope and intercept of Eq. (3.8) one obtains:

$$\beta = 3.1396 \tag{3.9}$$

$$\eta = \exp\left(-\frac{34.911}{\beta}\right) = 67478.84 \approx 67\,479 \tag{3.10}$$

Where the absolute value of the slope is used for $\beta > 0$.
Once the Weibull parameters are known, the model was used to estimate the 10-year failure probability associated with any fatigue life N_i provided by the manufacturer through the following equation:

$$F_{Weibull}(N) = 1 - \exp\left[-\left(\frac{N}{\eta}\right)^{\beta}\right] \tag{3.11}$$

Figure 99 shows the trend of the evaluated values compared with the experimental data, indicating a satisfactory overlap. This comparison confirms that the adopted distribution is able to represent the historical experience acquired by the company.

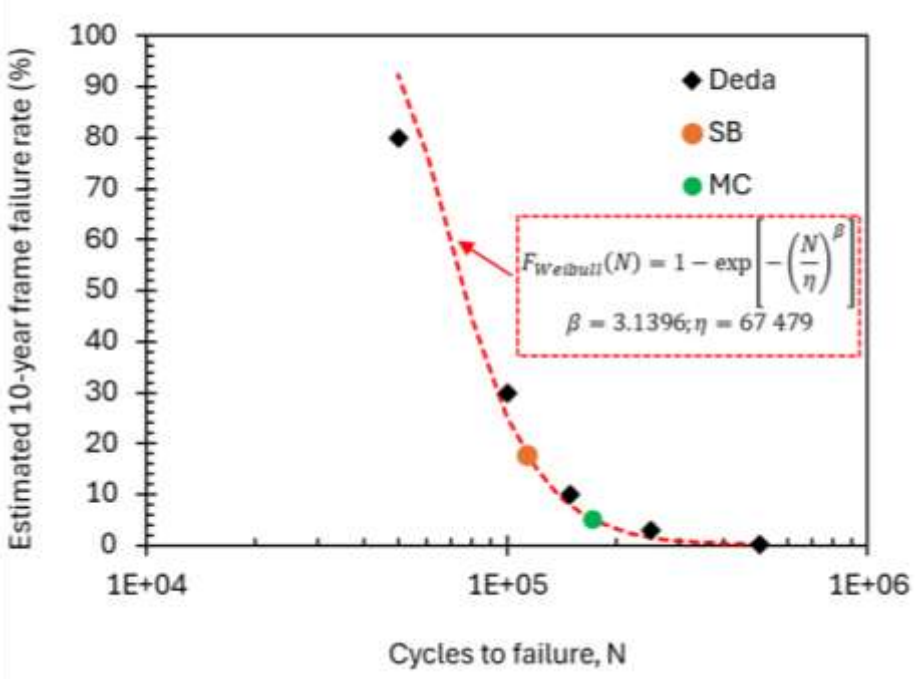

Figure 99 – Estimated 10-year frame failure rate as a function of cycles to failure.

The fatigue test results obtained on the frames with integrated joints, expressed in terms of cycles to failure, were used to evaluate, by means of Eq. (3.11), the corresponding 10-year failure probability, which is reported in Table 23 and illustrated in Figure 99.

Table 23 - Estimated 10-year failure probability as a function of fatigue life for the frames with integrated joints

Joints condition	**N_i**	**F_i (%)**
Sandblasted (SB)	113 152	17.9
Machined (MC)	171 437	5.2
Heat treated + Machined (HT)	-	-

For the first modular frame, which failed after 113 152 cycles, the estimated 10-year failure probability is about 18%, clearly above the 3% threshold that the manufacturer considers acceptable for commercial frames. For the second frame, which reached 171 437 cycles before failure, the model predicts a failure probability of approximately 5%, already much closer to the industrial target. While the result remains marginally above the desired threshold, this outcome signifies a substantial enhancement in fatigue reliability.

Despite the limited number of tested specimens, the probabilistic interpretation suggest that the fatigue performance of the modular frame is comparable to that of the conventional frame, evaluated in terms of failure probability over time. It is imperative to emphasise that the integration of the modular joint does not compromise the global fatigue reliability of the structure, provided that

appropriate design and post-processing strategies are implemented. The Weibull-based approach enables a meaningful and objective comparison between the modular concept and traditional frame designs, thereby facilitating a more comprehensive understanding of the relationship between laboratory fatigue tests and expected in-service performance.

The present study has demonstrated that LPBF AlSi10Mg ca be effectively employed to produce functional modular joints for aluminium e-bike frames, thereby enabling the development of separable structures without compromising global stiffness or safety. The fatigue tests demonstrates that joint performance is predominantly governed by the distribution of local stress and by the population of surface and subsurface defects intrinsic to LPBF. These defects can be mitigated by implementing suitable post-processing methodologies. This hypothesis is supported by the enhanced fatigue life of the machined joints and the associated reduction in predicted 10-year failure probability. When evaluated within a probabilistic model calibrated with industrial data, these findings suggest that modular frames integrated with LPBF-processed joints can achieve fatigue reliability levels comparable to those of conventional frames, provided that appropriate design, manufacturing and finishing strategies are employed.

6 Conclusions

The research activities discussed in this study has demonstrated that aluminium alloys produced by laser powder bed fusion can be employed to engineer lightweight and modular structures for light electric vehicles, with a crucial need in assessing the correlation between alloy chemistry, process parameters, microstructure and joining strategies.

Based on the results obtained, the following key observations can be summarised:

- At the material level, the results obtained for LPBF AlSi9Cu3 alloy demonstrate that the corrosion behaviour remains significantly influenced by the melt pool macrostructure. The distribution of Cu-rich precipitates at the melt pool boundaries, in conjunction with their galvanic coupling with the Al matrix, has been identified as the primary driving force for selective corrosion. Furthermore, the presence of such as nobler precipitates strongly affects the passive oxide film, facilitating the localise corrosion in chloride-containing environment. The ability to control the melt pool macrostructure through process parameters and post-process heat treatments, with subsequent microstructural changes, has emerged as a key design strategy for tailoring the corrosion resistance of LPBF alloys.

- The comparative analysis demonstrates that the corrosion behaviour of LPBF aluminium alloys is not only related to the intrinsic electrochemistry of alloying elements, but its content can affect also the microstructural features. The increase in copper content, particularly in conjunction with a less silicon network, lead to a more discontinuous precipitates-containing network, intensifying microstructural heterogeneity and resulting in enhanced corrosion phenomena.

- At the structural level, experimental and numerical investigation of non-periodic AlSi10Mg lattice structures manufactured by LPBF established a clear link between relative density, topological aspect ratio and deformation regime. This research demonstrated the efficacy of a combined use of Gibson-Ashby scaling laws and TAR in enabling the design of lattice configurations with tailored stiffness, strength and energy absorption. The lattice study also revealed the strong influence of specimen geometry, number of unit cells and manufacturing-induced imperfections on the transition between bending- and stretch-dominated behaviour, underscoring the need to integrate process-induced discrepancies into lattice design methodologies.

- The hybrid welding study, combining LPBF AlSi10Mg and 6xxx wrought alloys, corroborated that gas tungsten arc welding and friction stir welding result in significantly

different joint architectures and defect populations. It was established that GTAW hybrid joints are subject to limitations imposed by hydrogen-driven porosity and pronounced microstructural heterogeneity within the weld metal and heat-affected zone. These features exert a profound influence on the distribution of hardness and the susceptibility to corrosion. In contrast, the FSW method was found to be an effective solid-state joining process for LPBF and wrought alloys, enabling the formation of joints without the occurrence of porosity. Furthermore, the FSW approach resulted in joint efficiencies of up to approximately 70-74%, with failure occurring in the softened HAZ of the wrought alloy rather than in the LPBF material.

- The prototype activities translated the material- and structural-level findings into full-scale components. The integration of the rear triangle with the lattice structure demonstrated the viability of LPBF lattice structures in combination with conventional frames. Furthermore, the utilisation of an equivalent-material FEM approach enabled the prediction of the primary deformation modes and stress localisation under service-like loading conditions. Concurrently, the premature fracture observed during road testing highlighted the sensitivity of the lattice insert to process-induced porosity, surface condition and pre-weld solution treatment. These factors reduced the effective strength below that derived from as-built lattice specimens. The experimental investigation of modular joint prototypes has demonstrated the feasibility of employing LPBF AlSi10Mg in the fabrication of removable joints for aluminium frames, while maintaining optimal global stiffness. Subsequent fatigue testing and Weibull-based analysis have revealed that, with adequate machining and surface finishing, the 10-year failure probability of modular frames approaches the industrial target established for conventional frames.

7 List of figures

8 List of tables

9 References

[1] F. Jelti, A. Allouhi, K.A. Tabet Aoul, Transition Paths towards a Sustainable Transportation System: A Literature Review, Sustainability (Switzerland) 15 (2023). https://doi.org/10.3390/su152115457.

[2] D.M. Herold, K.H. Lee, Carbon management in the logistics and transportation sector: an overview and new research directions, Carbon Manag. 8 (2017) 79–97. https://doi.org/10.1080/17583004.2017.1283923.

[3] E. Commission, D.-G. for Mobility, Transport, Raising awareness of alternatives to private car – Pilot project – Final report, Publications Office, 2021. https://doi.org/doi/10.2832/57672.

[4] E. Commission, D.-G. for Mobility, Transport, C.E. Delft, Handbook on the external costs of transport – Version 2019 – 1.1, Publications Office, 2020. https://doi.org/doi/10.2832/51388.

[5] M. Delogu, L. Zanchi, C.A. Dattilo, M. Pierini, Innovative composites and hybrid materials for electric vehicles lightweight design in a sustainability perspective, Mater. Today Commun. 13 (2017) 192–209. https://doi.org/10.1016/j.mtcomm.2017.09.012.

[6] K. and P.A. and B.A. Makarova Irina and Shubenkova, Smart-Bike as One of the Ways to Ensure Sustainable Mobility in Smart Cities, in: F. and B.V. Magno Michele and Ferrero (Ed.), Sensor Systems and Software, Springer International Publishing, Cham, 2017: pp. 187–198.

[7] M.F. Ashby, D. Cebon, Materials selection in mechanical design, in: Journal De Physique, Publ by Editions de Physique, 1993: pp. 1–9. https://doi.org/10.1051/jp4:1993701.

[8] H.R. Shercliff, M.F. Ashby, Elastic Structures in Design, in: Reference Module in Materials Science and Materials Engineering, Elsevier, 2016. https://doi.org/10.1016/b978-0-12-803581-8.02944-1.

[9] C.C. Lin, S.J. Huang, C.C. Liu, Structural analysis and optimization of bicycle frame designs, Advances in Mechanical Engineering 9 (2017). https://doi.org/10.1177/1687814017739513.

[10] D. Covill, S. Begg, E. Elton, M. Milne, R. Morris, T. Katz, Parametric finite element analysis of bicycle frame geometries, in: Procedia Eng., Elsevier Ltd, 2014: pp. 441–446. https://doi.org/10.1016/j.proeng.2014.06.077.

[11] D. Covill, P. Allard, J.M. Drouet, N. Emerson, An Assessment of Bicycle Frame Behaviour under Various Load Conditions Using Numerical Simulations, in: Procedia Eng., Elsevier Ltd, 2016: pp. 665–670. https://doi.org/10.1016/j.proeng.2016.06.269.

[12] I.K. Ullah, A. Daniela, L. Rosa, S. Mihanyar, A design methodology of a product: bicycle frame for simultaneous improvement of mechanical and environmental performance, 2022.

[13] M.F. Ashby, Eco-data, in: Materials and the Environment, Elsevier, 2013: pp. 119–174. https://doi.org/10.1016/b978-0-12-385971-6.00006-3.

[14] R.J. Tapper, M.L. Longana, A. Norton, K.D. Potter, I. Hamerton, An evaluation of life cycle assessment and its application to the closed-loop recycling of carbon fibre reinforced polymers, Compos. B Eng. 184 (2020). https://doi.org/10.1016/j.compositesb.2019.107665.

[15] Q. Dai, J. Kelly, A. Elgowainy, Material Efficiencies and Recycling of Aluminum and Carbon Fiber Reinforced Plastics for Automotive Applications, 2016.

[16] N.S. Bahuriddin, M.Z.M. Saman, N. Mohamad-Ali, N.H.A. Ngadiman, M.I.I.M. Maulana, State of sustainability assessments of metal additive manufacturing: literature review and

triple-bottom-line perspectives, Environmental Science and Pollution Research 32 (2025) 20825–20843. https://doi.org/10.1007/s11356-025-36889-0.
[17] P. Nyamekye, R. Lakshmanan, V. Tepponen, S. Westman, Sustainability aspects of additive manufacturing: Leveraging resource efficiency via product design optimization and laser powder bed fusion, Heliyon 10 (2024). https://doi.org/10.1016/j.heliyon.2023.e23152.
[18] S. Jung, L.B. Kara, Z. Nie, T.W. Simpson, K.S. Whitefoot, Is Additive Manufacturing an Environmentally and Economically Preferred Alternative for Mass Production?, Environ. Sci. Technol. 57 (2023) 6373–6386. https://doi.org/10.1021/acs.est.2c04927.
[19] J.M. Costa, M.C. Maia, A.P. Fernandes, E.C. Oliveira, M.F. Vieira, E.W. Sequeiros, Topology optimization of an aluminum bicycle pedal crank using laser powder bed fusion, Materials Science in Additive Manufacturing 4 (2025). https://doi.org/10.36922/MSAM025040003.
[20] M. Helou, S. Kara, Design, analysis and manufacturing of lattice structures: An overview, Int. J. Comput. Integr. Manuf. 31 (2018) 243–261. https://doi.org/10.1080/0951192X.2017.1407456.
[21] C. Beyer, D. Figueroa, Design and Analysis of Lattice Structures for Additive Manufacturing, Journal of Manufacturing Science and Engineering, Transactions of the ASME 138 (2016). https://doi.org/10.1115/1.4033957.
[22] P.A. Rometsch, Y. Zhu, X. Wu, A. Huang, Review of high-strength aluminium alloys for additive manufacturing by laser powder bed fusion, Mater. Des. 219 (2022). https://doi.org/10.1016/j.matdes.2022.110779.
[23] A. Martucci, A. Aversa, M. Lombardi, Ongoing Challenges of Laser-Based Powder Bed Fusion Processing of Al Alloys and Potential Solutions from the Literature—A Review, Materials 16 (2023). https://doi.org/10.3390/ma16031084.
[24] A. Salmi, E. Atzeni, L. Iuliano, M. Galati, Experimental Analysis of Residual Stresses on AlSi10Mg Parts Produced by Means of Selective Laser Melting (SLM), in: Procedia CIRP, Elsevier B.V., 2017: pp. 458–463. https://doi.org/10.1016/j.procir.2016.06.030.
[25] M. Opprecht, J.-P. Garandet, G. Roux, C. Flament, M. Soulier, A solution to the hot cracking problem for aluminium alloys manufactured by laser beam melting, 2020.
[26] M. Kumar, G.J. Gibbons, A. Das, I. Manna, D. Tanner, H.R. Kotadia, Additive manufacturing of aluminium alloy 2024 by laser powder bed fusion: microstructural evolution, defects and mechanical properties, Rapid Prototyp. J. 27 (2021) 1388–1397. https://doi.org/10.1108/RPJ-10-2020-0241.
[27] S. Mohammad, H. Hojjatzadeh, N.D. Parab, Q. Guo, M. Qu, L. Xiong, C. Zhao, L.I. Escano, K. Fezzaa, W. Everhart, T. Sun, L. Chen, Direct observation of pore formation mechanisms during LPBF additive manufacturing process and high energy density laser welding, 2020.
[28] J. Fiocchi, A. Tuissi, C.A. Biffi, Heat treatment of aluminium alloys produced by laser powder bed fusion: A review, Mater. Des. 204 (2021). https://doi.org/10.1016/j.matdes.2021.109651.
[29] Z. Zhu, Z. Hu, H.L. Seet, T. Liu, W. Liao, U. Ramamurty, S.M. Ling Nai, Recent progress on the additive manufacturing of aluminum alloys and aluminum matrix composites: Microstructure, properties, and applications, Int. J. Mach. Tools Manuf. 190 (2023). https://doi.org/10.1016/j.ijmachtools.2023.104047.
[30] F. García-Moreno, Commercial applications of metal foams: Their properties and production, Materials 9 (2016). https://doi.org/10.3390/ma9020085.

[31] G. Li, G. Ruan, Y. Huang, Z. Xu, X. Li, C. Guo, C. Zhao, L. Cheng, X. Hu, X. Li, Q. Zhu, Facile and cost-effective approach to additively manufacture crack-free 7075 aluminum alloy by laser powder bed fusion, J. Alloys Compd. 928 (2022). https://doi.org/10.1016/j.jallcom.2022.167097.
[32] B. Blakey-Milner, P. Gradl, G. Snedden, M. Brooks, J. Pitot, E. Lopez, M. Leary, F. Berto, A. du Plessis, Metal additive manufacturing in aerospace: A review, Mater. Des. 209 (2021). https://doi.org/10.1016/j.matdes.2021.110008.
[33] M.D. Vijayakumar, V. Dhinakaran, T. Sathish, G. Muthu, P.M.B. Ram, Experimental study of chemical composition of aluminium alloys, in: Mater. Today Proc., Elsevier Ltd, 2020: pp. 1790–1793. https://doi.org/10.1016/j.matpr.2020.07.391.
[34] T. DebRoy, H.L. Wei, J.S. Zuback, T. Mukherjee, J.W. Elmer, J.O. Milewski, A.M. Beese, A. Wilson-Heid, A. De, W. Zhang, Additive manufacturing of metallic components – Process, structure and properties, Prog. Mater. Sci. 92 (2018) 112–224. https://doi.org/10.1016/j.pmatsci.2017.10.001.
[35] X. Yang, R. Li, T. Yuan, L. Ke, J. Bai, K. Yang, A comprehensive overview of additive manufacturing aluminum alloys: Classifications, structures, properties and defects elimination, Materials Science and Engineering: A 919 (2025). https://doi.org/10.1016/j.msea.2024.147464.
[36] R.C. Dorward, T.R. Pritchett, Advanced Aluminium Alloys for Aircraft and Aerospace Applications, n.d.
[37] G. Wang, X. Bian, W. Wang, J. Zhang, Influence of Cu and minor elements on solution treatment of Al-Si-Cu-Mg cast alloys, Mater. Lett. 57 (2003) 4083–4087. https://doi.org/10.1016/S0167-577X(03)00270-2.
[38] Z. Hu, Y. Qi, S. Gao, X. Nie, H. Zhang, H. Zhu, X. Zeng, Aging responses of an Al-Cu alloy fabricated by selective laser melting, Addit. Manuf. 37 (2021). https://doi.org/10.1016/j.addma.2020.101635.
[39] G.B. Hatch, P.H. Ralston, Localized Corrosion of Aluminum Alloys-A Review')*, Japan Society of Corrosion Engineering, 1972.
[40] P. Schmutz, G.S. Frankelt, Characterization of AA2024-T3 by Scanning Kelvin Probe Force Microscopy, n.d.
[41] W. Huo, J. Hu, H. Cao, Y. Du, W. Zhang, Y. Zhang, Simultaneously enhanced mechanical strength and inter-granular corrosion resistance in high strength 7075 Al alloy, J. Alloys Compd. 781 (2019) 680–688. https://doi.org/10.1016/j.jallcom.2018.12.024.
[42] M.O. Speidel, Stress Corrosion Cracking of Aluminum Alloys, n.d.
[43] C.A. Biffi, J. Fiocchi, A. Tuissi, Laser Weldability of AlSi10Mg Alloy Produced by Selective Laser Melting: Microstructure and Mechanical Behavior, J. Mater. Eng. Perform. 28 (2019) 6714–6719. https://doi.org/10.1007/s11665-019-04402-7.
[44] N. Takata, H. Kodaira, K. Sekizawa, A. Suzuki, M. Kobashi, Change in microstructure of selectively laser melted AlSi10Mg alloy with heat treatments, Materials Science and Engineering: A 704 (2017) 218–228. https://doi.org/10.1016/j.msea.2017.08.029.
[45] R.I. Revilla, H. Terryn, I. De Graeve, Growth kinetics and passive behavior of the native oxide film on additively manufactured AlSi10Mg versus the conventional cast alloy, Corros. Sci. 203 (2022). https://doi.org/10.1016/j.corsci.2022.110352.

[46] C. Li, W.X. Zhang, H.O. Yang, J. Wan, X.X. Huang, Y.Z. Chen, Microstructural origin of high strength and high strain hardening capability of a laser powder bed fused AlSi10Mg alloy, J. Mater. Sci. Technol. 197 (2024) 194–206. https://doi.org/10.1016/j.jmst.2024.01.067.
[47] M.S. Kenevisi, Y. Yu, F. Lin, A review on additive manufacturing of Al–Cu (2xxx) aluminium alloys, processes and defects, Materials Science and Technology (United Kingdom) 37 (2021) 805–829. https://doi.org/10.1080/02670836.2021.1958487.
[48] I. Raffeis, F. Adjei-Kyeremeh, U. Vroomen, S. Richter, A. Bührig-Polaczek, Characterising the microstructure of an additively built Al-Cu-Li alloy, Materials 13 (2020) 1–18. https://doi.org/10.3390/ma13225188.
[49] S. Bai, Z. Liu, X. Zhou, P. Xia, S. Zeng, Mg-controlled formation of Mg-Ag co-clusters in initial aged Al-Cu-Mg-Ag alloys, J. Alloys Compd. 602 (2014) 193–198. https://doi.org/10.1016/j.jallcom.2014.03.008.
[50] M. Laleh, E. Sadeghi, R.I. Revilla, Q. Chao, N. Haghdadi, A.E. Hughes, W. Xu, I. De Graeve, M. Qian, I. Gibson, M.Y. Tan, Heat treatment for metal additive manufacturing, Prog. Mater. Sci. 133 (2023). https://doi.org/10.1016/j.pmatsci.2022.101051.
[51] T. Maeshima, K. Oh-ishi, H. Kadoura, Microstructural evolution and hardening phenomenon caused by aging of AlSi10Mg alloy by laser powder bed fusion, Heliyon 10 (2024). https://doi.org/10.1016/j.heliyon.2024.e28006.
[52] M. Kaess, M. Werz, S. Weihe, Residual Stress Formation Mechanisms in Laser Powder Bed Fusion—A Numerical Evaluation, Materials 16 (2023). https://doi.org/10.3390/ma16062321.
[53] R.I. Revilla, J. Liang, S. Godet, I. De Graeve, Local Corrosion Behavior of Additive Manufactured AlSiMg Alloy Assessed by SEM and SKPFM, J. Electrochem. Soc. 164 (2017) C27–C35. https://doi.org/10.1149/2.0461702jes.
[54] S. Lorenzi, M. Cabrini, A. Carrozza, L. Gritti, L. Nani, T. Pastore, T. Tirelli, On the selective corrosion mechanism of LPBF-produced AlSi10Mg: Potentiostatic polarization effects, Electrochim. Acta 470 (2023). https://doi.org/10.1016/j.electacta.2023.143354.
[55] M. Cabrini, S. Lorenzi, T. Pastore, C. Testa, D. Manfredi, M. Lorusso, F. Calignano, M. Pavese, F. Andreatta, Corrosion behavior of AlSi10Mg alloy produced by laser powder bed fusion under chloride exposure, Corros. Sci. 152 (2019) 101–108. https://doi.org/10.1016/j.corsci.2019.03.010.
[56] P. Fathi, M. Mohammadi, X. Duan, A.M. Nasiri, A comparative study on corrosion and microstructure of direct metal laser sintered AlSi10Mg_200C and die cast A360.1 aluminum, J. Mater. Process. Technol. 259 (2018) 1–14. https://doi.org/10.1016/j.jmatprotec.2018.04.013.
[57] C. Verma, A. Alameri, I. Barsoum, A. Alfantazi, Review on corrosion-related aspects of metallic alloys additive manufactured with laser powder bed-fusion (LPBF) technology, Progress in Additive Manufacturing 10 (2025) 3195–3223. https://doi.org/10.1007/s40964-024-00810-x.
[58] G. Sander, J. Tan, P. Balan, O. Gharbi, D.R. Feenstra, L. Singer, S. Thomas, R.G. Kelly, J.R. Scully, N. Birbilis, Corrosion of additively manufactured alloys: A review, Corrosion 74 (2018) 1318–1350. https://doi.org/10.5006/2926.
[59] T. Rubben, R.I. Revilla, I. De Graeve, Influence of heat treatments on the corrosion mechanism of additive manufactured AlSi10Mg, Corros. Sci. 147 (2019) 406–415. https://doi.org/10.1016/j.corsci.2018.11.038.

[60] S. Lorenzi, A. Carrozza, M. Cabrini, L. Nani, F. Andreatta, E. Virtanen, T. Tirelli, T. Pastore, Corrosion behavior assessment of an Al-Cu alloy manufactured via laser powder bed fusion, Corros. Sci. 227 (2024). https://doi.org/10.1016/j.corsci.2023.111698.

[61] R.I. Revilla, D. Verkens, T. Rubben, I. De Graeve, Corrosion and corrosion protection of additively manufactured aluminium alloys—a critical review, Materials 13 (2020) 1–25. https://doi.org/10.3390/ma13214804.

[62] C. Örnek, Additive manufacturing–a general corrosion perspective, Corrosion Engineering Science and Technology 53 (2018) 531–535. https://doi.org/10.1080/1478422X.2018.1511327.

[63] N.N. Kumbhar, A. V. Mulay, Post Processing Methods used to Improve Surface Finish of Products which are Manufactured by Additive Manufacturing Technologies: A Review, Journal of The Institution of Engineers (India): Series C 99 (2018) 481–487. https://doi.org/10.1007/s40032-016-0340-z.

[64] M. Cabrini, S. Lorenzi, T. Pastore, S. Pellegrini, E.P. Ambrosio, F. Calignano, D. Manfredi, M. Pavese, P. Fino, Effect of heat treatment on corrosion resistance of DMLS AlSi10Mg alloy, Electrochim. Acta 206 (2016) 346–355. https://doi.org/10.1016/j.electacta.2016.04.157.

[65] M. Cabrini, F. Calignano, P. Fino, S. Lorenzi, M. Lorusso, D. Manfredi, C. Testa, T. Pastore, Corrosion behavior of heat-treated AlSi10Mg manufactured by laser powder bed fusion, Materials 11 (2018). https://doi.org/10.3390/ma11071051.

[66] L. Zhou, A. Mehta, E. Schulz, B. McWilliams, K. Cho, Y. Sohn, Microstructure, precipitates and hardness of selectively laser melted AlSi10Mg alloy before and after heat treatment, Mater. Charact. 143 (2018) 5–17. https://doi.org/10.1016/j.matchar.2018.04.022.

[67] M. Rafieazad, M. Mohammadi, A.M. Nasiri, On microstructure and early stage corrosion performance of heat treated direct metal laser sintered AlSi10Mg, Addit. Manuf. 28 (2019) 107–119. https://doi.org/10.1016/j.addma.2019.04.023.

[68] F. Bosio, P. Fino, D. Manfredi, M. Lombardi, Strengthening strategies for an Al alloy processed by in-situ alloying during laser powder bed fusion, Mater. Des. 212 (2021). https://doi.org/10.1016/j.matdes.2021.110247.

[69] B. Callegari, T.N. Lima, R.S. Coelho, The Influence of Alloying Elements on the Microstructure and Properties of Al-Si-Based Casting Alloys: A Review, Metals (Basel). 13 (2023). https://doi.org/10.3390/met13071174.

[70] J. Fiocchi, C.A. Biffi, A. Tuissi, Selective laser melting of high-strength primary AlSi9Cu3 alloy: Processability, microstructure, and mechanical properties, Mater. Des. 191 (2020). https://doi.org/10.1016/j.matdes.2020.108581.

[71] M. Roudnická, O. Molnárová, D. Dvorský, L. Křivský, D. Vojtěch, Specific Response of Additively Manufactured AlSi9Cu3Fe Alloy to Precipitation Strengthening, Metals and Materials International 26 (2020) 1168–1181. https://doi.org/10.1007/s12540-019-00504-y.

[72] L. Ilaria, G. Edoardo, M. Alessandra, B. Rachele, B. Stefania, L. Mariangela, On the role of additive manufacturing, heat treatment and machining on the microstructural evolution and corrosion behaviour of AlSi9Cu3(Fe) alloy, Mater. Charact. 224 (2025). https://doi.org/10.1016/j.matchar.2025.115089.

[73] J. Fiocchi, C. Colombo, L.M. Vergani, A. Fabrizi, G. Timelli, A. Tuissi, C.A. Biffi, materials Heat Treatments for Stress Relieving AlSi9Cu3 Alloy Produced by Laser Powder Bed Fusion, (2021). https://doi.org/10.3390/ma.

[74] A. Fabrizi, S. Capuzzi, A. De Mori, G. Timelli, Effect of T6 heat treatment on the microstructure and hardness of secondary AlSi9Cu3(Fe) alloys produced by semi-solid SEED process, Metals (Basel). 8 (2018). https://doi.org/10.3390/met8100750.
[75] S. Cecchel, G. Cornacchia, M. Gelfi, Corrosion behavior of primary and secondary AlSi high pressure die casting alloys, Materials and Corrosion 68 (2017) 961–969. https://doi.org/10.1002/maco.201709526.
[76] M. Fousova, V. Valesova, D. Vojtech, Corrosion of 3D-printed AlSi9Cu3Fe alloy, Manufacturing Technology 19 (2019) 29–36. https://doi.org/10.21062/ujep/240.2019/a/1213-2489/mt/19/1/29.
[77] M. Cabrini, S. Lorenzi, C. Testa, D. Manfredi, M. Lombardi, A. Aversa, F. Andreatta, L. Fedrizzi, Y. Dekhtyar, H. Sorokins, T. Pastore, Effect of heat treatment on microstructure and selective corrosion of lpbf-alsi10mg by means of skpfm and exo-electron emission, Materials 14 (2021). https://doi.org/10.3390/ma14195602.
[78] N. Zazi, Effect of heat treatments on the microstructure, hardness and corrosion behavior of nondendritic AlSi9Cu3(Fe) cast alloy, Medziagotyra 19 (2013) 258–263. https://doi.org/10.5755/j01.ms.19.3.1397.
[79] C. Monticelli, F. Zanotto, A. Balbo, V. Grassi, A. Fabrizi, G. Timelli, Corrosion behavior of high-pressure die-cast secondary AlSi9Cu3(Fe) alloy, Corros. Sci. 209 (2022). https://doi.org/10.1016/j.corsci.2022.110779.
[80] S. Gudić, L. Vrsalović, J. Krolo, A. Nagode, I. Dumanić Labetić, B. Lela, Corrosion Behaviour of Recycled Aluminium AlSi9Cu3(Fe) Machining Chips by Hot Extrusion and Thixoforming, Sustainability (Switzerland) 16 (2024). https://doi.org/10.3390/su16041358.
[81] S.L. dos Santos, F.R. Tolockzo, A.C.M. Neto, F.E.M. Cezario, D.M. da Silva, R.A. Antunes, Microstructural evolution and corrosion behavior of non-isothermally heat treated hypoeutectic Al-Si-Cu alloy, Next Materials 5 (2024). https://doi.org/10.1016/j.nxmate.2024.100262.
[82] A. Martucci, E. Bassini, M. Lombardi, Effect of Cu Content on the PBF-LB/M Processing of the Promising Al-Si-Cu-Mg Composition, Metals (Basel). 13 (2023). https://doi.org/10.3390/met13071315.
[83] E. Sjölander, S. Seifeddine, The heat treatment of Al-Si-Cu-Mg casting alloys, J. Mater. Process. Technol. 210 (2010) 1249–1259. https://doi.org/10.1016/j.jmatprotec.2010.03.020.
[84] L. Thijs, K. Kempen, J.P. Kruth, J. Van Humbeeck, Fine-structured aluminium products with controllable texture by selective laser melting of pre-alloyed AlSi10Mg powder, Acta Mater. 61 (2013) 1809–1819. https://doi.org/10.1016/j.actamat.2012.11.052.
[85] M. Fousova, D. Dvorsky, M. Vronka, D. Vojtech, P. Lejcek, The use of selective laser melting to increase the performance of AlSi9Cu3Fe alloy, Materials 11 (2018). https://doi.org/10.3390/ma11101918.
[86] O. Dedry, C. Bouffioux, H.S. Tran, J.G.S. Macías, A.M. Habraken, A. Mertens, Identification of AlSi10Mg matrix behavior by nanoindentation, in: ESAFORM 2021 - 24th International Conference on Material Forming, PoPuPS (University of LiFge Library), 2021. https://doi.org/10.25518/esaform21.2464.
[87] E. Rossi, J.M. Wheeler, M. Sebastiani, High-speed nanoindentation mapping: A review of recent advances and applications, Curr. Opin. Solid State Mater. Sci. 27 (2023). https://doi.org/10.1016/j.cossms.2023.101107.

[88] G. Di Egidio, L. Ceschini, A. Morri, C. Martini, M. Merlin, A Novel T6 Rapid Heat Treatment for AlSi10Mg Alloy Produced by Laser-Based Powder Bed Fusion: Comparison with T5 and Conventional T6 Heat Treatments, Metallurgical and Materials Transactions B: Process Metallurgy and Materials Processing Science 53 (2022) 284–303. https://doi.org/10.1007/s11663-021-02365-6.

[89] G. Lupi, G. Minerva, L. Patriarca, R. Casati, S. Beretta, Fracture toughness of AlSi10Mg alloy produced by LPBF: effects of orientation and heat treatment, Int. J. Fract. 247 (2024) 329–344. https://doi.org/10.1007/s10704-024-00787-2.

[90] D. Turnbull, H.S. Rosenbaum, H.N. Treaftist, KINETICS OF CLUSTERING IN SOME ALUMINUM ALLOYS*, n.d.

[91] S.L. dos Santos, F.R. Toloczko, A.C. Merij, N.H. Saito, D.M. da Silva, Investigation and nanomechanical behavior of the microconstituents of Al-Si-Cu alloy after solution and ageing heat treatments, Materials Research 24 (2021). https://doi.org/10.1590/1980-5373-MR-2020-0329.

[92] M. Fatmi, B. Ghebouli, M.A. Ghebouli, T. Chihi, M. Abdul Hafiz, The kinetics of precipitation in Al-2.4 wt% Cu alloy by Kissinger, Ozawa, Bosswel and Matusita methods, Physica B Condens. Matter 406 (2011) 2277–2280. https://doi.org/10.1016/j.physb.2011.03.053.

[93] J. Gauthier, P.R. Louchez, F.H. Samuel, Heat treatment of 319.2 aluminium automotive alloy Part 1, Solution heat treatment, Cast Metals 8 (1995) 91–106. https://doi.org/10.1080/09534962.1995.11819197.

[94] S. Bruschi, R. Bertolini, A. Ghiotti, H. Mahmood, C. Zanella, Manufacturing Letters Machinability of recycled aluminum alloys, 2024. www.sciencedirect.com.

[95] F. Bosio, I. Lagalante, D. Manfredi, M. Lombardi, Bespoke multi-step homogenization heat-treatment for a laser powder bed fused AlSi10Mg4Cu alloy synthesized via in-situ alloying, Mater. Charact. 195 (2023). https://doi.org/10.1016/j.matchar.2022.112506.

[96] W. Reif, S. Yu, J. Dutkiewicz, R. Ciach, J. Krol, Pre-ageing of AlSiCuMg alloys in relation to structure and mechanical properties, 1997.

[97] J. Pezda, J. Pezda, Effect of dispersion hardening process on change of Rm tensile strength of EN AC-46000 alloy, (n.d.). https://www.researchgate.net/publication/268203730.

[98] J. Pezda, J. Pezda, Effect of modification and heat treatment operations on impact strength of the EN AC-46000 alloy, (2010). https://www.researchgate.net/publication/267800341.

[99] J.A. Moreto, C.E.B. Marino, W.W. Bose Filho, L.A. Rocha, J.C.S. Fernandes, SVET, SKP and EIS study of the corrosion behaviour of high strength Al and Al-Li alloys used in aircraft fabrication, Corros. Sci. 84 (2014) 30–41. https://doi.org/10.1016/j.corsci.2014.03.001.

[100] G. Elatharasan, V.S.S. Kumar, Corrosion analysis of friction stir-welded aa 7075 aluminium alloy, Strojniski Vestnik/Journal of Mechanical Engineering 60 (2014) 29–34. https://doi.org/10.5545/sv-jme.2012.711.

[101] J.R. Scully, T.O. Knight, R.G. Buchheitt, D.E. Peeblest, ELECTROCHEMICAL CHARACTERISTICS OF THE AI2Cu, A13Ta AND A13Zr INTERMETALLIC PHASES AND THEIR RELEVANCY TO THE LOCALIZED CORROSION OF A1 ALLOYS, 1993.

[102] S.M.A. Mousavi, R. Pitchumani, A study of corrosion on electrodeposited superhydrophobic copper surfaces, Corros. Sci. 186 (2021). https://doi.org/10.1016/j.corsci.2021.109420.

[103] A.C. Lazanas, M.I. Prodromidis, Electrochemical Impedance Spectroscopy─A Tutorial, ACS Measurement Science Au 3 (2023) 162–193. https://doi.org/10.1021/acsmeasuresciau.2c00070.
[104] C. Örnek, C. Leygraf, J. Pan, Real-Time Corrosion Monitoring of Aluminum Alloy Using Scanning Kelvin Probe Force Microscopy, J. Electrochem. Soc. 167 (2020) 081502. https://doi.org/10.1149/1945-7111/ab8826.
[105] T. Rubben, R.I. Revilla, I. De Graeve, Influence of heat treatments on the corrosion mechanism of additive manufactured AlSi10Mg, Corros. Sci. 147 (2019) 406–415. https://doi.org/10.1016/j.corsci.2018.11.038.
[106] D. Culliton, A.J. Betts, D. Kennedy, Impact of intermetallic precipitates on the tribological and/or corrosion performance of cast aluminium alloys: A short review, International Journal of Cast Metals Research 26 (2013) 65–71. https://doi.org/10.1179/1743133612Y.0000000038.
[107] H.R. Kotadia, G. Gibbons, A. Das, P.D. Howes, A review of Laser Powder Bed Fusion Additive Manufacturing of aluminium alloys: Microstructure and properties, Addit. Manuf. 46 (2021). https://doi.org/10.1016/j.addma.2021.102155.
[108] C. Zhang, H. Zhu, H. Liao, Y. Cheng, Z. Hu, X. Zeng, Effect of heat treatments on fatigue property of selective laser melting AlSi10Mg, Int. J. Fatigue 116 (2018) 513–522. https://doi.org/10.1016/j.ijfatigue.2018.07.016.
[109] C.A. Brice, W.A. Tayon, J.A. Newman, M. V. Kral, C. Bishop, A. Sokolova, Effect of compositional changes on microstructure in additively manufactured aluminum alloy 2139, Mater. Charact. 143 (2018) 50–58. https://doi.org/10.1016/j.matchar.2018.04.002.
[110] Y. Sai, S.K. Ladhad, R. Ramesh, N.A. Bandekar, M.B. Khot, Design Optimization and Fabrication of Metal 3D Printed Wheel Hub Using AlSi10Mg: A Comprehensive Review, Journal of Advanced Manufacturing Systems 25 (2026) 65–111. https://doi.org/10.1142/S0219686726500046.
[111] E. Brandl, U. Heckenberger, V. Holzinger, D. Buchbinder, Additive manufactured AlSi10Mg samples using Selective Laser Melting (SLM): Microstructure, high cycle fatigue, and fracture behavior, Mater. Des. 34 (2012) 159–169. https://doi.org/10.1016/j.matdes.2011.07.067.
[112] E. Padovano, C. Badini, A. Pantarelli, F. Gili, F. D'Aiuto, A comparative study of the effects of thermal treatments on AlSi10Mg produced by laser powder bed fusion, J. Alloys Compd. 831 (2020). https://doi.org/10.1016/j.jallcom.2020.154822.
[113] R. Li, M. Wang, Z. Li, P. Cao, T. Yuan, H. Zhu, Developing a high-strength Al-Mg-Si-Sc-Zr alloy for selective laser melting: Crack-inhibiting and multiple strengthening mechanisms, Acta Mater. 193 (2020) 83–98. https://doi.org/10.1016/j.actamat.2020.03.060.
[114] O. Zobac, A. Kroupa, A. Zemanova, K.W. Richter, Experimental Description of the Al-Cu Binary Phase Diagram, Metall. Mater. Trans. A Phys. Metall. Mater. Sci. 50 (2019) 3805–3815. https://doi.org/10.1007/s11661-019-05286-x.
[115] C. Li, W.X. Zhang, H.O. Yang, J. Wan, X.X. Huang, Y.Z. Chen, Microstructural origin of high strength and high strain hardening capability of a laser powder bed fused AlSi10Mg alloy, J. Mater. Sci. Technol. 197 (2024) 194–206. https://doi.org/10.1016/j.jmst.2024.01.067.
[116] Q. Han, Y. Jiao, Effect of heat treatment and laser surface remelting on AlSi10Mg alloy fabricated by selective laser melting, International Journal of Advanced Manufacturing Technology 102 (2019) 3315–3324. https://doi.org/10.1007/s00170-018-03272-y.

[117] F. Trevisan, F. Calignano, M. Lorusso, J. Pakkanen, A. Aversa, E.P. Ambrosio, M. Lombardi, P. Fino, D. Manfredi, On the selective laser melting (SLM) of the AlSi10Mg alloy: Process, microstructure, and mechanical properties, Materials 10 (2017). https://doi.org/10.3390/ma10010076.
[118] K. Vašáková, J. Judas, J. Čupera, L. Pantělejev, D. Koutný, Effects of heat treatment on microstructure and mechanical properties of LPBF AlSi9Cu3 alloy, in: Procedia Structural Integrity, Elsevier B.V., 2025: pp. 99–105. https://doi.org/10.1016/j.prostr.2025.10.040.
[119] R. Ramesh, S. Gairola, R. Jayaganthan, M. Kamaraj, Microstructural evolution, mechanical behaviour and strengthening mechanisms of additively manufactured AlSi9Cu3 alloy, Journal of Materials Research and Technology 40 (2026) 1738–1752. https://doi.org/10.1016/j.jmrt.2025.12.221.
[120] J. Suchy, L. Pantelejev, D. Palousek, D. Koutny, J. Kaiser, Processing of AlSi9Cu3 alloy by selective laser melting, Powder Metallurgy 63 (2020) 197–211. https://doi.org/10.1080/00325899.2020.1792675.
[121] EOS Aluminium Al2139 AM Material Data Sheet Metal Solutions, n.d.
[122] A. Spadoni, M. Ruzzene, Mechanics of Materials and Structures NUMERICAL AND EXPERIMENTAL ANALYSIS OF THE STATIC COMPLIANCE OF CHIRAL TRUSS-CORE AIRFOILS NUMERICAL AND EXPERIMENTAL ANALYSIS OF THE STATIC COMPLIANCE OF CHIRAL TRUSS-CORE AIRFOILS, 2007.
[123] X. Ren, R. Das, P. Tran, T.D. Ngo, Y.M. Xie, Auxetic metamaterials and structures: A review, Smart Mater. Struct. 27 (2018). https://doi.org/10.1088/1361-665X/aaa61c.
[124] C.F. Bănică, A. Sover, D.C. Anghel, Printing the Future Layer by Layer: A Comprehensive Exploration of Additive Manufacturing in the Era of Industry 4.0, Applied Sciences (Switzerland) 14 (2024). https://doi.org/10.3390/app14219919.
[125] N. Khan, A. Riccio, A systematic review of design for additive manufacturing of aerospace lattice structures: Current trends and future directions, Progress in Aerospace Sciences 149 (2024). https://doi.org/10.1016/j.paerosci.2024.101021.
[126] D.J. Yoo, Computer-aided porous scaffold design for tissue engineering using triply periodic minimal surfaces, International Journal of Precision Engineering and Manufacturing 12 (2011) 61–71. https://doi.org/10.1007/s12541-011-0008-9.
[127] C.M. Bidan, K.P. Kommareddy, M. Rumpler, P. Kollmannsberger, P. Fratzl, J.W.C. Dunlop, Geometry as a Factor for Tissue Growth: Towards Shape Optimization of Tissue Engineering Scaffolds, Adv. Healthc. Mater. 2 (2013) 186–194. https://doi.org/10.1002/adhm.201200159.
[128] L. Chougrani, J.P. Pernot, P. Véron, S. Abed, Parts internal structure definition using non-uniform patterned lattice optimization for mass reduction in additive manufacturing, Eng. Comput. 35 (2019) 277–289. https://doi.org/10.1007/s00366-018-0598-2.
[129] J. Bühring, M. Nuño, K.U. Schröder, Additive manufactured sandwich structures: Mechanical characterization and usage potential in small aircraft, Aerosp. Sci. Technol. 111 (2021). https://doi.org/10.1016/j.ast.2021.106548.
[130] C. Borsellino, G. Di Bella, Paper-reinforced biomimetic cellular structures for automotive applications, Mater. Des. 30 (2009) 4054–4059. https://doi.org/10.1016/j.matdes.2009.05.013.
[131] L. Riva, P.S. Ginestra, E. Ceretti, Mechanical characterization and properties of laser-based powder bed-fused lattice structures: a review, (n.d.). https://doi.org/10.1007/s00170-021-06631-4/Published.

[132] M. Leary, M. Mazur, J. Elambasseril, M. McMillan, T. Chirent, Y. Sun, M. Qian, M. Easton, M. Brandt, Selective laser melting (SLM) of AlSi12Mg lattice structures, Mater. Des. 98 (2016) 344–357. https://doi.org/10.1016/j.matdes.2016.02.127.
[133] A. Pirinu, T. Primo, A. Del Prete, F.W. Panella, F. De Pascalis, Mechanical behaviour of AlSi10Mg lattice structures manufactured by the Selective Laser Melting (SLM), International Journal of Advanced Manufacturing Technology 124 (2023) 1651–1680. https://doi.org/10.1007/s00170-022-10390-1.
[134] A. Alghamdi, T. Maconachie, D. Downing, M. Brandt, M. Qian, M. Leary, Effect of additive manufactured lattice defects on mechanical properties: an automated method for the enhancement of lattice geometry, International Journal of Advanced Manufacturing Technology 108 (2020) 957–971. https://doi.org/10.1007/s00170-020-05394-8.
[135] U. Hossain, S. Ghouse, K. Nai, J.R. Jeffers, Controlling and testing anisotropy in additively manufactured stochastic structures, Addit. Manuf. 39 (2021). https://doi.org/10.1016/j.addma.2021.101849.
[136] M. Munford, U. Hossain, S. Ghouse, J.R.T. Jeffers, Prediction of anisotropic mechanical properties for lattice structures, Addit. Manuf. 32 (2020). https://doi.org/10.1016/j.addma.2020.101041.
[137] W. Brooks, C. Sutcliffe, W. Cantwell, J. Todd, R. Mines, Rapid design and manufacture of ultralight cellular materials, (2005).
[138] S. Kechagias, R.N. Oosterbeek, M.J. Munford, S. Ghouse, J.R.T. Jeffers, Controlling the mechanical behaviour of stochastic lattice structures: The key role of nodal connectivity, Addit. Manuf. 54 (2022). https://doi.org/10.1016/j.addma.2022.102730.
[139] M.F. Ashby, The properties of foams and lattices, Philosophical Transactions of the Royal Society A: Mathematical, Physical and Engineering Sciences 364 (2006) 15–30. https://doi.org/10.1098/rsta.2005.1678.
[140] M. Leary, Design of titanium implants for additive manufacturing, in: Titanium in Medical and Dental Applications, Elsevier, 2018: pp. 203–224. https://doi.org/10.1016/B978-0-12-812456-7.00009-3.
[141] M. Benedetti, A. du Plessis, R.O. Ritchie, M. Dallago, N. Razavi, F. Berto, Architected cellular materials: A review on their mechanical properties towards fatigue-tolerant design and fabrication, Materials Science and Engineering R: Reports 144 (2021). https://doi.org/10.1016/j.mser.2021.100606.
[142] T.A. Alwattar, A. Mian, Development of an elastic material model for bcc lattice cell structures using finite element analysis and neural networks approaches, Journal of Composites Science 3 (2019). https://doi.org/10.3390/jcs3020033.
[143] A. Koeppe, C.A. Hernandez Padilla, M. Voshage, J.H. Schleifenbaum, B. Markert, Efficient numerical modeling of 3D-printed lattice-cell structures using neural networks, Manuf. Lett. 15 (2018) 147–150. https://doi.org/10.1016/j.mfglet.2018.01.002.
[144] C. Pisarciuc, I. Dan, R. Cioară, The Influence of Mesh Density on the Results Obtained by Finite Element Analysis of Complex Bodies, Materials 16 (2023) 2555. https://doi.org/10.3390/ma16072555.
[145] S. Ruiz de Galarreta, J.R.T. Jeffers, S. Ghouse, A validated finite element analysis procedure for porous structures, Mater. Des. 189 (2020). https://doi.org/10.1016/j.matdes.2020.108546.

[146] C. Florence, K. Sab, A rigorous homogenization method for the determination of the overall ultimate strength of periodic discrete media and an application to general hexagonal lattices of beams, European Journal of Mechanics, A/Solids 25 (2006) 72–97. https://doi.org/10.1016/j.euromechsol.2005.06.011.
[147] G. Dong, Y. Tang, Y.F. Zhao, A survey of modeling of lattice structures fabricated by additive manufacturing, Journal of Mechanical Design 139 (2017). https://doi.org/10.1115/1.4037305.
[148] D.M. Kochmann, J.B. Hopkins, L. Valdevit, Multiscale modeling and optimization of the mechanics of hierarchical metamaterials, MRS Bull. 44 (2019) 773–781. https://doi.org/10.1557/mrs.2019.228.
[149] R.N. Glaesener, C. Lestringant, B. Telgen, D.M. Kochmann, Continuum models for stretching- and bending-dominated periodic trusses undergoing finite deformations, Int. J. Solids Struct. 171 (2019) 117–134. https://doi.org/10.1016/j.ijsolstr.2019.04.022.
[150] M. Shojaee, I. Valizadeh, D.K. Klein, P. Sharifi, O. Weeger, Multiscale modeling of functionally graded shell lattice metamaterials for additive manufacturing, Eng. Comput. 40 (2024) 2019–2036. https://doi.org/10.1007/s00366-023-01906-8.
[151] J.C. Mehta, M. Salviato, J. Wollschlager, Multiscale Optimization of Weav3D Lattice-Reinforced Composites for Lightweight Structural Design, 2025.
[152] N. Cardone, Strategie di ottimizzazione topologica di strutture lattice da produrre mediante Fabbricazione Additiva, n.d.
[153] O. Abdelaal, F. Hengsbach, M. Schaper, K.P. Hoyer, LPBF Manufactured Functionally Graded Lattice Structures Obtained by Graded Density and Hybrid Poisson's Ratio, Materials 15 (2022). https://doi.org/10.3390/ma15124072.
[154] M. Dallago, B. Winiarski, F. Zanini, S. Carmignato, M. Benedetti, On the effect of geometrical imperfections and defects on the fatigue strength of cellular lattice structures additively manufactured via Selective Laser Melting, Int. J. Fatigue 124 (2019) 348–360. https://doi.org/10.1016/j.ijfatigue.2019.03.019.
[155] R. De Biasi, Simulations techniques for lattice structure design, 2024.
[156] P. Zhang, F. Bai, Y. Liu, Y. Ma, W. Zeng, Y.J. Yang, L. Liu, W. Wang, Design and optimization of high stiffness tetrahedral lattice structure, Addit. Manuf. 102 (2025). https://doi.org/10.1016/j.addma.2025.104719.
[157] D. Zhang, S. Sun, D. Qiu, M.A. Gibson, M.S. Dargusch, M. Brandt, M. Qian, M. Easton, Metal Alloys for Fusion-Based Additive Manufacturing, Adv. Eng. Mater. 20 (2018). https://doi.org/10.1002/adem.201700952.
[158] Datasheet_Aidro_AlSi10Mg_30um, (n.d.).
[159] G. Pollara, D. Palmeri, R. Licari, A. Barcellona, On the Effect of the Cell Size and Beam Radius on the Compressive Strength and Residual Stresses of Ti-6Al-4V BCC Lattice Sandwich Structures Manufactured by L-PBF, Journal of Manufacturing and Materials Processing 9 (2025). https://doi.org/10.3390/jmmp9060192.
[160] Y. Xu, X. Li, G. Han, T. Li, L. Chen, H. Li, The Effect of Number and Size of Cellular Structures on Compressive Properties, Deformation Behavior, and Energy Absorption Characteristics of Ti6Al4V Lattice Structures Fabricated by Selective Laser Melting, Adv. Eng. Mater. (2025). https://doi.org/10.1002/adem.202501328.
[161] U. Zerbst, G. Bruno, J.Y. Buffière, T. Wegener, T. Niendorf, T. Wu, X. Zhang, N. Kashaev, G. Meneghetti, N. Hrabe, M. Madia, T. Werner, K. Hilgenberg, M. Koukolíková, R.

Procházka, J. Džugan, B. Möller, S. Beretta, A. Evans, R. Wagener, K. Schnabel, Damage tolerant design of additively manufactured metallic components subjected to cyclic loading: State of the art and challenges, Prog. Mater. Sci. 121 (2021). https://doi.org/10.1016/j.pmatsci.2021.100786.

[162] E. Yang, M. Leary, B. Lozanovski, D. Downing, M. Mazur, A. Sarker, A.M. Khorasani, A. Jones, T. Maconachie, S. Bateman, M. Easton, M. Qian, P. Choong, M. Brandt, Effect of geometry on the mechanical properties of Ti-6Al-4V Gyroid structures fabricated via SLM: A numerical study, Mater. Des. 184 (2019). https://doi.org/10.1016/j.matdes.2019.108165.

[163] K.M. Park, Y.S. Roh, B.C. Lee, Effects of the unit-cell size and arrangement on the compressive behaviors of lattice structures in powder bed fusion additive manufacturing, Results in Materials 22 (2024). https://doi.org/10.1016/j.rinma.2024.100587.

[164] R. Gandhi, M. Salmi, B. Roy, L. Paglari, F. Concli, Mechanical performance, fatigue behaviour, and biointegration of additively manufactured architected lattices, Virtual Phys. Prototyp. 20 (2025). https://doi.org/10.1080/17452759.2025.2530733.

[165] H. Zhong, T. Song, C. Li, R. Das, J. Gu, M. Qian, The Gibson-Ashby model for additively manufactured metal lattice materials: Its theoretical basis, limitations and new insights from remedies, Curr. Opin. Solid State Mater. Sci. 27 (2023). https://doi.org/10.1016/j.cossms.2023.101081.

[166] V.S. Deshpande, M.F. Ashby, N.A. Fleck, FOAM TOPOLOGY BENDING VERSUS STRETCHING DOMINATED ARCHITECTURES, 2001. www.elsevier.com/locate/actamat.

[167] A. du Plessis, N. Razavi, M. Benedetti, S. Murchio, M. Leary, M. Watson, D. Bhate, F. Berto, Properties and applications of additively manufactured metallic cellular materials: A review, Prog. Mater. Sci. 125 (2022). https://doi.org/10.1016/j.pmatsci.2021.100918.

[168] L.Y. Chen, S.X. Liang, Y. Liu, L.C. Zhang, Additive manufacturing of metallic lattice structures: Unconstrained design, accurate fabrication, fascinated performances, and challenges, Materials Science and Engineering R: Reports 146 (2021). https://doi.org/10.1016/j.mser.2021.100648.

[169] P. Gradl, D.C. Tinker, A. Park, O.R. Mireles, M. Garcia, R. Wilkerson, C. Mckinney, Robust Metal Additive Manufacturing Process Selection and Development for Aerospace Components, J. Mater. Eng. Perform. 31 (2022) 6013–6044. https://doi.org/10.1007/s11665-022-06850-0.

[170] A. Schwarz, M. Schleser, B. Gerhards, P. Popoola, A. Gebhardt, WELDING OF ADDITIVE MANUFACTURED ALSI10MG: USING LASER WELDING IN A VACUUM FOR HIGH QUALITY WELD SEAMS — A NEW APPROACH TO WELDING LPBF MANUFACTURED ALSI10MG, South African Journal of Industrial Engineering 32 (2021) 99–112. https://doi.org/10.7166/32-4-2513.

[171] J. Yang, Y. Wang, F. Li, W. Huang, G. Jing, Z. Wang, X. Zeng, Weldability, microstructure and mechanical properties of laser-welded selective laser melted 304 stainless steel joints, J. Mater. Sci. Technol. 35 (2019) 1817–1824. https://doi.org/10.1016/j.jmst.2019.04.017.

[172] A. Ascari, A. Fortunato, E. Liverani, A. Gamberoni, L. Tomesani, New possibilities in the fabrication of hybrid components with big dimensions by means of Selective Laser Melting (SLM), in: Phys. Procedia, Elsevier B.V., 2016: pp. 839–846. https://doi.org/10.1016/j.phpro.2016.08.087.

[173] Y. Huang, P. li Liu, H. Xiang, S. xi Deng, Y. jie Guo, J. feng Li, Mechanical properties, corrosion and microstructure distribution of a 2195-T8 Al[sbnd]Li alloy TIG welded joint, J. Manuf. Process. 90 (2023) 151–165. https://doi.org/10.1016/j.jmapro.2023.02.007.
[174] L. Cui, D. Wu, Y. Chang, X. Guo, X. Wu, W. Shao, D. He, Microstructural evolution and mechanical property of friction stir welded joints in AlSi10Mg alloys fabricated by laser powder bed fusion, CIRP J. Manuf. Sci. Technol. 47 (2023) 228–243. https://doi.org/10.1016/j.cirpj.2023.11.002.
[175] M. Olabode, P. Kah, J. Martikainen, Aluminium alloys welding processes: Challenges, joint types and process selection, Proc. Inst. Mech. Eng. B J. Eng. Manuf. 227 (2013) 1129–1137. https://doi.org/10.1177/0954405413484015.
[176] T. DebRoy, T. Mukherjee, H.L. Wei, J.W. Elmer, J.O. Milewski, Metallurgy, mechanistic models and machine learning in metal printing, Nat. Rev. Mater. 6 (2021) 48–68. https://doi.org/10.1038/s41578-020-00236-1.
[177] G.A. Rao, B.R. Kumar, G.N. Kumar, P. Mahender, T.U. Kumar, Study the effect process of parameters on friction welding of dissimilar metals AISI 304 steel and AA 2219 aluminium, in: AIP Conf. Proc., American Institute of Physics Inc., 2021. https://doi.org/10.1063/5.0036450.
[178] R.P. Verma, K.N. Pandey, K. András, R. Khargotra, T. Singh, Difficulties and redressal in joining of aluminium alloys by GMA and GTA welding: a review, Journal of Materials Research and Technology 23 (2023) 2576–2586. https://doi.org/10.1016/j.jmrt.2023.01.183.
[179] L. Zaraska, G.D. Sulka, J. Szeremeta, M. Jaskuła, Porous anodic alumina formed by anodization of aluminum alloy (AA1050) and high purity aluminum, Electrochim. Acta 55 (2010) 4377–4386. https://doi.org/10.1016/j.electacta.2009.12.054.
[180] M. Olabode, P. Kah, E. Hiltunen, J. Martikainen, Effect of Al2O3 film on the mechanical properties of a welded high-strength (AW7020) aluminium alloy, Engineering Manufacture (2015). https://doi.org/10.1177/0954405415600678.
[181] M. Mazur, Porosity in aluminium welds, Welding International 6 (1992) 929–931. https://doi.org/10.1080/09507119209548317.
[182] Gene. Mathers, The welding of aluminium and its alloys, CRC Press ; Woodhead Pub., 2002.
[183] F. Beckmann, C. Emmelmann, Optimization of the weldability of laser additive manufactured aluminum by means of hydrogen minimization in the component and welding parameter optimization, n.d.
[184] C. Weingarten, D. Buchbinder, N. Pirch, W. Meiners, K. Wissenbach, R. Poprawe, Formation and reduction of hydrogen porosity during selective laser melting of AlSi10Mg, J. Mater. Process. Technol. 221 (2015) 112–120. https://doi.org/10.1016/j.jmatprotec.2015.02.013.
[185] X. Zhan, Y. Zhao, Z. Liu, Q. Gao, H. Bu, Microstructure and porosity characteristics of 5A06 aluminum alloy joints using laser-MIG hybrid welding, J. Manuf. Process. 35 (2018) 437–445. https://doi.org/10.1016/j.jmapro.2018.08.011.
[186] R.D. Ardika, T. Triyono, N. Muhayat, Triyono, A review porosity in aluminum welding, in: Procedia Structural Integrity, Elsevier B.V., 2021: pp. 171–180. https://doi.org/10.1016/j.prostr.2021.10.021.
[187] J. Yu, D. Kim, Effects of welding current and torch position parameters on minimizing the weld porosity of zinc-coated steel, International Journal of Advanced Manufacturing Technology 95 (2018) 551–567. https://doi.org/10.1007/s00170-017-1180-6.

[188] W. Qiang, G. Yingchun, C. Baoqiang, Q. Bojin, Laser cleaning of commercial Al alloy surface for tungsten inert gas welding, J. Laser Appl. 28 (2016). https://doi.org/10.2351/1.4943909.
[189] K. Li, F. Lu, H. Cui, X. Li, X. Tang, Z. Li, Investigation on the effects of shielding gas on porosity in fiber laser welding of T-joint steels, International Journal of Advanced Manufacturing Technology 77 (2015) 1881–1888. https://doi.org/10.1007/s00170-014-6538-4.
[190] M. Olabode, P. Kah, A. Salminen, M. Olabode, P. Kah, A. Salminen, OVERVIEW OF LASER SYSTEMS AND OPTICS APPLICABLE TO HYBRID LASER WELDING OF ALUMINIUM ALLOYS, 2015.
[191] J. Cheng, G. Song, X. Zhang, C. Liu, L. Liu, Review of techniques for improvement of softening behavior of age-hardening aluminum alloy welded joints, Materials 14 (2021). https://doi.org/10.3390/ma14195804.
[192] R.P. Verma, M. Kumar Lila, A short review on aluminium alloys and welding in structural applications, in: Mater. Today Proc., Elsevier Ltd, 2021: pp. 10687–10691. https://doi.org/10.1016/j.matpr.2021.01.447.
[193] Z.Y. Zhu, C.Y. Deng, Y. Wang, Z.W. Yang, J.K. Ding, D.P. Wang, Effect of post weld heat treatment on the microstructure and corrosion behavior of AA2219 aluminum alloy joints welded by variable polarity tungsten inert gas welding, Mater. Des. 65 (2015) 1075–1082. https://doi.org/10.1016/j.matdes.2014.10.056.
[194] M. Ahmed, M. Javidani, A. Maltais, X.G. Chen, Microstructure and Mechanical Properties of High-Strength AA6011 Aluminum Alloy Welding with Novel 4xxx Filler Metals, Materials 17 (2024). https://doi.org/10.3390/ma17020380.
[195] M. Pakdil, G. Çam, M. Koçak, S. Erim, Microstructural and mechanical characterization of laser beam welded AA6056 Al-alloy, Materials Science and Engineering: A 528 (2011) 7350–7356. https://doi.org/10.1016/j.msea.2011.06.010.
[196] M. Nahmany, I. Rosenthal, I. Benishti, N. Frage, A. Stern, Electron beam welding of AlSi10Mg workpieces produced by selected laser melting additive manufacturing technology, Addit. Manuf. 8 (2015) 63–70. https://doi.org/10.1016/j.addma.2015.08.002.
[197] C. Zhang, Y. Bao, H. Zhu, X. Nie, W. Zhang, S. Zhang, X. Zeng, A comparison between laser and TIG welding of selective laser melted AlSi10Mg, Opt. Laser Technol. 120 (2019). https://doi.org/10.1016/j.optlastec.2019.105696.
[198] V. Fahimpour, S.K. Sadrnezhaad, F. Karimzadeh, Corrosion behavior of aluminum 6061 alloy joined by friction stir welding and gas tungsten arc welding methods, Mater. Des. 39 (2012) 329–333. https://doi.org/10.1016/j.matdes.2012.02.043.
[199] G. Mathers, Weld defects and quality control, in: The Welding of Aluminium and Its Alloys, Elsevier, 2002: pp. 199–215. https://doi.org/10.1533/9781855737631.199.
[200] R. García, V.H. López, E. Bedolla, Welding of aluminium by the MIG process with indirect electric arc (MIG-IEA), J. Mater. Sci. 42 (2007) 7956–7963. https://doi.org/10.1007/s10853-006-1287-x.
[201] P.L. Threadgilll, A.J. Leonard, H.R. Shercliff, P.J. Withers, Friction stir welding of aluminium alloys, International Materials Reviews 54 (2009) 49–93. https://doi.org/10.1179/174328009X411136.
[202] Z. Du, H.C. Chen, M.J. Tan, G. Bi, C.K. Chua, Investigation of porosity reduction, microstructure and mechanical properties for joining of selective laser melting fabricated

aluminium composite via friction stir welding, J. Manuf. Process. 36 (2018) 33–43. https://doi.org/10.1016/j.jmapro.2018.09.024.
[203] F. Scherillo, A. Astarita, U. Prisco, V. Contaldi, P. di Petta, A. Langella, A. Squillace, Friction Stir Welding of AlSi10Mg Plates Produced by Selective Laser Melting, Metallography, Microstructure, and Analysis 7 (2018) 457–463. https://doi.org/10.1007/s13632-018-0465-y.
[204] Y.S. Sato, M. Urata, H. Kokawa, Parameters Controlling Microstructure and Hardness during Friction-Stir Welding of Precipitation-Hardenable Aluminum Alloy 6063, n.d.
[205] Y.S. Sato, F. Yamashita, Y. Sugiura, S.H.C. Park, H. Kokawa, FIB-assisted TEM study of an oxide array in the root of a friction stir welded aluminium alloy, Scr. Mater. 50 (2004) 365–369. https://doi.org/10.1016/j.scriptamat.2003.10.008.
[206] M. Jariyaboon, A.J. Davenport, R. Ambat, B.J. Connolly, S.W. Williams, D.A. Price, The effect of welding parameters on the corrosion behaviour of friction stir welded AA2024-T351, Corros. Sci. 49 (2007) 877–909. https://doi.org/10.1016/j.corsci.2006.05.038.
[207] A. Saxena, K.K. Saxena, B. Singh, S.K. Rajput, B. Yelamasetti, Study and effect of GTAW parameters on mechanical properties of aluminium dissimilar welded joints: optimization technique, International Journal on Interactive Design and Manufacturing 18 (2024) 1231–1241. https://doi.org/10.1007/s12008-023-01683-0.
[208] T. Luijendijk, Welding of dissimilar aluminium alloys, n.d.
[209] B. Yelamasetti, G. Venkat Ramana, T. Vishnu Vardhan, Weldability and mechanical properties of AA5052 and AA7075 dissimilar joints developed by GTAW process, in: Mater. Today Proc., Elsevier Ltd, 2021: pp. 4162–4166. https://doi.org/10.1016/j.matpr.2021.04.446.
[210] E.A. Gadallah, M.I.A. El Aal, A.Y. Mohamed, H.H. El-Fahhar, Effects of filler on the microstructure and corrosion of similar and dissimilar gas inert tungsten arc welding aluminum alloys joints, Sci. Rep. 13 (2023). https://doi.org/10.1038/s41598-023-44421-y.
[211] Application of Friction Stir Welding to Dissimilar Welding, (n.d.).
[212] M.O.M. Segaetsho, V. Msomi, V. Moni, Corrosion behaviour of friction stir welded dissimilar joints produced from AA5083 and other alloys of aluminium: A critical review, Mater. Today Proc. 56 (2022) 1696–1701. https://doi.org/10.1016/j.matpr.2021.10.333.
[213] N. Sabarirajan, A.N. Sait, S. Thanikodi, J. Giri, A novel technique to examine the corrosion resistance of FSW dissimilar aluminium alloys under three different corrosion solutions, International Journal of Advanced Manufacturing Technology 136 (2025) 133–144. https://doi.org/10.1007/s00170-024-13879-z.
[214] L. Cui, Z. Peng, Y. Chang, D. He, Q. Cao, X. Guo, Y. Zeng, Porosity, microstructure and mechanical property of welded joints produced by different laser welding processes in selective laser melting AlSi10Mg alloys, Opt. Laser Technol. 150 (2022). https://doi.org/10.1016/j.optlastec.2022.107952.
[215] A. Thakur, V. Sharma, N. Minhas, S. Manda, V.S. Sharma, Microstructure and mechanical properties of dissimilar friction stir welded joints of laser powder bed fusion processed AlSi10Mg and conventional hot rolled 6061-T6 thin sheets, Opt. Laser Technol. 163 (2023). https://doi.org/10.1016/j.optlastec.2023.109382.
[216] S. Fritsche, J. Draper, A. Toumpis, A. Galloway, S.T. Amancio-Filho, Refill friction stir spot welding of AlSi10Mg alloy produced by laser powder bed fusion to wrought AA7075-T6 alloy, Manuf. Lett. 34 (2022) 78–81. https://doi.org/10.1016/j.mfglet.2022.09.010.

[217] C.S. Paglia, R.G. Buchheit, A look in the corrosion of aluminum alloy friction stir welds, Scr. Mater. 58 (2008) 383–387. https://doi.org/10.1016/j.scriptamat.2007.10.043.
[218] S. Wu, X. Yu, R. Zuo, W. Zhang, H. Xie, J. Jiang, Porosity, Element Loss and Strength Model on Softening Behavior of Hybrid Laser Arc Welded Al-Zn-Mg-Cu Alloy with Synchrotron Radiation Analysis, (2013). https://doi.org/10.1016/j.optlastec.2019.105696.
[219] V. Dimatteo, E. Liverani, A. Ascari, A. Fortunato, Weldability and mechanical properties of dissimilar laser welded aluminum alloys thin sheets produced by conventional rolling and Additive Manufacturing, J. Mater. Process. Technol. 302 (2022). https://doi.org/10.1016/j.jmatprotec.2022.117512.
[220] W. Fyen, F. Holsteyns, T. Bearda, S. Arnauts, J. Van Steenbergen, G. Doumen, K. Kenis, P.W. Mertens, A Detailed Study of Semiconductor Wafer Drying, in: Developments in Surface Contamination and Cleaning: Second Edition, Elsevier Inc., 2008: pp. 795–854. https://doi.org/10.1016/B978-0-323-29960-2.00019-8.
[221] R. Nunes, K. Faes, W. De Waele, A. Simar, W. Verlinde, M. Lezaack, W. Sneyers, J. Arnhold, A Review on the Weldability of Additively Manufactured Aluminium Parts by Fusion and Solid-State Welding Processes, Metals (Basel). 13 (2023). https://doi.org/10.3390/met13101724.
[222] H. Yi, L. Yang, L. Jia, Y. Huang, H. Cao, Porosity in wire-arc directed energy deposition of aluminum alloys: Formation mechanisms, influencing factors and inhibition strategies, Addit. Manuf. 84 (2024). https://doi.org/10.1016/j.addma.2024.104108.
[223] W. Song, J. Du, Y. Xu, B. Long, A study of hydrogen permeation in aluminum alloy treated by various oxidation processes, 1997.
[224] S.R. Sri, R. Devi, G.P. Rao, C.U. Kiranmai, Partially Melted Zone in A356 Al-Si Alloy Welds-Effect of Technique and Prior Condition, n.d.
[225] R. Xu, R. Li, T. Yuan, C. Yu, H. Zhu, Towards the hydrogen pore in additively manufactured AlMgScZr alloy: Influencing factors, formation kinetics mechanism, J. Mater. Sci. Technol. 199 (2024) 125–144. https://doi.org/10.1016/j.jmst.2024.01.092.
[226] X.F. Tan, M. Kim, Q. Gu, J. Pinzon Piraquive, G. Zeng, S.D. McDonald, K. Nogita, Na-modified cast hypo-eutectic Mg–Mg2Si alloys for solid-state hydrogen storage, J. Power Sources 538 (2022). https://doi.org/10.1016/j.jpowsour.2022.231538.
[227] A.M. Samuel, E. Samuel, V. Songmene, F.H. Samuel, A Review on Porosity Formation in Aluminum-Based Alloys, Materials 16 (2023). https://doi.org/10.3390/ma16052047.
[228] H. Ji, Y. Hu, R. Yu, S. Liu, W. Pei, B. Wang, Experimental study on TIG full welding and single pass welding quality of 6061-T6 aluminum alloy sheet, Journal of Materials Research and Technology 27 (2023) 5965–5976. https://doi.org/10.1016/j.jmrt.2023.11.043.
[229] Z. Zhang, S. Dong, Y. Wang, B. Xu, J. Fang, P. He, Microstructure characteristics of thick aluminum alloy plate joints welded by fiber laser, Mater. Des. 84 (2015) 173–177. https://doi.org/10.1016/j.matdes.2015.06.087.
[230] Q. Chu, R. Bai, H. Jian, Z. Lei, N. Hu, C. Yan, Microstructure, texture and mechanical properties of 6061 aluminum laser beam welded joints, Mater. Charact. 137 (2018) 269–276. https://doi.org/10.1016/j.matchar.2018.01.030.
[231] R. Casanueva, C. Brañas, F.J. Diaz, F.J. Azcondo, D. Ferreño, J. Setien, Characterization of an energy efficient pulsed current TIG welding process on AISI 316 and 304 stainless steels, Heliyon 9 (2023). https://doi.org/10.1016/j.heliyon.2023.e19819.

[232] I.M. Rani, R.N. Marpu, Effect of Pulsed Current Tig Welding Parameters on Mechanical Properties of J-Joint Strength of Aa6351, (2012). www.theijes.com.
[233] C.A. J, K.T. Thilagham, High Frequency Gas Tungsten Arc Welding Process for Dressing of Weldment, International Journal of Advanced Engineering Research and Science 4 (2017) 229–235. https://doi.org/10.22161/ijaers.4.3.37.
[234] Z. Zhang, Z. Zhao, X. Li, B. Wang, P. Bai, Effect of Direct Aging on Corrosion Behavior of AlSi10Mg Alloy Fabricated by Laser Powder Bed Fusion, Acta Metallurgica Sinica (English Letters) 37 (2024) 266–282. https://doi.org/10.1007/s40195-023-01628-2.
[235] S. Lorenzi, D. Asperti, M. Cabrini, L. Nani, M. Lombardi, I. Lagalante, A. Martucci, T. Pastore, The effect of macro and microstructure on the mechanical and corrosion behaviour of an innovative LPBF-processed AlSi9Cu3 alloy, Corros. Sci. 258 (2026). https://doi.org/10.1016/j.corsci.2025.113410.
[236] J. Kim, S. Shin, S. Lee, Correlation between microstructural evolution and corrosion resistance of hypoeutectic Al–Si–Mg alloy: Influence of corrosion product layer, Mater. Charact. 193 (2022). https://doi.org/10.1016/j.matchar.2022.112276.
[237] E.M.A. Mccloy, EVALUATION OF THE CORROSION CHARACTERISTICS OF SLM ALSI10MG WELDED WITH ER5356 AND ER4047 FILLER WIRE, 2021.
[238] P. Wei, M. Wu, D. Liu, Z. Zhao, Y. Liang, Z. Dong, Electrochemical Corrosion Behavior of MIG-Welded 7N01-T4 Aluminum Alloy by ER5356 and ER5087 Welding Wires, Materials 15 (2022). https://doi.org/10.3390/ma15103737.
[239] K.E. Ahmed, B.M. Nagesh, B.S. Raju, D.N. Drakshayani, Studies on the effect of welding parameters for friction stir welded AA6082 reinforced with Aluminium Oxide, in: Mater. Today Proc., Elsevier Ltd, 2020: pp. 108–119. https://doi.org/10.1016/j.matpr.2019.10.059.
[240] P.M.G.P. Moreira, M.A.V. de Figueiredo, P.M.S.T. de Castro, Fatigue behaviour of FSW and MIG weldments for two aluminium alloys, Theoretical and Applied Fracture Mechanics 48 (2007) 169–177. https://doi.org/10.1016/j.tafmec.2007.06.001.
[241] J. Adamowski, M. Szkodo, 404 Journal of Achievements in Materials and Manufacturing Engineering, n.d. www.journalamme.org.
[242] M. Abbasi Gharacheh, A.H. Kokabi, G.H. Daneshi, B. Shalchi, R. Sarrafi, The influence of the ratio of "rotational speed/traverse speed" (ω/v) on mechanical properties of AZ31 friction stir welds, Int. J. Mach. Tools Manuf. 46 (2006) 1983–1987. https://doi.org/10.1016/j.ijmachtools.2006.01.007.
[243] A.K. Hussein, O.S. Barrak, M.M. Hamzah, S.K. Hussein, Friction stir welding AA6061-T6 with multi-objective optimization of parameters, Advances in Science and Technology Research Journal 19 (2025) 162–172. https://doi.org/10.12913/22998624/207049.
[244] Y. Zhao, J. Han, J.P. Domblesky, Z. Yang, Z. Li, X. Liu, Investigation of void formation in friction stir welding of 7N01 aluminum alloy, J. Manuf. Process. 37 (2019) 139–149. https://doi.org/10.1016/j.jmapro.2018.11.019.
[245] H. Das, D. Chakraborty, T. Kumar Pal, High-cycle fatigue behavior of friction stir butt welded 6061 aluminium alloy, Transactions of Nonferrous Metals Society of China (English Edition) 24 (2014) 648–656. https://doi.org/10.1016/S1003-6326(14)63107-1.
[246] Z. Yang, I. Erdle, C. Liu, J. Banhart, Clustering and precipitation in Al-Mg-Si alloys during linear heating, J. Mater. Sci. Technol. 120 (2022) 78–88. https://doi.org/10.1016/j.jmst.2021.11.062.

[247] M.M. Moradi, H. Jamshidi Aval, R. Jamaati, S. Amirkhanlou, S. Ji, Microstructure and texture evolution of friction stir welded dissimilar aluminum alloys: AA2024 and AA6061, J. Manuf. Process. 32 (2018) 1–10. https://doi.org/10.1016/j.jmapro.2018.01.016.
[248] P.K. Ma, D.P. Jiang, H.L. Jia, Y.X. Zhang, Y.H. Yang, W. Liu, J.W. Song, M. Zha, Microstructures and mechanical behaviors of FSW 6082-T6 Al alloy joints, Int. J. Mech. Sci. 310 (2026). https://doi.org/10.1016/j.ijmecsci.2025.111072.
[249] G. Moeini, S. V. Sajadifar, T. Wegener, C. Rössler, A. Gerber, S. Böhm, T. Niendorf, On the influence of build orientation on properties of friction stir welded Al-Si10Mg parts produced by selective laser melting, Journal of Materials Research and Technology 12 (2021) 1446–1460. https://doi.org/10.1016/j.jmrt.2021.03.101.
[250] N. Minhas, V. Sharma, S.S. Bhadauria, Enhancing the properties of friction stir welded joints of L-PBF printed AlSi10Mg alloy via multi-variable optimization, Archives of Civil and Mechanical Engineering 23 (2023). https://doi.org/10.1007/s43452-022-00601-7.
[251] A. Thakur, S. Mehlwal, N. Minhas, V. Sharma, Influence of tool rotational speed on the microstructural characterization and mechanical properties of friction stir welded Al-Si10Mg parts produced by DMLS additive manufacturing process, Materials Science and Engineering: B 278 (2022). https://doi.org/10.1016/j.mseb.2022.115612.
[252] X.H. Zeng, P. Xue, D. Wang, D.R. Ni, B.L. Xiao, K.S. Wang, Z.Y. Ma, Material flow and void defect formation in friction stir welding of aluminium alloys, Science and Technology of Welding and Joining 23 (2018) 677–686. https://doi.org/10.1080/13621718.2018.1471844.
[253] S. Verma, Meenu, J.P. Misra, Study on temperature distribution during Friction Stir Welding of 6082 aluminum alloy, in: Mater. Today Proc., Elsevier Ltd, 2017: pp. 1350–1356. https://doi.org/10.1016/j.matpr.2017.01.156.
[254] N.T. Kumbhar, S.K. Sahoo, I. Samajdar, G.K. Dey, K. Bhanumurthy, Microstructure and microtextural studies of friction stir welded aluminium alloy 5052, Mater. Des. 32 (2011) 1657–1666. https://doi.org/10.1016/j.matdes.2010.10.010.
[255] T. Huang, L. Shuai, A. Wakeel, G. Wu, N. Hansen, X. Huang, Strengthening mechanisms and Hall-Petch stress of ultrafine grained Al-0.3%Cu, Acta Mater. 156 (2018) 369–378. https://doi.org/10.1016/j.actamat.2018.07.006.
[256] J. Zhao, C.S. Wu, H. Su, Acoustic effect on the tensile properties and metallurgical structures of dissimilar friction stir welding joints of Al/Mg alloys, J. Manuf. Process. 65 (2021) 328–341. https://doi.org/10.1016/j.jmapro.2021.03.057.
[257] F. Andreatta, L. Fedrizzi, The use of the electrochemical micro-cell for the investigation of corrosion phenomena, Electrochim. Acta 203 (2016) 337–349. https://doi.org/10.1016/j.electacta.2016.01.099.
[258] A.I. Ikeuba, C.N. Njoku, O.O. Ekerenam, D.I. Njoku, I.I. Udoh, E.F. Daniel, P.C. Uzoma, I.I.N. Etim, B.O. Okonkwo, A review of the electrochemical and galvanic corrosion behavior of important intermetallic compounds in the context of aluminum alloys, RSC Adv. 14 (2024) 31921–31953. https://doi.org/10.1039/d4ra06070a.
[259] C. Padovani, L. Fratini, A. Squillace, F. Bellucci, ELECTROCHEMICAL ANALYSIS ON FRICTION STIR WELDED AND LASER WELDED 6XXX ALUMINIUM ALLOYS T-JOINTS, n.d.
[260] M. Cabrini, S. Lorenzi, C. Testa, T. Pastore, D. Manfredi, M. Lorusso, F. Calignano, P. Fino, Statistical approach for electrochemical evaluation of the effect of heat treatments on the

corrosion resistance of AlSi10Mg alloy by laser powder bed fusion, Electrochim. Acta 305 (2019) 459–466. https://doi.org/10.1016/j.electacta.2019.03.103.

[261] Y. Zou, Q. Liu, Z. Jia, Y. Xing, L. Ding, X. Wang, The intergranular corrosion behavior of 6000-series alloys with different Mg/Si and Cu content, Appl. Surf. Sci. 405 (2017) 489–496. https://doi.org/10.1016/j.apsusc.2017.02.045.

[262] C. Yang, B.B. Wang, B.H. Yu, L.H. Wu, P. Xue, X.M. Zhang, G.Z. He, D.R. Ni, B.L. Xiao, K.S. Wang, Z.Y. Ma, High-cycle fatigue and fracture behavior of double-side friction stir welded 6082Al ultra-thick plates, Eng. Fract. Mech. 226 (2020). https://doi.org/10.1016/j.engfracmech.2020.106887.

[263] M.B. Prime, T. Gnäupel-Herold, J.A. Baumann, R.J. Lederich, D.M. Bowden, R.J. Sebring, Residual stress measurements in a thick, dissimilar aluminum alloy friction stir weld, Acta Mater. 54 (2006) 4013–4021. https://doi.org/10.1016/j.actamat.2006.04.034.

[264] A. Turnbull, Corrosion pitting and environmentally assisted small crack growth, Proceedings of the Royal Society A: Mathematical, Physical and Engineering Sciences 470 (2014). https://doi.org/10.1098/rspa.2014.0254.

[265] Z. Wang, Y. Xue, R. Wang, J. Wu, Y. Zhang, H. Xue, Review on crack growth driving force at the tip of stress corrosion cracking in the safe end dissimilar metal welded joint, Nuclear Engineering and Design 429 (2024). https://doi.org/10.1016/j.nucengdes.2024.113609.

[266] E. Uribe-Lam, C.D. Treviño-Quintanilla, E. Cuan-Urquizo, O. Olvera-Silva, Use of additive manufacturing for the fabrication of cellular and lattice materials: a review, Materials and Manufacturing Processes 36 (2021) 257–280. https://doi.org/10.1080/10426914.2020.1819544.

[267] A. Seharing, A.H. Azman, S. Abdullah, A review on integration of lightweight gradient lattice structures in additive manufacturing parts, Advances in Mechanical Engineering 12 (2020). https://doi.org/10.1177/1687814020916951.

[268] T. Decker, S. Kedziora, C. Wolf, Practical Implementation of Functionally Graded Lattice Structures in a Bicycle Crank Arm, n.d.

[269] H. Yin, W. Zhang, L. Zhu, F. Meng, J. Liu, G. Wen, Review on lattice structures for energy absorption properties, Compos. Struct. 304 (2023). https://doi.org/10.1016/j.compstruct.2022.116397.

[270] Y. Chang, H. Joo, W. Yong, Y. Jo, S. Kim, H. Kim, Y.W. Kim, K.T. Kim, J.M. Park, A Parametric Study on the L-PBF Process of an AlSi10Mg Alloy for High-Speed Productivity of Automotive Prototype Parts, Journal of Powder Materials 31 (2024) 390–398. https://doi.org/10.4150/jpm.2024.00325.

[271] E. Ossola, A.A. Shapiro, A. Pate, S. Firdosy, E. Brusa, R. Sesana, Fabrication defects and limitations of AlSi10Mg lattice structures manufactured by selective laser melting, Proceedings of the Institution of Mechanical Engineers, Part L: Journal of Materials: Design and Applications 235 (2021) 2071–2082. https://doi.org/10.1177/14644207211012726.

[272] U. Gebhardt, T. Gustmann, L. Giebeler, F. Hirsch, J.K. Hufenbach, M. Kästner, Additively manufactured AlSi10Mg lattices – Potential and limits of modelling as-designed structures, Mater. Des. 220 (2022). https://doi.org/10.1016/j.matdes.2022.110796.

[273] Li, Title: Fatigue properties of triangular and octet-truss lattices, n.d. http://research-information.bristol.ac.uk.

[274] M.R. O'Masta, L. Dong, L. St-Pierre, H.N.G. Wadley, V.S. Deshpande, The fracture toughness of octet-truss lattices, J. Mech. Phys. Solids 98 (2017) 271–289. https://doi.org/10.1016/j.jmps.2016.09.009.
[275] M.S. Bisht, V. Gaur, I. V. Singh, On mechanical properties of SLM Al–Si alloy: Role of heat treatment-induced evolution of silicon morphology, Materials Science and Engineering: A 858 (2022). https://doi.org/10.1016/j.msea.2022.144157.
[276] N. Nudelis, P. Mayr, Defect-based analysis of the laser powder bed fusion process using X-ray data, International Journal of Advanced Manufacturing Technology 123 (2022) 3223–3232. https://doi.org/10.1007/s00170-022-10407-9.
[277] J.C. Hastie, M.E. Kartal, L.N. Carter, M.M. Attallah, D.M. Mulvihill, Classifying shape of internal pores within AlSi10Mg alloy manufactured by laser powder bed fusion using 3D X-ray micro computed tomography: Influence of processing parameters and heat treatment, Mater. Charact. 163 (2020). https://doi.org/10.1016/j.matchar.2020.110225.
[278] T. Peng, K. Kellens, R. Tang, C. Chen, G. Chen, Sustainability of additive manufacturing: An overview on its energy demand and environmental impact, Addit. Manuf. 21 (2018) 694–704. https://doi.org/10.1016/j.addma.2018.04.022.
[279] C. Oliveira, M. Maia, J.M. Costa, Production of an Office Stapler by Material Extrusion Process, using DfAM as Optimization Strategy, U.Porto Journal of Engineering 9 (2023) 28–41. https://doi.org/10.24840/2183-6493_009-001_001635.
[280] J.M. Costa, Teaching Design for AM to Science Materials Engineering Graduate Students: Hand-on Approach, Modern Concepts in Material Science 6 (2024). https://doi.org/10.33552/mcms.2024.06.000640.
[281] D. Brackett, I. Ashcroft, R. Hague, TOPOLOGY OPTIMIZATION FOR ADDITIVE MANUFACTURING, n.d.
[282] J. Plocher, A. Panesar, Review on design and structural optimisation in additive manufacturing: Towards next-generation lightweight structures, Mater. Des. 183 (2019). https://doi.org/10.1016/j.matdes.2019.108164.
[283] O. Ibhadode, Z. Zhang, J. Sixt, K.M. Nsiempba, J. Orakwe, A. Martinez-Marchese, O. Ero, S.I. Shahabad, A. Bonakdar, E. Toyserkani, Topology optimization for metal additive manufacturing: current trends, challenges, and future outlook, Virtual Phys. Prototyp. 18 (2023). https://doi.org/10.1080/17452759.2023.2181192.
[284] J. Su, W.L. Ng, J. An, W.Y. Yeong, C.K. Chua, S.L. Sing, Achieving sustainability by additive manufacturing: a state-of-the-art review and perspectives, Virtual Phys. Prototyp. 19 (2024). https://doi.org/10.1080/17452759.2024.2438899.
[285] N.A.S. Sotomayor, F. Caiazzo, V. Alfieri, Enhancing design for additive manufacturing workflow: Optimization, design and simulation tools, Applied Sciences (Switzerland) 11 (2021). https://doi.org/10.3390/app11146628.
[286] X.H. Arvelo Rodriguez, Designing for Sustainable Bicycle Manufacturing, n.d. https://repository.rit.edu/theses.
[287] Z. Sánchez, P. Hollins, M. Zamora, Topological Optimisation of Bicycle Frame Connections Using 3D Printing Design Font i Codinachs, Roc Title: Topological optimisation of bicycle frame connections using 3D printing design, 2023.

[288] J.F. Teixeira, H. Rocha, A. Couto, Intermodal mobility: A psychometric and behavioural analysis of public transport users in Porto Metropolitan Area, Travel Behav. Soc. 40 (2025). https://doi.org/10.1016/j.tbs.2025.101027.
[289] N.T. Aboulkhair, I. Maskery, C. Tuck, I. Ashcroft, N.M. Everitt, Improving the fatigue behaviour of a selectively laser melted aluminium alloy: Influence of heat treatment and surface quality, Mater. Des. 104 (2016) 174–182. https://doi.org/10.1016/j.matdes.2016.05.041.
[290] I. Koutiri, E. Pessard, P. Peyre, O. Amlou, T. De Terris, Influence of SLM process parameters on the surface finish, porosity rate and fatigue behavior of as-built Inconel 625 parts, J. Mater. Process. Technol. 255 (2018) 536–546. https://doi.org/10.1016/j.jmatprotec.2017.12.043.
[291] M.A. Bernevig-Sava, C. Stamate, N.M. Lohan, A.M. Baciu, I. Postolache, C. Baciu, E.R. Baciu, Considerations on the surface roughness of SLM processed metal parts and the effects of subsequent sandblasting, in: IOP Conf. Ser. Mater. Sci. Eng., Institute of Physics Publishing, 2019. https://doi.org/10.1088/1757-899X/572/1/012071.
[292] B. AlMangour, J.M. Yang, Improving the surface quality and mechanical properties by shot-peening of 17-4 stainless steel fabricated by additive manufacturing, Mater. Des. 110 (2016) 914–924. https://doi.org/10.1016/j.matdes.2016.08.037.
[293] S. Beretta, S. Romano, A comparison of fatigue strength sensitivity to defects for materials manufactured by AM or traditional processes, Int. J. Fatigue 94 (2017) 178–191. https://doi.org/10.1016/j.ijfatigue.2016.06.020.
[294] M.H. Nasab, A. Giussani, D. Gastaldi, V. Tirelli, M. Vedani, Effect of surface and subsurface defects on fatigue behavior of AlSi10Mg alloy processed by laser powder bed fusion (L-PBF), Metals (Basel). 9 (2019). https://doi.org/10.3390/met9101063.
[295] S. Fini, D. Croccolo, M. De Agostinis, G. Olmi, L. Paiardini, C. Scapecchi, M. Mele, Fatigue response of AlSi10Mg by laser powder bed fusion: influence of build orientation, heat, and surface treatments, Progress in Additive Manufacturing 10 (2025) 1385–1403. https://doi.org/10.1007/s40964-024-00712-y.
[296] N.E. Uzan, R. Shneck, O. Yeheskel, N. Frage, Fatigue of AlSi10Mg specimens fabricated by additive manufacturing selective laser melting (AM-SLM), Materials Science and Engineering: A 704 (2017) 229–237. https://doi.org/10.1016/j.msea.2017.08.027.
[297] T. Tomaszewski, Fatigue life analysis of steel bicycle frame according to ISO 4210, Eng. Fail. Anal. 122 (2021). https://doi.org/10.1016/j.engfailanal.2020.105195.
[298] W.S. de Carvalho, J. Draper, T. Terrazas-Monje, A. Toumpis, A. Galloway, S.T. Amancio-Filho, Fatigue life assessment and fracture mechanisms of additively manufactured metal-fiber reinforced thermoplastic hybrid structures produced via ultrasonic joining, Journal of Materials Research and Technology 26 (2023) 5716–5730. https://doi.org/10.1016/j.jmrt.2023.08.305.
[299] P.S. Effertz, V. Infante, L. Quintino, U. Suhuddin, S. Hanke, J.F. Dos Santos, Fatigue life assessment of friction spot welded 7050-T76 aluminium alloy using Weibull distribution, Int. J. Fatigue 87 (2016) 381–390. https://doi.org/10.1016/j.ijfatigue.2016.02.030.